Paramagnetic Defects in CVD Diamonds

Daniel Talbot-Ponsonby
Oriel College

A thesis submitted for the degree of Doctor of Philosophy
at the University of Oxford

Trinity Term, 1997

Paramagnetic Defects in CVD Diamonds

A thesis submitted for the degree of Doctor of Philosophy at the University of Oxford

D. F. Talbot-Ponsonby, Oriel College, Oxford

Trinity Term, 1997

Abstract

Paramagnetic defects in free standing polycrystalline diamond films made by chemical vapour deposition (CVD) have been studied using electron paramagnetic resonance (EPR), electron-nuclear double resonance (ENDOR) and infrared absorption.

EPR experiments at a range of frequencies (1–35 GHz) confirm the ^{1}H hyperfine parameters for the recently identified H1 defect (*Zhou et al., Phys. Rev. B, 54:7881 (1996)*). In the samples studied here, H1 is always accompanied by another defect at g=2.0028(1). Saturation recovery measurements are consistent with two defects centred on g=2.0028. The spin–lattice relaxation rate of H1 is a factor of 10–100 times more rapid than the single substitutional nitrogen centre (N_S^0), which is known to be incorporated into the bulk diamond.

^{1}H matrix ENDOR measurements indicate that the H1 centre is in an environment with hydrogen atoms 2–10 Å distant from the centre. The near neighbour hydrogen identified by the EPR was not detected in the ENDOR experiments. The concentration of H1 correlates with the total integrated C–H stretch absorption in the samples studied here. All the evidence is consistent with H1 being located at hydrogen decorated grain boundaries (or in intergranular material) rather than in the bulk diamond.

The affect of annealing the films *in vacuo* up to 1900 K has been studied. On annealing at 1700 K it was found that some of the hydrogen on internal grain boundaries became mobile but was not lost from the sample, and the intensity of the EPR absorption at g=2.0028 decreased. Annealing at 1900 K severely degraded the optical properties of the samples, and a new defect with g=2.0035(2) was created. Infrared measurements show that hydrogen is lost from most CVD diamond samples when annealed to 1900 K for four hours.

An EPR imaging (EPRI) probe was designed and built. This comprised a 3-loop, 2-gap loop-gap resonator and a pair of anti-Helmholtz coils providing a magnetic field gradient $\partial B_z/\partial z$. Using this probe the distribution of N_S^0 was measured in the growth direction of four CVD diamonds to a resolution of 20 μm. The distribution of N_S^0 is shown to be different to the distribution of defects with g=2.0028.

Two-dimensional images of the spin density of N_S^0 in single crystal type Ib diamonds made by the high temperature and pressure (HTP) method have been generated, demonstrating a resolution of 100 μm. A two-dimensional image of the spin density of g=2.0028 defects in a CVD sample is compared to a photograph of the same sample, showing the correlation between the distribution of the defects with the distribution of non-diamond material in the sample.

The distribution of the $[N–N]^+$ defect in a natural diamond has been examined using $\partial B_z/\partial B_x$ field gradient coils.

Acknowledgements

I would like to thank

Professor R. A. Cowley and Professor R. J. Cashmore, Doctor Lee's Professors of Experimental Philosophy, for providing the facilities of the Clarendon Laboratory,

Professor J. M. Baker and Dr. M. E. Newton for their supervision of this work, their encouragement, and many helpful discussions,

the Clarendon Refrigerants group,

Mr. G. Matthews for his time, patience and humour in the Research workshop,

the staff of the Clarendon Laboratory workshop, especially Mr. M. R. Witney,

Mr. P. J. Hirst, Dr. D. T. Smith and Mr. T. J. Hastings for their aid and advice with electronics,

Dr. G. S. Scarsbrook, Dr. A. J. Whitehead, Dr. R. S. Sussmann, Dr. C. M. Welbourn and Mr. A. Taylor of De Beers Industrial Diamond Division, for the provision of samples and continuing interest in the work,

De Beers Industrial Diamond Division for a CASE award,

the Engineering and Physical Sciences Research Council for a studentship,

the National Biomedical ESR Centre, Milwaukee, USA, for the use of their multi-frequency EPR facilities,

my colleagues Daniel Twitchen, Damian Hunt, James Pfeffer, Owain Tucker and many others for their friendship and companionship,

Rachel Cairns, for her support for the last six years, and encouragement and patience over the last six months, and for proof reading the manuscript,

and my family for their encouragement and support.

Contents

List of Figures

List of Tables

Chapter 1

Introduction

1.1 Diamonds in history

Diamonds have been known to man since about 800 BC. They were found in alluvial deposits in the beds of active or dried up rivers in India, and this was the only known source for 2,000 years. The earliest references to them are hard to isolate, because it is not known positively what certain names refer to. In the Bible, Exodus 28:18, an instruction to Moses, *jahalom*, is translated in the revised version as diamond, but the stone referred to would have been bigger than the famous Koh-i-Nûr diamond. Jeremiah 17:1, written perhaps 600 years later in 600 BC, describes an iron pen with a point of a hard mineral, which may have been diamond. Pliny the Elder wrote about diamonds in about AD 70, mixing rational statements, such as an account of their hardness, with myths about cleaving them using ram's blood. The Alexandrian astronomer Ptolemy (AD 90–168) refers to a diamond river in India. The Greek word ἀδάμας, which means "unconquerable", usually referred to iron or an iron alloy, but Ovid may have meant diamond when he used it in the second half of the first century BC.

The first modern account of diamond is given by Jean Baptiste Tavernier, who described mining of the alluvial deposits in the Kollur gorge of the Krishna river in India, and visited a number of such mines between 1630 and 1688. Apart from

Borneo, where diamonds were probably first mined in the sixteenth century, no sources of diamond outside India were known until 1725, when alluvial deposits were found by the Portuguese in the gravels of river workings in the Minas Gerais region of Brazil. Brazil replaced India as the chief source of supply for the eighteenth and first half of the nineteenth century, and was succeeded by South Africa.

The first record of a diamond discovered in Africa was in 1859 on the banks of the river Vaal, and the first authenticated find was just south of the Orange River in 1867. The rush for diamonds took off in 1869, and the first "pipe mine" at Koffiefontein was started in 1870. Mining started in Kimberley one year later. The Kimberley mine was worked until 1914, by which time it had yielded just over 3 tons of diamond from 25 million tons of rock and earth removed. Today natural diamonds are found in Australia, Zaire, Botswana, Russia, South Africa, Namibia and Brazil, and the worldwide annual production of diamond was around 101 million carats[1] in 1994. Very small (diameter $\sim 10\,\mu m$ or less) diamonds have been found in meteorites. Although not a significant source of supply they have aroused interest and speculation about their origin [1, 2].

1.2 Diamond synthesis and CVD

Natural diamond is no longer the only source of diamond. The synthesis of diamond was first announced by the General Electric company in 1955 [3], and since then the size of synthetic diamonds and volume of production have grown considerably. World production is now of the order of 300 million carats, or three times the production of natural diamonds. A good overview of the technique of production of synthetic diamond by the high temperature and pressure method can be found in Wilks and Wilks [4].

Most of this thesis is concerned with diamond grown by the technique of *Chemical Vapour Deposition* (CVD). Rather than trying to mimic the conditions under which

[1] 1 carat = 200 mg.

diamond is naturally formed in the earth, as is the case with the high temperature and pressure (HTP) method, diamond is grown from a mixture of hydrogen and hydrocarbons in the vapour phase. The first report of diamond grown from a vapour source is that of Eversole [5], who introduced methane at low pressure over fine diamond powders at 1300 K. Although a certain amount of interest persisted, the technique did not take off industrially until substrate surface temperatures and gas phase temperatures were decoupled in 1981 [6, 7, 8]. However, in the years since then the technique has improved very rapidly and a vast number of methods and reactor set-ups has been developed, and the volume of research into the properties and growth mechanisms of CVD diamond is still increasing. The best quality CVD diamond now has thermal and optical qualities comparable to the best natural or synthetic single crystal diamond.

1.3 Applications

The most obvious everyday use of diamonds is as jewellery, and this has been the case almost since their discovery, although in the very early days they were regarded to have supernatural powers and were kept as talismans rather than as "pretty stones".

The largest industrial application of diamond is still in its use in tools for turning, grinding, sawing and drilling, exploiting its remarkable hardness. The size of tools used varies from drill bits in oil wells several kilometres deep to precise surgical implements. The other unique properties of diamond, its exceptionally high thermal conductivity, optical transparency and resistance to corrosion mean that new applications are becoming important with the increase in quantity and quality of available material. Some of these applications are listed below:

- Optical windows: pure diamond transmits light from 0.22 μm in the ultra-violet to $\sim 3.7\,\mu$m in the infra-red, and then again after 6 μm. Even between 2.7 and 6 μm the absorbance is low, but there is high reflectance due to high refractive index. These optical qualities coupled with its scratch resistance, great strength

and chemical inertness make it ideal for windows in harsh environments, such as space craft or pressure cells [9, 10].

- Thermal management: at room temperature natural type IIa diamond has a thermal conductivity five times higher than copper, and diamonds with the percentage of the isotope ^{13}C reduced can have thermal conductivities that are higher still. Diamond is used to fabricate heat sinks for devices such as laser diodes which can require a lot of energy to be dissipated over extremely small areas.

- Radiation detectors: diamond is extremely radiation hard, and recent experiments [11, 12] have shown that CVD diamond detectors would operate with little degradation for ten years in the high radiation zones of the Large Hadron Collider.

- Electronic: diamond is not a good semiconductor, but efforts have been made over the years to dope it to form both p and n-type semiconductors and some diamond devices have been made, of which the most successful have been cold cathode emitters and photodetectors. Boron is a deep acceptor in diamond, but n-type diamonds showing significant conductance still seem some way off [13]. Although diamond is unlikely to ever be a major competitor to modern semiconductors there are a few niche applications where its other properties may prove useful.

As the technology of CVD diamond growth develops, new applications may become apparent. It is already possible to grow diamond films in almost any physical configuration, and their use as protective coatings is an obvious possibility. Wires have been coated with diamond, and the idea of a diamond fibre composite material is not far from reality [14]. The low cost of producing the material compared to the HTP method will also invite interest.

1.4 EPR in diamond

Many of the properties of diamonds in practice are affected, or even determined, by the presence of point defects and impurities in the lattice. In order to exploit diamond industrially further it is necessary to understand these defects. A large amount of optical data has been gathered on diamond. Optical techniques are sensitive and frequently experimentally simple, but have been largely unsuccessful in actually identifying the atomic configuration of defects. Electron Paramagnetic Resonance (EPR) is the tool which was largely used in the understanding of the behaviour of point defects or dopants in silicon, in part leading to its large scale use today. In diamond it is extremely sensitive, but limited to defects with unpaired electrons. However, more than 100 paramagnetic defects have been discovered in diamond thus far, and there is steady progress in identifying them.

CVD diamond is generally polycrystalline. This means that one of the key advantages of EPR, its ability to determine the symmetry of defects by recording spectra in many different orientations, is not available when CVD diamonds are examined using this technique. This is probably the chief reason why very little EPR has been done on CVD diamond.[2] However, there are paramagnetic defects in CVD diamond that appear to be unique to this form of diamond, and which have not been identified explicitly by optical methods. The bulk of this thesis is devoted to the study of these defects. As the techniques for the growth of CVD diamond become more sophisticated, it is important to know exactly what is going on during the growth process. EPR can help in identifying defects, and determining what elements are incorporated into the structure as growth progresses. The difference between defects incorporated into the diamond lattice in individual crystallites and defects at the surfaces or in between crystallites can also be investigated.

Double resonance techniques, such as Electron Nuclear Double Resonance (ENDOR) have also recently been applied to diamond [15, 16]. ENDOR has the advantage

[2] A review of the work that has been done is given in the next chapter.

that individual nuclei can be explicitly identified by their g-value, and combines the sensitivity of EPR with the higher resolution of nuclear magnetic resonance (NMR). This technique has not been applied to CVD diamond before and is employed in this thesis to detect protons near EPR defects.

EPR imaging (EPRI) is another manifestation of the EPR technique. It is mainly used in biological research for specimens physically much larger than diamond, although Zommerfelds [17] among others has examined the distribution of nitrogen in diamond. In this thesis the technique has been used to look at the nitrogen distribution in single crystal HTP diamonds, and at nitrogen and hydrogen-related defects in CVD diamond. The groundwork for improving the sophistication of this technique has been laid and it is potentially a very useful tool for examining diamond in the future. In particular, the measurement of the distribution of defects in the growth direction of samples could prove useful in helping to understand some of the mechanisms involved in sample growth, and the role played by nitrogen.

1.5 Diamond classification and defect names

Although this thesis is predominantly concerned with CVD diamond, a brief summary of the classification system for diamond is given here to avoid the necessity of further explanation in the text when natural or HTP diamonds are referred to. Wilks and Wilks [4] give a full explanation of the types of diamond.

Diamonds are essentially classed by the optical centres they contain. Diamonds containing little or no nitrogen are classed as type II. Of such diamonds, those exhibiting no electrical conductivity are type IIa, and semiconducting specimens (usually due to the presence of boron) are classed type IIb. When nitrogen is the major impurity the sample is classed type I. If the nitrogen is present in the form of aggregates the diamond is type Ia: if these aggregates are A-centres (two nitrogen atoms) the diamond is type IaA, and if they are B-centres (four nitrogen atoms) the diamond is type IaB. Diamonds containing nitrogen as single substitutional atoms are classed Ib.

Clearly these classifications are not mutually exclusive and the system is not perfect, but most samples do fit into just one category. Polycrystalline CVD diamond films do not fit neatly into this classification system, and it has not been used to identify them, although all CVD samples would fall into either Ib, or type II.

The convention in EPR when naming defects in diamond has been to use the first letter of the institution or place where the defect was discovered followed by a number, for example R1 was the first defect found at the University of Reading. In general, where the structure of a defect is known, it is labelled in this thesis by the atomic configuration, e.g. the P1 single substitutional nitrogen centre is generally referred to as N_S^0. Here the subscript S stands for substitutional site and the superscript indicates the charge state. The exception to the rule above is the H1 centre discussed in chapters 5 and 6, which has been named as such because it involves hydrogen, rather than after the place of its discovery or identification. This is not to be confused with the H1 optical centre [18]. Optical centres follow a different naming system, but where necessary will again be referred to by their atomic structure.

Chapter 2

Literature Review

2.1 Introduction

The resurgence of interest in diamond as a subject of research in recent years means that the body of literature is increasing at a rate so fast that there is no possibility of covering it all in one short review. Even on the subject of CVD diamond alone, there were more than a thousand papers published within the last three years. If the related topic of amorphous, or "diamond-like", carbon is included then a complete review would be long indeed. For an overall review of the current state of research using EPR techniques in diamond, the reader is referred to the theses of Newton, Cox, Tucker and Twitchen[1] [19, 20, 21, 22]. As most of this thesis is devoted to EPR in CVD diamond, the review presented here will concentrate on that, paying particular attention to the behaviour of hydrogen and nitrogen in CVD diamond. However, a short overview of the growth techniques of CVD diamond will also be presented.

2.2 Diamonds and diamond physics

The state of research in diamond as a whole is well represented in two books by Field [23, 24] and Wilks and Wilks [4]. These give a good overview of the growth,

[1] In preparation—expected publication 1997.

classification, properties and applications of diamond, although much work in CVD particularly has been done since their publication. A great deal of attention in both books is also given to the mechanical properties of diamond. Davies [25] has brought together a great deal of information and devotes more space to the properties of impurities in diamond. This book also includes a large section reviewing the state of the art in CVD growth as it was in 1994.

2.3 CVD Diamond Growth

The idea that it was possible to grow diamond from the vapour phase is not a new one. Experiments were being performed in the early 1950s, and it was certainly no foregone conclusion that diamond would be made by the high temperature and pressure (HTP) method before the CVD method. However, the first report of diamond grown from a vapour source was in 1962 by Eversole [5], who introduced methane at 0.15 Torr over fine diamond powders at 1300 K. A detailed set of experiments was made by Angus *et al* in 1968 [26], who passed methane at 0.3 Torr over diamond powders of size 0–1 μm and 1.5 μm at 1050°C and observed increases in the weight of the powder of up to 15 %.

It was not until 1981 that it became possible to grow diamond on substances other than diamond. Spitsyn, Bouilov and Derjaguin [6] continued work begun by Derjaguin *et al.* [27] in 1968, based on the addition of atomic hydrogen to the methane. This atomic hydrogen was generated from molecular hydrogen either by a hot filament or electric discharge in the methane, and has the effect of keeping the growing diamond free of graphite, and it also appears to promote the growth process. Spitsyn *et al.* [6] were the first to show that the temperature of the substrate had a critical effect on whether the diamond was single or polycrystalline, and were also able to grow diamond on substrates made of materials such as copper, tungsten and silicon. The rate of nucleation of the diamonds was between 10 and 100 times faster on elements forming carbides, and about 100 times faster on polycrystalline than single crystal

material. The rate of nucleation was greatly enhanced by scratching the substrate prior to deposition.

These techniques were developed further by Matsumoto *et al.* [7]. Methane was again used as the carbon source but the concentration of hydrogen was greatly increased: the molecular *methane* concentration was 0.5–5%. The atomic hydrogen was produced from the molecular hydrogen by a tungsten filament at 2000°C. The gas pressure was 10–100 Torr and $\sim 5\,\mu m$ crystals were deposited on silicon, molybdenum and silica substrates. The morphology of the crystals depended on pressure, temperature, rate of flow and constitution of the gas mixture.

After the breakthroughs described above, the number of techniques for growing diamond from the vapour phase has multiplied fast. The techniques differ essentially in the methods used to create atomic hydrogen and decompose carbon carrier gases. The most common gas phase activation methods, with references, are as follows:

- Hot filaments [7, 28, 29]. This was the first gas phase activation method, as described above. It is a relatively cheap method to set up, but the diamonds can contain traces of the filament material. The filament is usually between 2000°C and 2400°C, and the growth rates are of the order of 1 μm per hour. The hot filament technique is summarised by Haubner and Lux [30] and Gat and Angus [31] in the datareview edited by Davies [25].

- Combustion flames [32, 33, 34, 35, 36]. This is a fairly recently developed technique. Most combustion CVD processes use a simple oxyacetylene torch with the substrate placed in the feather. It is possible to perform *in situ* diagnostics of the physical properties of the transient gas species in the flames [37, 38, 39, 40, 41, 42], thus helping gain understanding of the chemical processes taking place. The combustion technique is summarised by Morrison and Glass [43].

- DC Plasma [44, 45, 46, 47]. This is the simplest way to form an electrical discharge at low pressures. The gas temperature remains fairly low, and some-

times the substrate must be heated to bring it to the desired temperature. The substrate is placed on the anode of the reactor; if it is placed on the cathode then amorphous carbon is preferentially formed. The growth rate varies from $< 0.1\,\mu$m per hour at low pressure and power up to 20–250 μm per hour at 200 mbar and 0.5–10 A cm^{-2}. The temperature varies from 1400°C at low pressure/power up to $>$ 6000°C for high pressure/power. The substrate temperature is 600–1100°C.

- DC Arcs and DC Jets. If the pressure in a DC plasma system is increased a plasma jet can be generated [48, 49]. This approach was first used by Matsumoto and researchers at Fujitsu Laboratories [50]. The substrate is typically cooled to maintain a temperature of 800–1100°C, and the gas is maintained at >5000°C. Linear growth rates vary from 20–1000 μm hour^{-1}: good diamond quality is obtained for $P > 40$ mbar [51].

- Radiofrequency Plasmas [52, 53, 54, 55]. This technique would seem to be the most likely to be easily scaled up to industrial levels, due to the availability of fully developed equipment capable of coating a variety of substrates with a variety of coating materials. However, at the low pressures needed to take advantage of this method amorphous carbon is formed and not diamond. Atmospheric pressure inductively coupled RF thermal plasma torches are gradually coming to be used [56, 57, 58]. Similar gas mixtures as for the other techniques are used. The substrate is usually at 700–1200°C, and the gas is at $<$ 1500°C for low pressure discharges, or $>$ 5000°C for high pressure torches. Growth rates are $< 0.1\,\mu$m hour^{-1} (low pressure) and 30–180 μm hour^{-1} (RF torch) [51].

- Microwave Plasmas [8, 59, 60, 61, 62, 63, 64]. All of the samples used in this thesis were made by the microwave plasma CVD method. The method was first reported by Kamo *et al* in 1983 [8] using a 2.45 GHz plasma. It is this and the hot filament technique that have moved diamond films closer to an industrially applicable technology. Microwave plasma systems allow for a large

substrate size and reduce contamination problems because it is possible to generate a ball of plasma that only touches the substrate surface [61]. Jiang and Klages [65] demonstrated that a bias voltage between substrate and plasma greatly enhances the nucleation density, doing away with the need for abrasion of the substrate. A good overview of the various sorts of plasma CVD techniques is given by Bachmann [51], comparing the output rates, temperatures, gas composition, flow rates, etc. of the various methods.

In the paper "Towards a general concept of diamond chemical vapour deposition," Bachmann *et al.* [66] collated all the information available at the time (1991) about the different methods of diamond CVD. They introduced a C–H–O phase diagram for the relative concentrations of carbon, hydrogen and oxygen, and discovered that diamond synthesis was only feasible within a well defined region of that diagram. Experiments using all the methods outlined above were included. They were able to predict the outcome of six experiments of their own, and were able to give an explanation for the quality variations of diamonds deposited for different gas mixtures. The "diamond growth" region was situated in the hydrogen-rich area of the phase diagram, and was sandwiched between the carbon-rich area, where amorphous carbon growth was prevalent, and the oxygen-rich area, where no growth took place at all. The vast majority of CVD experiments started from $< 5\%$ methane in hydrogen: with any more methane than this no diamond is grown.

They also showed that the diamond growth rate is heavily dependent on the hot regions in the gas phase, with higher temperatures fostering higher growth rates. New phase diagrams would be necessary for systems which use halogens instead of or as well as oxygen, and there are a few points which do not seem to fit in exactly, but it is the most exhaustive attempt to date to bring the data from all the different methods together.

The chemistry of what is happening at the growth surface of the diamond is the subject of some debate. Under the low pressure conditions used in CVD, diamond should be unstable relative to graphite, yet diamond is formed in practice. There

are two approaches to explaining why this should be the case. The first is to try to understand the gas phase kinetics and behaviour of radicals [66, 67, 68, 69, 70, 71], looking at the systems that produce diamond and working from there. The general conclusion reached using this approach is that the growth species is normally the methyl radical [72, 73], but could be the acetylene molecule [74, 75], and between 1% [75, 76] and 10% [77] of surface sites are unsaturated by diamond under most growth conditions.

The second approach is energetic modelling. This involves calculating the internal energy of formation and migration of surface species. Heggie *et al* [78] give a review of the various theoretical methods used to do this and compare theoretical results with experiment. They also suggest that graphite can play a role in nucleating diamond, rather than simply being formed in competition with it and being etched away. Graphite formation may be a precursor to diamond, converting to diamond by the action of H or other radicals.

A different approach again was put forward by Bar-Yam and Moustakas [79], who suggested that very high vacancy concentrations are present near the growth face of the diamond film, raising the formation energy of graphite above that of diamond, since the formation energy of vacancies is lower in diamond than in graphite. This permits nucleation and stable growth of diamond. This model predicts that the growth of films with low defect concentrations will be difficult. Whether this model is correct or not (and the necessary theoretical vacancy concentration is very high at 1–8%) vacancies may well play a significant role in the growth process.

2.4 CVD Diamond Properties

There is as much in the literature about the characterization of CVD diamond as there is about its growth. Characterization and growth are intrinsically related, as investigations centre on what effect different growth conditions have on the defects incorporated and on the morphology of the samples. CVD diamond seems to have been

examined, like its HTP counterpart, using mainly optical techniques to determine its composition, and mechanically, considering its adhesion to substrates and behaviour as a protective coating. A discussion of the mechanical properties of diamond can be found in Field [24] and Wilks and Wilks [4].

2.4.1 Optical

A general review of the optical absorption and luminescence of diamond can be found in Wilks and Wilks [4]. Many of the defects giving rise to the spectra found in natural and synthetic HTP diamond can be found in samples grown by CVD. There are, however, defects unique to CVD diamond that produce absorption and luminescence bands.

The highest quality CVD produced today has a visible transparency comparable to natural type IIa diamond [80]. However, there is still some absorption in the ultraviolet spectral region not present in natural type IIa diamond.

Infrared

Many samples of CVD diamond exhibit C–H stretch and bend modes in the infrared absorption spectra at around 3000 cm^{-1} and 1400 cm^{-1} [81, 82, 83, 84]. These bands are strong in poor quality CVD diamond, but virtually absent in the highest quality CVD material, suggesting that the hydrogen is not incorporated into the bulk of the crystal. This absorption is discussed at length in chapters 5 and 6.

Silicon–related defects

A luminescence system with a zero-phonon line at 1.681 eV is frequently observed in CVD diamond [85, 86, 87]. Yokota *et al.* [87] found that the relative intensity was a function of the nitrogen doping of their samples. Collins *et al.* [88] were able to show that this line was not the neutral vacancy, as had been suggested by Robins *et al.* [86] and Yokota [87], but involved silicon, as had been suggested by Vavilov

in 1980 [85]. Radiation and annealing experiments performed by Collins *et al.* [89] have demonstrated that a vacancy is trapped at the defect site and it appears that a silicon atom, nitrogen atom and vacancy are all involved. Uniaxial stress and Zeeman splitting measurements performed by Sternschulte *et al.* [90] show that the defect is large, but are consistent with the presence of silicon, nitrogen and a vacancy. Clark *et al.* [91] confirmed the presence of silicon by growing HTP synthetic diamonds doped with silicon. They analyzed the fine structure of the luminescence line and found that the relative strengths of the optical absorption for the three groups of lines was the same as the ratio of abundances of the natural isotopes of silicon, ^{28}Si, ^{29}Si and ^{30}Si. They suggested a model for the defect of a substitutional silicon atom accompanied by a vacancy.

Oxygen–related defects

New cathodoluminescence (CL) peaks have been discovered by Ruan *et al.* [92], who found that there was a difference between the CL spectra of CVD samples grown with and without oxygen. They found an extra peak at 2.561 eV and six other peaks in the range 2.676–2.725 eV in samples grown with 0.1% oxygen in the reaction gas mixture. They concluded that oxygen was being incorporated into the diamond lattice during growth, and that the CL peaks were due to defects associated with oxygen as an impurity in the diamond lattice.

Broadband photoluminescence

There is a broadband luminescence extending from approximately 1.5 to 2.5 eV which has been observed by PL in films grown by a variety of CVD methods [93, 94, 95, 96]. Studies using CL in single crystal types Ia and Ib diamonds have shown that similar broadband luminescence has its origin in the electron–lattice coupling of nitrogen related centres with zero-phonon lines (ZPL) at 1.945 and 2.154 eV [97, 98]. Bergman *et al.* [99] found that the temperature behaviour precluded the possibility that this was the case in CVD, and suggested that the broadband PL is due to optical transitions

in an in-gap state distribution introduced by the amorphous phase of the sp^2 hybrid bonds.

Nitrogen–related centres in PL and CL

Bergman *et al.* [99] found, along with many others [85, 100, 101], the ZPLs at 1.945 and 2.154 eV in films doped with nitrogen. (Many authors quote 2.156 rather than 2.154 eV). Davies *et al.* [98] have suggested that the 1.945 eV line is due to the substitutional nitrogen–vacancy optical centre $[N–V]^-$. Collins and Lawson [97] proposed that the 2.156 eV band results from a transition in a centre consisting of a single substitutional nitrogen atom with one or more vacancies. Behr *et al.* [102] investigated the distribution of the 2.156 eV line in a homoepitaxial sample using Raman spectroscopy and found a pronounced maximum in intensity at the film/substrate interface, indicating enhanced nitrogen incorporation at the interface.

Bergman *et al.* [99] also found a line in PL at 1.967 eV in the N-doped sample, also observed by Ruan *et al.* [103] in CL, which might be due to a nitrogen related centre.

Cathodoluminescence features in undoped films and radiation damage

Studies using CL have shown spectral features common to all undoped films, irrespective of methods of growth, with the blue "band A" centred around 2.8 eV being the predominant feature [104]. On the low energy side of the band A peak, there is a series of ZPLs at 2.33, 2.42, 2.48 and 2.57 eV, and another sharp ZPL is found at 2.99 eV near the maximum of the band A. Khong *et al.* [105] were able to show using time-resolved CL that the 2.99 eV was not the same as the N3 band (ZPL 2.985 eV) observed in natural diamond.

Other systems have been produced by irradiation of single crystal CVD samples [88]. The 2.156 eV ZPL centre discussed above appears, as do systems with ZPLs at 3.188 and 2.807 eV (associated with an interstitial carbon atom together with a single nitrogen atom [97]). The TR12 and 3H systems, with ZPLs at 2.638eV and 2.462 eV

respectively, also appear. On annealing, the TR12 and 3H systems disappear, but the H3 centre is evident (ZPL at 2.463 eV). This is a vacancy trapped at a pair of nearest neighbour substitutional nitrogen atoms. The 3.188 eV line appears in polycrystalline CVD even without radiation damage [100].

2.4.2 Electrical

As with the optical properties, the electronic properties of CVD diamond can generally be understood using data established for bulk diamond. The major differences lie in the fact that, in polycrystalline material, scattering at the grain boundaries drastically reduces the carrier mobilities, and electronic surface states at the grain boundaries act as donors, which compensate p-type acceptors. The electrical properties of diamond are summarised in Davies [25], and a useful short overview of p-type conductivity in diamond can be found in Collins [106].

p-type conductivity

Boron doping of polycrystalline CVD films produces semiconducting material; the boron acts as an acceptor just as in single crystal diamond. The carrier concentration shows a very sharp drop with decreasing dopant density [107]. This is also the case for B-doped polycrystalline silicon, and von Windheim *et al.* [107] attribute this to surface states at grain boundaries acting as trapping centres. Mobilities are typically in the range 1–30 $cm^2V^{-1}s^{-1}$ due to scattering of the carriers at grain boundaries [108]. Impurity conduction is observed at high doping levels.

The best behaviour for polycrystalline film is reported by Stoner *et al.* [108]: mobility values of up to 165 $cm^2V^{-1}s^{-1}$ were obtained in a lightly boron-doped layer grown on top of an oriented textured film with {100} faces. The acceptor ionisation energies for such films are around 0.35 eV, close to the value for natural type IIb diamond.

Homoepitaxial CVD diamond layers can provide better mobilities still. Fujimori *et al.* [109] achieved mobilities of 600 $cm^2V^{-1}s^{-1}$ in a {100} layer at a carrier con-

centration of $7 \times 10^{13}\,\mathrm{cm}^{-3}$, although this mobility fell dramatically with increasing carrier concentration, and was less than 8 $\mathrm{cm}^2\mathrm{V}^{-1}\mathrm{s}^{-1}$ at a carrier concentration of $7 \times 10^{16}\,\mathrm{cm}^{-3}$. The mobilities in {110} layers were less than 6 $\mathrm{cm}^2\mathrm{V}^{-1}\mathrm{s}^{-1}$. The temperature dependence of the mobility was similar to that observed for natural type IIb diamond.

Surface conducting layers

Sometimes undoped films which have been exposed to a hydrogen plasma during the shut-down period of growth show similar conductivity to doped films. Gildenblat *et al.* [110] showed that this conductivity could be attributed to a surface conducting layer and could be removed by chemical cleaning. They also showed that natural type IIa diamond exposed to a hydrogen plasma generated a conducting layer. Hydrogenation of the surface leads to a *p*-type conducting layer and field effect transistors have been fabricated using this layer [111].

n-type conductivity

Many samples of CVD and natural type IIa diamond exhibit small levels of *n*-type conduction at high temperatures, with activation energies in the region 1.6–2.0 eV [13]. This is probably associated with the small concentrations of isolated substitutional nitrogen. No technique has been found to produce a useful level of *n*-type conductivity in any diamond. Attempts have been made to dope with lithium [112] and phosphorus [113]. The phosphorus incorporation seems to be almost exclusively at grain boundaries [114], and films doped with P are highly resistive [114].

2.4.3 Thermal conductivity

Diamond has a higher thermal conductivity than any other material. The chief mechanism for limiting thermal conductivity in diamond at room temperature is phonon scattering by defects. The highest thermal conductivity reported in single crystal

diamond with natural abundance ^{13}C is 25 $W\,cm^{-1}K^{-1}$ [115]. Conventional Debye theory predicts that isotopically enriching diamond with ^{12}C should improve the conductivity by ~ 5 %, but Anthony *et al.* [116] successfully grew a sample with 0.07 % ^{13}C which had a thermal conductivity of 33.2 $W\,cm^{-1}K^{-1}$. Berman [24, 117] showed that this was still in accordance with theory if three-phonon normal (N) processes are considered in the phonon scattering as well as Umklapp processes.

In the case of CVD material, thermal conductivity was originally found to be significantly below the values for the best single crystals. Morelli *et al.* [118] in 1988 measured thermal conductivities of 10 $W\,cm^{-1}K^{-1}$, and successfully fitted the temperature dependence of their data above 30 K, by considering the extra scattering by grain boundaries. In 1993 [119] they measured the mean free path of the phonons in better samples (room temperature $\kappa = 17.8\,W\,cm^{-1}K^{-1}$), and found it to be bigger than the grain size. They concluded that some phonons were being transmitted through grain boundaries, but that there was a lot of scattering by defects at grain boundaries.

McNamara-Rutledge *et al.* [120] found that the thermal conductivity of polycrystalline films was dependent on the quantity of hydrogen in the films, measured by NMR and IR absorption, and that the majority of hydrogen was rigidly bound in passivation of surfaces. The films they studied contained varying amounts of hydrogen, and the thermal conductivities varied over the range 1–22 $W\,cm^{-1}K^{-1}$. The thermal conductivities were in general lower than predicted from scattering at grain boundaries alone and they predicted that voids of similar dimension to the phonon mean free path that they found in their samples were also significant. They also recorded anisotropies in the thermal conductivity: κ parallel to the growth surface increases with film thickness, but levels off after film thickness of 200 μm. κ normal to the growth surface is greater than $\kappa_{||}$. This is in accord with other authors' observations [121] and reflects the morphology of the columnar growth of the films.

Graebner *et al.* [122] grew CVD films isotopically enriched so that they contained only 0.055% ^{13}C. They obtained thermal conductivities normal to and parallel to the

growth surface of $\kappa_\perp = 26$ and $\kappa_{||} = 21.8\,\mathrm{W\,cm^{-1}K^{-1}}$. They concluded that the high conductivity, though improved by purification, is still limited by extrinsic scattering mechanisms and even higher conductivity can be expected with more perfect CVD made with isotopically enriched methane.

2.5 EPR in CVD diamond

Despite the large volume of work performed by EPR in diamond, relatively little work has been done on CVD using this technique. However, since 1988, when the first reports of EPR in CVD diamond appeared [123], there has been a steadily increasing volume of work appearing, with a surge of interest in the last two years. Some of the reports seem to contradict others, and this discussion attempts to sort out where the consensus lies. Not many paramagnetic defects have been identified in CVD diamond: generally only defects arising from the growth process have been studied, with very little in the way of artificially induced defects. Complex centres would be difficult to identify in polycrystalline films because of the lack of information about the symmetry of the defect.

2.5.1 Nitrogen

Watanabe and Sugata [123] were the first to report EPR in CVD diamond. They found signals at $g = 2.0027 \pm 0.0005$ in CVD films grown by the microwave plasma method, which they attributed to dangling bonds (see next section), and another signal with hyperfine structure and the same g-value, which they attributed to single substitutional nitrogen (N_S^0). A comparison with a simulated spectrum of N_S^0 in diamond powder confirmed this attribution.

Hoinkis *et al.* [124] observed a similar signal with much narrower lines ($\Delta B = 21\,\mu\mathrm{T}$), again in microwave plasma CVD, and were able to simulate it successfully using the parameters of the P1 (N_S^0) centre in single crystal diamond ($g = 2.0023$, $A_{||} = 114.0\,\mathrm{MHz}$, $A_\perp = 81.3\,\mathrm{MHz}$). They found the concentration of spins to be of the order

of 10^{17} cm^{-3}, and by using secondary ion mass spectroscopy (SIMS) they measured the total concentration of nitrogen in the samples to be comparable, and concluded that all the nitrogen was incorporated in point defect form.

By contrast, Zhou *et al.* [125] found no correlation between the strength of the N_S^0 signal and the total concentration of nitrogen in microwave plasma CVD samples. They did observe an inverse correlation between N_S^0 concentration and the hydrogen content of the films as measured by NMR. However, for the number of samples shown in their study, this data was by no means conclusive.

Rohrer *et al.* [126] found a different situation again. They grew MWCVD diamond films with a range of concentrations of nitrogen in the source gas of 0–4 %, and using Elastic-Recoil-Detection experiments measured the nitrogen incorporated into the films to be in the range 10–132 ppm. They could initially only observe the signal from N_S^0 centres in the sample with 10 ppm of nitrogen, and even in this sample only 1 % of the nitrogen was paramagnetic; however, when the samples with more nitrogen were illuminated with band-gap UV light the N_S^0 resonance was observed. They concluded that in samples with high nitrogen concentration the nitrogen donors are empty, and that the Fermi level is below the nitrogen donor level, with light exposure causing a partial filling of these states. In a second paper by the same authors [127] the N_S^0 centre is shown to give rise to a deep donor state about 1.5 eV below the conduction band.

Lukins and Khachan [128] also identified N_S^0 in microwave plasma CVD diamond. They demonstrated that the EPR signal saturated at only a few microwatts of microwave power. They also found that in samples grown with argon introduced to the reaction vessel there was no signal from N_S^0 centres.

The signal from N_S^0 has been used by Graeff *et al.* [129] to characterize the disorder in textured polycrystalline CVD films. A study of the possibility of this was also performed by Cox [20]. The broadening of the hyperfine satellite lines by crystal disorder was used to obtain the orientation distribution function of the crystallites in the films. The method was able to distinguish between rotations around the direction

of growth and other contributions to the disorder, and the results were checked against an x-ray analysis.

2.5.2 Dangling bond defects and hydrogen

In 1988 Watanabe *et al.* [123], as well as the N_S^0 centre, observed an EPR resonance at $g = 2.0027 \pm 0.0005$. This resonance has since been observed by many other workers [130, 131, 132, 133, 134, 135, 136, 128, 137, 138, 139, 140, 125, 141, 142, 126, 127, 143, 144, 145, 83, 84], although there are some variations in the lineshapes and widths reported, and a number of different interpretations placed on the presence of the line.

Watanabe *et al.* [123] found that the resonance had "shoulders" and fitted it to a narrow and a broad component. They found that the line was narrower and the spin concentration lower (although still always $\geq 10^{18}\,\mathrm{cm}^{-3}$) for higher quality films (as characterized by Raman). They ascribed the resonance to dangling bonds unpassivated by hydrogen during the growth process.

In 1992 Zhang *et al.* [130] reported a similar defect in HFCVD and arc discharge plasma CVD. Their line had much more pronounced shoulders but they still fitted it to a narrow Gaussian and a broad Gaussian ($\Delta B_{p-p} = 0.36$ mT and 1.25 mT respectively), which they ascribed to unpaired electrons in bonds of C atoms in diamond and graphite respectively. They found variations in the spin density when the sample was annealed in a nitrogen atmosphere at temperatures 200–800°C, but there was no overall trend. They also examined the C–H region in the IR absorption spectra, and found that the absorption decreased on annealing. They concluded that the C–H bonds broken during annealing were the same as the dangling bonds giving rise to the EPR spectra.

Many other groups have adopted the same method of fitting the line to a narrow and a broad component. Jia *et al.* [133] fitted their line to two Lorentzians rather than Gaussians ($\Delta B_{p-p} = 0.14$ mT and 0.45 mT), although they recognized that the shoulders were a separate entity, of which more shortly. Fanciulli and Moustakas [131, 132, 138] fitted to a narrow Lorentzian and broad Gaussian. Our own studies,

published last year [145], seemed to support the fitting to two Lorentzians. Where groups largely differed was in the interpretation of what these lines were, and whether the "shoulders" or satellites, as I shall call them from now on, have any significance.

With regard to the line fitted to a narrow and a broad component, there were two main schools of thought. Following the example of the original paper by Watanabe [123] many workers [130, 136, 143, 144] ascribed the narrow line to sp^3 dangling bonds, i.e. in the diamond phase, and the broad line to sp^2 dangling bonds in amorphous carbon or graphite. Fanciulli and Moustakas [131, 132, 138] agreed that dangling bonds are probably responsible, but suggested that the dangling bonds were in multivacancies or dislocations. They also suggested vacancy related sites could be responsible. The two different linewidths arise because of different local concentrations. Rohrer *et al.* [126] attributed the lines to a vacancy-related defect. They found a linear increase in spin concentration with nitrogen content. They also found evidence of a charge transfer taking place with N_S^0 centres under UV illumination [127]. Other authors simply state that the resonance is due to dangling bonds and do not speculate any further.

Jia *et al.* [133] compared HFCVD grown using H_2-CH_4 mixtures with samples grown using D_2-CD_4 mixtures. They found that in the samples grown with hydrogen the spectra were as reported elsewhere, but when deuterium was used instead of hydrogen the spectra were the same in all respects except that the satellites were not present. They therefore concluded that the lines are caused by spin-$\frac{1}{2}$ defects hyperfine-coupled to nearby protons. They also found that the spectra were unchanged by annealing below $\sim$ 1500°C, but after annealing at 1500°C they were reduced by a factor of $\sim$ 4.5. Zhou *et al.* [125] found the same on annealing.

Holder, Rowan and Krebs [139] broke the mould by fitting their line to two Lorentzians of *identical* width separated by a small amount. They were the first group to consider spectra recorded at microwave frequencies other than X-band (10 GHz): they also recorded spectra at Q-band (35 GHz), and found that the satellites were still visible, but had moved apart, so their separation had increased by a factor of $\sim$ 3. This

suggested to them that there were dipolar interactions between the unpaired electron and neighbouring atoms, causing an admixture of nuclear spin levels and resulting in microwave induced flipping of environmental nuclear spins. They therefore ascribed the whole lineshape to electrons in dangling bonds interacting with protons: in their model the "single" central line is formed by allowed transitions, $\Delta M_I = 0$, and the satellites are formed by forbidden transitions, $\Delta M_I = \pm 1$.

Zhou *et al.* [140, 125] used this theory as a starting point, but obtained spectra at frequencies of 14 GHz and 20 GHz as well as 10 GHz and 35 GHz in an attempt to determine the frequency dependence of the satellites. They found they could explain the whole lineshape by considering a single well defined defect consisting of an unpaired electron spin with a single hydrogen atom ~ 1.9 Å away. They named this defect H1. They also found a second defect at the same g-value which was only observed in samples with low hydrogen concentration, which they concluded was similar but with the hydrogen atom ~ 2.3 Å away. They named this defect H2. They concluded that both defects arise when a single hydrogen atom enters a weak stretched C–C bond at a grain boundary or other extended misfit region, bonding to one carbon and activating the dangling bond of the other as the two carbons relax backwards. The theory for this model is given in §3.2.5 and it is discussed in more detail in §5.2.3.

The results of Zhou *et al.* seem to indicate that the fitting of the line to a narrow and a broad component is incorrect. However, there may be differences between samples examined by different groups. Amorphous carbon, sometimes called diamond-like carbon (DLC), displays an EPR signal at or near $g = 2.0028$ [146], which arises from dangling bonds in the material but which is different to the H1 centre found by Zhou *et al.*, and if films contain a significant quantity of DLC then there may be more than one signal superimposed on top of each other. Not all lines reported at $g = 2.0028$ display the satellites; whether they are simply unresolved because of linewidth or are actually not there is not always clear. Show *et al.* [143, 144] fit spectra from CVD diamond films to narrow and broad Lorentzians with no satellites, and demonstrate

different relaxation times for the two components. They were also able to reduce the broad component by heat treatment of the samples in an oxygen atmosphere. The electrical conductivity decreased at the same temperature (600°C). They concluded that the narrow component was uniformly distributed through the sample while the broad component was concentrated in a "surface conductive layer". Colineau *et al.* [147] grew films doped with varying concentrations of boron. Although they could not see any signals due to the boron, they found that the lines (again fitted to narrow and broad Lorentzians with no satellites) reduced significantly with increasing boron concentration, and that the two components behaved differently. It appears that the model proposed by Zhou *et al.* is a significant step forward in the understanding of these defects, but that there is still a lot of work to be done.

2.5.3 Phosphorus

Although there is no reason why most of the defects observed in HTP or natural diamond could not exist in CVD diamond, the CVD growth process is such that most of them do not occur. For instance, a lot of defects in HTP diamond arise because the growth process involves a metal solvent or catalyst. In CVD, contamination can occur from the sides of the reaction vessel, but in general there are not many elements that can get into the film. Defects seem usually to involve nitrogen, hydrogen or vacancies. As mentioned above, complex defects are hard to identify in a polycrystalline film, because there is no available information about the symmetry of a defect and it is difficult to determine the hyperfine interaction, especially if it is anisotropic.

Phosphorus arouses interest because of its potential as an n-type dopant. Zvanut *et al.* [134] implanted phosphorus during the growth process of microwave plasma CVD films grown on natural type IIa substrates. They observed two lines in the EPR at X-band, 2.7 mT apart, centred on $B = 339$ mT, and ascribed them to hyperfine interactions with a nuclear spin $I = \frac{1}{2}$. Since they did not appear in undoped samples or in similarly doped Na or As-doped samples they ascribed these lines to a phosphorus-related defect. The spin concentration as measured by EPR

was the same as the concentration of P measured by SIMS. As the pair of lines are isotropic they concluded that the phosphorus is in a high symmetry site, probably substitutional. The centre is at least partially ionized at room temperature.

Chapter 3

Theory

3.1 Introduction

In this chapter a brief overview of electron paramagnetic resonance is given, followed by treatment of more specific aspects relevant to the particular experiments undertaken in this thesis. However, the theoretical problems encountered in the imaging experiments (chapter 7) and their solutions are discussed in §7.3.

3.2 EPR and electron spin

The theory of electron paramagnetic resonance is well known, and is described in detail by, among many others, Weil, Wertz and Bolton [148]. A short description will be given here. A constant magnetic field (Zeeman field) is applied to the sample under investigation, together with an oscillating magnetic field perpendicular to it, provided by microwaves of a given frequency. This oscillating field provides quanta of energy which are absorbed by the sample under certain conditions, and it is these conditions which give information about the defect or sample under investigation.

3.2.1 Magnetic dipole of the electron

A magnetic dipole is defined as $\mu_d \equiv I\delta s$, where δs is the area enclosed by a circulating current I. In the classical situation of an electron travelling in a circular orbit of radius r, then $\delta s = \pi r^2$ and $I = qv/2\pi r$, where $q = -e$, the electronic charge, and v is the velocity of the electron. This implies that

$$|\boldsymbol{\mu}_d| \equiv I\delta s = \frac{qv}{2\pi r}\pi r^2 = \frac{q}{2m_e} m_e v r = |\gamma_e \hbar \boldsymbol{l}| \tag{3.1}$$

where γ_e is the *magnetogyric ratio* [149], and $m_e v r$ is equal to the angular momentum. For a quantum mechanical system the angular momentum can be written as $\sqrt{l(l+1)}\hbar$. For an electron in an atomic orbital the equation must be modified slightly by the Dirac equation: an electron has intrinsic spin as well as orbital angular momentum, which contributes to the magnetic moment. For an electron in an s orbital the angular momentum is zero, and the magnetic moment is determined entirely by the spin. This finally gives the relationship between the magnetic moment operator and the spin operator:

$$\hat{\boldsymbol{\mu}} = -\frac{e\hbar}{2m_e c} g_e \hat{\mathbf{S}} \tag{3.2}$$

where $\hat{\mathbf{S}}$ is the spin operator. The Bohr magneton is defined as $\mu_B = e\hbar/2m_e c$. $g_e = 2.0023193044(2)$ is a constant. This was calculated by Dirac to be equal to 2, but quantum electrodynamics (QED) considerations add the 0.0023... correction.

A magnetic field lifts the degeneracy of the spin states of the electron: classical electromagnetism predicts the energy dependence of a magnetic moment in a magnetic field as $E = -\boldsymbol{\mu} \cdot \mathbf{B}$, and quantum mechanically the system is described by the Hamiltonian

$$\mathcal{H} = -\hat{\boldsymbol{\mu}} \cdot \mathbf{B} = g_e \mu_B \hat{\mathbf{S}} \cdot \mathbf{B} \tag{3.3}$$

3.2.2 Resonance conditions

If the z-axis of the spin operator is chosen to coincide with the direction of the Zeeman field then the eigenstates of equation 3.3 are $\left|\pm\frac{1}{2}\right\rangle$ with energies of $E_\pm = \pm\frac{1}{2} g_e \mu_B B$.

If the quanta of energy provided by the microwave photons are in the region of the difference between these energy levels there is a probability that transitions will occur between the energy levels, so in its simplest form the condition for resonance is

$$h\nu = g\mu_B B \tag{3.4}$$

where ν is the frequency of the applied radiation.

There are two variables in equation 3.4, the microwave frequency and the Zeeman field. It is experimentally difficult to vary the frequency of the microwaves, so the microwaves are kept at a constant frequency and the magnetic field is varied, with the change in the absorption of the microwaves recorded.

The Einstein coefficients for induced emission and absorption are equal, which would suggest that no continuous absorption will be observed because the energy levels will populate equally. However, there is normally a thermodynamic distribution of population between the energy levels, maintained by *spin–lattice relaxation*, that is non-radiative relaxation pathways produced by the interaction of the electron with the crystal lattice. This means that there are a greater number of spins in the lower energy levels.

3.2.3 Spin Hamiltonian

Equation 3.3 is over-simplified, as the electron is not isolated but part of a solid-state system. Therefore the electron will experience other interactions, for example with other electrons, with nearby nuclei, or with the crystal field, which will affect the position of the energy levels. These can all be represented in an effective spin Hamiltonian

$$\begin{aligned}\mathcal{H} &= \underbrace{\mu_B \hat{\mathbf{S}} \cdot \underline{\boldsymbol{g}} \cdot \mathbf{B}}_{1} + \underbrace{\hat{\mathbf{S}} \cdot \underline{\hat{\mathbf{D}}} \cdot \hat{\mathbf{S}}}_{2} + \sum_j [\underbrace{\hat{\mathbf{S}} \cdot \underline{\hat{\mathbf{A}}}_j \cdot \hat{\mathbf{I}}_j}_{3} - \underbrace{\mu_N g_{N_j} \hat{\mathbf{I}}_j \cdot \mathbf{B}}_{4} + \underbrace{\hat{\mathbf{I}}_j \cdot \underline{\hat{\mathbf{P}}}_j \cdot \hat{\mathbf{I}}_j}_{5}] \\ &+ \text{higher order terms}\end{aligned} \tag{3.5}$$

where the terms labelled 1–5 are:

1. The electron Zeeman interaction described in the previous section. Spin orbit coupling with excited states has the effect that g is written as a tensor.

2. Electron–electron interactions, described in §3.2.6.

3. Hyperfine interaction of electrons with nuclei having non-zero spin, described in §3.2.4.

4. Nuclear Zeeman interaction (§3.2.4).

5. Nuclear quadrupole interaction. This occurs only for $I \geq 1$.

A short description of some of these terms, where they affect the results in this thesis, is given in the following sections.

3.2.4 Nuclear effects

Terms 3, 4 and 5 in equation 3.5 reflect the contribution of the nuclei to the spin system. The tensor $\underline{\mathbf{A}}$ is normally referred to as the hyperfine interaction. It can be split into an isotropic and anisotropic part. The isotropic interaction, also called the contact or Fermi interaction, depends on the unpaired electron density at the nucleus and is given by:

$$a = A_{\text{iso}} = A_s = \frac{2\mu_0}{3} g_e \mu_B g_N \mu_N |\Phi(0)|^2 \tag{3.6}$$

where μ_N is the nuclear magneton, or $e\hbar/2m_pc$, and g_N is the g-factor of the nucleus. $\Phi(0)$ is the wavefunction of the electron at the nucleus. This interaction arises for s electrons which have a non-zero distribution function at the nucleus. For the two nuclei normally encountered in diamond, the unpaired electron (2s) produces a coupling of 1881 MHz for ^{14}N and 3777 MHz for ^{13}C [150].

The anisotropic dipolar term is produced by the magnetic dipolar interaction between the nucleus and the electron. This is the case for an electron in a p orbital, or for nuclei at a distance from the electron. The Hamiltonian for this dipolar interaction

is given by:

$$\mathcal{H}_{dip} = \left(\frac{\mu_0}{4\pi}\right)\left[\frac{\hat{\boldsymbol{\mu}}_1 \cdot \hat{\boldsymbol{\mu}}_2}{r^3} - \frac{3(\hat{\boldsymbol{\mu}}_1 \cdot \boldsymbol{r})(\hat{\boldsymbol{\mu}}_2 \cdot \boldsymbol{r})}{r^5}\right] \tag{3.7}$$

where r is the vector between the two dipoles. For the magnetic dipoles of an electron and a nucleus, as considered here, the approximate contribution to the Hamiltonian can be written as

$$\mathcal{H}_{dip} = -\left(\frac{\mu_0}{4\pi}\right)\mu_B\mu_N g_N \hat{\mathbf{S}} \cdot \underline{\boldsymbol{g}} \cdot \underline{\mathbf{T}} \cdot \mathbf{I} \tag{3.8}$$

where

$$\underline{\mathbf{T}} = \begin{pmatrix} \left\langle \frac{r^2-3x^2}{r^5} \right\rangle & -\left\langle \frac{3xy}{r^5} \right\rangle & -\left\langle \frac{3xz}{r^5} \right\rangle \\ -\left\langle \frac{3xy}{r^5} \right\rangle & \left\langle \frac{r^2-3y^2}{r^5} \right\rangle & -\left\langle \frac{3yz}{r^5} \right\rangle \\ -\left\langle \frac{3xz}{r^5} \right\rangle & -\left\langle \frac{3yz}{r^5} \right\rangle & \left\langle \frac{r^2-3y^2}{r^5} \right\rangle \end{pmatrix}$$

$\underline{\mathbf{T}}$ is often considered to have an angular dependence of $1 - 3\cos^2\theta$, although this is only a first order approximation [151]. Small contributions are made to the hyperfine interaction by polarization, correlation and relativistic effects [20].

When the hyperfine interaction is axial the number of free parameters reduces to two, and the tensor can be written

$$\underline{\mathbf{A}} = \begin{pmatrix} A_{\|} & 0 & 0 \\ 0 & A_{\perp} & 0 \\ 0 & 0 & A_{\perp} \end{pmatrix} \tag{3.9}$$

and can be separated into its isotropic and anisotropic parts, labelled a and b respectively:

$$a = (A_{\|} + 2A_{\perp})/3 \tag{3.10}$$

$$b = (A_{\|} - A_{\perp})/3 \tag{3.11}$$

The nuclear Zeeman interaction (term 4 in equation 3.5) is analogous to the electron Zeeman interaction. It is useful as a means of identifying nuclei directly by determination of their g-values. It is not usually possible to determine g_N from EPR measurements as the strong allowed electronic transitions obey the selection rules $\Delta m_S = 1$, $\Delta m_I = 0$ and are therefore independent of the interaction. It is, however, possible to measure g_N accurately when performing ENDOR experiments.

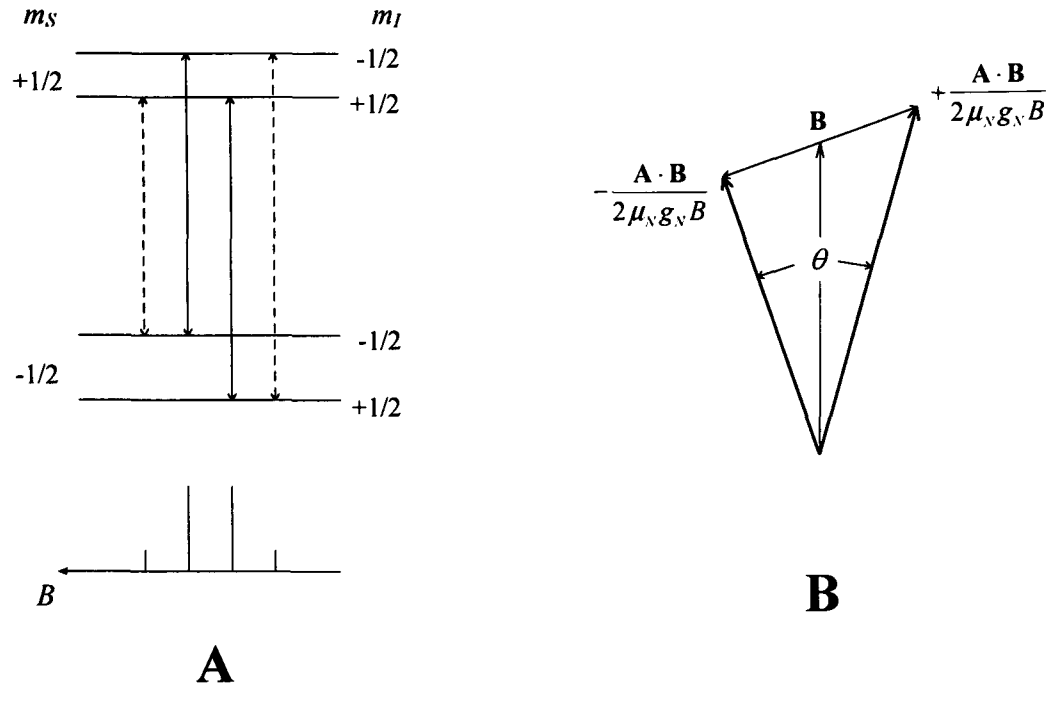

Figure 3.1: (A) Energy level diagram showing allowed (solid arrows) and forbidden (dotted arrows) EPR transitions for an $S = \frac{1}{2}$ electron spin coupled to an $I = \frac{1}{2}$ nucleus with $|\mathbf{A}| < 2|g_N \mu_N \mathbf{B}|$. (B) The effective magnetic field at the nucleus for the two m_S states.

3.2.5 The H1 centre

The H1 centre in polycrystalline CVD diamond is described in §5.2.3 and §5.4.2. The EPR signal consists of a central line with two satellites. The theory is explained by Zhou *et al.* [125] but it provides a good example of the combination of the hyperfine interaction and the nuclear Zeeman interaction, and is fundamental to almost all the spectra examined in this thesis, so a brief description is given here.

The H1 centre is known to consist of an electron with spin $S = \frac{1}{2}$. It is thought that the satellites on the EPR line are caused by forbidden nuclear spin flip transitions of a hydrogen atom weakly coupled to the unpaired electron spin [139], so we are looking at a proton with nuclear spin $I = \frac{1}{2}$. The spin Hamiltonian for such a system with isotropic g is

$$\mathcal{H} = g\mu_B \mathbf{S}\cdot\mathbf{B} + \mathbf{S}\cdot\underline{\mathbf{A}}\cdot\mathbf{I} - g_N\mu_N \mathbf{I}\cdot\mathbf{B}. \tag{3.12}$$

This leads to four energy levels associated with the $m_S = \pm\frac{1}{2}$ and $m_I = \pm\frac{1}{2}$ states. Figure 3.1(A) demonstrates these states, showing the allowed transitions with solid arrows and the forbidden transitions with dotted arrows. The nuclear part of the

Hamiltonian becomes, to first order in $A/g\mu_B B$,

$$\mathcal{H}_N = -g_N \mu_N \mathbf{I} \cdot \left(\mathbf{B} - \frac{\underline{\mathbf{A}} \cdot \mathbf{B} m_S}{g_N \mu_N B} \right). \tag{3.13}$$

The bracketed term represents an effective magnetic field at the nucleus. When $\underline{\mathbf{A}}$ is anisotropic the two components inside can point in different directions. So the direction of quantization of the nucleus is different for the two m_S states, as shown in figure 3.1(B), and the orthogonality of the $m_I = \pm\frac{1}{2}$ nuclear quantization states between the two is destroyed. The EPR intensity of the transitions is given by

$$I\left(+\frac{1}{2}, m_I \leftrightarrow -\frac{1}{2}, m_I'\right) \propto \left| \left\langle +\frac{1}{2} | S_+ | -\frac{1}{2} \right\rangle \right|^2 |\langle m_I | m_I' \rangle|^2 H_1^2 \tag{3.14}$$

where $|\langle m_I | m_I' \rangle|^2 = \cos^2(\theta/2)$ for the $\Delta m_I = 0$ transitions and $\sin^2(\theta/2)$ for the $\Delta m_I = \pm 1$ transitions, θ is the angle between the nuclear quantization axes for $m_S = \pm\frac{1}{2}$, and H_1 is the amplitude of the microwave field. θ can depart substantially from zero when the anisotropy in $\underline{\mathbf{A}} \sim 2 g_N \mu_N B$, leading to significant intensity in the forbidden $\Delta m_I = \pm 1$ transitions. As B increases, θ decreases as B^{-1}, the forbidden intensities decrease as B^{-2}, ($B \approx B_0 = \frac{h\nu}{g\mu_B}$) and the satellite positions, from equation 3.12, approach field values of $\pm(g_N \mu_N / g\mu_B)B$ to either side of the central line. See §5.4.2 and figure 5.5 for an illustration.

3.2.6 Dipolar broadening

The width of a resonance line can have a large number of contributory factors. Factors arising from the experimental system, such as inhomogeneous Zeeman or microwave fields, or unstable frequencies, may broaden lines. Higher order terms in the Hamiltonian causing unresolved splittings lead to apparently broader resonances. In this thesis the defects examined generally only have spin $\frac{1}{2}$ and the dominant broadening mechanism is dipolar electron–electron and electron–nuclear coupling. This is most easily described as the effect on the unpaired electron of the local change in magnetic field generated by the magnetic moments of nearby nuclei and other, similar, defects.

The theory of dipolar broadening is explained by Slichter [151], Kittel and Abrahams [152] and in the landmark paper by Van Vleck [153]. The interaction energy

between two magnetic moments is given by the Hamiltonian in equation 3.7. However, we are now looking at the contribution to the Hamiltonian made by a large number of spins, and the general dipolar contribution to the Hamiltonian for N spins becomes [151]

$$\mathcal{H}_d = \frac{1}{2}\left(\frac{\mu_0}{4\pi}\right)\sum_{j=1}^{N}\sum_{k=1}^{N}\left[\frac{\hat{\boldsymbol{\mu}}_1\cdot\hat{\boldsymbol{\mu}}_2}{r_{jk}^3} - \frac{3(\hat{\boldsymbol{\mu}}_1\cdot\boldsymbol{r}_{jk})(\hat{\boldsymbol{\mu}}_2\cdot\boldsymbol{r}_{jk})}{r_{jk}^5}\right] \tag{3.15}$$

where the $\frac{1}{2}$ is needed to prevent summing twice over j and k.

When $\hat{\boldsymbol{\mu}}_1$ and $\hat{\boldsymbol{\mu}}_2$ are written in spherical components the dipolar part of the Hamiltonian can be split into individual terms, which act as a perturbation on the Zeeman term. Many of these terms are off-diagonal matrix elements, and their net effect is to produce subsidiary absorption lines at different frequencies. These terms therefore do not contribute to the width of the main line and it is a good approximation to drop them from the Hamiltonian, leaving a simplified version with the remaining dipolar terms of

$$(\mathcal{H}_d)_{SS} = \frac{1}{4}\left(\frac{\mu_0}{4\pi}\right) g^2\mu_B^2\sum_{k,l}\frac{1-3\cos^2\theta}{r_{k,l}^3}(3S_{zk}S_{zl} - \hat{\mathbf{S}}_k\cdot\hat{\mathbf{S}}_l) \tag{3.16}$$

for the interaction between like spins. For unlike spins (e.g. electron–nuclear interactions) the degeneracy of coupling between states of type[1] $|+-\rangle$ and $|-+\rangle$ is lifted and even more terms can go. The coupling between unlike spins is

$$(\mathcal{H}_d)_{SI} = \left(\frac{\mu_0}{4\pi}\right) g g_N\mu_B\mu_N\sum_{k,l}\frac{1-3\cos^2\theta}{r_{k,l}^3}S_{zk}I_{zl}. \tag{3.17}$$

These two equations differ primarily in the numerical factor of the zz-term, with equation 3.17 being small by a factor of $\frac{2}{3}$.

Moments

The nth moment of an absorption line with lineshape $f(\omega)$ is defined by

$$\langle\Delta\omega^n\rangle = \frac{\int_0^\infty(\omega-\langle\omega\rangle)^n f(\omega)\mathrm{d}\omega}{\int_0^\infty f(\omega)\mathrm{d}\omega} \tag{3.18}$$

[1] See Slichter [151] p.58.

and the expression for $n = 2$ is called the "second moment". From equations (3) and (4) in Van Vleck [153], and converting from frequency units to field, the second moment is derived to be[2]

$$\langle \Delta B^2 \rangle = \frac{3}{4} \left(\frac{\mu_0}{4\pi} \right)^2 g^2 \mu_B^2 S(S+1) \frac{1}{N} \sum_{j,k} \frac{(1 - 3\cos^2 \theta_{j,k})^2}{r_{jk}^6} \tag{3.19}$$

for like spins and

$$\langle \Delta B^2 \rangle = \frac{1}{3} \left(\frac{\mu_0}{4\pi} \right)^2 g_N^2 \mu_B^2 I(I+1) \frac{1}{N} \sum_{j,k} \frac{(1 - 3\cos^2 \theta_{j,k})^2}{r_{jk}^6} \tag{3.20}$$

for unlike spins. In this case it has been assumed the second spin is nuclear, hence the use of g_N and I. The cosines can be averaged over a sphere to give expressions for a powder or polycrystalline material, e.g. Van Vleck's equation (14) [153] for like spins

$$\langle \Delta B^2 \rangle = \frac{3}{5} \left(\frac{\mu_0}{4\pi} \right) g^2 \mu_B^2 S(S+1) \sum_k r_{jk}^6. \tag{3.21}$$

For a magnetically dilute lattice, if each site has a probability f of being occupied by a magnetic system then this factor f precedes the sum in each case (e.g. for broadening by ^{13}C nuclei, the value of f is 0.011 for the natural abundance of 1.1 %).

The fourth moment in each case is also derived by Van Vleck [153], but the expressions rapidly become very complicated. Kittel and Abrahams [152] show how some simple approximations can be made in a magnetically dilute lattice, and give the fourth moment in a simple cubic lattice due to like spins as

$$\langle \Delta B^4 \rangle = 3[\langle \Delta B^2 \rangle]^2 \times (0.742 + f^{-1}[0.098 - 0.021(S^2 + S)^{-1}]). \tag{3.22}$$

For unlike spins, in a system with small f, the last term in Van Vleck's equation (29) gives the fourth moment, i.e.

$$\langle \Delta B^4 \rangle = \left(\frac{\mu_0}{4\pi} \right)^4 g_N^4 \mu_N^4 \frac{1}{5} (I(I+1) - \frac{1}{3}) f \sum_k \frac{(1 - 3\cos^2 \theta_{jk})^4}{r_{jk}^{12}}. \tag{3.23}$$

These moments are useful because it enables the relationship between the width of the resonance lines and the concentration of defects to be determined [151, 152]. As

[2]Slichter [151] pp.63–71.

an example, the second and fourth moments for the single substitutional nitrogen (N_S^0) line in diamond can predict the width of the line due to dipolar broadening by the 1.1% abundant ^{13}C nuclei in the lattice. This predicted width is 4 μT, which corresponds reasonably with the narrowest measured N_S^0 lines [154] in diamond with natural abundance ^{13}C, with width 7 μT.

Throughout this treatment the effect of exchange interactions between spins has been ignored. For interactions between unlike spins the exchange energy will be small, and if f is small enough and the distances between interacting spins large enough, then the exchange energy will always be negligible compared to the dipolar energy, and for all the cases in this work this has been the case and it is a reasonable assumption to make.

3.3 ENDOR

Electron Nuclear Double Resonance (ENDOR) was first performed by Feher in 1957 [155]. It is possible when there is a hyperfine interaction. It is detected by monitoring the intensity of an EPR transition while applying an oscillating radio frequency magnetic field normal both to the Zeeman field and to the microwave field. When the radio frequency matches the energy of an NMR transition between the nuclear energy levels, the relaxation for the system is altered and a change in the EPR intensity is observed. The advantage of this technique is that it often has the high resolution of NMR but with the high sensitivity of EPR, due to the much higher energy of the EPR quantum than the NMR quantum, and the much higher sensitivity at EPR frequencies than NMR frequencies. A detailed description of ENDOR is given by Abragam and Bleaney [156], but it can be simply illustrated by considering the possible system of energy levels and relaxation pathways for a system with $S = \frac{1}{2}$ and $I = \frac{1}{2}$ shown in figure 3.2. For this system the assumption has been made that the hyperfine interaction is small compared to the electron Zeeman interaction. At thermal equilibrium the relative populations for the levels $m_S = \pm\frac{1}{2}$ are approximately $1 \mp \delta_e/2$ where

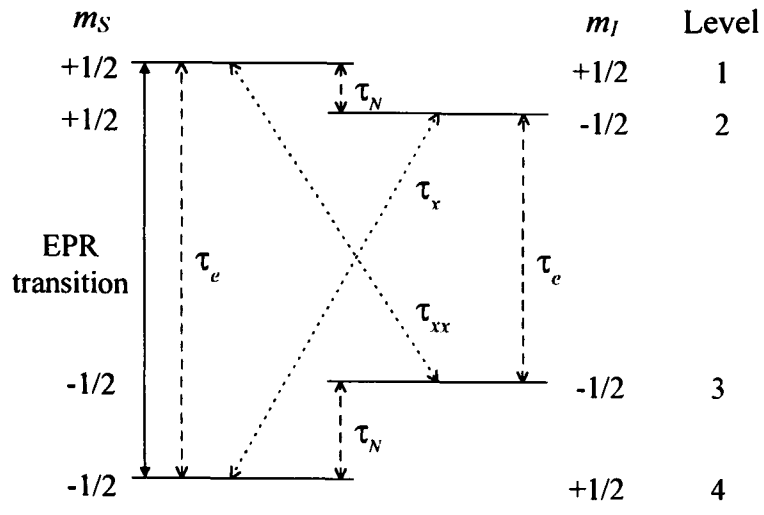

Figure 3.2: Four possible relaxation paths for a system with $S = \frac{1}{2}$, $I = \frac{1}{2}$ and $A > g_N \mu_N B$. When the EPR transition is saturated ENDOR is observable from nuclear transitions between $1 \leftrightarrow 2$ and $3 \leftrightarrow 4$. In the absence of τ_{xx} only transitions between levels $1 \leftrightarrow 2$ would be seen.

$\delta_e = g\mu_B B/kT$, and the small population difference between levels with $m_I = \pm 1$ is ignored. The four relaxation paths shown in the figure are:

- The electron spin–lattice relaxation time, τ_e.
- The nuclear spin–lattice relaxation time, τ_N.
- Spin flip relaxation time from transitions with $\Delta m_S + \Delta m_I = 0$, τ_x.
- Spin flip relaxation time from transitions with $\Delta m_S + \Delta m_I = \pm 2$, τ_{xx}.

In general (exceptions are discussed in works such as ref. [156]), $\tau_N \gg \tau_x, \tau_{xx} > \tau_e$. The populations of levels 1 and 4 are equalized by saturating the EPR transition between them. The spins in level 1 can return to level 4 by the direct route with rate $1/\tau_e$, or via level 2 or level 3, with rates $1/(\tau_N + \tau_x)$ and $1/(\tau_N + \tau_{xx})$ respectively. If an RF field is applied at the nuclear resonance frequency corresponding to $E_1 - E_2$, transitions can be induced at a rate much faster than $1/\tau_N$, meaning $1/\tau_x$ becomes the dominating factor in determining the rate of the relaxation path $1 \rightarrow 2 \rightarrow 4$ and the rate is increased to $1/\tau_x$. This opens another relaxation path, which can affect the saturation and therefore change the EPR signal.

3.3.1 Matrix ENDOR

The most prominent ENDOR line in most solid disordered systems (such as amorphous carbon) is the matrix ENDOR line occurring at the free nuclear frequency. This line has been interpreted as being due to a purely dipolar interaction between an unpaired electron and surrounding magnetic nuclei in the matrix [157, 158]. Hyde, Rist and Eriksson [157] have developed a simple model for matrix ENDOR lineshapes, and this is summarized below.

Following Seidel [159] it is assumed the ENDOR signal height is proportional to the nuclear spin–lattice relaxation rate, τ_{1N}^{-1}. Then a general expression for the matrix ENDOR line shape is

$$f(\nu) = N' \int_0^{2\pi} \int_0^{\pi} \int_{\bar{a}}^{r} \tau_{1N}^{-1}(r,\theta,\phi) g[\nu - \nu_0(r,\theta,\phi)] r^2 \sin\theta \mathrm{d}\phi \mathrm{d}\theta \mathrm{d}r, \tag{3.24}$$

where $g(\nu - \nu_0)$ is the nuclear spin packet line shape centred at a resonant frequency ν_0, and N' is a constant which affects the amplitude but not the shape of the line. The lower limit $r = \bar{a}$ represents the distance at which the "matrix" nuclei begin for which only a dipolar interaction is considered. The ϕ dependence of τ_{1N} and $g(\nu)$ can be eliminated if the magnetic moments are considered to be aligned along the external magnetic field. Abragam [160] gives the expression for τ_{1N} for matrix nuclei in a dilute paramagnet as

$$\tau_{1N}^{-1} = \frac{9}{4} \tau_{1e}^{-1} \frac{g_e^2 g_N^2 \mu_B^2 \mu_N^2}{\hbar^2} \frac{\sin^2\theta \cos^2\theta}{(2\pi\nu_p)^2 r^6}. \tag{3.25}$$

A Lorentzian lineshape is chosen for $g(\nu)$ with linewidth (HWHH) α, although the ENDOR lineshape is essentially insensitive to the choice of either Gaussian or Lorentzian lineshapes for $g(\nu)$. Integration up to $r = \infty$ yields results comparable to a finite upper limit because the very distant protons make small dipolar contributions. An upper limit of 10 Å is usually found to be sufficient [157]. The line shape expression then becomes

$$f(\nu) = N \int_0^{\pi} \int_{\bar{a}}^{\infty} \frac{\cos^2\theta \sin^2\theta}{r^4} \left[\frac{1}{\alpha^2 + [\nu - (q/r^3)]^2} + \frac{1}{\alpha^2 + [\nu + (q/r^3)]^2} \right] \mathrm{d}\theta \mathrm{d}r \tag{3.26}$$

where $q = \frac{1}{4\pi\hbar} g_e g_N \mu_B \mu_N (3\cos^2\theta - 1)$. This expression only contains the two parameters α and $\bar{a}$ and forms a very useful model for determining the effective distribution of the electron wavefunction and the distance between the electron spin and nearby nuclear spins. Better models include the various relaxation paths explicitly as well as the nuclear RF and microwave magnetic fields [161, 162].

Chapter 4

Experimental details

4.1 Introduction

In this thesis the main spectroscopic tool employed was Electron Paramagnetic Resonance (EPR). Electron Nuclear Double Resonance (ENDOR) was also used. The standard EPR spectrometer was also used with gradient coils to perform imaging of the distribution of paramagnetic centres. The main techniques were complemented by optical absorption and Raman spectroscopy. EPR measurements were performed at Q-band (33 GHz) and X-band (9 GHz) in the main, with a few at lower frequencies down to 1 GHz. ENDOR was performed using one of the Q-band spectrometers. The optical excitation and the imaging were performed using the X-band spectrometer. Each spectrometer will be discussed in turn on the following pages.

EPR and ENDOR spectrometry has been well documented in the past, and I shall just give a brief overview of each instrument used, concentrating on additions and changes made during the course of this work. All of the equipment for imaging was new and will be explained in more detail. Weil, Wertz and Bolton [148] give a good general overview of EPR techniques, while a more detailed treatment of the individual parts of the spectrometer is given by Poole [163].

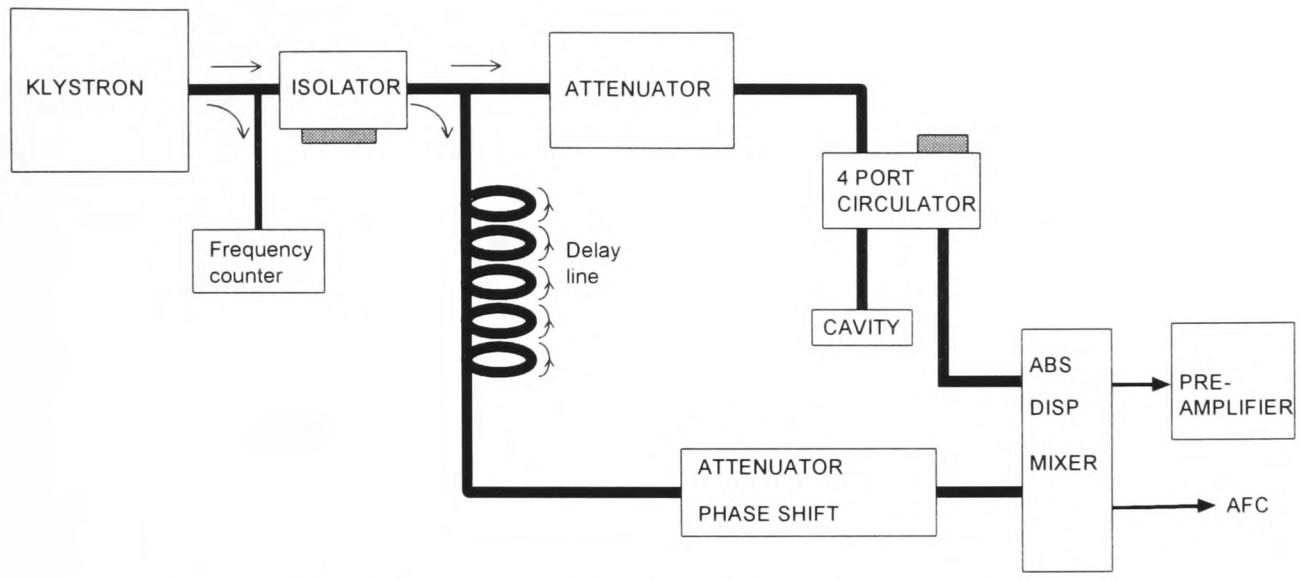

Figure 4.1: Schematic of Bruker Q-band microwave bridge

4.2 Q-band

4.2.1 Description of Bruker spectrometer

The simpler of the two Q-band spectrometers[1] was used only for the determination of the lineshape of the N_S^0 defect and the defect containing H1, because it arrived two thirds of the way through this work. The microwave bridge is depicted schematically in figure 4.1. The reference arm (containing the delay line) is necessary to allow collection of data in either absorption or dispersion. Field modulation and phase sensitive detection allowed detection of either the first or second harmonic EPR signal. The resonator used was a cylindrical cavity with modes TE_{011} and TE_{012}, mounted with the axis vertically. The field modulation coils were outside the cavity. The sample could be cooled using a standard Bruker continuous flow nitrogen system.

4.2.2 Description of Clarendon spectrometer

The more complex reference-arm Q-band spectrometer was designed and built in the Clarendon Laboratory. It was designed to be used to detect either in homodyne

[1]Bruker model ER 200 D - SRC.

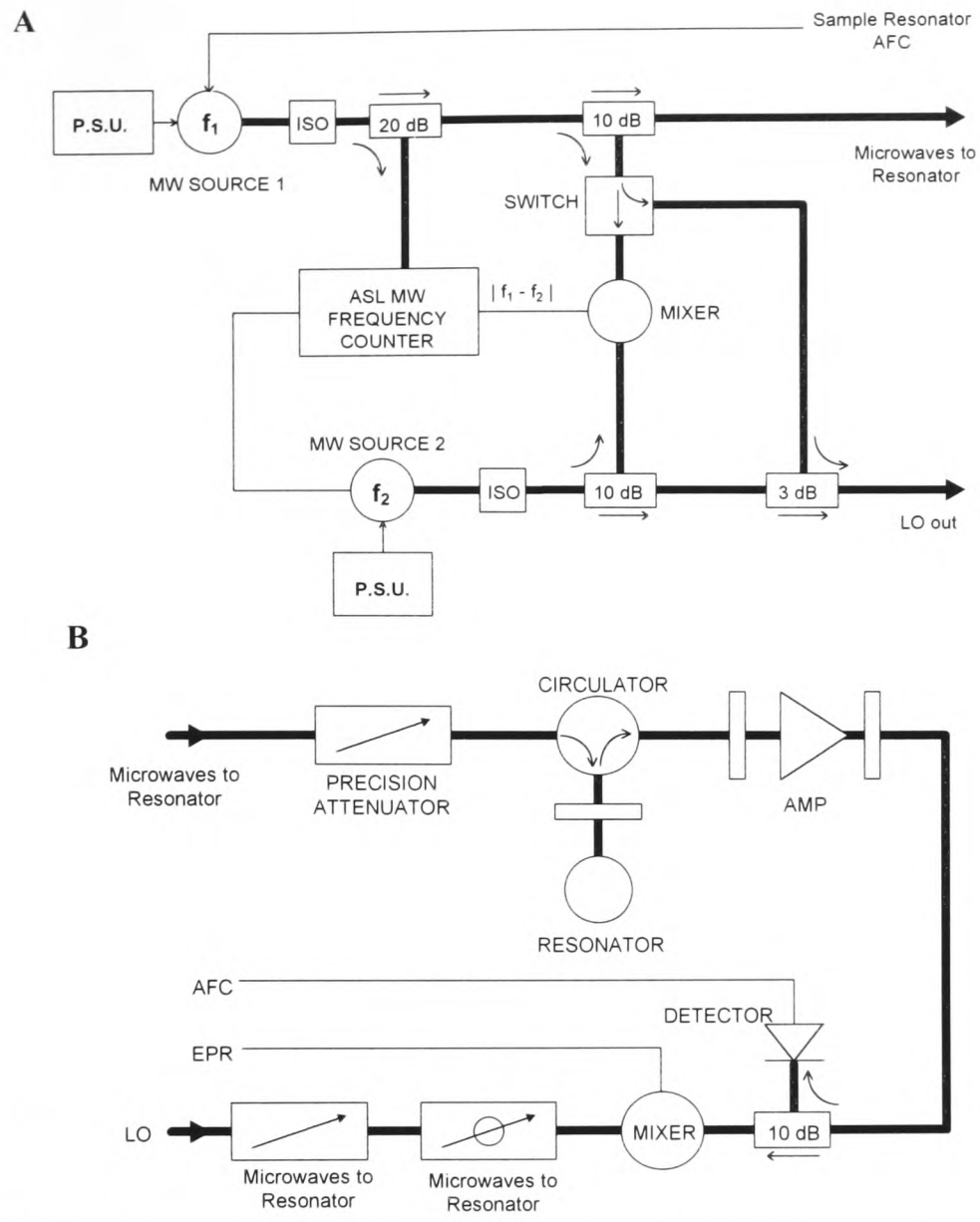

Figure 4.2: Schematic of bridge of Clarendon Q-band spectrometer, showing (A) superheterodyne and reference arm bridge microwave source, and (B) microwave receiver.

mode using the standard field modulation method, or by the superheterodyne method. None of my measurements were taken in the superheterodyne mode, and I shall leave description of this to Twitchen[2] [22]. A schematic representation of the bridge is shown in figure 4.2. The spectrometer could run in dispersion or absorption, and record either the first or second harmonic of the signal. Field modulation for all the experiments in this work was at 115 kHz.

Cavity

The microwave cavity used was a cylindrical cavity operating in the TE_{011} mode. The cavity is depicted in figure 4.3. The axis of the cylinder was horizontal, and the cavity could be rotated around this axis. The magnet could be rotated around the cavity about a vertical axis, and this gave two degrees of freedom, enabling very easy

[2]Thesis unpublished at time of going to press.

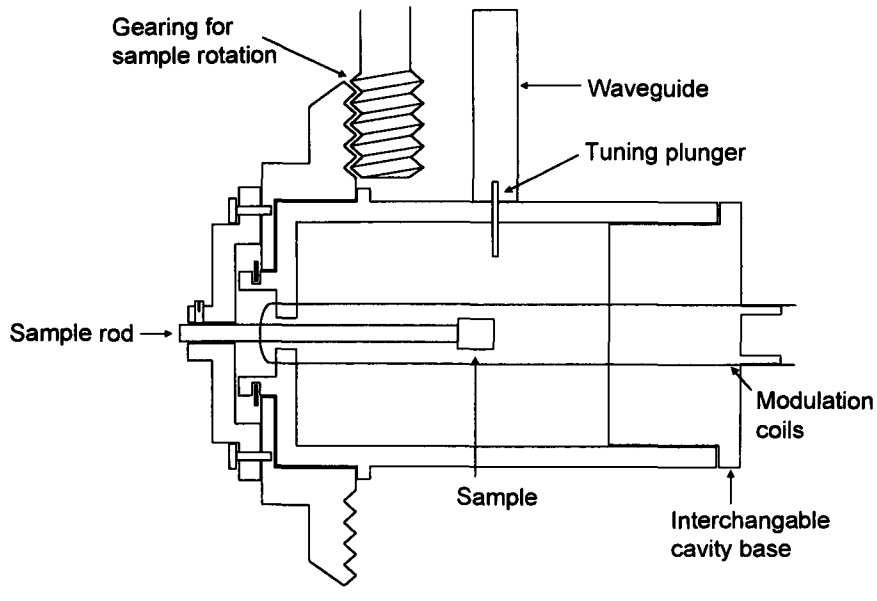

Figure 4.3: Depiction of TE_{011} cavity used in Clarendon spectrometer.

orientation of samples. The cavity had a high Q ($\sim$ 2500).

Microwave sources

A great increase in the sensitivity of the spectrometer was achieved by the development of very low noise microwave sources. These were designed by R A Strangeway, T K Ishii and J S Hyde and built in the Clarendon. The source is depicted in figure 4.4.

Sensitivity

A comparison was made with the existing X-band spectrometer (see §4.3) in use within the group in order to see the increase in sensitivity afforded by this spectrometer. A sample of CVD diamond containing the single substitutional nitrogen (N_S^0) defect (see §5.4.1) was placed in the rectangular Bruker cavity of the X-band spectrometer and in the Q-band spectrometer and spectra recorded under optimum conditions in both cases. In the Q-band spectrometer spectra were recorded in absorption and in dispersion: the dispersion spectra could be converted to absorption by means of a Hilbert transform. These spectra are shown in figure 4.5. The ratio of signal to rms noise was determined in each case, and was found to be 20 for X-band, 20 for Q-band absorption and 440 for Q-band dispersion. So it is clear that the Q-band spectrometer

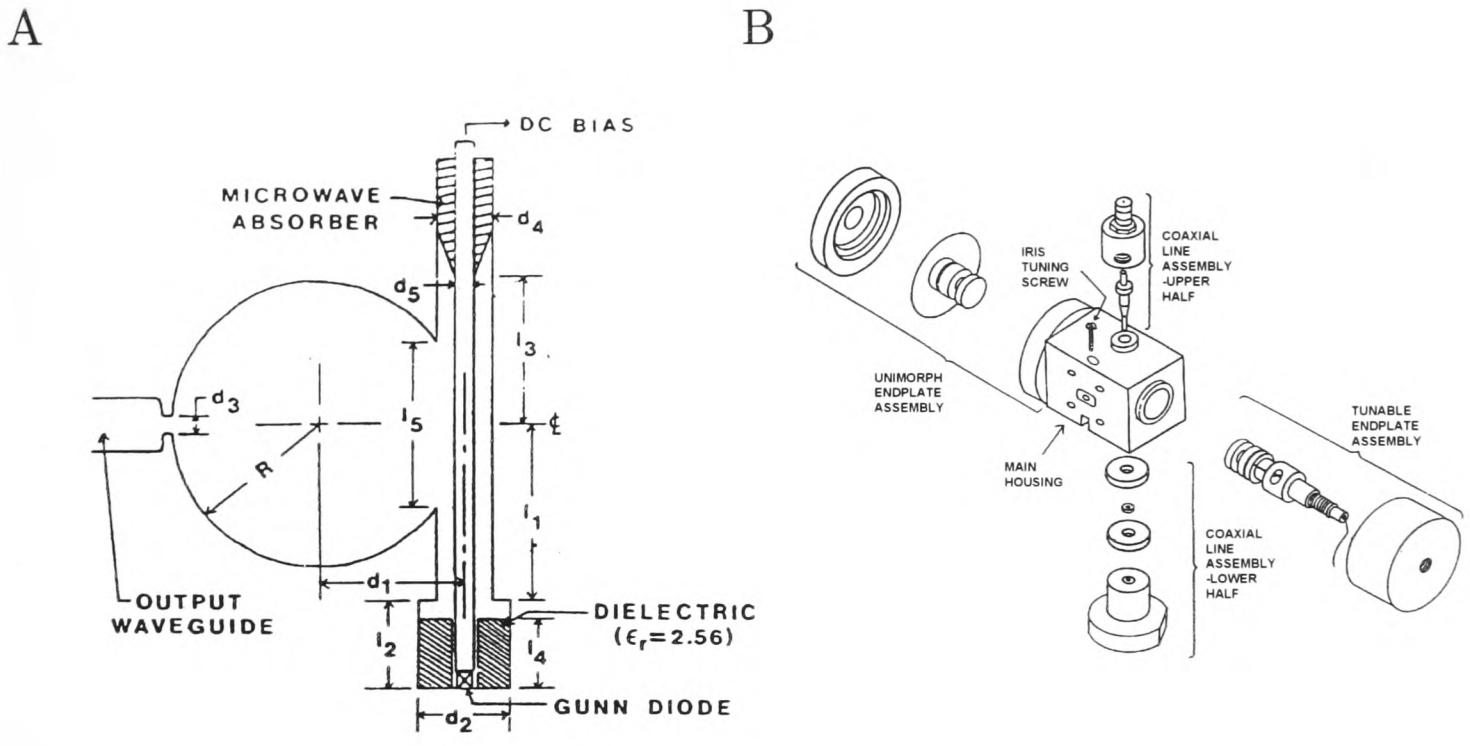

Figure 4.4: Detail of Q-band oscillator: (A) schematic diagram of the transmission cavity stabilised Gunn diode oscillator (d_1=6.4, d_2=3.6, d_3=2.1, d_4=3.2, d_5=1.6, l_1=11.8, l_2=1.9, l_3=12, l_4=0.8, l_5=8.4, R=6.35, cavity length = 7.6 mm), and (B) sketch of assembly showing unimorph and piezo.

has in increase in sensitivity of at least 22 over the X-band spectrometer.

Temperature control

For most measurements the sample was cooled using an Oxford Instruments continuous flow system.[3] This allowed measurements to be made at any temperature between 3.5 K and 300 K. The whole cavity was enclosed in a chamber containing helium exchange gas, with the continuous flow system installed around the outside of this chamber. This arrangement, shown in figure 4.6, was employed to ensure the stability of the temperature in the cavity and to prevent small fluctuations in the helium flow having any effect on the impedance of the cavity.

In order to produce temperatures down to 1.5 K, the sample could be cooled using a Clarendon-built immersion cryostat. This was filled with liquid helium and the temperature reduced by pumping with a large displacement rotary pump.[4]

[3]Oxford Instruments model CF200

[4]Edwards Speedivac high vacuum pump, single stage, model ISC 900.

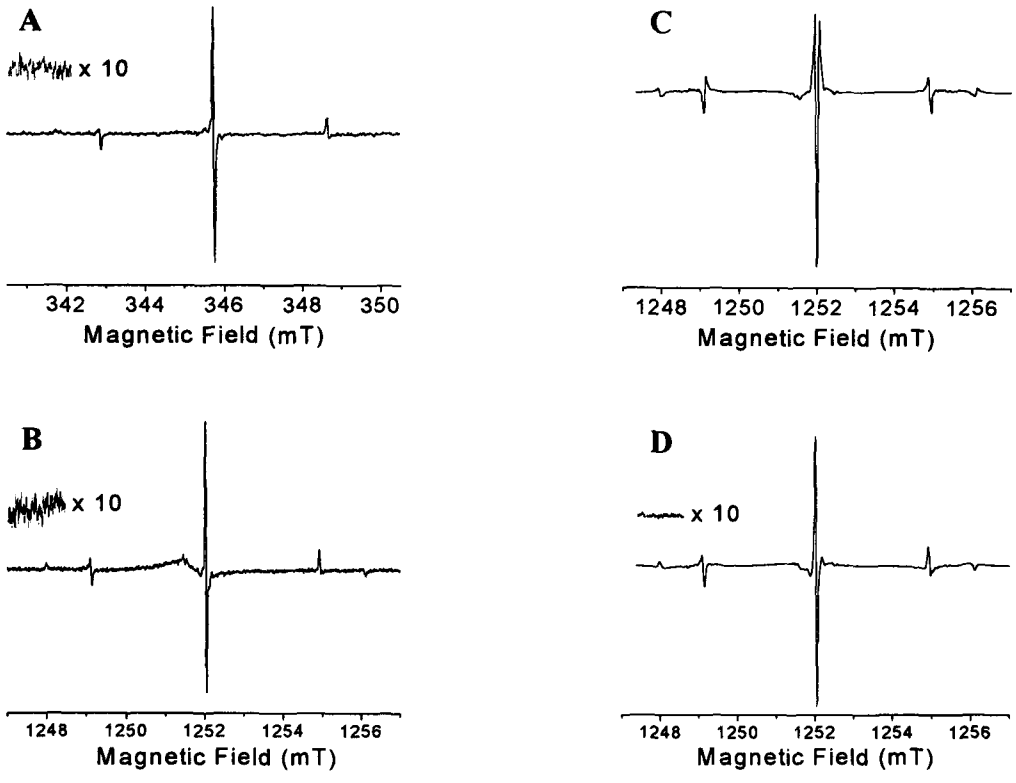

Figure 4.5: Spectra from N_S^0 defect in CVD sample. (A) X-band absorption. (B) Q-band absorption. (C) Q-band dispersion. (D) Q-band dispersion converted to absorption using Hilbert transform. Sample size for Q-band 6.2 × smaller than for X-band. All spectra obtained at room temperature. Microwave power in each case adjusted for maximum signal to noise, all other parameters identical.

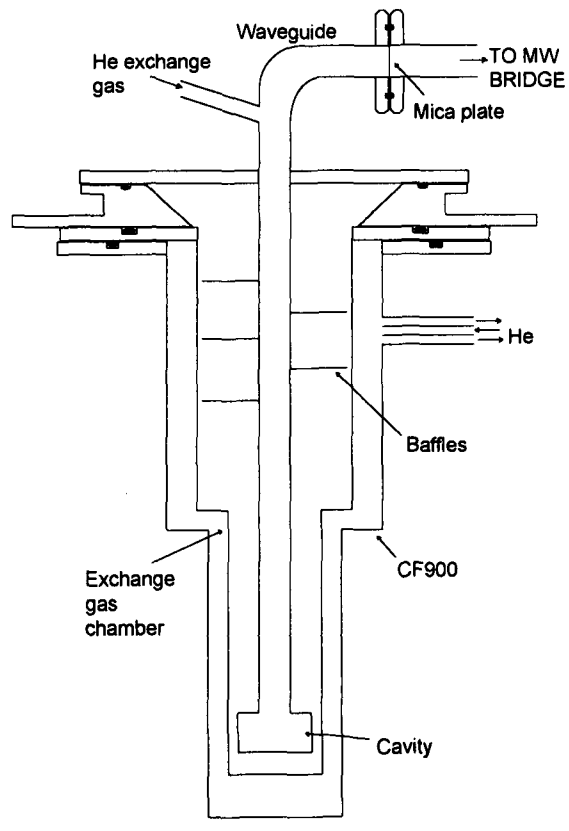

Figure 4.6: Arrangement for cooling sample in Q-band spectrometer.

Computer control of spectrometer

Tucker [21], in his DPhil thesis, explains modifications made to the X-band spectrometer to allow the magnetic field to be controlled by a computer. The same system was used with this spectrometer: the field was set using a Hall Probe, and measured accurately at the start and end of each scan using a Bruker NMR magnetometer.[5] The Bruker magnetometer also output "ticks" every 0.1 mT, which were recorded in the experimental spectrum, allowing extremely accurate field measurement during the course of scans for slow scans. All of the software originally developed for the X-band spectrometer was used with this spectrometer.

4.2.3 Electron Nuclear Double Resonance (ENDOR)

The ENDOR study of the H1 defect described in §5.4.2 was performed using the Clarendon Q-band spectrometer described in §4.2.2 above. The cavity used was the same as for the EPR measurements, as shown in figure 4.3, but a coil was also introduced in order to introduce a radio frequency (RF) field into the cavity. This coil was a single turn coil which ran the length of the cavity and was about 3 mm wide; it was exactly the same as the coil providing field modulation but perpendicular to it. The coil was terminated with a 50 Ω load and the maximum RF power used was 20 Watts.

The ENDOR signal was detected in double phase sensitive detection. With just the field modulation no signal could be seen in the samples we were examining, and the optimum conditions were found to be a field modulation at 115 kHz, as before, and a RF modulation at 70–80 Hz, normally with a 50 kHz depth to avoid broadening the lines. Spectra were recorded at 5 K using the temperature control system described in §4.2.2. The microwave power used when collecting ENDOR spectra was 2 mW. Great care had to be taken to prevent the wires carrying RF to the cavity from radiating.

[5] Bruker NMR Gaussmeter ER035M.

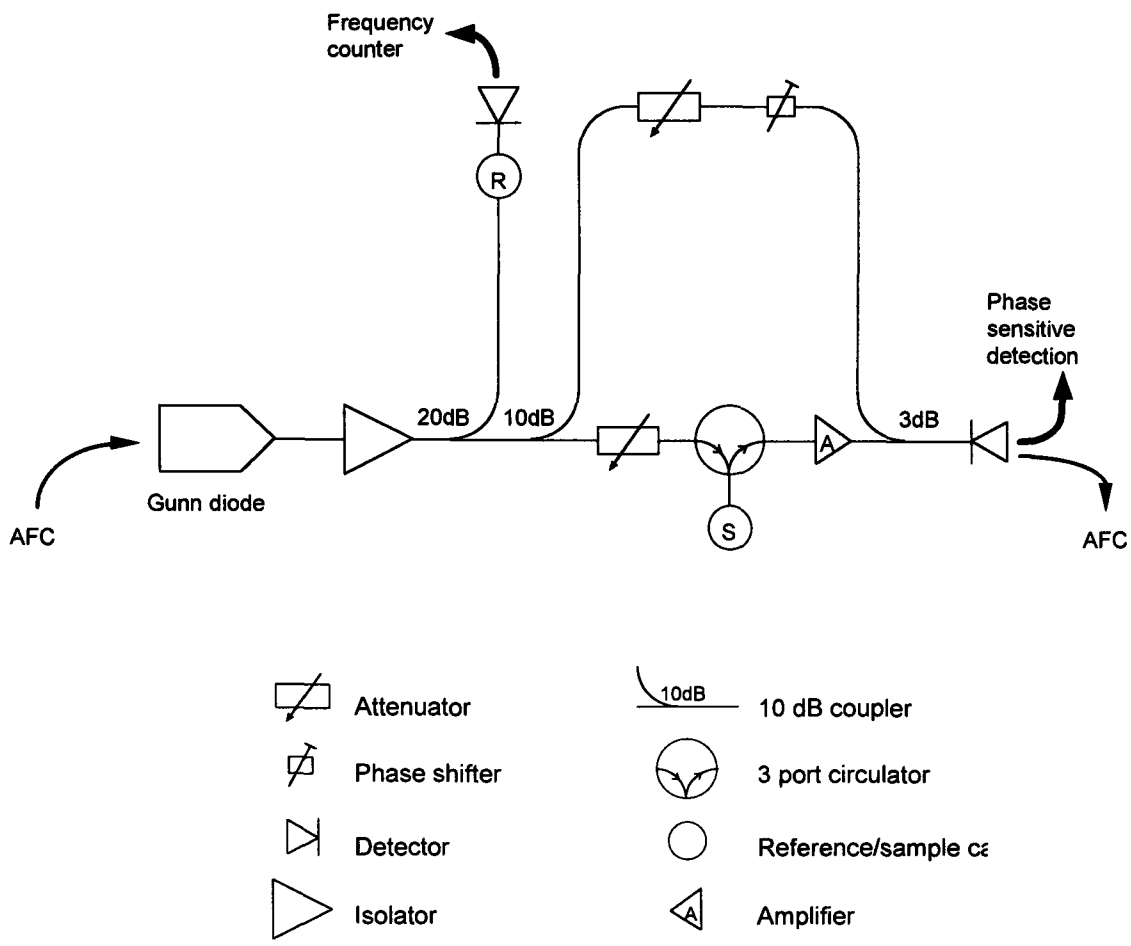

Figure 4.7: Schematic of the X-band bridge

4.3 X-band

The reference-arm X-band spectrometer was the piece of apparatus used more than any other in this work. It has been developed over a number of years [19, 20], and the most recent developments are described by Tucker [21]. Figure 4.7 shows a schematic of the bridge. For most experiments a Bruker TE_{104} rectangular cavity was used; the sample in this cavity could be cooled to any temperature down to 4 K using a cold finger.[6] Changes made during the course of this work are outlined here.

4.3.1 Change of magnet power supply

The magnet power supply and automatic field control system described by Tucker [21] was replaced by a power supply and automatic field controller bought from and

[6] Oxford Instruments ESR900 continuous flow system.

installed by Jagmar.[7] This power supply could be controlled directly from a computer via a GPIB interface. Since the phase-sensitive detector[8] could also be controlled via a GPIB interface this enabled all aspects of electronic control to be automated.

The important difference that the new field controller brought to the spectrometer was that with the old system the field was controlled externally and ramped with a voltage source (either an analogue or digital sweeper), and the field was then measured for each data point using a Hall probe or the "ticks"from the NMR gaussmeter (see §4.2.2 and Tucker [21]). The new field controller has a feedback loop to a Hall probe and ramps the field in a series of 4096 steps. This has two important consequences:

1. There is no need to measure the field subsequently, making the data collection much more straightforward.

2. Because each spectrum consists of the same number of data points, with each point being at a pre-determined field, signal averaging is possible.

To illustrate the importance of signal averaging, figure 4.8 shows spectra of the N_S^0 defect in polycrystalline CVD diamond taken after varying numbers of scans. In theory the signal to noise should be proportional to the square root of the number of scans. Figure 4.9 shows this relationship for the spectra shown in figure 4.8 up to 200 scans. Eventually coherent noise will become evident, but it is clear that the new field controller has provided the potential for more than an order of magnitude improvement in the signal to noise of spectra.

A brief description of the computer control is given in §4.5.1.

4.3.2 Computer driven goniometer

The goniometer controlling the orientation of the sample in the cavity was originally operated by hand, and was marked in graduations of 2°, with a Vernier scale graduated

[7]Electromagnet power supply EPS-10/1, Magnetic field controller MS-10/GPIB, Technical University of Wroclaw, Poland.

[8]Princeton Applied Research EG&G model 5209 lock-in amplifier.

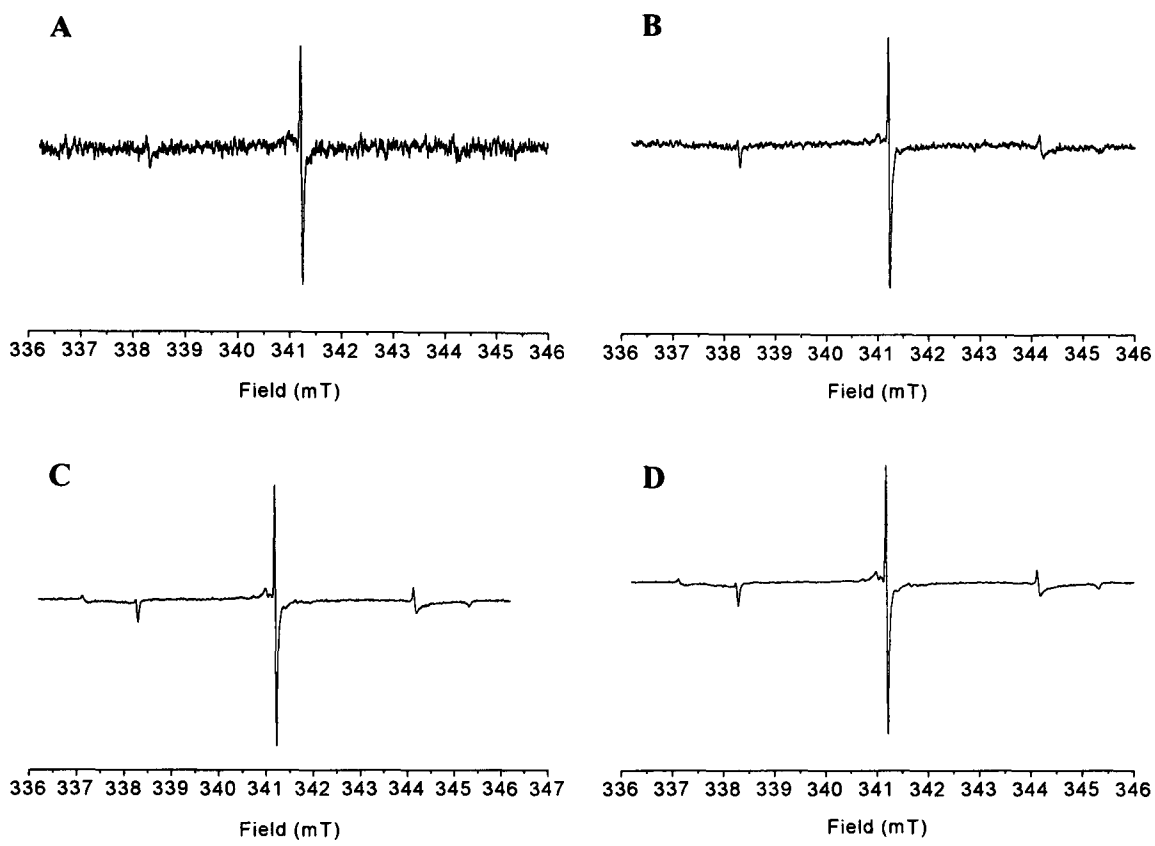

Figure 4.8: Spectra of the N_S^0 centre in polycrystalline CVD diamond taken after (A) 1, (B) 9, (C) 81 and (D) 200 scans illustrating improvement of signal to noise. Spectra recorded at room temperature, field modulation 10 μT, microwave power 3 μW.

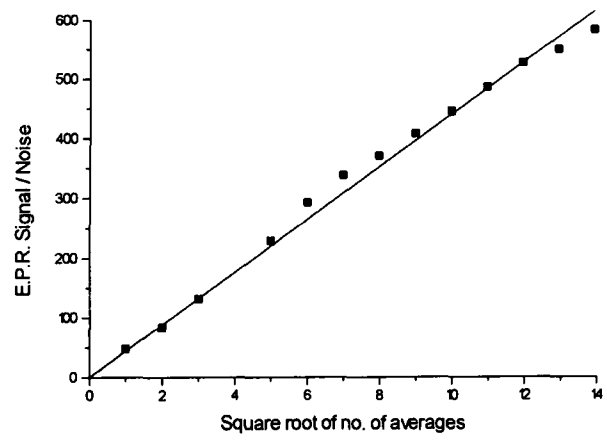

Figure 4.9: Signal to noise compared with the square root of number of scans. Data is taken from same sample used for figure 4.8. Noise defined as rms deviation from zero away from any signal. Signal measured as p–p height.

to 0.2°. It was very difficult to produce an accurate orientation in a repeatable fashion, especially if the goniometer was turned in both directions. This proved to be of particular importance when imaging samples (see chapter 7).

Therefore, in an effort both to increase the accuracy of orientation of the sample and to automate further the operation of the spectrometer, a stepper motor[9] was installed to drive the goniometer. This was controlled by a driver[10], whose clock was controlled by a series of pulses output from the parallel port of the computer. 12000 pulses were required to turn the goniometer through 360°, giving a theoretical resolution of 0.03°, which is better than we were ever going to need. The computer control is described in §4.5.1. A photograph of the stepper motor in place is shown in figure 4.13.

The presence of automatic control for the goniometer had two main benefits:

- Samples could be orientated with a very high degree of precision.
- Entire "road maps" of the behaviour of lines with orientation, or sets of back-projections of 2-D images (see §7.3.4) could be generated automatically. The combination of this with the signal averaging capability of the new magnet field controller enabled the spectrometer to be left running overnight on numerous occasions, greatly increasing the efficiency with which data could be collected.

4.3.3 Loop–gap resonator

For most experiments a rectangular cavity was used. This had a very high Q ($\sim$ 10000), but also a large volume. For the imaging experiments described in chapter 7, a new resonator was designed and built in the Clarendon. The motive for this was to produce a resonator which occupied a smaller space than a standard X-band cavity, and which was more sensitive for samples with finite size.

The choice of optimal microwave resonator depends on the specific application. Hyde and Froncisz [164] have discussed the sensitivity considerations and show that

[9]RS440-442 Stepping motor.
[10]RS332-098 Stepper motor driver.

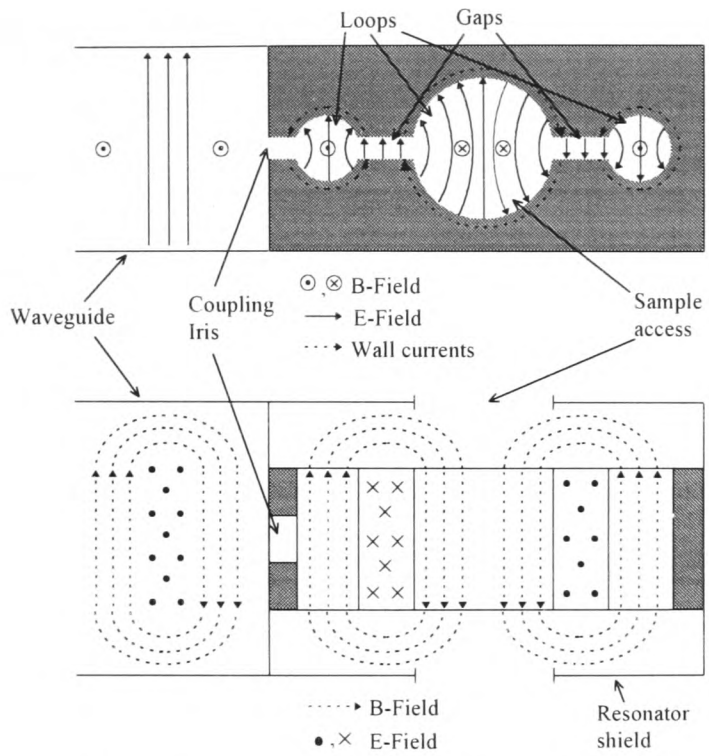

Figure 4.10: 3-loop 2-gap loop–gap resonator coupled to a waveguide [166].

Loop–Gap Resonators (LGRs) offer better absolute spin sensitivity than conventional cavity resonators when the sample size is limited [164]. In a loop–gap resonator the loops are inductive elements, one of them surrounding the sample, and the gaps are capacitive elements. The dimensions of the structure should be small compared with one-quarter wavelength of the microwaves being used, $\lambda/4$. Capacitive and inductive elements are separated in space, and to a fair approximation the microwave magnetic field is in the loops and the microwave electric field in the gaps. It is in the nature of high resolution EPR imaging in small samples that the amount of sample in which the resonance condition is fulfilled is limited, so LGRs offer substantially better performance than cavity resonators. LGRs with closed flux return paths allow gradient coils to be placed close to the resonator without perturbing the microwave element, which makes the generation of large gradients considerably easier.

The resonator designed and built was a three-loop two-gap LGR [165, 166], which can have a high filling factor and has very good flux containment in the high frequency mode, permitting juxtaposition of the gradient coil and resonator without any reduction in the resonator performance. Figure 4.10 shows such a resonator. The best sensitivity is achieved with a small sample loop and large flux return loops: however,

in order to use the resonator with the ESR900 flow cryostat, we built several with sample loops 11.5mm in diameter following the design described by Hyde *et al.* [166]. Their *absolute* sensitivity is comparable with the standard TE_{102} rectangular cavity [166]. The microwave B-field in this LGR is very homogeneous [166], which is important for uniform sensitivity over a sample. The Q of these resonators was found to be 2500.

More than one resonator was built so that they could run at slightly different frequencies: when the cold finger of the ESR900 cryostat was in place the resonant frequency of the resonator was reduced, so different resonators were required to run with and without the cryogenics in place. The standard method of increasing the frequency of these resonators is to reduce the radius of the flux return loops. However, it was found we could not raise the frequency of the resonator high enough, without compromising the sensitivity, to cope with the introduction of the cold finger. It was found, however, that by inserting silver tubes into the flux return loops the frequency could be raised further, and the cryogenics could be used.

In order to contain the microwave flux the resonator was enclosed inside a shield. The experimental arrangement, showing the ESR900 cold finger and 115 kHz field modulation coils, is shown in figure 4.11.

One problem worthy of note is that any movement of the sample inside the resonator changed the microwave coupling drastically, and was an unwanted source of noise. With the samples mounted on rods entering the cavity from above, there was enough movement for this to be significant. This was overcome by mounting the samples on a rod which ran right through the resonator and was held in place at the top and the bottom of the cavity. This also had the advantage of ensuring that the rod was absolutely straight in the cavity. When the cryogenics were in place, the cold finger acted to hold the sample in position and the longer sample rod was not necessary.

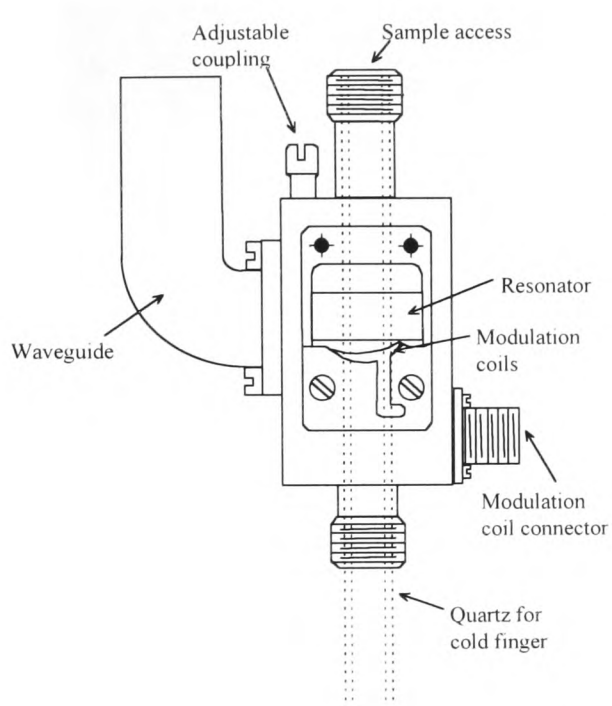

Figure 4.11: Depiction of LGR in place in shield, showing cold finger and field modulation coils [166].

4.3.4 $\partial B_z/\partial z$ Gradient coils

In order to produce images of samples (see chapter 7), it was necessary to produce a field gradient in the same direction as the Zeeman field—i.e. $\partial B_z/\partial z$, where the constant Zeeman field is in the z-direction. This was achieved by the use of two coils in an anti-Helmholtz configuration, mounted either side of the loop–gap resonator shield. The coils were designed and built in the Clarendon.[11] They had 212 and 215 turns of copper wire respectively, and were water cooled. Figure 4.12 shows the arrangement of the coils; figure 4.13 shows them in place.

The coils were wired together in parallel and powered by a constant voltage source. It was found that the maximum practical voltage at which they could be run was 30 V. At 30 V the temperature at the outside of the coils (away from the cooling water) was $\sim 75°C$, and above this temperature the resin would start to degrade. The coils took about half an hour to reach equilibrium, at which stage the current was

[11] Coils wound by A. Hickman.

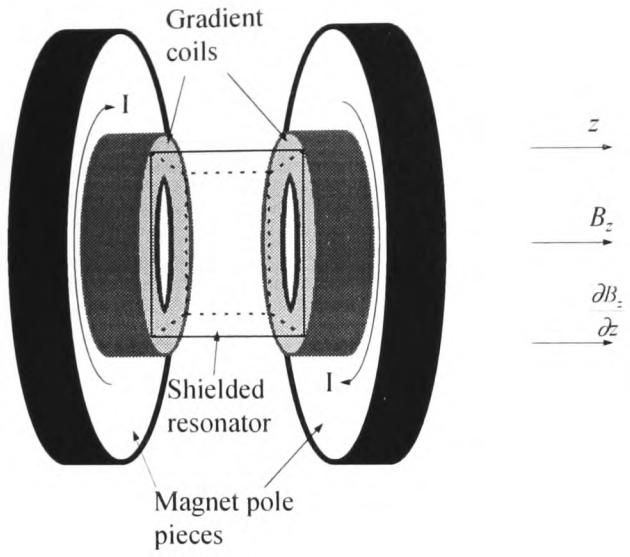

Figure 4.12: Arrangement of coils in anti-Helmholtz configuration to provide gradient dB_z/dz.

7.6 A. The field gradient with this current was 1.3 mT mm^{-1} (see §7.3.2 for details of gradient measurement). The homogeneity of the gradient across the central 5 mm of the coils was better than 99 %.[12] The separation of the coils was 2.9 mm.

4.3.5 Cryogenics

The X-band system was cooled by an Oxford Instruments ESR900 cold finger. This continuous flow system is described by Newton [19]. In many of the experiments described in this thesis, particularly those with signals small enough that long collection times with many signal averages were required, temperature stability over time periods ranging from a second to twenty-four hours were vital because:

- The impedance of the cavity changed with the quantity and temperature of helium gas present.
- The susceptibility of samples were temperature dependent.
- The relaxation mechanisms within samples were temperature dependent.

Temperature fluctuations were generally caused by constrictions or heat leaks within the helium transfer siphons. A siphon with a cold touch onto its helium capillary has a tendency to form "snowballs" of solid CO_2 and ice in the capillary, which then

[12]Confirming calculations performed by Graham Watt.

A

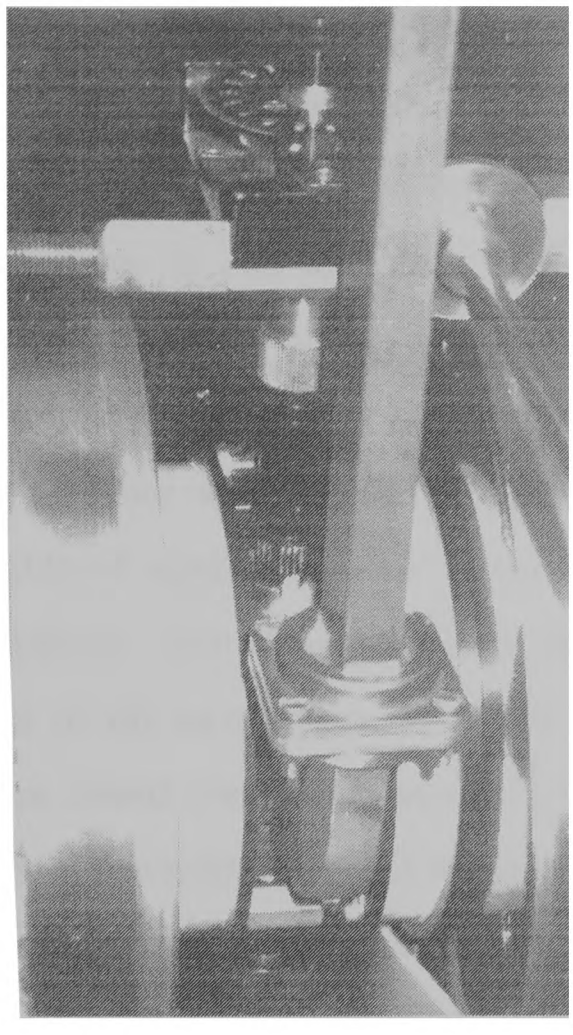

B

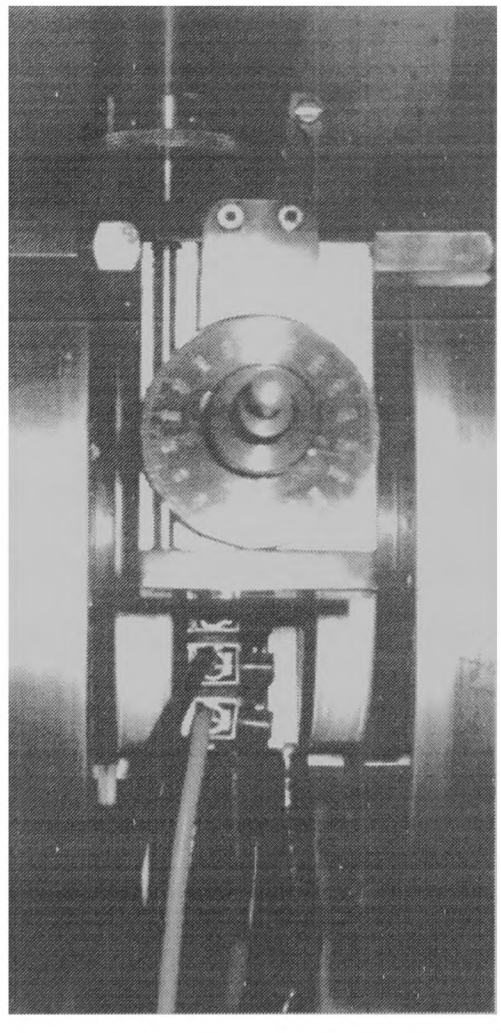

C

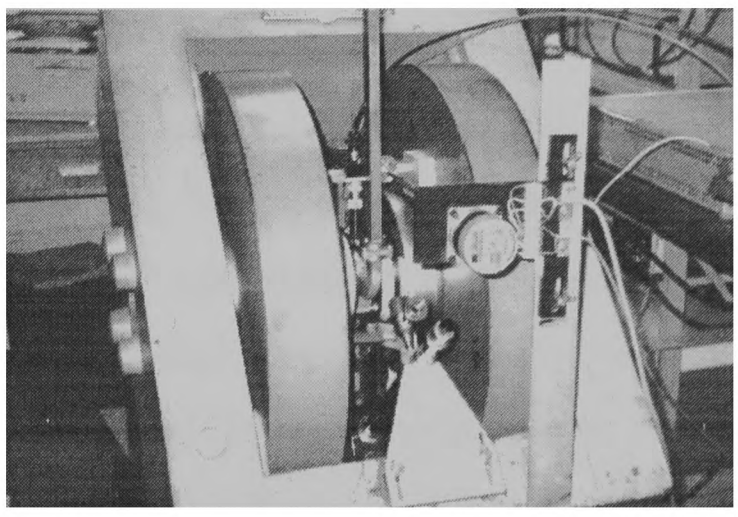

Figure 4.13: Photographs of imaging setup showing pole pieces of magnet providing constant Zeeman field B_Z, gradient coils providing gradient $\partial B_z/\partial z$ and automatic control of goniometer. (A) shows view from side, (B) shows view from top, (C) shows whole magnet, and stepper motor, and cryogenics underneath the resonator.

blocks. These "snowballs" could also form if the siphon had not been flushed with gaseous helium before use. This necessitated the warming to room temperature of the whole system, and removal of the siphon, flushing with gaseous helium, and re-insertion into the helium dewar and cryostat. The temperature stability problem was also exacerbated by the high flow rates needed to maintain a constant temperature of 5 K. These high flow rates ($\sim$ 2 litres/hour) were also expensive due to the cost of liquid helium.

This problem was eventually solved by the purchase of a new siphon.[13] This was capable of operating with liquid nitrogen as well as helium because it had a larger capillary. The larger capillary also removed the risk of "snowballs". Another advantage of the new siphon was that the needle valve at the bottom of the leg in the helium dewar was much more reliable, allowing closer control of the flow. The cryostat was reconditioned and upgraded to work with the new system: this involved the insertion of a large thermal mass in the cryostat. The new system was then found to have a temperature stability of better than 0.1 K.

4.3.6 Optical illumination

The optical illumination system used in the imaging of the $[N–N]^+$ centre (§7.8) is described in detail by Tucker [21]. He replaced the *black light* used by Cox [20] with a 100 W high pressure Hg lamp[14] and modified it to allow the use of a xenon[15] bulb. The Xe spectrum is much smoother than the Hg spectrum at short wavelengths, which allows much closer control of the wavelength used if required. The lamps were mounted in a lamp housing which had forced ventilation, a back reflecting mirror and an adjustable collecting lens.[16] The bulbs and lenses were UV-grade quartz.

Light was channelled in to the microwave cavity using a spectrosil quartz light guide. The sample was mounted on the end of the light guide using araldite around

[13]Oxford Instruments GFS600 transfer tube, with 1.2 m leg.
[14]Osram HBO100/2.
[15]Osram XBO150.
[16]Spiers Robertson LH150 universal lamp housing, with Spectral Energy LPS 251 SR PSU.

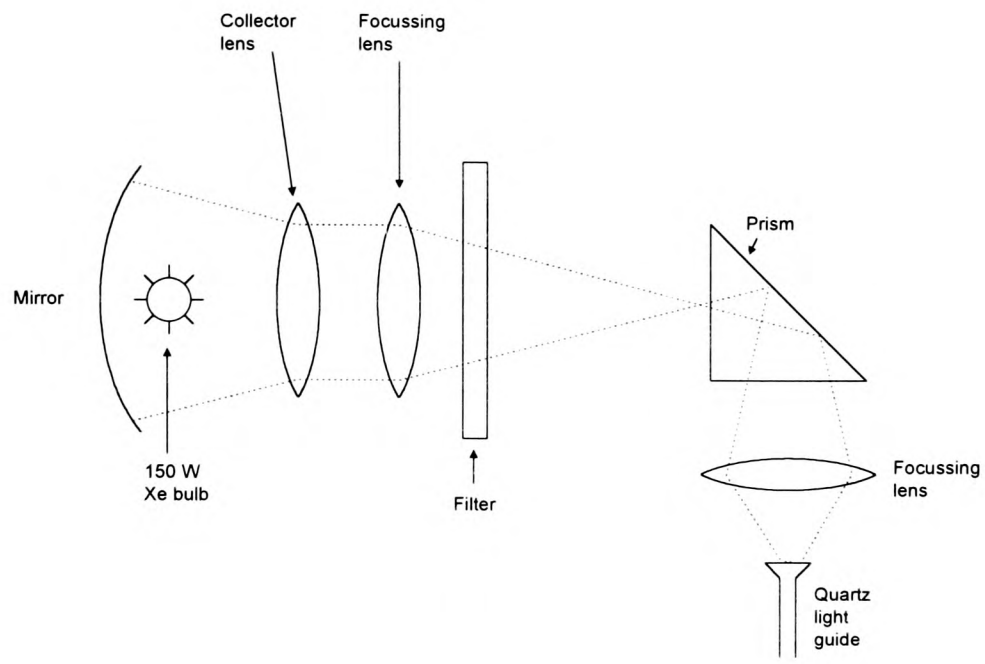

Figure 4.14: Illumination of the sample using prism and quartz light guide.

the edge of the sample. High-vacuum grease was used initially, but it was found that paramagnetic centres were created in the grease by the light with similar g-values to those of the centres under investigation in the samples, so this was abandoned. The light was directed into the top of the light guide by a series of focussing lenses and a quartz right-angled prism. The illumination system is shown in figure 4.14.

4.4 Optical measurements

Infrared absorption

Infrared absorption measurements were made at room temperature using a Perkin–Elmer 1710 Fourier Transform Infrared spectrometer. It was important to ensure that samples were free of grease when making infrared measurements as small quantities of grease on the sample led to absorption signals. These occurred in the same region as the C–H absorptions in CVD diamond samples, so it was vital to clean samples thoroughly. This was achieved by immersing the samples in a strong detergent in an ultrasound bath for fifteen minutes, and then rinsing in de-ionised water.

In order to calibrate the infrared absorption signals from samples, all the spectra

were arranged on a vertical scale so that the absorption at 3000 cm^{-1} corresponded to the known value of 12.3 cm^{-1} for diamond. Samples were polished on both sides where possible to minimise scattering; however, sometimes internal scattering from crystallites inside the samples increased the noise.

The other major sources of noise were CO_2 and H_2O in the spectrometer. It was often necessary to purge the chamber with dry nitrogen for a few hours before and during experiments.

Raman measurements

Raman spectra were obtained using a Reinshaw Ramanoscope with CCD detection system and excitation at 633 nm.[17] For a typical sample four spectra would be taken with the excitation beam focussed in different places each time to ensure there was no change across samples. Two of these spectra would be obtained from each side of the sample.

4.5 Software

The software written during this thesis was programmed in Borland Pascal version 7.0. The most important subroutines and programs are outlined in appendix A.

4.5.1 Data collection

After the installment of the Jagmar X-band magnet field controller all the new software written for the control of the magnetic field and processing of "ticker" data described by Tucker [21] became unnecessary, although it was then transferred to the Clarendon Q-band spectrometer.

Instead the existing ENDOR data collection program written by O'Connell [167] and Newton [19] was adapted to run the magnet field controller. This program was

[17]Experiments performed at DeBeers Industrial Diamond Division, Charters, Sunninghill, Ascot.

used as the starting base because it was designed to be used with a GPIB interface, as was the case with the new field controller.

The ENDOR program operated by outputting instructions to a Marconi RF signal generator to increase the frequency in a series of steps, and recording the signal through the PSD after each step. It was, therefore, trivial to adapt it to instruct the field controller in the same manner.

All parameters were set up before the start of a scan: the sensitivity, time constant and field modulation were controlled from the computer and output to the PSD, and then the field controller was set to a particular field and scan width, which it automatically subdivided into 4096 points. All the computer then had to do was collect the data, tell the field to go up one point, collect data, repeating until the scan was complete. The data was read in from the PSD via the GPIB interface. The frequency was read from the frequency counter,[18] also via the GPIB interface.

It was also possible to control the orientation of the sample from the computer; pulses were output through the LPT port to the stepper motor control board. Once the spectrometer was tuned, it was therefore possible to leave spectra being collected, with the computer controlling

- the magnetic field
- the number of scans to average to form each spectrum
- the number of orientations
- the angle moved between each spectrum
- all settings of detector (time constant, sensitivity, field modulation level)

and recording the microwave frequency for each spectrum.

[18]Hewlett Packard 5343A microwave frequency counter.

4.5.2 Simulation of data from Hamiltonian

Until a few years ago a specific program had to be written to extract spin Hamiltonian parameters from experimental spectra for each system studied. Recently more general programs have been written that can be adapted to different effective electron and nuclear spins. The program used in this thesis is EPRNMR.FOR [168]. It performs an exact diagonalization of the effective spin Hamiltonian and can include high spin terms, such as octupolar crystal field effects, in addition to the more common parameters. It could also average over all directions to simulate spectra in powders and polycrystalline material. EPRNMR.FOR was used for simulation of EPR and ENDOR spectra.

4.5.3 Fitting experimental data

In order to make sense of experimental spectra it was often necessary to identify the presence of overlapping lines. A number of programs was written, based on the Levenburg–Marquadt method of least-squares fitting [169], to fit spectra iteratively to a variety of functions. These functions could be generated from algebraic equations, other experimental spectra, simulations generated by EPRNMR.FOR, or combinations of all three. The main uses were as follows:

- Fitting data to anything up to five Lorentzian or Gaussian lines.
- Fitting to a combination of Lorentzian lines and simulated H1 spectra (see §5.4.2).
- Fitting to a convolution of experimental line and series of strips (see §7.3.3).
- Fitting to a convolution of experimental line and theoretical spin distribution (see §7.8).

4.6 Concentration measurements

EPR is a very sensitive technique, capable of detecting as few as 10^{11} spins in a sample [148]. Many of the phenomena discussed in this thesis depend on the concentration of spins, so it is important that the spin concentration should be measured accurately. Two methods of determining absolute spin concentration can be used.

1. Absolute measurement, involving calculation of the sensitivity of the spectrometer based on the microwave power, Q and filling factor of the cavity, temperature, sample losses and other factors. This method is seldom used due to the large numbers of possible sources of systematic error.

2. Relative measurement by comparison with a reference sample with known concentration of spins.

The second technique was employed in this thesis. The reference sample used was a single crystal synthetic type Ib diamond containing the single substitutional nitrogen defect at a concentration of 3.9×10^{19} cm^{-3} $\pm 10\%$, determined by infrared absorption using the parameters determined by Woods *et al.* [170]. Now the configuration of the spectrometer is not a factor in the measurement, as it is the same for the sample as for the reference. The intensity of a spectrum is determined by double integration after baseline correction, since the spectra are recorded as first harmonics, and the intensities of the signal in the sample and the reference compared.

The relative intensities must still be corrected for microwave power and magnetic field modulation, but these are easily compared. It is also important to check that the microwave power is low enough that the signal from the sample is not saturated.

4.7 Vacuum furnace

The furnace used for annealing samples was purchased in 1994. It is a silicon carbide vacuum furnace[19] capable of running at up to 5 kW and reaching a temperature of

[19]Severn Furnaces Ltd. model SC50/2.5/1600.

1600°C. The sample tube is made from recrystallized alumina and has an internal bore of 50 mm, and the furnace temperature is constant over a region of length 250 mm. The furnace is controlled by a Eurotherm 902–904 controller which allows heating/cooling rates and set points to be maintained automatically. The furnace was evacuated with a diffusion pump, via a cold stage, backed by a rotary pump, capable of pumping the furnace down to 5×10^{-7} mBar.

Once the samples were loaded, the furnace was purged with oxygen-free argon three times and pumped out with the rotary pump, then pumped down to minimum pressure. There was significant outgassing every time the furnace was used above 800°C, so the temperature was ramped to 800°C and kept there for at least six hours, and normally overnight, to allow the pumping rate to keep up with the outgassing. The temperature was then increased slowly while the pressure was continuously monitored in order to maintain the pressure below 5×10^{-6} mBar. The temperature could be ramped down at up to 5°C min^{-1}.

Chapter 5

The H1 and P1 defects

5.1 Introduction

In this chapter the two EPR defects in CVD diamond are examined: the single substitutional nitrogen (P1) centre, well known in single crystal diamond since 1959 [171], and first observed in CVD diamond by Watanabe and Sugata [123], and the defects giving rise to absorptions around g=2.0028.

Comparison is made between our results and models for the g=2.0028 defects, and the EPR data are correlated with infrared absorption measurements. The presence and behaviour of hydrogen in this defect and in relation to the growth of diamond by CVD are discussed. An ENDOR experiment is described which confirms the presence of protons near the g=2.0028 defects.

5.2 Background

5.2.1 Nitrogen in CVD diamond

The role of nitrogen in CVD growth is very important, and is discussed in more detail in §7.4.1. The N_S^0 centre in diamond has been extensively studied [171, 15]: the nitrogen bonds with its four carbon neighbours, the extra electron being localized

Detection method	Sensitivity (ppm)	Comment
EPR [145, 124]	0.01	Only detects paramagnetic nitrogen e.g. N_S^0.
UV absorption [175]	1	N_S^0 identified.
IR absorption [170]	1	N in lattice only (specific signatures). N_S^0, A– and B–centres identifiable [24].
Secondary Ion Mass Spectroscopy (SIMS) [174, 176]	30	All forms of N detected.
Elastic Recoil Detection (ERD) [126, 127, 177]	0.5	All forms of N detected. Graeff and Rohrer only detected N_S^0 by EPR in samples with low N concs measured by ERD.
X-ray Photoemission Spectroscopy (XPS) [178]	5000	All forms of N detected.
Combustion analysis [125]	200	All forms of N detected.
Nuclear Reaction Analysis (NRA) [179]	0.1	Sensitive to ^{15}N. Samlenski *et al.* [179] added $^{15}N_2$ to the CVD source gas.

Table 5.1: Methods and sensitivities for nitrogen detection in CVD diamond.

in an antibonding orbital between the nitrogen and one of the carbon neighbours. This unique N–C bond is estimated to be 20–30% longer than the normal C–C bond [172, 173, 16], and forms the principal axis of the defect, which has C_{3v} symmetry. The nitrogen donor is thought to be about 2 eV below the conduction band edge [173]. There is experimental evidence that nitrogen can act as a deep donor compensating acceptor states in as grown CVD diamond [174]. Other nitrogen related defects observed in CVD diamond include the negatively charged nitrogen vacancy centre ($[NV]^-$) [98, 99] observed by photoluminescence, optical absorption and EPR (weak in cathodoluminescence); and the centre with the 575 nm zero phonon line observed by cathodoluminescence [97] (weak in photoluminescence), which is widely believed to be $[NV]^0$. The concentrations of the 575 nm centre and $[NV]^-$ are usually lower than a few ppm in as grown CVD diamond.

The detection of nitrogen in CVD diamond is problematic. EPR is the most

sensitive technique (we have measured concentrations down to 2×10^{15} cm^{-3}, or 10 ppb), but is only sensitive to centres with unpaired electrons, which normally means the N_S^0 centre. There may be nitrogen incorporated into the lattice in other forms, e.g. interstitial sites. N_S^+ also is diamagnetic and not detectable by EPR. It is also possible that nitrogen is found between the individual crystals in a sample. There are methods which detect all the nitrogen in a sample, but with much lower levels of accuracy. Table 5.1 gives a short summary.

5.2.2 Hydrogen in CVD diamond

Hydrogen incorporation into diamond has been studied for many years. In natural type Ia diamond a sharp infrared absorption line at 3107 cm^{-1} has been attributed to a C–H stretch [180]. Recently, the creation of the 3107 cm^{-1} centre has been reported in synthetic diamond grown at high temperature and pressure (HTP) by high temperature annealing [181]. This result indicates that hydrogen may be incorporated into HTP synthetic diamond, in a form not so far detected, and the migration of the hydrogen on annealing produces the defect with the local mode at 3107 cm^{-1}.

In recent years the incorporation of hydrogen into polycrystalline diamond films grown by CVD has attracted considerable attention. The 3107 cm^{-1} absorption has not been reported in CVD diamond films. However, infrared absorption studies have revealed several different C–H stretch vibrations in the region 2750–3300 cm^{-1} arising from carbon–hydrogen bonds in different environments [81, 82].

McNamara *et al.* [82] have suggested that at low concentrations (less than 0.2 atomic percent) the hydrogen content is consistent with the hydrogen being located at grain boundaries; and when the bulk concentration is higher, in amorphous hydrogenated carbon in between grains. High quality CVD diamond films show little or no C–H related absorption in the region 2750–3300 cm^{-1}.

A grain boundary, which separates identical crystallites, is a two-dimensional extended defect which contains point defects. In polycrystalline silicon the silicon dangling bond defect has been identified, and passivation of this defect with hydrogen

has been studied [182]. The formation and dissociation of a grain boundary point defect, possibly consisting of an isolated hydrogen atom at the bond-centre site of a pre-strained Si–Si bond, has been postulated as being responsible for changes in the electrical conductivity of polycrystalline silicon [183].

The unique properties of diamond (optical transparency, thermal conductivity, radiation hardness, etc.) have encouraged interest in the fabrication of polycrystalline diamond electronic devices (e.g. solar blind photoconductive detectors, UV-blind photoconductive detectors, particle detectors). If these applications are to succeed, a thorough understanding of electrically active point defects at grain boundaries is required.

5.2.3 The H1 defect

An EPR defect centred on g=2.0028 is commonly observed in polycrystalline CVD diamond [123, 130, 132, 139, 145]. Observations at X-band (8–12 GHz) sometimes reveal partially resolved satellites separated by 1.25($\pm$0.15) mT at 9.6 GHz and centred on g=2.0028. Measurements on the positions and intensity of the satellites made at approximately 35 GHz, taken together with the X-band data, suggested that they arise from forbidden nuclear spin flip transitions of a hydrogen atom weakly coupled to the unpaired electron spin [139].

Studies of the satellite separation at microwave frequencies between 1 and 9.6 GHz showed that the satellites did not originate from forbidden spin flip transitions with a hydrogen atom with a vanishingly small hyperfine coupling to the unpaired electron [145]. It was found that the defect could be fitted to two Lorentzian lines of different widths centred on g=2.0028, with the satellites arising from a biradical dipolar interaction between two electron spins $\sim$ 10 Å apart [145]. However, the data at above 18 GHz showed this model to be incorrect.

Zhou *et al.* [140, 125] analyzed the EPR absorption at g=2.0028 in several different CVD diamond films at microwave frequencies between 9.8 and 35 GHz and concluded from simulations of the EPR lineshape that the EPR absorption was due

to a single well defined defect consisting of an unpaired electron coupled to a hydrogen atom ~ 2 Å away. They proposed that this defect (labelled H1) was created by a hydrogen atom entering a stretched C–C bond at a grain boundary, allowing the carbon atoms to relax back, one bonding to the hydrogen and the other with an unpaired electron predominantly localized in its dangling bond. The hyperfine coupling parameters used in the powder simulation of the lineshape were $A_{||} = 27.5(2.5)$ MHz and $A_{\perp} = -5.5(2.5)$ MHz. At microwave frequencies above 9.6 GHz the intensity of the satellites is primarily controlled by the square of the magnitude of the anisotropic component of the hyperfine coupling $b = (A_{||} - A_{\perp})/3 = 11.0$ MHz. Simulation of the narrow central line of the spectrum requires $A_{||}$ to be small, which necessitates a non-zero isotropic hyperfine coupling $a = (A_{||} + 2A_{\perp})/3 = 5.5$ MHz. The theory behind this defect is explained more fully in §3.2.5.

5.3 Experimental details

5.3.1 Samples

EPR and infrared absorption experiments were carried out on 40 free-standing films of polycrystalline CVD diamond. The samples were grown by microwave-plasma assisted chemical vapour deposition under a variety of different synthesis conditions to obtain a range of samples of different quality. The samples were typically $10 \times 5 \times 0.5$ mm. They ranged in quality from optically transparent to black and completely opaque. This chapter presents results for nine of these samples, which demonstrate the full range of behaviour found in all the samples.

Characterization

The samples were characterized by Raman and infrared absorption. The Raman measurements were obtained at room temperature with a Reinshaw Ramanoscope incorporating a CCD detection system and excitation at 633 nm. All films exhibited

the first-order diamond Raman peak at 1332 cm^{-1}, with the full width at half height (FWHH) varying from 2.3–6.0 cm^{-1} in different samples. Weak broad structure was observed in the range 1200–1600 cm^{-1} in most samples, which has been attributed to double– or triple–bonded carbon [184]. The infrared absorption measurements were made with a Perkin-Elmer 1710 FTIR spectrometer at room temperature. All samples displayed the fundamental diamond absorption in the two–phonon region. The lower quality[1] samples also showed absorption in the C–H stretch region.

5.3.2 EPR and ENDOR spectrometers

Continuous wave measurements were made at 1.2, 1.8, 2.3, 3.5, 5.8, 9.6 and 34–35.0 GHz. The spectrometers operating at frequencies between 1.2 and 5.8 GHz were all constructed and operated at the National Biomedical ESR Center [185]. They all utilized a loop-gap resonator as the microwave element [186]. Measurements were made at temperatures down to 100 K by inserting the loop-gap resonator into a Varian Q-band nitrogen flow dewar. The spectrometer operating at 9.6 GHz was constructed in the Clarendon Laboratory and is described in §4.3. A Bruker TE_{104} cavity was used and spectra recorded at temperatures between 4 and 300 K.

The two Q-band spectrometers described in §4.2 were used. ENDOR was performed in the Clarendon-built spectrometer as described in §4.2.3. ^1H ENDOR was detected at temperatures between 4 and 100 K via double phase sensitive detection, initially at the field modulation frequency (115 kHz) and then at the radio-frequency (rf) modulation frequency (87 Hz).

5.4 Measurements

EPR spectra taken from a typical sample are shown in figure 5.1. These were recorded at X-band (9.6 GHz), at 4K at two different microwave powers. In (A) the incident microwave power is 30 μW: the P1 (N_S^0) spectrum is strongly saturated such that

[1]Quality defined by the linewidth of the 1332 cm^{-1} Raman line and the optical transparency.

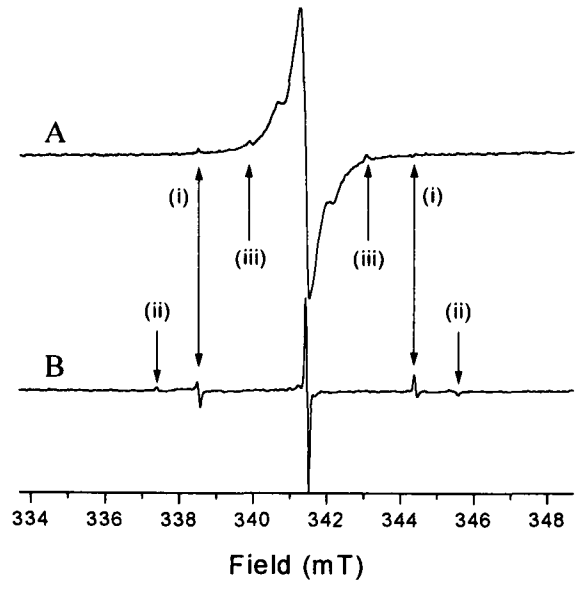

Figure 5.1: EPR spectra from typical type A CVD film (see §5.4.2) at X-band (9.6 GHz) at microwave powers of (A) 30 μW and (B) 3 nW. The double ended arrows (i) indicate the $m_I = +1 \leftrightarrow +1$ and $m_I = -1 \leftrightarrow -1$ allowed N_S^0 EPR transitions where the coupling is $A_\perp$. The single ended arrows (ii) indicate the allowed transitions where the coupling is $A_{||}$. The single ended arrows (iii) indicate the N_S^0 forbidden EPR transitions observed at high microwave powers.

the allowed transitions, marked with double ended arrows, are very small and the forbidden transitions, marked with the single arrows, are observable but weak. Under these conditions the EPR absorption is dominated by the centres at g=2.0028, which saturate much less readily. In (B) the microwave power is reduced by 40 dB to 3 nW, diminishing the signal at g=2.0028 by a factor of 100. This brings the N_S^0 out of saturation and the EPR is now dominated by it. The spectrum is not quite powder-like because of preferential growth of specifically oriented crystallites resulting in a textured film. The film is of type A: this classification is explained in §5.4.2.

5.4.1 The P1 (N_S^0) defect

The N_S^0 centre was first observed by EPR in CVD films by Watanabe and Sugata [123], having g=2.0024(1). It was observable in about half of the films examined in this work, with concentrations ranging from 2×10^{16} cm^{-3} to 4×10^{17} cm^{-3}. A typical EPR spectrum compared with a simulation of the N_S^0 centre in a powder is shown in figure 5.2.

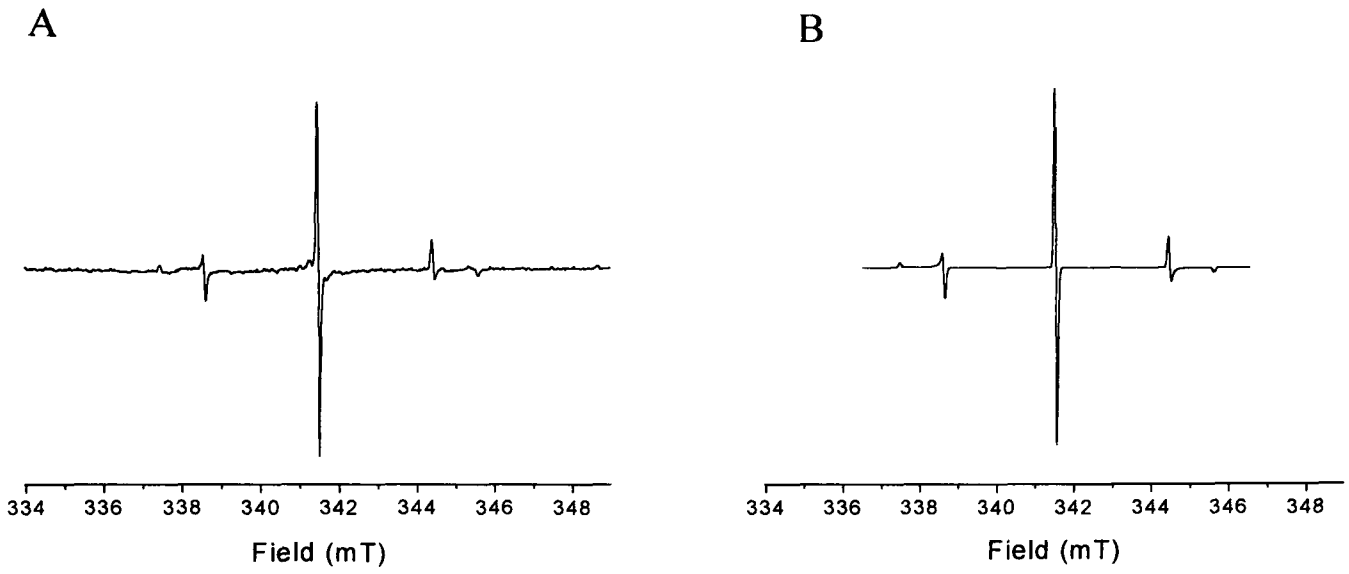

Figure 5.2: Spectrum (A) and powder simulation (B) of N_S^0 centre. The simulation does not include the lines produced by hyperfine interaction with the ^{13}C nucleus at 1.1 % abundance which are visible close to the central line in (A).

Spectra were recorded at X-band and at Q-band (34–35 GHz), under conditions such that the line was not saturated and not broadened, in order to obtain the linewidth and lineshape. The central line was analysed by comparison with simulations using EPRNMR.FOR [168].

Figure 5.3 shows the N_S^0 line at 9.57 GHz (A) and at 34 GHz (B). Surprisingly, the line seems to be narrower at Q-band than at X-band. If the linewidth arises exclusively from dipole–dipole broadening the linewidths would be expected to be the same. Any contribution from anisotropy in g will be greater at higher frequencies and therefore broaden the line more at Q-band than at X-band. So other contributions to the position of the $m_I = 0 left right arrow 0$ transition must be considered. Following the second order perturbation theory outlined by Abragam and Bleaney [156], for an axially symmetric system with $S = \frac{1}{2}$ and $I = 1$ it can be seen that the position of the $m_I = 0 \leftrightarrow 0$ transition is shifted by

$$\frac{(A_{||}^2 + A^2)A_{\perp}^2}{2A^2 g \mu_B B} \tag{5.1}$$

where

$$g^2 A^2 = g_{||}^2 A_{||}^2 \cos^2\theta + g_{\perp}^2 A_{\perp}^2 \sin^2\theta$$

and θ is the angle between the principal axis of the centre and the applied magnetic field. It is clear that contributions due to this term are bigger at lower frequencies

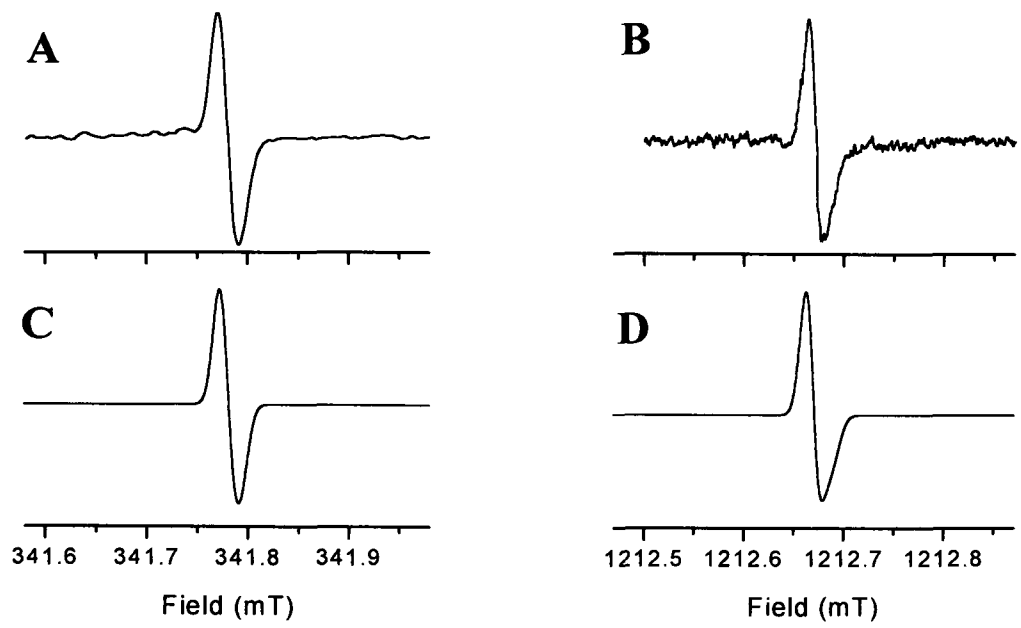

Figure 5.3: The line arising from the $m_I = 0 \leftrightarrow 0$ transition at X-band and Q-band. (A) shows line at 9.57 GHz. (B) shows line at 34 GHz. (C) and (D) show simulations generated by exact diagonalization of the Hamiltonian with the following parameters: $g_{||} = 2.00238$, $g_{\perp} = 2.00241$, $A_{||} = 114.034$ MHz, $A_{\perp} = 81.325$ MHz. Averaged over 826 directions and convolved with a Gaussian of width (HWHH) 15 μT. (C) is simulation at 9.57 GHz and (D) at 34 GHz.

(smaller B). Zhang *et al.* [187] attempted to measure the g-anisotropy in a single crystal synthetic isopure ^{12}C type IIa diamond (99.95 : 0.05 ^{12}C : ^{13}C), but failed to take this term into account. Their sample gave very narrow ($\Delta B_{pp} = 4\,\mu$T) lines that enabled the line position variation with orientation to be determined to a very high accuracy. Using their data it is possible to fit this variation, and determine the value for the g-anisotropy to be $g_{\perp} - g_{||} = +0.00003(1)$.

The expected polycrystalline signals obtained with this g-anisotropy are shown in figure 5.3 (C) and (D). The lines were simulated using an exact diagonalization of the Hamiltonian, convolved with a *Gaussian* lineshape with width (HWHH) 15 μT. A powder simulation was used, averaging over 826 orientations, so the contributions due to the hyperfine anisotropy (equation 5.1) and to the g-anisotropy were averaged together. It is clear that the fit obtained with these parameters is good. It was confirmed that $g_{\perp} - g_{||} > 0$ in accordance with theory [188].

What is unexpected about this fit is the fact that a Gaussian had to be used. The

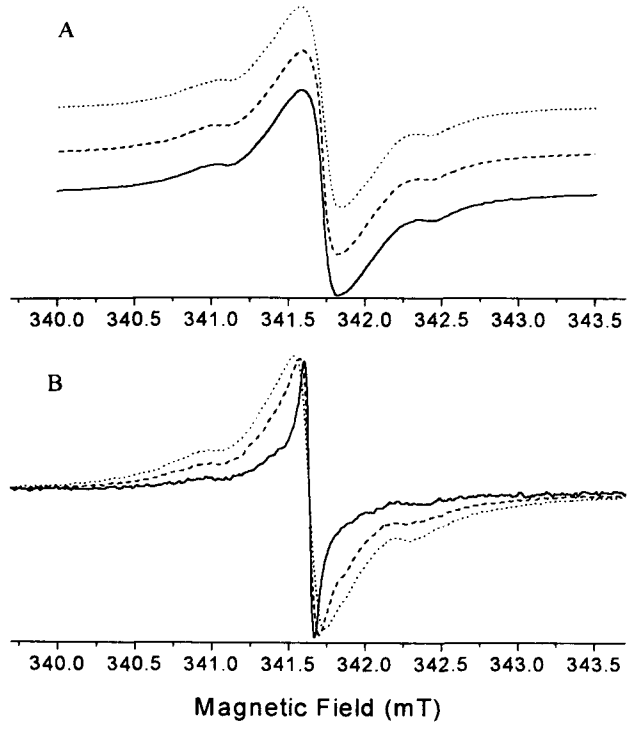

Figure 5.4: X-band (9.6 GHz) EPR spectra from CVD diamond sample (A) type A at 298 K (solid line), 117 K (dashed line) and 5.2 K (dotted line) and (B) type B at 150 K (solid line), 60 K (dashed line) and 5 K (dotted line). Spectra recorded under conditions of low microwave power to avoid saturation and low modulation amplitude to avoid distortion of the lineshape.

nearest fit obtainable with a Lorentzian used lines of width 12 μT, but was much less good. A Lorentzian lineshape would be expected if the linewidth were determined by dipole–dipole broadening at low concentration ($<$ 10000 ppm). The concentration in this case is well inside the Lorentzian limit. The narrowest lines observed in diamond with natural abundance ^{13}C have width 7.5 μT [154], in good accordance with the predicted width of 5 μT [152] caused by dipolar broadening by ^{13}C nuclei. Clearly there is some broadening on top of this in these films. If the nitrogen is not uniformly distributed through the films but is concentrated in regions of higher concentration the lines would be broadened: however, the concentrations are still low enough that this broadening would be Lorentzian. The Gaussian lineshape may indicate that the source of this broadening is strain in the lattice.

5.4.2 The defects at g=2.0028

Figure 5.4(A) shows the X-band spectra centred on g=2.0028(1) typical of most of the polycrystalline CVD diamond samples studied. The g value was checked by

comparison with the N_S^0 signal and by comparison with a solution of 2,2-diphenyl-1-picryl-hydrazil (DPPH) in benzene [148] used as a g marker.[2] These are referred to as type A samples. The spectra look similar to others reported in the literature [123, 130, 132, 139, 125] (see §5.2.3). The resolution of the satellites is sample dependent. As shown in figure 5.4(A) the lineshape is temperature independent, and in addition the EPR intensity follows the Curie Law. The concentration of these centres varies between samples in the range 0.8–13$\times 10^{17}$ cm^{-3}. The degree of resolution of the satellites correlates neither with the total concentration of paramagnetic defects nor with the total integrated absorption strength in the C–H stretch region of the infrared. Figure 5.4(A) is similar to the X-band EPR spectrum shown by Zhou *et al.* [140, 125], but the satellites are weaker relative to the central line. Figure 5.4(B) shows spectra recorded in a sample of type B; EPR absorption from this and similar samples shows a marked temperature dependence. The EPR absorption is dominated by a narrow central line centred on g=2.0028(1) at high temperature, but as the temperature is decreased this line broadens rapidly. At low temperatures the EPR spectrum is dominated by the spectrum observed in type A samples.

Unambiguous interpretation of EPR spectra taken at a single frequency is often difficult. Figure 5.5 shows the results of measurements at 1.2, 3.4, 9.6 and 34.0 GHz on a type A sample. The calculated EPR spectra for the H1 centre using the parameters from Zhou *et al.* [125] are shown alongside the experimental data. The calculated spectra are generated using the simulation software EPRNMR.FOR [168] (see §4.5.2).

The 34.0 GHz data appears to be in good agreement with the H1 model. However, as the microwave frequency is reduced the model fails to reproduce the experimental data. The discrepancy becomes more marked with decreasing frequency, but the positions of the satellites are still predicted correctly.

[2] g=2.0037(2) for DPPH dissolved in benzene [148].

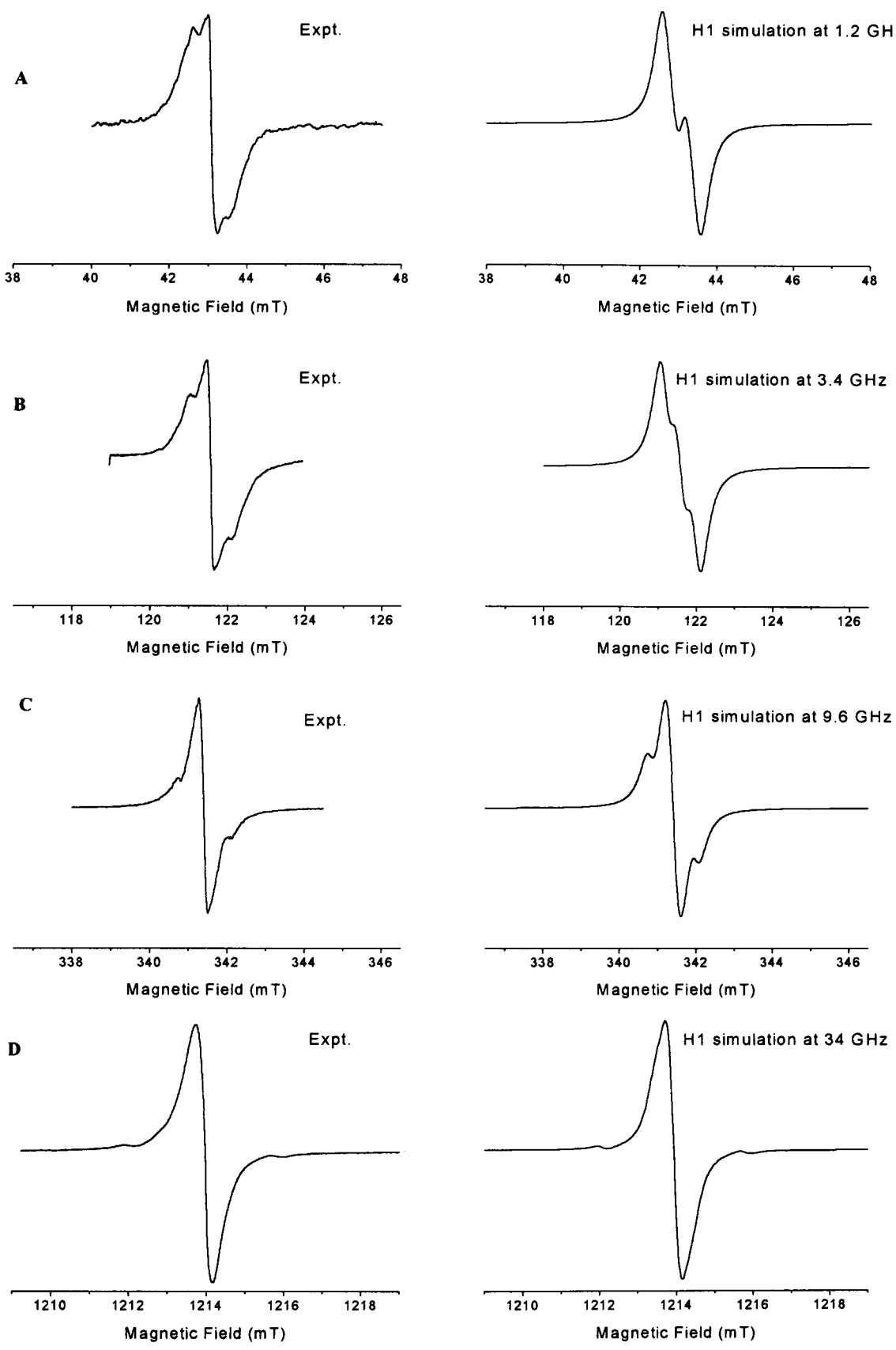

Figure 5.5: EPR spectra obtained from a type A sample at microwave frequencies of (A) 1.2 GHz, (B) 3.4 GHz, (C) 9.6 GHz and (D) 34 GHz. The sample temperature was 100 K, spectra were recorded under conditions of low microwave power to avoid saturation and low modulation amplitude to avoid distortions of the lineshape. Alongside each experimental spectrum is the simulation of the H1 EPR spectrum at the specified microwave frequency. Powder simulation used a Lorentzian lineshape with half width at half height 0.30 mT.

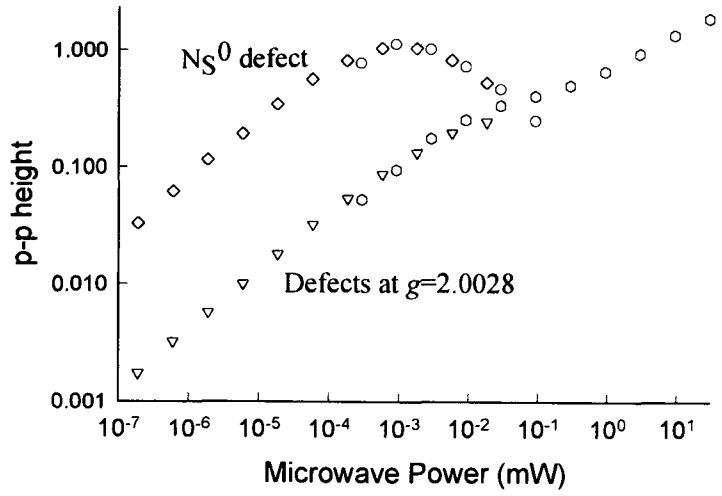

Figure 5.6: Saturation curves at 5K for N_S^0 and g=2.0028 defect in type A sample at 5 K.

Saturation behaviour of P1 and g=2.0028 defect

As shown in figure 5.1, it is possible to isolate either the N_S^0 signal or the g=2.0028 signal by judicious use of the spectrometer conditions. This is because the N_S^0 saturates at a much lower power than the g=2.0028 defect. Figure 5.6 shows the saturation curves for the two defects in the same sample.

Although the defects at g=2.0028 are hard to saturate, at very high powers at low temperature it is possible to saturate the line. When this happens the lineshape changes as shown in figure 5.7. What appears to take place is that the H1 defect broadens but saturates less easily than the other defect(s) at g=2.0028.

5.4.3 Comparison of FTIR and EPR data

The infrared absorption for a high quality type A sample is shown in figure 5.8(A). The region 2750–3100 cm^{-1} is shown for a lower quality sample. This region corresponds to the C–H stretch vibrations. The structure of the absorption in this region, and the C–H stretches which form it are discussed in §6.4.1.

Figure 5.9 shows the EPR spin concentration measured at 5K, less any contribution from the N_S^0 centre, plotted against the total integrated absorption in the C–H stretch region of the infrared spectrum for nine samples. The EPR concentration for the species centred on g=2.0028 correlates with the total absorption in the C–H

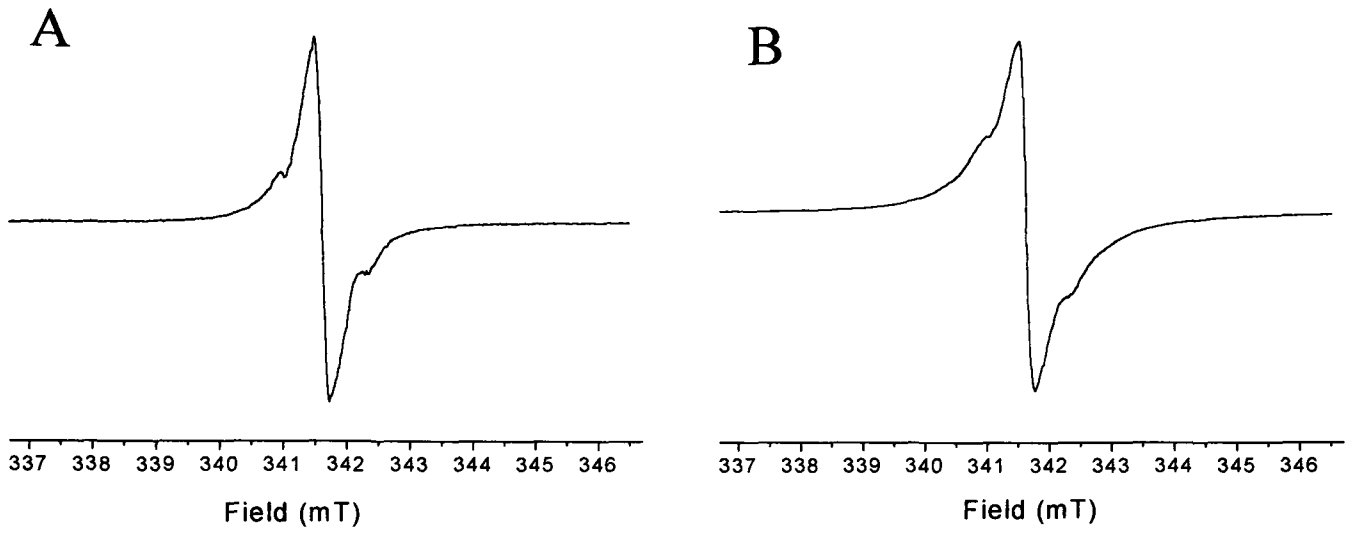

Figure 5.7: Change in lineshape with saturation at g=2.0028. (A) shows lineshape at 9 μW microwave power, unsaturated. (B) show lineshape at high power (9 mW). Change in relative intensities of satellites is clear.

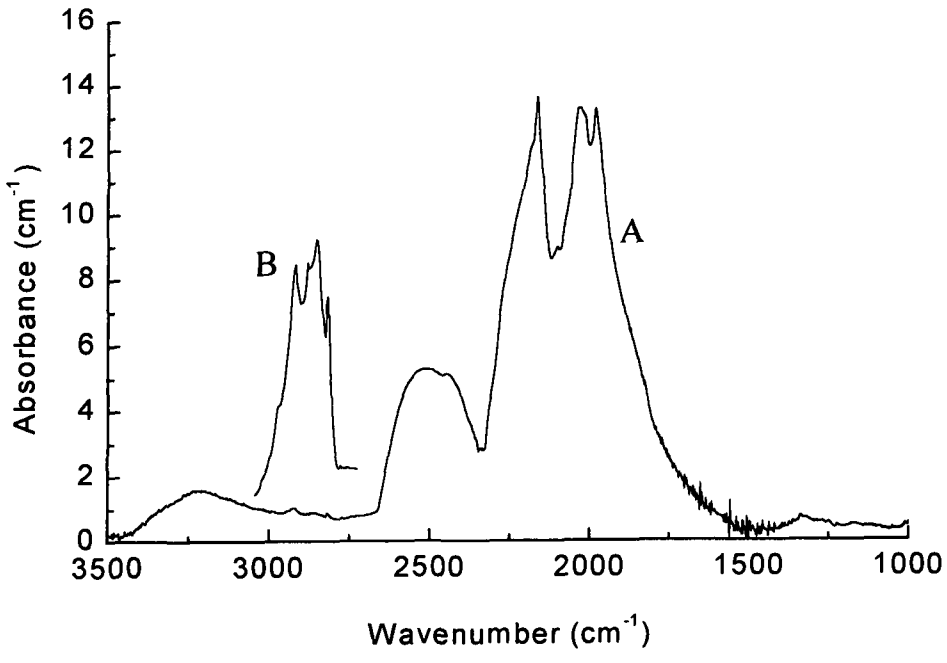

Figure 5.8: (A) Infrared absorption spectrum from sample 1. (B) shows region of C–H stretch (2750–3100 cm^{-1}) in lower quality sample (sample 20) on the same vertical scale.

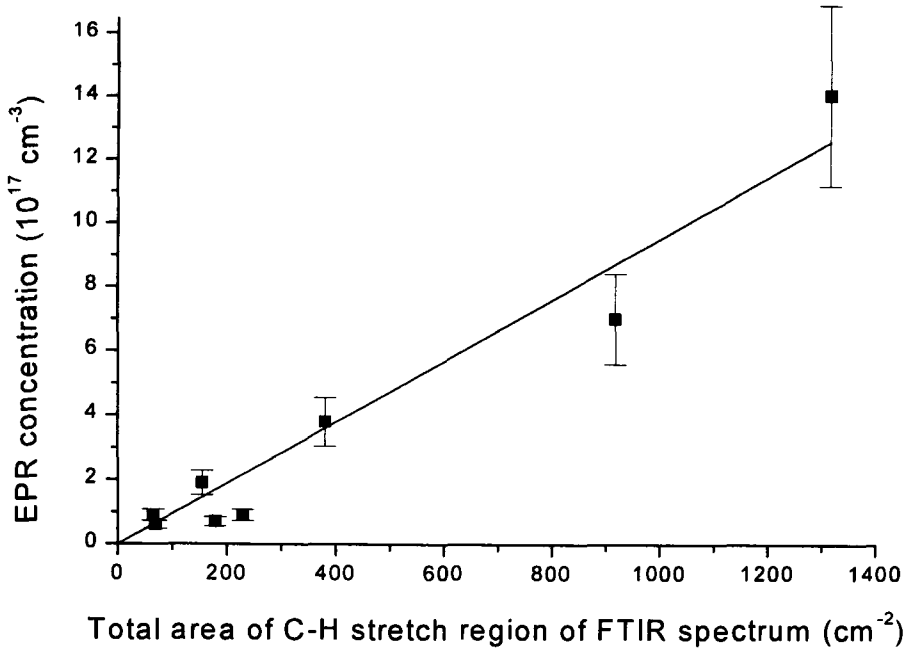

Figure 5.9: Integrated EPR spin concentration (excluding any contribution from N_S^0) plotted against integrated absorption in C–H region of infrared spectrum.

stretch region, but there is no correlation with the N_S^0 centre concentration.

5.4.4 ^{1}H ENDOR

Observation of hydrogen spin-flip satellites centred on g=2.0028 stimulated a ^{1}H ENDOR study of the hydrogen atom(s) neighbouring the unpaired electron. The ENDOR detection system detailed in §4.2.3 and §5.3.2 produces first derivative lineshapes. Figure 5.10 shows the integrated ENDOR spectrum obtained from a type A sample at 5 K. The ENDOR resonance is centred on the ^{1}H nuclear Zeeman frequency, and is typical of ^{1}H matrix ENDOR signals observed in disordered solids [158]. No ENDOR resonances were detected at the frequencies predicted by the parameters for the H1 model. This is demonstrated in figure 5.11. The ^{1}H matrix ENDOR signal was detected at temperatures up to 100 K without any appreciable change in lineshape. The signal to noise diminished appreciably with increasing temperature. At 5 K a ^{1}H matrix ENDOR signal could be detected with the magnetic field set to resonance at g=2.0028 in all type A and type B samples studied.

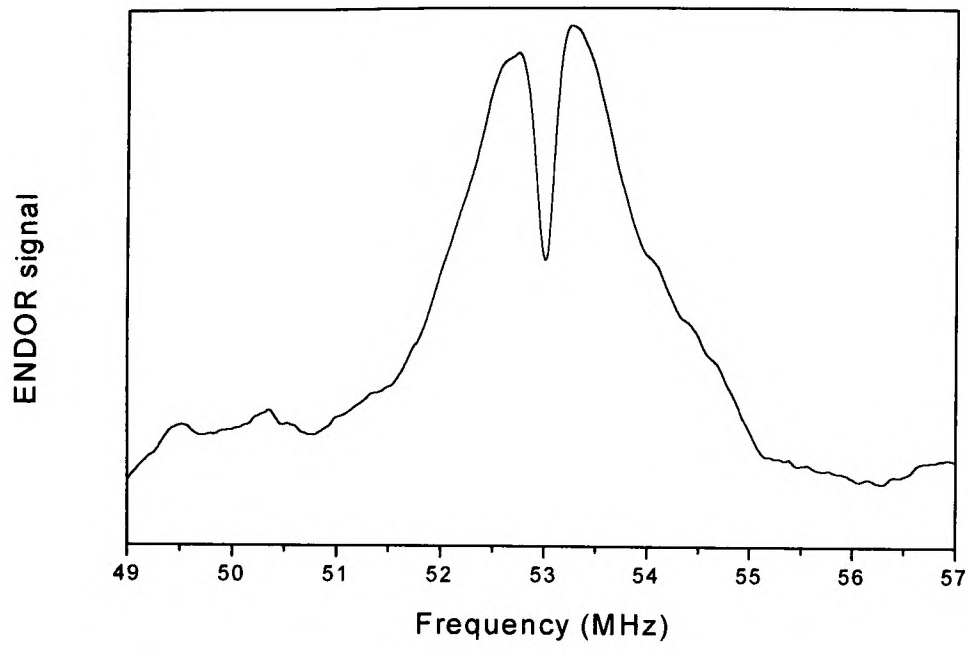

Figure 5.10: ENDOR spectrum from a type A sample. Temperature 4.5 K, microwave frequency 34.85 GHz, microwave power 2 mW, rf power 20 W. Spectrum recorded using double lock-in detection at field modulation frequency (115 kHz) and rf frequency modulation frequency (87 Hz), and integrated to produce pure absorption signal.

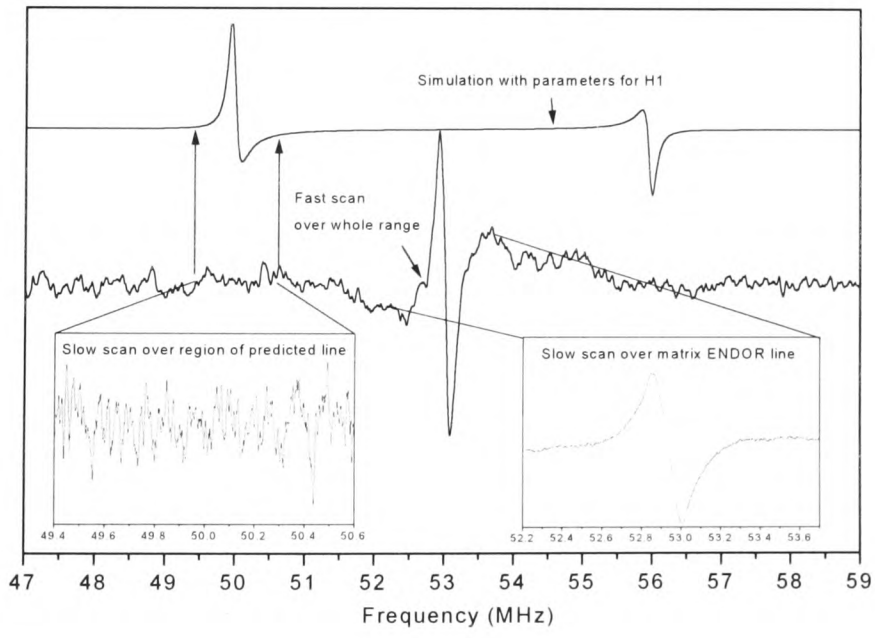

Figure 5.11: As detected ENDOR spectrum from a type A sample and simulation of H1 ENDOR signal from parameters determined by Zhou *et al.* [125]. Temperature 4.5 K, microwave frequency 34.85 GHz, microwave power 2 mW, rf power 20 W. Spectrum recorded using double lock-in detection at field modulation frequency (115 kHz) and rf frequency modulation frequency (87 Hz).

5.4.5 Saturation Recovery measurements

Detection of continuous wave ENDOR signals is dependent on achieving an appropriate balance of relaxation rates. The temperature dependence of the spin lattice relaxation rate was studied between 10 and 100 K using the technique of saturation recovery.[3] All of the methods of measuring the electron spin–lattice relaxation rates are complicated by the necessity of eliminating the effects of spectral diffusion. Spectral diffusion leads to a spreading of saturation over the inhomogeneously broadened line, from spins that are on resonance to other spins which are not owing to different hyperfine couplings, defect orientations, etc. Spectral diffusion contributes to the recovery from saturation by the observed spin packet in competition with intrinsic spin–lattice relaxation processes. The importance of spectral diffusion can be assessed by observation of the recovery from saturation as a function of saturating pulse length. Experiments on type A and type B samples showed that the recovery was not well described by a single exponential: a better fit could be obtained with a combination of two exponentials. The dependence of the two relaxation rates determined by fitting the data to two exponentials on the saturating pulse length is shown in figure 5.12(A). For short pulses spectral diffusion significantly affects the measured recovery rates. As the saturating pulse length is increased the spectral diffusion channels are progressively saturated. Figure 5.12(B) shows the variation of the relaxation rates of the two components of the recovery with temperature (400μs saturating pulse).

5.5 Discussion

5.5.1 The H1 centre—EPR and infrared behaviour

The multifrequency EPR (9.8–35 GHz) data presented in figure 3 of Zhou *et al.* [125] was satisfactorily reproduced by the H1 defect (with a sample dependent linewidth) without any other components. The low frequency EPR data presented in figure

[3]Experiments performed at the National Biomedical ESR Center [185] by Dr. M. E. Newton.

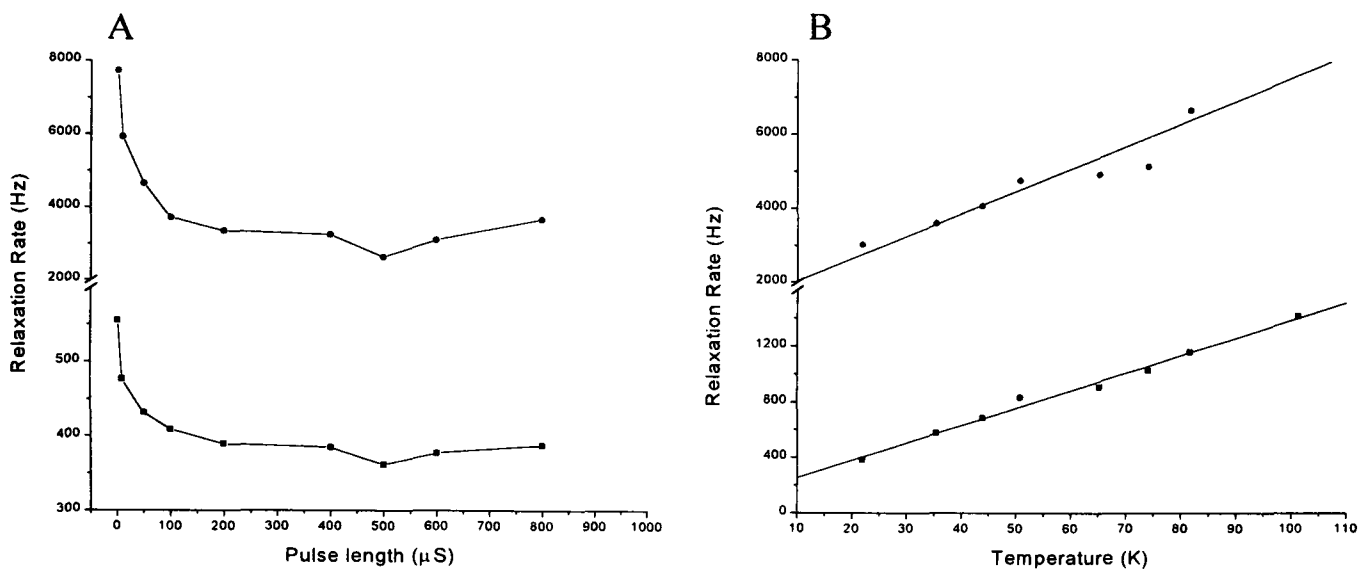

Figure 5.12: (A) Time dependence of the relaxation rates for the g=2.0028 EPR resonance in a type A CVD diamond sample at 20 K, obtained by fitting the saturation recovery response to a sum of two exponential functions, on the duration of the saturating microwave pulse. (B) Temperature dependence of the relaxation rates determined as described in (A) with a saturating pulse length of 400μs. Solid lines are a linear fit to the observed dependence.

5.5 are not reproduced by the H1 centre alone. However, a convincing fit can be obtained at all frequencies using the H1 defect plus an additional isotropic resonance at g=2.0028. The experimental data and fits are shown in figure 5.13. The asymmetry in the Q-band data (figure 5.13(D)) probably indicates a small anisotropy in the g-matrix. The additional isotropic resonance at g=2.0028 has a Lorentzian lineshape, a half width at half height of 0.22(2) mT and is present at the same relative intensity (0.6 $\times$ intensity of H1) at all microwave frequencies in this sample.

EPR investigations indicate that the H1 defect is a commonly observed defect. Studies of the EPR lineshape as a function of microwave frequency permit the identification of the neighbouring hydrogen atom and its hyperfine coupling parameters. The data in figure 5.5 confirms the parameters, $a = 11.0(2.5)$ MHz and $b = -5.5(2.5)$ MHz, determined by Zhou *et al.* [140, 125]. We can find no other model which is consistent with the experimental data. The X-band and Q-band data presented in figure 5.5 could be fitted using a similar model to H1, with smaller hyperfine pa-

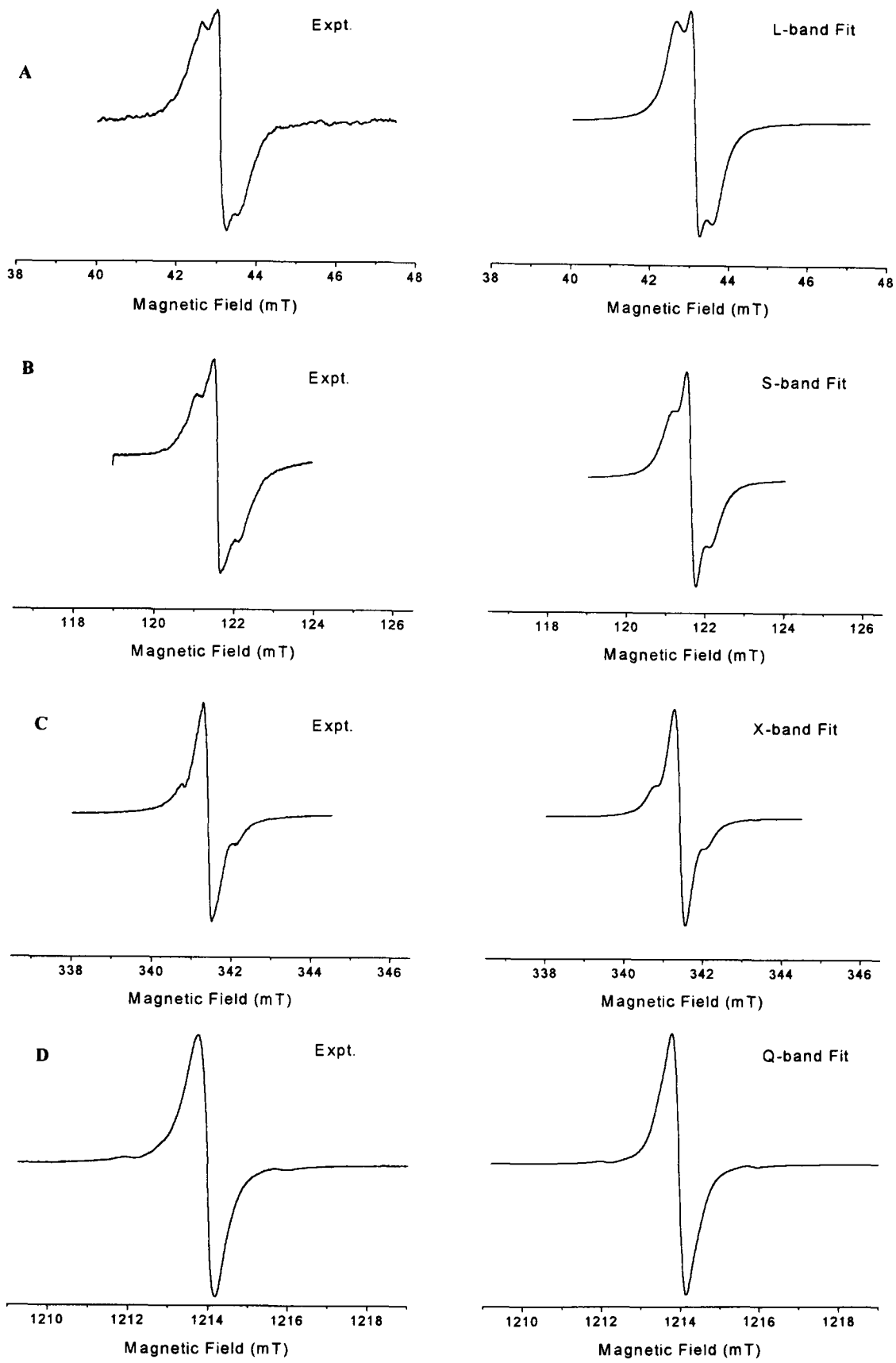

Figure 5.13: Fit to experimental EPR spectra obtained from a type A sample at microwave frequencies of (A) 1.2 GHz, (B) 3.4 GHz, (C) 9.6 GHz and (D) 34 GHz. The fits to the data are obtained using the H1 defect (HWHH 0.3 mT) plus an additional resonance at g=2.0028(1) (HWHH 0.22 mT). The EPR linewidth and the relative intensity of the two components is fixed for all frequencies, but is sample dependent.

rameters (although still within the error bars given by Zhou *et al.*) and no extra component: however, these parameters do not reproduce the low frequency data, and this unambiguously indicates the presence of an additional resonance at g=2.0028. It appears that the relative concentrations of H1 and the additional EPR centre are sample dependent. The possibility cannot be ruled out that this additional resonance is the H2 centre identified by Zhou *et al.* [125]. H2 has not been observed in the absence of H1 in any of the samples studied in this work: however, all the samples have contained H1, and observation of the satellites belonging to H2 is impossible under the relatively strong H1 line. It is difficult to speculate further as to the origin of this line in the absence of any further information. The primary difficulty in the analysis of these centres is that they are all fairly broad, isotropic and centred on the same point in the spectrum, meaning that they can be distinguished only with a great deal of difficulty.

The difference in saturation between the g=2.0028 defects and the N_S^0 defect shown in figure 5.6 shows that there is no interaction between the centres. There were no cross relaxation processes between the two centres. This contrasts with the work of Cox [20], who found that nickel and nitrogen centres in the same growth sectors of HTP diamonds showed strong cross relaxation effects. This suggests that the g=2.0028 centres and N_S^0 centres are found in different regions of the sample.

For all samples from which data is shown in figure 5.9, the H1 defect makes the dominant contribution to the total unpaired electron concentration. The correlation between the concentration of H1 and the total C–H infrared absorption is consistent with H1 being located on hydrogen decorated grain boundaries, or in hydrogenated non-diamond material in between grain boundaries. In the samples labelled type A we have shown the absorption at g=2.0028 originates from two defects: in over 40 samples none have been found containing only H1.

5.5.2 The H1 centre—ENDOR behaviour

The assumption that the H1 centre is located in hydrogenated regions of the sample is supported by observation of a ^{1}H ENDOR line at the free nuclear Zeeman frequency. This line originates from hydrogen atoms surrounding the unpaired electron and weakly coupled to it via the electron–nuclear dipolar interaction. It is usually referred to as the ^{1}H matrix ENDOR line [158]. The dip in the centre of the line arises from nuclear coherence effects and suggests the presence of more than one ^{1}H neighbour [189]. Information about the distribution of the unpaired electron and the local environment can be extracted from the matrix ENDOR lineshape. A simple but useful model for the lineshape assumes a uniform ^{1}H distribution and contains only two parameters, the lower limit of the electron–proton separation (separation at which only a dipolar interaction need be considered) and the width of the nuclear spin packet[4] [157]. Following this approach we find that the experimental matrix ENDOR lineshape is best reproduced with this simple model with a lower limit of separation of the order of next-nearest diamond separation (2.5 Å), if we assume that the nuclear spin-packet half width at half height is 100 kHz, which is in accord with previous observations [190]. NMR studies show that the majority of hydrogen in diamond films gives rise to a Gaussian NMR signal with a full width at half maximum of 50–70 kHz [191]. However, it is well known that NMR lineshapes are not characteristic of the nuclear lineshapes appropriate to matrix ENDOR. Matrix ENDOR only detects those nuclei near a paramagnetic species; for those nuclei the nuclear relaxation time will be less than for the bulk nuclei and hence the nuclear line broader.

No ^{1}H ENDOR lines were observed from the hydrogen neighbour at 1.9 Å, as shown in figure 5.11 (B). This negative result suggests that the matrix ENDOR response is much stronger than that of the near neighbour. This is not unreasonable since the matrix ENDOR response probably arises from many ^{1}H neighbours which all add to the resonance around the nuclear Zeeman frequency, whereas the ENDOR intensity from the single near neighbour is spread out by the anisotropic component of

[4]See §3.3.1.

its hyperfine interaction. No temperature dependence of the width of the ^{1}H matrix ENDOR signal could be detected up to 100 K; this is consistent with the hydrogen being rigidly bound.

5.5.3 Saturation recovery and the g=2.0028 defects

In §5.4.5 it was shown that spectral diffusion can significantly alter the measured saturation recovery rates. Two processes that contribute to spectral diffusion are electron spin–spin interactions which will occur on a time scale of the phase memory-decay (T_2) and electron–nuclear spin–spin interactions which occur on a much slower time scale. For long saturating pulses, when the spectral diffusion channels are saturated, the recovery was found to be best fitted by the sum of two exponentials. For a given spin we would expect a single exponential recovery; hence, one possible explanation of the two-component decay is that the resonance at g=2.0028 consists of two components with different spin–lattice relaxation rates. This is consistent with the multifrequency EPR data which indicated the presence of H1 and another defect. At high microwave powers the change in continuous wave EPR lineshape shown in figure 5.7 suggests that one defect is being preferentially saturated. This is consistent with the two defects having different relaxation rates, as shown in figure 5.12(B). The linear dependence of both relaxation rates with temperature indicates that the direct mechanism [156] dominates spin–lattice relaxation in this temperature region. The spin–lattice relaxation rate for N_S^0 is of order 10–100 times less than that for the H1 centre.

5.5.4 Linewidths and concentrations

The lines in figure 5.13 have been shown to consist of the H1 defect with HWHH 0.30(2) mT, plus a single Lorentzian HWHH 0.22(2) mT. These linewidths are sample dependent, but in all samples the widths are in the range 0.28–0.36 mT for the H1, and 0.18–0.28 mT for the single Lorentzian, so we can consider them all to have

linewidths of 0.32±0.04 mT for the H1, and 0.24±0.05 mT for the Lorentzian. These linewidths are independent of microwave frequency.

Magnetic dipolar broadening could account for the width of the EPR lines. This could be caused either by interaction with other unpaired electrons in similar defects, or by interaction with nearby protons. First we consider the possibility of dipolar broadening with other electrons. Assuming a random distribution of paramagnetic centres over a diamond lattice with a probability f that a lattice site is occupied by an unpaired electron, it can be shown (see §3.2.6) that for a single spin species, in the limit of negligible exchange broadening, in a polycrystalline material, the second and fourth moments of the absorption lines are [192]

$$M_2 = \frac{3}{5}\left(\frac{\mu_0}{4\pi}\right)^2 g^2\mu_B^2 S(S+1)f\sum_k r_{jk}^{-6} \tag{5.2}$$

$$M_4 = 3M_2^2[0.778 + f^{-1}(0.142 - 0.033(S^2+S)^{-1})] \tag{5.3}$$

where r_{jk} is the separation between the jth and kth unpaired spin, S is the electron spin quantum number and the summation is over all lattice sites. At low concentration both M_2 and M_4 are proportional to the concentration of paramagnetic centres. For $f < 0.01$ the lineshape is approximately Lorentzian, whereas for $f > 0.1$ the lineshape is approximately Gaussian [152]. The concentration of impurities can, in principle, be determined from M_2 alone. However, for a Lorentzian line numerical evaluation of M_2 leads to a result which is proportional to the cut-off limit of the calculation. This is not a satisfactory approach. It can be shown [152] that the HWHH Δ of a Lorentzian line is approximated by

$$\Delta = \frac{\pi}{2\sqrt{3}}\sqrt{\frac{M_2^3}{M_4}}. \tag{5.4}$$

Now Δ can be determined by fitting the EPR spectra and the fractional concentration calculated using the three equations above and the result

$$\sum_k r_{jk}^{-6} = 776a_0^{-6} \tag{5.5}$$

where a_0 is the diamond lattice constant [132]. If these defects are at grain boundaries or between diamond grains, and not in the diamond lattice, then equation 5.5 does not, strictly speaking, apply, but the carbon–carbon separation in hydrogenated amorphous carbon is similar, and it is impossible to compute the sum in a more general fashion. If the linewidth is predominantly caused by electron broadening, then linewidths of 0.24 and 0.32 mT indicate unpaired electron concentrations of 3.2×10^{19} and 4.3×10^{19} cm^{-3} respectively. Calculations using this treatment appear consistent with the the EPR linewidth and concentration of the N_S^0 centre in synthetic Ib diamond. A concentration of 4×10^{19} cm^{-3} in a diamond lattice suggests a defect separation of $\sim$ 28 Å. At this separation we would expect the exchange interaction between spins to be very small. This treatment provides an idea of the local concentration of these defects, taking into account that if the defects are not in the diamond lattice the numbers will not be right, although they will still be of the right order. As the bulk concentrations of these defects are in the range 0.8–13$\times 10^{17}$ cm^{-3}, clearly if this is the cause of the linewidth then the defects are concentrated in $\sim$ 2 % of the sample.

The other possible source for dipolar broadening of the line is the interaction between the unpaired electron and protons. It is clear there are protons near the defects from the ENDOR and from the structure of the H1 defect; we need to determine whether the separations are realistic. Now the interactions are between unlike spins and the second moment is given by

$$M_2 = \frac{4}{15}\left(\frac{\mu_0}{4\pi}\right)^2 g_N^2 \mu_N^2 I(I+1) f \sum_k r_{jk}^{-6} \tag{5.6}$$

where g_N is the g value for the nuclear spin, in this case the proton. The likely value of f is now high enough that a Gaussian approximation ought to be reasonable: however, the Lorentzian system should also be considered. The fourth moment for a single crystal of diamond for dipolar broadening between unlike spins is (see §3.2.6)

$$M_4 = \left(\frac{\mu_0}{4\pi}\right)^4 g_N^4 \mu_N^4 \frac{1}{5}(I(I+1) - \frac{1}{3}) f \sum_k \frac{(1 - 3\cos^2\theta_k)^4}{r_k^{12}} \tag{5.7}$$

The linewidth of a Gaussian line is related to the second moment by

$$\Delta = \sqrt{2 \ln 2 M_2} \tag{5.8}$$

and this allows a prediction for the concentration of protons. Linewidths of 0.24 and 0.32 mT predict occupation probabilities f of 0.07 and 0.12 respectively, leading to an average electron–proton distance of 4.2 and 3.4 Å.

In the Lorentzian approximation, since we do not have the sum over powder orientations for M_4, we use the single crystal summation[5] for M_2 as well, averaging over different directions. Using the approximation in equation 5.4 the predicted values of f are 0.15 and 0.2 for the two linewidths, leading to average electron–proton distances of 3.3 and 3 Å.

Again, the approximation that the surroundings of the electron correspond to a well-defined diamond lattice is not necessarily correct, but the distance 3–4 Å for the average separation between the electron and nearby protons is physically reasonable, and a diamond lattice will not be so far from the truth. This also ties in with the detection of protons by the ENDOR experiment at a *minimum* distance of 2.5 Å.

5.5.5 g=2.0028 defects in type B samples

In the samples labelled type B, a previously unreported defect centred on g=2.0028(1) is observed. The temperature dependance of the EPR was difficult to follow, especially at low temperatures, because of overlapping resonances from the H1 defect and the other unidentified defect at g=2.0028. The temperature dependence of the defects at X-band is shown in figure 5.14. The 100 K lineshape was reproduced in experiments at other microwave frequencies. The temperature dependence is suggestive of the resonance being exchange narrowed at temperatures above about 50 K, and as the temperature is reduced below 50 K the lifetime of distinguishable states increases and the resonance broadens. At high temperatures the lifetime of any state is so short that any hyperfine splitting is averaged to zero, and, as in the limit of very slow exchange,

[5]See §3.2.6, equation 3.20.

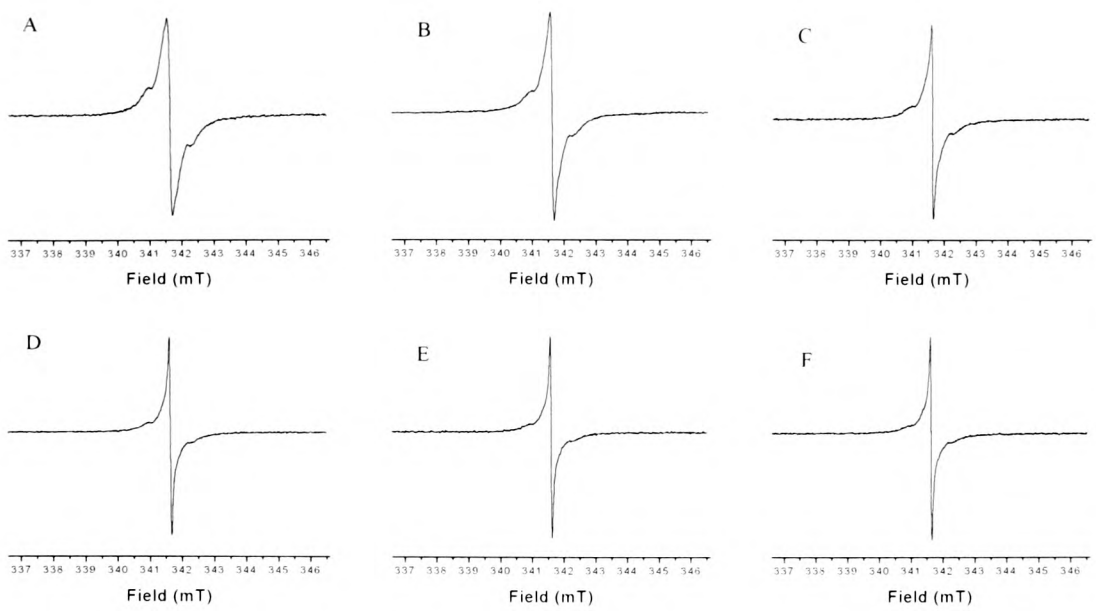

Figure 5.14: Temperature dependence of resonance at g=2.0028 in type B sample. Temperatures are: (A) 5 K. (B) 15K. (C) 30 K. (D) 60 K. (E) 100 K. (F) 150 K.

hyperfine couplings could broaden the EPR appreciably. Therefore the centre may be much more easily detected in the rapid exchange limit due to the resonance being so narrow. Several different exchange mechanisms (e.g. electron exchange, electron transfer, proton exchange, thermal effects) could be invoked to explain the observed phenomena.

5.6 Conclusions

The EPR measurements support the proposal of Zhou *et al.* that the H1 centre is a well defined defect with a unique hydrogen neighbour about 1.9 Å away from the unpaired electron. However, the low frequency EPR measurements show conclusively that in the samples studied here H1 is always accompanied by another defect at g=2.0028(1). This second defect could be a new centre whose presence is related to the growth conditions pertaining to the samples we have studied, or it could be the H2 centre [125]. The saturation recovery also indicates the presence of two defects at g=2.0028.

^{1}H matrix ENDOR indicates that in addition to the near neighbour hydrogen, H1 is in an environment with other hydrogen atoms 2–10 Å away. The spin–lattice

relaxation rate of H1 is much more rapid than that of the substitutional nitrogen centre which is incorporated into the diamond lattice. The H1 linewidth could arise from dipole–dipole broadening, for which there are two possible sources:

- Unpaired electrons in similar defects at a local concentration of $\sim 4 \times 10^{19}\,\mathrm{cm}^{-3}$ (mean electron–electron separation 28 Å). If this is the source of the linewidth it suggests the defects are concentrated in ~ 2 % of the sample.

- Nearby protons at a mean distance of ~ 3 Å. This agrees with the ENDOR data.

The correlation between the EPR intensity at g=2.0028 and the intensity of infrared absorption in the C–H stretch region is consistent with their being related. All the evidence is consistent with the H1 defect being located at grain boundaries, not in the bulk diamond.

Another new defect centred on g=2.0028 has been observed, but not identified. The temperature dependence of this defect indicates exchange narrowing at high temperatures.

The N_S^0 centre fits the established parameters. The small width and Gaussian shape of the line suggest that it is distributed homogeneously through the lattice and may be broadened slightly by strain in the lattice.

Chapter 6

Annealing studies

6.1 Introduction

In this chapter the effect of annealing polycrystalline CVD diamond *in vacuo* up to 1900 K is discussed. This has been studied using EPR and infrared absorption. The correlation between the behaviour of C–H stretch modes in the infrared absorption and the EPR defects with g=2.0028 is studied.

6.2 Background

6.2.1 C–H stretch modes in infrared absorption spectra

In the previous chapter it was shown that the EPR signals seen in all polycrystalline CVD films at g=2.0028 arise from the H1 defect [125] and at least one other defect. These defects were suggested to be located on grain boundaries or in amorphous hydrogenated carbon between grains. ^{1}H ENDOR showed the presence of hydrogen near these defects. The correlation between the concentration of these defects and the intensity of C–H stretch modes in the infrared absorption has been demonstrated.

The infrared absorption spectra in CVD diamond samples described in the previ-

Wavenumber (cm^{-1})	Characteristic group
2820	N–CH_3
2833	O–CH_3
2850	sym. sp^3 CH_2
2875	sym. sp^3 CH_3
2920	asym. sp^3 CH_2
2965	sym. sp^3 CH_3
2980	sym. sp^2 CH_2
3025	sp^2 CH

Table 6.1: Wavenumbers and characteristic groups of C–H region of infrared absorption [82]. Dischler *et al.* [81] ascribe the 2820 and 2833 cm^{-1} groups to hydrogen adsorbed onto a (111) diamond surface.

ous chapter can be analyzed and individual modes identified [81, 82]. The C–H stretch signatures of hydrogen bonded to sp^2-bonded carbon appear above 2950 cm^{-1}, while those associated with sp^3-bonded carbon appear below 3000 cm^{-1} [193, 194]. Other absorptions are present at frequencies (2820, 2833 cm^{-1} [81, 82]) below those normally observed for C–H stretching vibrations in amorphous hydrogenated carbon. McNamara *et al.* [82] have associated the peaks at 2820 and 2833 cm^{-1} with N–CH_3 and O–CH_3 groups respectively. However, they could originate from hydrogen bonded directly on a diamond (111) surface [81]. Chin *et al.* [195] found a single sharp peak at 2830 cm^{-1} from H adsorbed on a (111) surface. Table 6.1 details the frequencies and assignations of these modes.

6.2.2 Annealing CVD diamond

Post processing (e.g. annealing) of CVD diamond films has attracted very little attention [133, 196], but may prove useful for the fabrication of material for specific applications. There has also been little work reported on the annealing behaviour of H1 and other g=2.0028 centres in polycrystalline CVD diamond; Jia *et al.* [133] found that the intensity and lineshape of the EPR absorption at g=2.0028 in hot filament CVD samples did not vary with annealing up to 1400 K, but annealing a

sample (which had been ground into a powder) to 1800 K with an oxyacetylene torch for 20 minutes reduced the overall spin density by a factor of 4.5, and the relative intensity of the satellites increased with respect to the central line. No mention was made in this study of sample graphitisation. In an inert environment (vacuum better than 2×10^{-6} mBar) the conversion of diamond to graphite is not normally detectable for annealing below 1800 K, but diamond is attacked by oxygen and water vapour at temperatures as low as 900 K [197].

6.3 Experimental

6.3.1 Samples

The polycrystalline CVD diamond samples used were a subset of the 40 samples described in the previous chapter. They were made by a proprietary microwave CVD process under a variety of conditions to obtain a wide range of material properties. In five of the samples the N_S^0 concentration was less than 2×10^{15} cm^{-3} as measured by EPR, and in the others it ranged between 2×10^{16} and 4×10^{17} cm^{-3}. All the samples contained the defects with g=2.0028, as described in the previous chapter. The samples were all polished in order to reduce surface scattering in infrared absorption measurements, and to reduce the surface area when annealing. The optical quality ranged from opaque to clear with an optical transparency approaching that of the best natural diamond.

6.3.2 Vacuum furnace

The samples were annealed at temperatures between 1100 and 1900 K in a silicon carbide vacuum furnace, which is described in detail in §4.7. Once the samples were loaded, the furnace was purged with oxygen-free argon before pumping and annealing. The initial heating rate was kept low in order to match the rate of furnace out-gassing. The furnace was held at the set annealing temperature for 4 hours and then cooled

Sample no.	Concentration N_S^0 (No. cm^{-3})	Concentration of defects centred on g=2.0028 (No. cm^{-3})
1	$< 2 \times 10^{15}$	0.62×10^{17}
3	2.3×10^{17}	0.9×10^{17}
5	$< 2 \times 10^{15}$	1.4×10^{17}
10	0.9×10^{17}	0.9×10^{17}
20	$< 2 \times 10^{15}$	14×10^{17}
22	$< 2 \times 10^{15}$	1.9×10^{17}
23	0.9×10^{17}	7.2×10^{17}
25	$< 2 \times 10^{15}$	3.8×10^{17}
30	0.6×10^{17}	0.9×10^{17}
33	5×10^{15}	1×10^{16}

Table 6.2: Average bulk spin concentrations determined by double integration of EPR spectra and comparison to a reference. The relative concentrations of different samples are accurate to ± 10 %, but the errors on the absolute values are ± 20 %.

at approximately 5 K per minute. During annealing the sample chamber pressure was kept below 5×10^{-6} mBar. The samples were mounted in between pieces of CVD diamond film while being annealed to further reduce the risk of graphitisation. Even at the highest annealing temperatures the surface graphitisation rate was very low. To remove any surface graphite the samples were cleaned after annealing in a solution of concentrated H_2SO_4 and KNO_3 held at 550–600 K for 30 minutes. After this treatment the samples were washed in conc. H_2SO_4 and then distilled water. No mass loss was detected for any samples after annealing and cleaning, confirming that the surface graphitisation rate was very low.

6.3.3 EPR Measurements

EPR measurements were made after each anneal using the X-band spectrometer described in §4.3. The measurements were made at temperatures between 4 and 300 K using the TE_{104} cavity operating at approximately 9.6 GHz. The spin concentrations were determined using the technique described in §4.6, and are given in table 6.2.

6.3.4 Infrared measurements

Infrared absorption measurements were made with the sample at room temperature using a Perkin–Elmer 1710 FTIR spectrometer. Several measurements were made in different places on each sample to check for the inhomogeneous distribution of defects; the infrared beam was of similar dimensions to the sample and it was found that the measurements were reproducible without having to position the sample carefully for each measurement.

6.4 Measurements

6.4.1 Infrared absorption

It was shown in §5.4.3 that the intensity of the infrared absorption in the C–H region and the concentration of defects at g=2.0028 are related. Figure 6.1 shows the absorption in the C–H band in more detail. The individual lines can be identified and fitted to Lorentzians, using the frequencies of the lines obtained from McNamara [82]. These frequencies and the groups associated with them are shown in table 6.1. This spectrum is taken from sample 20, which was opaque, and is typical of the absorption in this region in all of the samples except sample 5. The samples which were optically transparent had a very low absorption in this region. The dominance of the stretch signatures of hydrogen bonded to sp^3 bonded carbon was repeated for all samples. The absorption spectrum for sample 5 is discussed in §6.4.2.

6.4.2 Behaviour of EPR and infrared on annealing

All of the samples were annealed at temperatures between 1100 and 1900 K. After each anneal the EPR spectra were recorded with a range of microwave powers in order to isolate the N_S^0 signal, when it was present, at low power; and the signals at g=2.0028 at high power.

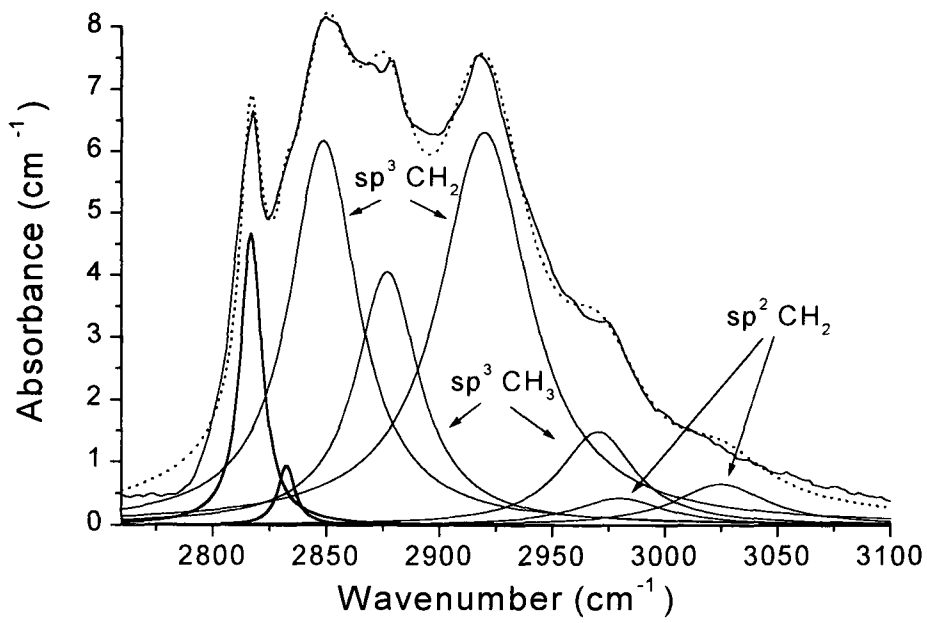

Figure 6.1: C–H region of infrared absorption spectrum of sample 20 showing fit to lines from individual absorptions. Frequencies of lines given in table 6.1. Dotted line shows fit to experimental data.

Behaviour of N_S^0 signal

Five out of the ten samples contained observable concentrations of the N_S^0 centre. Annealing up to the maximum temperature used here (1900 K) had no effect on the concentration of this impurity, or on the linewidth or lineshape. This enabled it to be used as a marker when monitoring the concentrations of the other defects in the samples in which it was present.

Behaviour of g=2.0028 signal and infrared absorption signal

Annealing the samples below 1500 K produced little or no observable change in the intensity or shape of the EPR absorption at g=2.0028. However, annealing the samples for 4 hours at temperatures above 1500 K produced dramatic changes in the EPR intensity and lineshape, and in some cases the infrared absorption. Not all of the samples behaved in the same way. Figure 6.2 shows the results for three of the samples which are representative of those observed for the ten samples studied. Figure 6.2(A) presents the data from an opaque CVD sample (sample 23) which shows strong C–H infrared absorption. The presence of N_S^0 does not influence the annealing behaviour of the resonance at g=2.0028. On annealing to 1700 K the resonance at

g=2.0028 narrows appreciably, the amplitude of the satellites relative to the central peak-to-peak height decreases and the overall intensity is reduced. The 2820 cm^{-1} infrared absorption peak increases dramatically, and there are also less pronounced reductions in the infrared absorptions at higher energies. Overall the strength of the C–H absorption band does not change appreciably. Annealing further to 1900 K produces a strong EPR resonance at g=2.0035(2), without apparently reducing the intensity of the g=2.0028 resonance further. This is shown in figure 6.3. Annealing at 1900 K dramatically degrades the optical quality of the samples, which become much darker. This is not graphitisation of the external sample surfaces. The infrared absorption of the overall C–H absorption band is reduced, with the highest reduction in the 2820 cm^{-1} absorption. Figure 6.4 shows the behaviour of the g=2.0028 EPR intensity and the strength of the 2820 cm^{-1} absorption peak as a function of annealing temperature in sample 20, which behaved in similar fashion to sample 23.

Figure 6.2(B) presents the annealing data for sample 30, in which the integrated absorption of the g=2.0028 EPR resonance was 8 times less than that for sample 23 (figure 6.2(A)). The total C–H absorption band was also considerably weaker with no resolvable 2820 cm^{-1} peak. This sample was transparent. The satellites on the g=2.0028 resonance in sample 30 are less well resolved than in sample 23, and the central peak is slightly broader. On annealing to 1700 K the g=2.0028 resonance narrows, the amplitude of the satellites relative to the central peak to peak height decreases and the overall intensity is reduced. Further annealing to 1900 K produces the new resonance at g=2.0035(2). In this respect samples 23 and 30 behave in the same fashion. However, the infrared absorption spectra for sample 30 do not change appreciably with annealing. With the final anneal at 1900 K this sample, like sample 23, became much darker. Once again this was not graphitisation of the external sample surfaces.

Figure 6.2(C) shows the annealing data for sample 5. Before annealing, the g=2.0028 EPR absorption looked similar to that of sample 30 with poorly resolved satellites. However, the C–H infrared absorption band was markedly different with

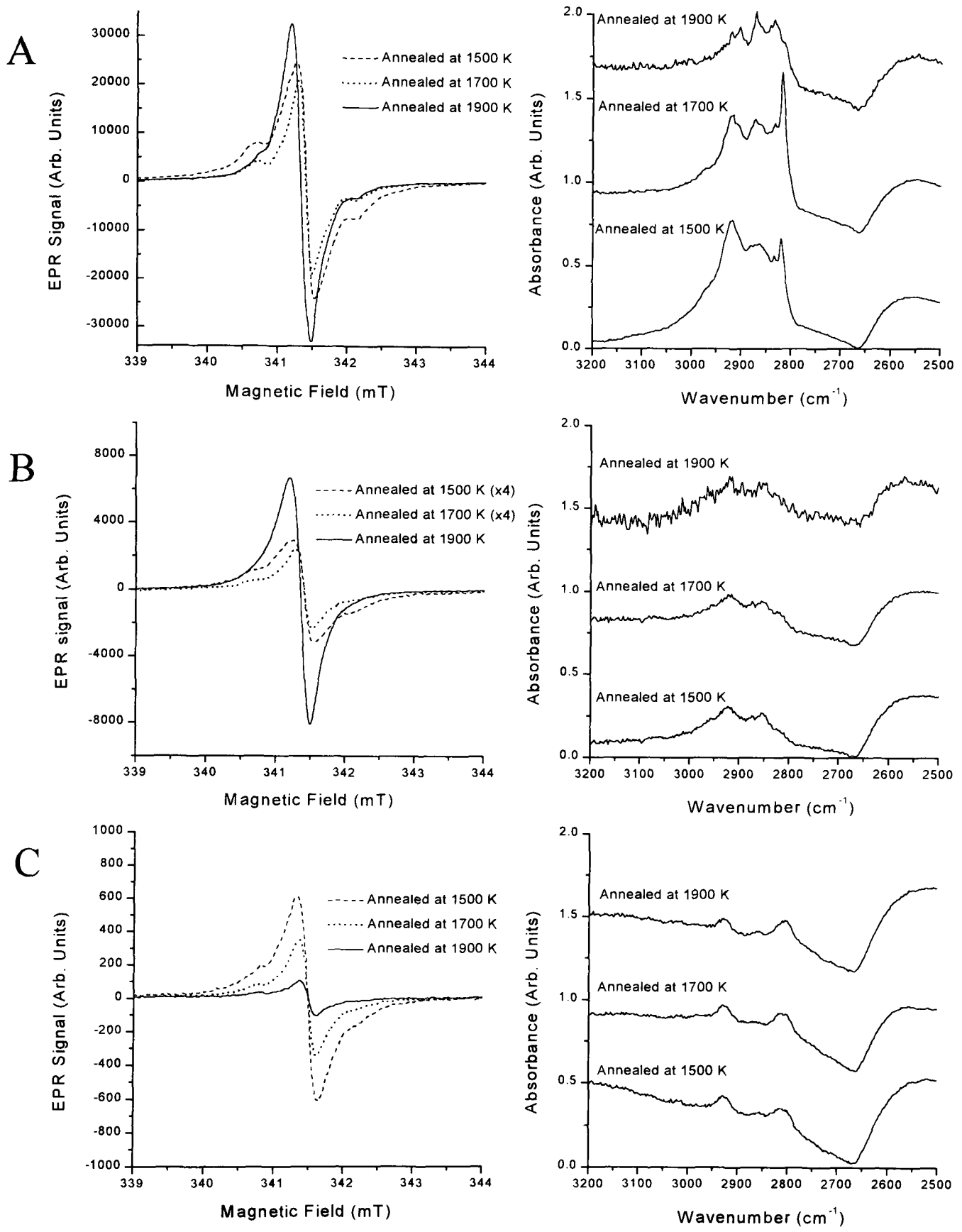

Figure 6.2: X-band (9.6 GHz) EPR spectra recorded at 5.0 K and room temperature infrared absorption spectra in C–H region from (A) sample 23, (B) sample 30 and (C) sample 5, taken following annealing *in vacuo* for 4 hours at 1500, 1700 and 1900 K.

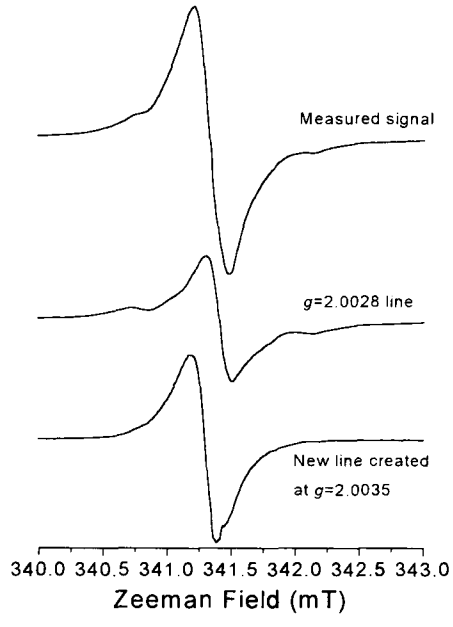

Figure 6.3: EPR spectra before and after 1900 K anneal, showing new defect formed with g=2.0035(2)

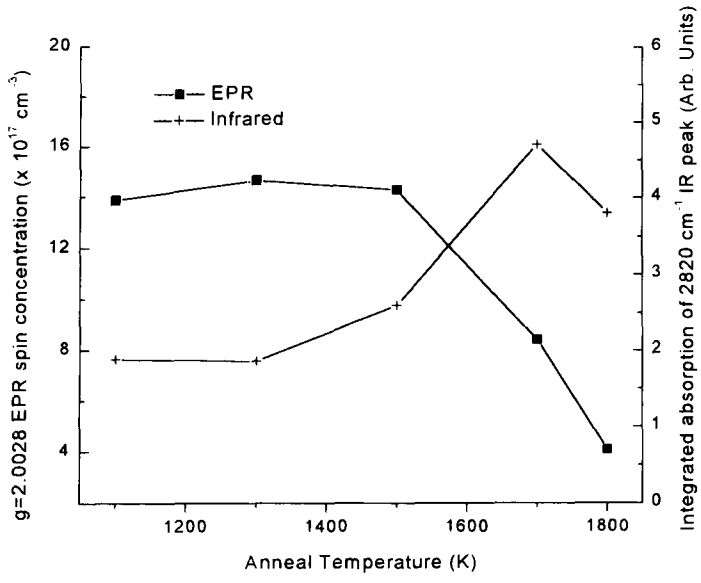

Figure 6.4: The g=2.0028 EPR spin concentration and the integrated absorption of 2820 cm^{-1} infrared peak as a function of annealing temperature for sample 20.

only three broad peaks centred at 2924(5) cm^{-1}, 2850(5) cm^{-1} (weak) and 2810(5) cm^{-1}. The first two peaks are characteristic of the asymmetric and symmetric stretching respectively of CH_2 groups where the carbon is sp^3 bonded. The inequality in the intensities of these two lines has been commented on by others [82]. We can find no reference in the literature to the 2810(5) cm^{-1} line. Upon annealing, the g=2.0028 EPR absorption diminishes in intensity without significant changes in the lineshape, but the g=2.0035(2) resonance does not appear on annealing to 1900 K. No changes are observed in the infrared absorption when annealing up to 1900 K and this sample did not show such a marked deterioration in optical quality.

Annealing a CVD sample in stages to a maximum temperature, holding the temperature for 4 hours at each stage, produced the same overall change as annealing a piece of the same as grown sample to the maximum temperature for 4 hours.

6.5 Discussion

6.5.1 Effect of annealing on N_S^0 concentration

The aggregation of N_S^0 centres to form A centres has been studied by many workers [198, 199, 200, 201]. When thermally annealing type Ib diamonds, it has been shown that the rate of formation of A centres is proportional to the square of the initial concentration of N_S^0 showing that the A centre consists of two nitrogen atoms [200]. It is now accepted that the A centre consists of a pair of adjacent substitutional nitrogen atoms [98, 172, 16]. The rate of aggregation can be substantially increased if the diamond is subjected to radiation damage [202]. In the CVD diamond samples studied the maximum N_S^0 concentration was 4×10^{17} cm^{-3}. With the concentration this low no significant aggregation of N_S^0 was expected at temperatures up to 1900 K. This is consistent with the N_S^0 concentration being unchanged by annealing. No evidence of thermally activated charge transfer altering the concentration of N_S^0 (N_S^0 donating an electron to a trap, or N_S^+ trapping an electron) was detected on annealing. The N_S^0 signal made a useful internal reference for studying the changes in concentrations of

other centres during annealing.

6.5.2 Effect of annealing on the concentration of EPR centres at g=2.0028 and C–H infrared absorption band

In all samples studied the intensity of the EPR absorption at g=2.0028 was reduced on annealing above 1500 K, but the details of the changes are sample dependent. In most samples, on annealing to 1700 K the resonance narrowed and the satellites became better resolved. Neither before nor after annealing could the shape of the g=2.0028 EPR signal be successfully simulated with only the H1 EPR resonance. The relative contribution of H1 to the signal at g=2.0028 is sample dependent and can change on annealing to 1700 K. This is consistent with other paramagnetic centres contributing to the g=2.0028 resonance, and these centres annealing at a different rate to H1.

In samples which exhibit strong C–H absorption, changes in this band can be observed concurrently with changes in the EPR spectra. Figure 6.4 shows the change in the g=2.0028 spin concentration and the change in the 2820 cm^{-1} absorption peak on annealing in such a sample (sample 3). The total change in the the C–H absorption band in a sample of this type (sample 2) is shown in figure 6.5; here the as-grown infrared absorption spectrum has been subtracted from the annealed spectrum. The changes in the C–H infrared absorption band are not significant below 1500 K, but at 1700 K we find a redistribution of intensity with some peaks growing and others falling in intensity. There appears to be no overall loss of strength in the band. There is a redistribution of hydrogen amongst different bonding configurations, and the reduction in the peak around 2920 cm^{-1} indicates a loss of CH_2 groups where the carbon is sp^3 bonded. This loss is mirrored by a growth in intensity of the 2820 cm^{-1} peak, which has been attributed alternatively to a N–CH_3 group [82] or to hydrogen adsorbed on a diamond surface [81].

For samples with much lower concentrations of the g=2.0028 EPR centres, the EPR signal behaves on annealing to 1700 K in the same fashion as for samples with

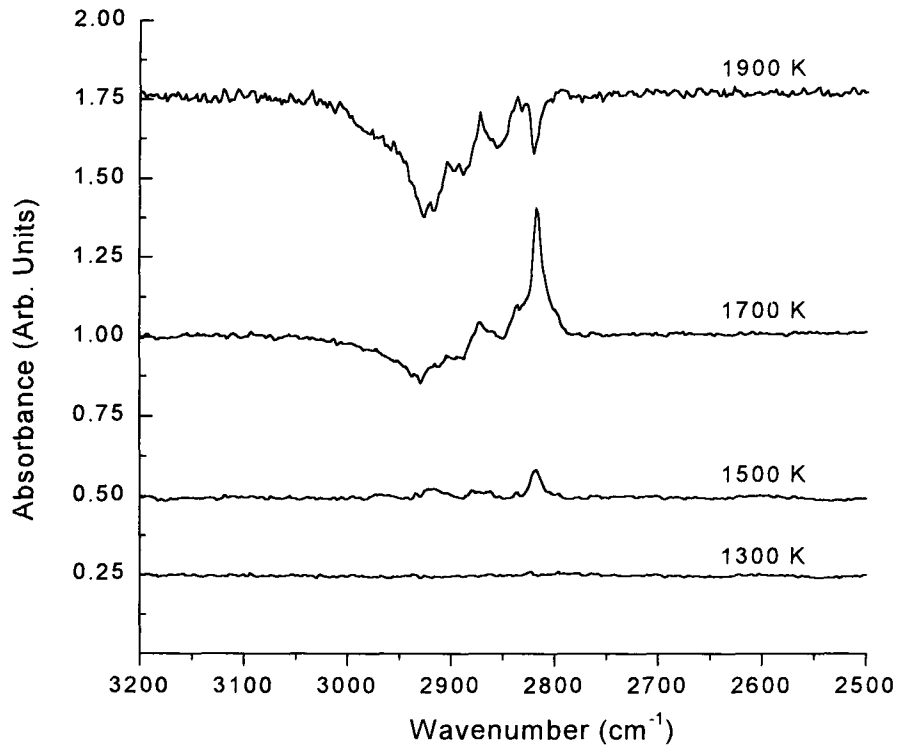

Figure 6.5: Room temperature infrared difference spectra (annealed spectrum minus the as grown absorption spectrum) for sample 23.

strong C–H absorption, but there are no significant changes in the absorption band, presumably because of the low number of hydrogen atoms redistributed during the anneal. Too many different processes are occurring to correlate the change in the EPR spectra with a specific band in the infrared, but an increase in the 2820 cm^{-1} absorption peak at 1700 K is always accompanied by a reduction in the g=2.0028 EPR signal strength.

Previous studies [125, 145] and the previous chapter have indicated that H1 and the other g=2.0028 defects are probably located on grain boundaries or in hydrogenated intergranular material. We have found that the EPR absorption at g=2.0028 reduces at temperatures where some of the hydrogen is mobile, but below 1700 K no hydrogen (as monitored by infrared absorption) is lost from the CVD diamond samples. Annealing to 1900 K produced a new EPR centre at g=2.0035(2) in all samples except one (sample 5, figure 6.2(C)). The lineshape is asymmetric, indicating a small g-matrix anisotropy. No hyperfine structure was observed. We have no reliable model for this defect.

After annealing to 1900 K the overall C–H absorption band was reduced in intensity in most samples (e.g. figure 6.4), indicating that hydrogen was either lost from the sample or incorporated in a non–infrared–active form. The first explanation seems the more likely. In some samples it was not possible to measure the change, due to a significant reduction in transmission caused by the significant darkening of all except sample 5 during the 1900 K anneal. The deterioration of optical quality of the samples was pronounced: it appeared that severe internal degradation of the samples was taking place, but there was no graphitisation of the external surfaces. The conclusion drawn is that the loss and redistribution of hydrogen during the high temperature anneals destabilises the internal grain boundaries, and diamond is being converted into graphite or hydrogenated amorphous carbon.

The anomalous behaviour of sample 5 is not understood. As can be seen from figure 6.2(C), the g=2.0028 EPR absorption decreases on the 1900 K anneal but no new defects are created. The optical quality and infrared absorption in the C–H region did not change on annealing to 1900 K. The C–H infrared absorption spectrum for this sample is unusual: we have not seen the broad peak at 2810 cm^{-1} in any other diamond CVD sample. It is possible that the grain boundaries in this material are stabilized by a different, more stable, C–H species.

6.5.3 Modelling the kinetics of reduction in the EPR absorption at g=2.0028 on annealing

Quantitative analysis of isochronal annealing data is difficult, and especially so for the results presented here, because of the possibility that many different processes which affect the concentrations of defects are occurring simultaneously. However, the reduction in the concentration of the EPR absorption at g=2.0028 invites an attempt at analysis.

If the model for The H1 centre (hydrogen entering a weak C–C bond at a grain boundary, bonding with one of the other carbons and leaving an unpaired electron in

the dangling orbital on the other) is correct, it could be destroyed by the evolution of hydrogen on annealing, or by a hydrogen atom bonding with the dangling carbon orbital. In the following discussion we assume that destruction occurs by the first process. As long as the rate of creation of H1 during annealing is vanishingly small, and the hydrogen released is permanently trapped at another, more stable, site, whose concentration is high enough to consider the number of available sites as non saturable, we would expect the reduction of concentration of H1 to follow first order kinetics. That is

$$[\mathrm{H1}]_i = [\mathrm{H1}]_{i-1} \exp(-k\tau) \tag{6.1}$$

where $[\mathrm{H1}]_i$ is the concentration after the ith anneal, and τ the time of the anneal at a temperature T. The rate constant is given by

$$k = A_0 \exp(-E_A/k_B T), \tag{6.2}$$

where A_0 is a constant, and E_A the activation energy. A_0 and E_A for breaking a C–H bond can be estimated from the C–H stretch frequency and the C–H bond energy respectively, giving $A_0 \sim 5 \times 10^9$ Hz and $E_A \sim 4.3$ eV.

The isochronal annealing data for the EPR concentration at g=2.0028 (figure 6.4) is reproduced reasonably well using first order kinetics and the parameters for breaking a C–H bond, especially when the error bars for the concentration($\pm$10–20%) are taken into account. This is shown in figure 6.6. It should be remembered here that the EPR absorption at g=2.0028 in the samples studied here arises from the H1 centre and one or more other defects, and the relative concentration of different defects changes on annealing. Therefore it is not possible to draw any specific conclusions about the destruction of H1 or other defects on annealing. However, it is apparent that hydrogen is mobile at 1700 K, and that the annealing rate of the EPR signal at g=2.0028 is consistent with the requirement of breaking a C–H bond in order to reduce the signal. EPR centres containing unpaired electrons in carbon dangling orbitals could be destroyed if a hydrogen atom is evolved and the dangling orbital forms a bond with another such orbital. In addition, the hydrogen atom released could

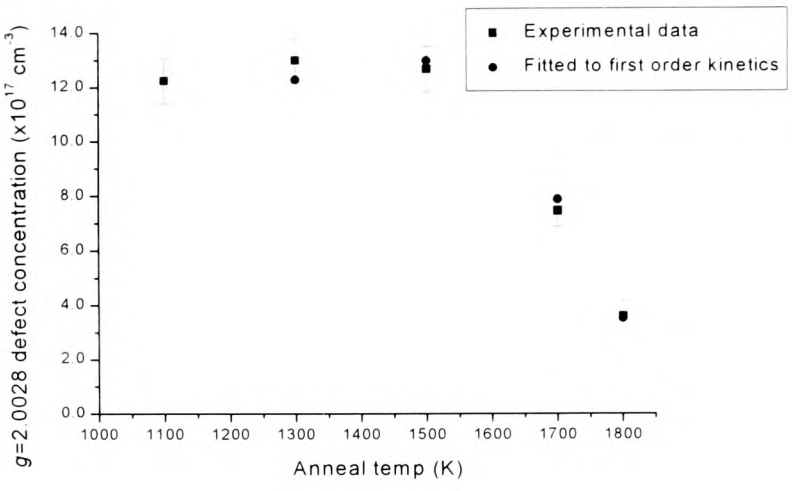

Figure 6.6: Behaviour of EPR signal at g=2.0028 in sample 20 modelled using first order kinetics (see equations 6.1 and 6.2).

bond with a carbon dangling orbital to reduce the concentration of unpaired electrons. It is therefore possible for a redistribution of hydrogen to reduce the concentration of paramagnetic defects, as was found to be the case below 1700 K. Annealing at 1900 K results in the breaking of C–H bonds and the loss of hydrogen from the sample. New paramagnetic defects are created in this process.

6.6 Conclusions

The infrared absorption and concentration of the EPR centres at g=2.0028 are found to be unaffected by annealing at temperatures below about 1500 K in the CVD diamond samples studied, which is consistent with work previously reported [133]. However, prolonged annealing at higher temperatures changes both the EPR and infrared absorption. At 1700 K some of the hydrogen on internal grain boundaries or in intergranular material becomes mobile. The intensity of the EPR absorption at g=2.0028 decreases, but the detailed behaviour is complicated, indicating the presence of different defects all contributing to the EPR resonance. However, the annealing rate is consistent with the requirement to break a C–H bond to reduce the EPR signal at g=2.0028. In samples with strong C–H infrared absorption there is a decrease in the peak at 2920 cm^{-1} and an increase in the peak at 2820 cm^{-1} on annealing at 1700

K. The 2820 cm^{-1} peak is strongest in samples with intense C–H absorption bands. Its strength does not correlate with the N_S^0 concentration, and the increase in intensity on annealing appears to depend only on the availability of hydrogen. Therefore it is more likely that the 2820 cm^{-1} peak originates from a hydrogen centre on a diamond surface rather than an impurity species.

Annealing for 4 hours at 1900 K, in all except one case, severely degraded the optical properties of the sample and a new EPR defect at g=2.0035(2) was created. Infrared measurements show that hydrogen is lost from most CVD diamond samples on annealing at 1900 K. One sample, with an unusual C–H absorption spectrum, did not show the dramatic changes in optical quality and no new EPR centres were created by the 1900 K anneal.

This chapter has shown that the concentration of paramagnetic defects and the distribution of hydrogen can be altered by high temperature annealing. Annealing to 1900 K can severely degrade the optical quality of polycrystalline films. The processes involved in the degradation are not fully understood but appear to involve loss of hydrogen from the sample.

Chapter 7

Imaging

7.1 Introduction

This chapter describes the experiments performed using a field gradient to obtain the spatial distribution of defects in samples. Both one-dimensional and two-dimensional images were produced. It starts by outlining the problems particular to EPR imaging, both in the experimental setup and in the interpretation of the results. A short overview of the limitations and potential of the apparatus is given.

A study of the distribution of single substitutional nitrogen through the thickness of a number of CVD films was performed. This is of particular current interest because of the role of nitrogen in the growth processes of these films. A comparison between the nitrogen distribution and the distribution of the defect at g=2.0028 (see §5.4.2) through a film is made.

Two-dimensional images of synthetic Ib single crystals were produced, and different growth sectors identified. An image of a CVD sample was also created, relating the distribution of dark intergranular material to the distribution of the defect at g=2.0028.

The distribution of the $[N\text{–}N]^+$ centre created by optical excitation in a single crystal HTP diamond was studied, and the possibility of field gradients in different directions explored.

7.2 Background

EPR imaging is a well established technique. It has been used for many years, especially in medical and biological fields. Several reviews have appeared in the last few years (e.g. [203, 204, 205]). Although most EPR imaging has been done at low frequencies for biological applications, studies have been made at higher frequencies in condensed matter materials, including diamond [206, 207]. However, very little work has been done on studying the distribution of defects within diamond using this technique. The narrow linewidths of EPR in diamond make it an ideal candidate with which to attempt high resolution imaging.

7.2.1 EPR imaging—overview

While there is no need to reproduce one of the excellent reviews of the technique [203, 204], a brief discussion of the important aspects as used in this work will be given.

EPR imaging has been developed mainly as a technique for use with biological applications. As a consequence of this, most of the work that has been done with it has been at low frequencies (L-band: 1.1 GHz, or radio frequency: 250 MHz) for two main reasons: firstly the samples used are typically too large to fit inside a higher frequency resonator; and secondly, being biological specimens, the samples contain water, which is very lossy at high frequencies, and totally impractical in, for instance, an X-band resonator at 9 GHz.

However, imaging has been done at higher frequencies. Hoch and Day [206] showed that it was possible to distinguish between two paramagnetic diamonds 2.5 mm apart, and to show this in a two-dimensional spin density map.

In its simplest form, the technique simply consists of applying a field gradient $\partial B_z/\partial z$ across the sample, in addition to the Zeeman field B_z (see figure 7.1). As the magnetic field is swept, the paramagnetic defects in the sample come into resonance depending on their position in the sample. The critical factor in determining the

resolution of this technique is therefore the field gradient. At X-band, with sample sizes typically of the order of 2mm or less, and linewidths of the order of 0.1 mT, the required gradient for a resolution of 100 μm is 1 mT mm^{-1}. Hoch [206] was working with a gradient of 0.5 mT mm^{-1}.

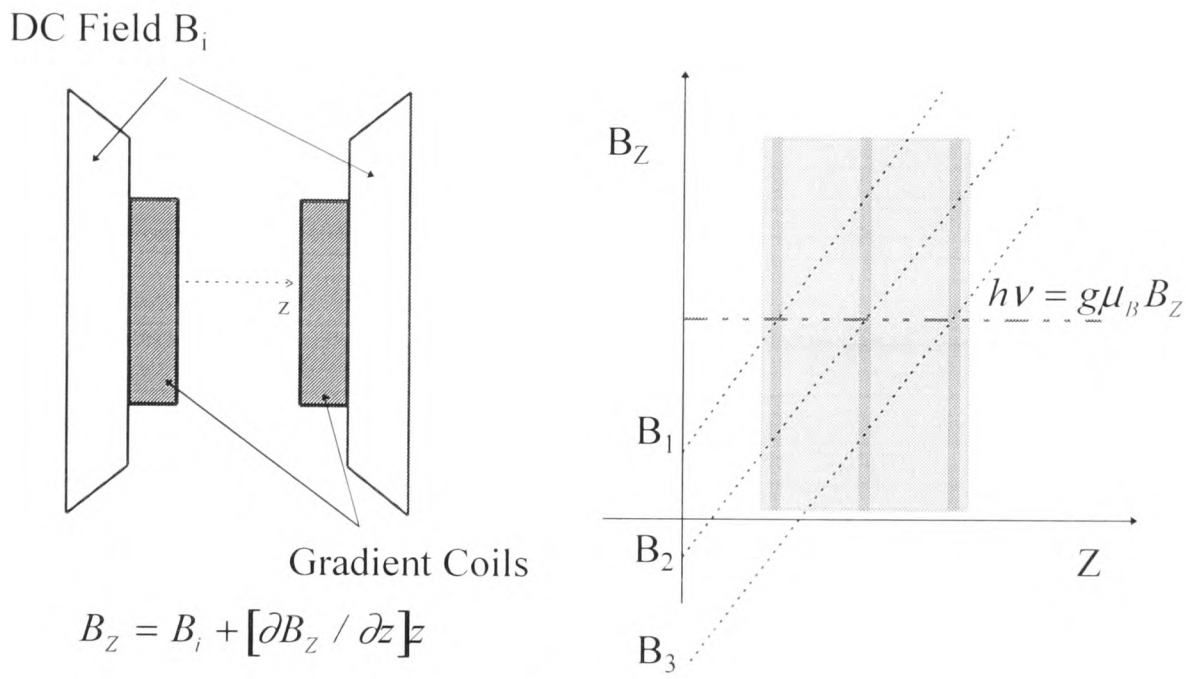

Figure 7.1: (A) Arrangement of gradient coils. (B) Demonstration of how different parts of sample are recorded at different fields.

The gradient is normally provided by anti-Helmholtz coils [208], ferromagnetic wedges [209, 210] or by splaying the main magnetic field coils [211], and in general gradients of mT mm^{-1} have been used but Ohno [212] achieved a gradient of 30 mT mm^{-1} over a very small volume with miniature coils inside the cavity. The problem with ordinary anti-Helmholtz coils is the heat generated when running at the currents necessary for high gradients, and this is normally solved by using oil-cooled coils [206] or by pulsing the current [213, 214].

There are many refinements possible to this basic technique, such as electron spin echo imaging [215, 216], ENDOR-detected imaging [217], spectral-spatial imaging [218], but they are not directly relevant to this work.

7.3 The experiments

All of the imaging experiments were performed using the X-band spectrometer described in §4.3. The signal averaging capability was used extensively, and the motor driven goniometer described in §4.3.2 was installed especially for these experiments. The loop–gap (3 loop, 2 gap) resonator was designed and built in the Clarendon (see §4.3.3) and [165, 166]). This resonator had three important relevant properties:

- A high degree of homogeneity of microwave field across the active region [166].
- A high filling factor leading to good sensitivity.
- Small size enabling the gradient coils to be close together to produce the anti-Helmholtz configuration.

Although the best sensitivity is achieved with a small sample loop and large flux return loops [165], the sample loop in this case was 11.5 mm diameter in order to allow use of the ESR900 flow cryostat to examine the samples at 4 K.

7.3.1 The gradient coils

The $\partial B_z/\partial z$ coils used are described in §4.3.4. They were designed and wound in the Clarendon Laboratory[1]. They had 212 and 215 turns, were water cooled, wired together in parallel in an anti-Helmholtz configuration and powered by up to 30 V.[2] At 30 V with the water cooling they carried a current of 7.6 A, so dissipating more than 100 W in each coil. The homogeneity of the gradient across the central 5mm was better than 95 % [219].

7.3.2 Measurement of gradient

The theoretical gradient for these coils carrying 7.6 A is 1.8 mT mm^{-1}. However, this does not take into account the finite width of the coils or the iron pole pieces

[1] Wound by Mr. A. Hickman
[2] PSU made by Power 10 Inc. 0–60 V, 0–30 A.

and yoke of the magnet inside which they were located. Although the field could be calibrated with a Hall probe on a micrometer stage, a more reliable method was to examine several dummy samples consisting of crystals of 2,2-diphenyl-1-picryl-hydrazil (DPPH) mounted with known separations, these separations provided by mica or rexolite. Figure 7.2(A) shows a typical spectrum of such a sample (mica thickness 155 μm). The narrowest separation used was 60 μm, in which the individual lines were just resolved. The gradient we obtained was 1.3 mT mm^{-1} at 7.6 A. This was checked using separations of between 60μm and 2mm to confirm the homogeneity.

The resolution of the system depends on two factors: the sensitivity of the resonator and the size of the gradient. Even using deconvolution techniques, the best resolution attainable assuming a large enough signal is given by $\Delta z \simeq \Delta B_{p-p}/G_Z$ [220] where ΔB_{p-p} is the linewidth of the signal without gradient applied and G_Z is the gradient. So in the case of DPPH, where the peak to peak separation of the line is 0.1 mT, the maximum resolution is 75 μm. Figure 7.2(B) shows the spectrum obtained with the 60 μm DPPH crystal separation, which is at the theoretical limit of resolution.

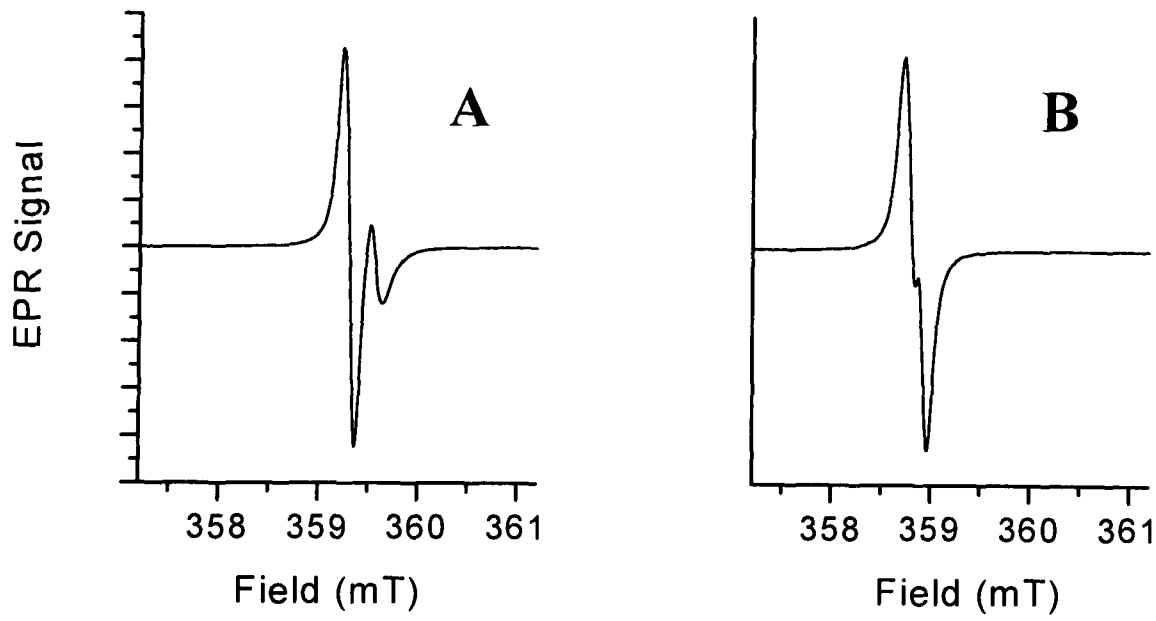

Figure 7.2: Two spectra of DPPH separated by mica with gradient on. In (A) the separation is 155 μm. In (B) the separation is 60 μm. Gradient is 1.3 mT mm^{-1}

7.3.3 Deconvolution

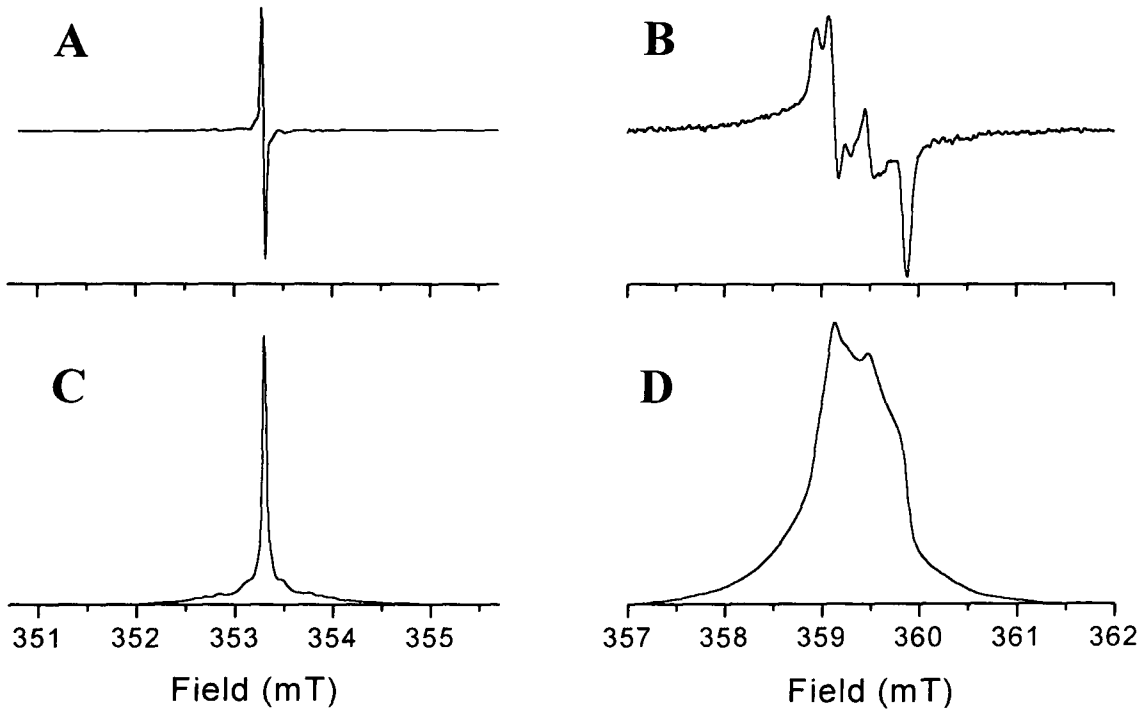

Figure 7.3: N_S^0 spectra through CVD film (A,C) without and (B,D) with gradient. (A) and (B) are spectra as recorded in first derivative. (C) and (D) are integrated to give absorption signals. Gradient is 1.3 mT mm^{-1}. Spectra recorded at room temperature. Spectra recorded from sample 4.

Figure 7.3 shows the spectrum, with and without gradient, of the N_S^0 defect in a CVD diamond film, detected as a first harmonic spectrum. If the gradient-on spectrum is integrated to give a pure absorption signal, this should give some indication of the spin distribution of the nitrogen through the sample. However, even though the linewidth of the N_S^0 is very small (25 μT), the resolution is very poor. However, if we "remove" the linewidth of the experimental line we expect a much better resolution. This is possible because the spectrum we see is a convolution of the spin distribution with the shape of the line.

Consider the Zeeman term in the spin Hamiltonian. In a field B_0 the resonance frequency of a system of paramagnetic centres is

$$\hbar\omega_0 = g\mu_B B_0. \tag{7.1}$$

Assume an isotropic g. The natural linewidth is $\Delta\omega \sim 1/T_2$ where T_2 is the transverse

relaxation time. The lineshape function is given by $F(\omega)$. Experimentally the spectra are measured by sweeping field rather than frequency, but the treatment is exactly the same.

If a linear magnetic field gradient G is superimposed on the steady Zeeman field B_0, the magnetic field is position-dependent

$$B(Z) = B_0 + GZ \tag{7.2}$$

where Z is parallel to B_0 and the gradient direction. The spectrum is inhomogeneously broadened and the new lineshape function may be written as the convolution integral

$$\begin{aligned} L(B) &= F(B) * S(B) \\ &= \int_{-\infty}^{\infty} F(\xi) S(B - \xi)\, \mathrm{d}\xi \end{aligned} \tag{7.3}$$

where $S(B)$ is the spin distribution function expressed in the field domain.

Clearly

$$S(B) \propto S(Z) = \iint \rho(X, Y, Z)\, \mathrm{d}X\, \mathrm{d}Y \tag{7.4}$$

where $\rho(X, Y, Z)$ is the spin density in the sample at the position X, Y, Z referred to laboratory axes.

So information on $S(B)$ and thus on the spin density in the sample can be extracted from the lineshape $L(B)$. More generally the convolution theorem can be used to obtain $S(B)$ from the Fourier transforms of $L(B)$ and $F(B)$. Thus

$$\begin{gathered} F(B) * S(B) \bigotimes f(\kappa_B) S(\kappa_B) \\ \text{and} \\ L(B) \bigotimes l(\kappa_B) = f(\kappa_B) S(\kappa_B) \end{gathered} \tag{7.5}$$

where $\bigotimes$ denotes that the quantities are a Fourier transform pair, and κ_B is the representation of B in reciprocal space.

To obtain this spin density there are two possible ways to proceed. The obvious way, analytically, is simply to take the Fourier transforms of the lineshape $L(B)$ and $F(B)$, divide one by the other and transform back, i.e.

$$S(B) \bigotimes \frac{l(\kappa_B)}{f(\kappa_B)} \tag{7.6}$$

However, this can present a number of problems practically.

- If $F(B)$ and $L(B)$ are noisy this noise can be magnified.
- If there is not sufficient baseline on both sides of the signal, "wraparound" problems can occur. This can be overcome by adding zeros to the spectra either side.
- There is a high chance of division by zero in the combination of the Fourier transforms.

Some of these problems can be overcome by fitting $F(B)$ to a well-defined function with no zeros, e.g. a Lorentzian [221], but in many cases, particularly in the examples in this work, the lineshape $F(B)$ is not simple and the experimental spectrum must be used.

Another approach is therefore necessary, and it has been found [222] that iterative fitting of the experimental spectra is more reliable.

A spin distribution was generated by choosing the position of the ends of the distribution, corresponding to the edges of the sample, and dividing the space between into up to 40 strips. This distribution function $S(B)$ was convolved *numerically* with the gradient-off lineshape $F(B)$ to give a first guess lineshape $M(B)$. This was compared with the experimental spectrum $L(B)$. A least squares fitting algorithm (see §4.5.3) was then used to change the heights of the strips until the best possible fit of $M(B)$ to $L(B)$ was achieved. This is shown in figure 7.4. The advantages of numerical convolution, which is a very slow, computer-intensive process, over taking Fourier transforms of both functions, multiplying and transforming back are that there are no wraparound problems, and that a higher degree of accuracy is obtained.

Initially this fitting was performed using the lineshapes generated by integrating the experimental spectra, i.e. pure absorption lineshapes. However it was found that by using the spectra as taken in the first derivative, the baseline was less variable and the spin distributions were less noisy. The actual spin distributions generated were, however, the same.

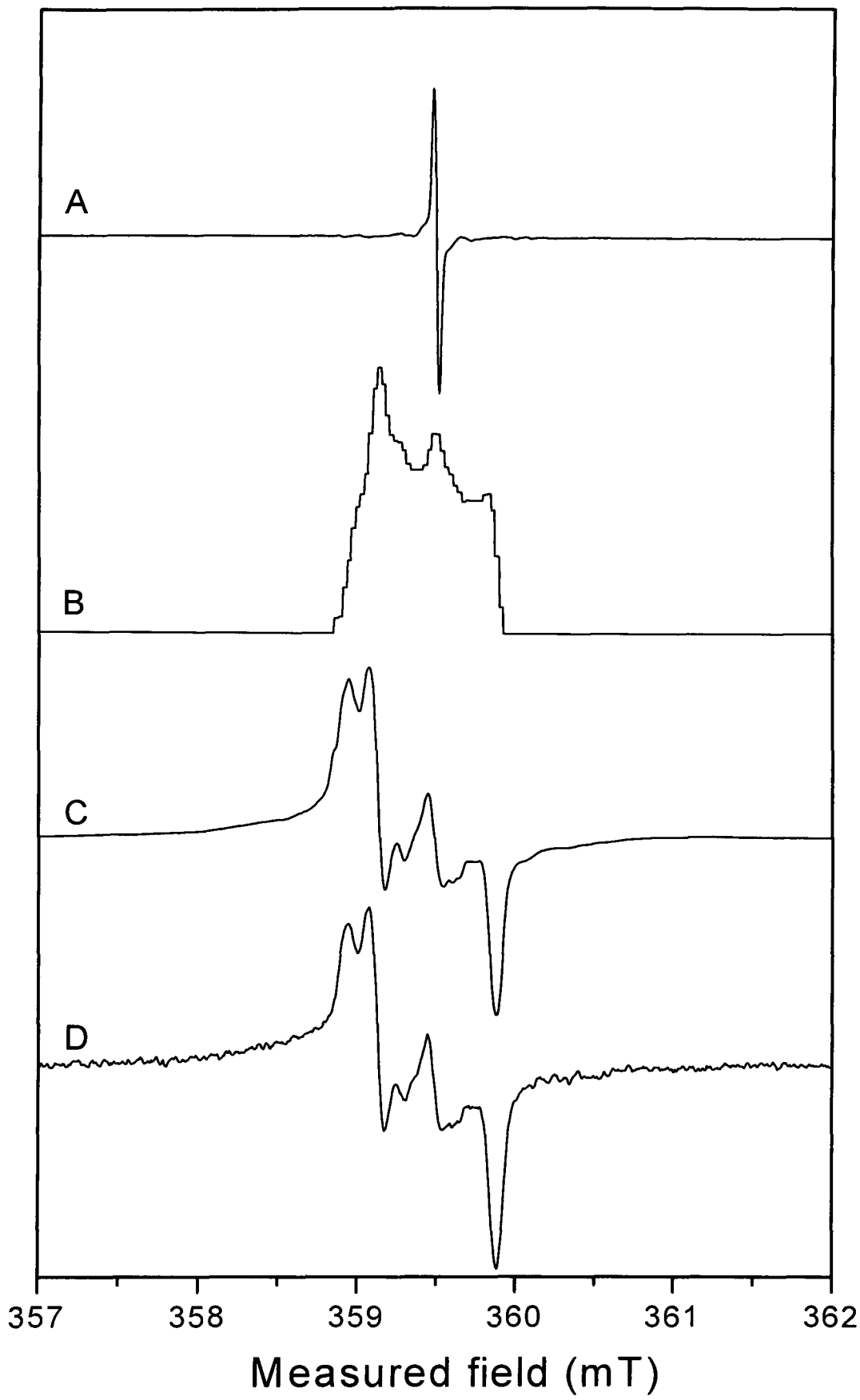

Figure 7.4: Demonstration of deconvolution showing (A) gradient-off lineshape $F(B)$, (B) predicted spin distribution $S(B)$, (C) generated lineshape $M(B)$ and (D) experimental lineshape $L(B)$. CVD sample 4, room temperature, field gradient 1.3 mT mm^{-1}, film thickness 820 μm, measurement through-film.

The number of strips that could be used depended on the field gradient, width of sample and linewidth of the gradient-off line $F(B)$. As mentioned in §7.3.2 above, the best resolution attainable is given by $\Delta B_{p-p}/G_Z$ [17]. There is no point in using strips whose separation corresponds to a smaller distance than this, as there is not enough information contained in the spectrum. What happens if this is tried is that "noise" is generated—the strips alternate high and low (see figure 7.5). For example, in a sample 1 mm across, examining a line of width 0.2 mT, in a field gradient of 1 mT mm^{-1}, the maximum resolution is 200μm. In 1 mm there are therefore only 5 strips. The program used to deconvolve the experimental data is given in appendix A.2.1.

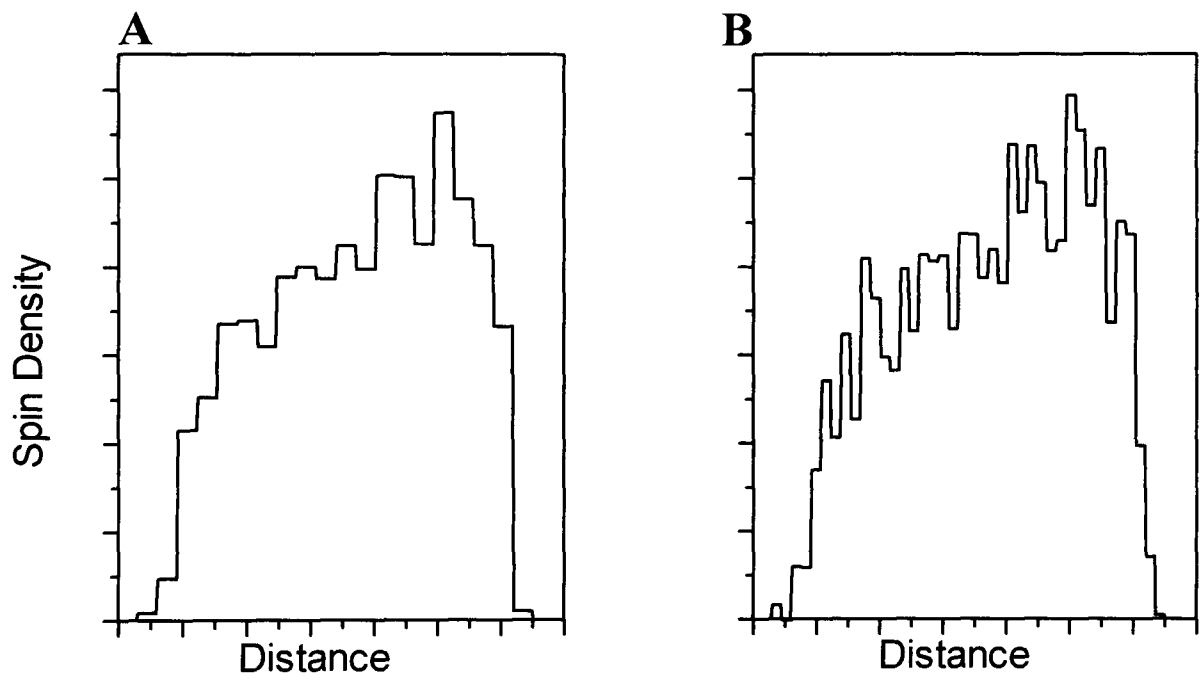

Figure 7.5: Demonstration of resolution. (A) shows strips at limit of resolution. (B) shows double the number of strips introducing noise.

7.3.4 Two-dimensional images

The theory behind two-dimensional image reconstruction is given by Woods *et al.* [223], among others. There are many complex mathematical methods used to generate images of any number of dimensions, but as our equipment is only capable of two-dimensional imaging the treatment is much simpler, and we used the *direct filtered*

backprojection method.

Backprojections

To produce a 2-D image we rotate the sample about an axis perpendicular to the magnetic field, recording spectra at a series of orientations. For each orientation, from equation 7.4, $S(B)$ corresponds to a one-dimensional *projection* of the spin density in the sample with the projection direction perpendicular to the gradient direction. Figure 7.6 shows the projection generated by a sample with uniform spin distribution but a finite, irregular shape. For simplicity we define x_1 as the direction of the gradient for the first spectrum taken, and then θ is the angle moved round. s is the distance in the direction of the gradient.

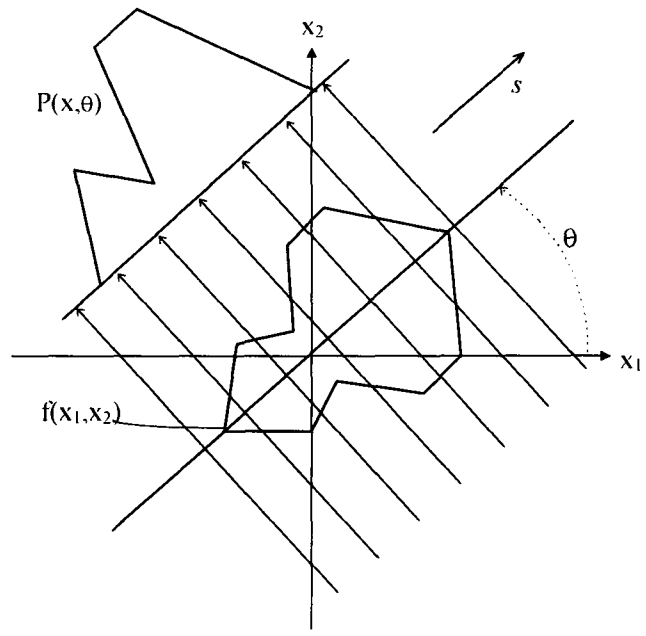

Figure 7.6: Line integration defining a projection in 2-D.
x_1 is the direction of the gradient for the first spectrum taken. θ is the angle moved round, and s is the distance in the direction of the gradient.

Having generated these projections, they are combined using the formulation

$$f(\vec{x}_2) = \frac{1}{N_1} \sum_{i=1}^{N_1} P^*(s, \theta_i) W \tag{7.7}$$

where $s = x_1 \cos(\theta_i) + x_2 \sin(\theta_i)$, and $W = 1$.

The selection of angles is given by

$$\theta_i = (i - 0.5)\tfrac{\pi}{N_1} \quad i = 1, 2, \ldots, N_1.$$

P^* is the appropriately filtered distribution in the direction in which the spectrum was taken. Filtering is discussed in §7.3.5 below.

DPPH dummy samples were again used to check that this was going to be possible, and to verify that the rotation was accurate enough, and to get some idea of how well it would work. Figure 7.7 shows the image generated from a sample consisting of five pieces of DPPH mounted in rexolite in the form of a cross, each separation being 2mm. Each projection was obtained by simple integration of the recorded spectrum, to get a pure absorption signal. Because of the separations and linewidths involved, it was not necessary to deconvolve or filter the lineshape in this case. The projections were determined every 15°.

In order to determine the centre of rotation, spectra were recorded every 15° right through 360°. Then each spectrum was compared with its 180° conjugate pair, and the centre was taken as the midpoint between the "centres of gravity" of the two spectra. This approach also serves to remove problems generated when investigating a centre with anisotropic g.

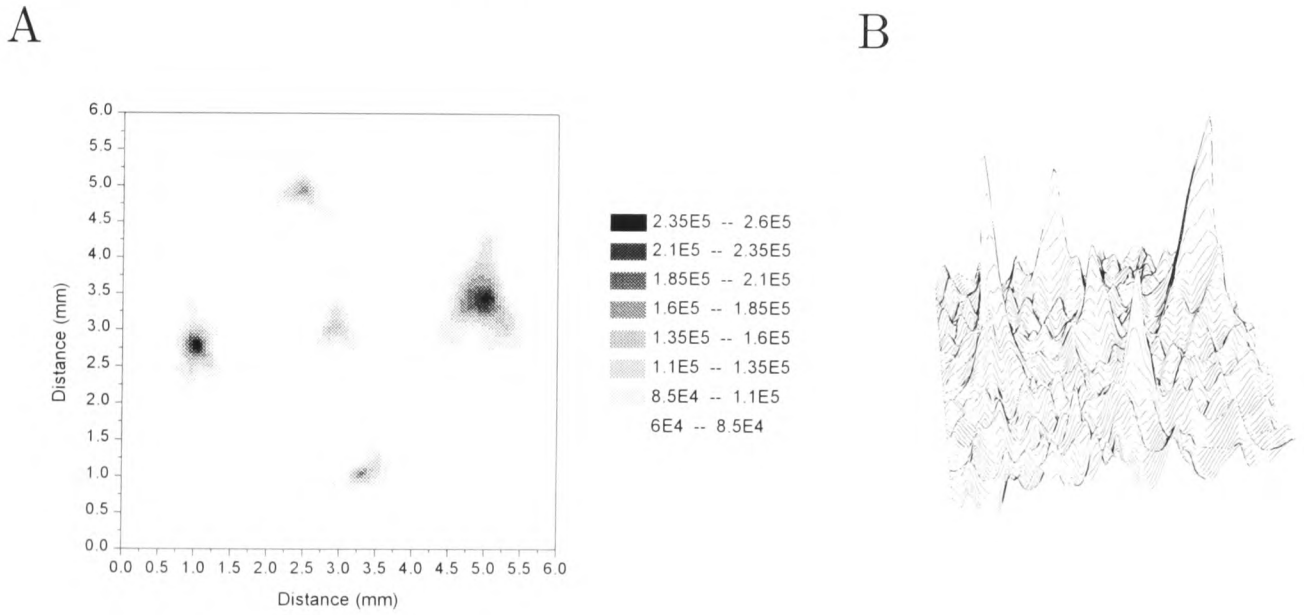

Figure 7.7: Image of DPPH cross. (A) shows spin density map. (B) shows surface plot. Artifacts in (B) are caused by oversampling array with too few projections (see §7.3.6). Room temperature, 12 projections, field gradient 7.6 mT mm^{-1}.

7.3.5 Filtering

In the previous section it was shown that five discrete pieces of DPPH were easily resolvable in a 2-D image generated from equation 7.7, even without deconvolution. However, in practice we are concerned with continuous distributions in finite samples. So we have the problem of distinguishing the distribution of spins within a sample, while at the same time the measured spin distribution changes across a spectrum due to the shape of the sample (see figure 7.6). If we simply take the projections and combine them as they are, then the edges of the sample will be blurred out. This is most graphically illustrated for the case of a circular disc with a uniform spin distribution (see figure 7.8). All the projections will look like figure 7.8(A), and when combined will give a bell shaped image, rather than the original disc with well-defined edges.

The solution is to apply an appropriate filter to each projection. In equation 7.7 the projections P^* were quoted as being appropriately filtered, but that has been ignored up until now. A discussion of the need for and the finer points of digital filtering can be found in Woods [223]. Essentially, filtering can be regarded as the linear convolution of the projection $P(s)$ with a filter $h(s)$. The aim of the filter is to minimize the frequency response of the projection outside the projection passband. Because the spectra are discretely sampled most filters introduce high frequency "ringing", and therefore also require low-pass filtering. The Ram–Lak filter [224] is the simplest in two dimensions, and defines $h(s)$ as the inverse FT of $H(k)$ where

$$\begin{aligned} H(k) &= |k| \quad |k| \leq b \\ H(k) &= 0 \quad |k| > b \end{aligned} \tag{7.8}$$

so $h(s) = (b/(\pi s))\sin(bs) - (1 - \cos(bs))/(\pi s^2)$. b is the bandlimit of the filter.

The Shepp–Logan filter [225] also includes low-pass filtering and was the one used in this work. The frequency response is $H(k) = (2/a)|\sin(ka/2)|$ where π/a defines

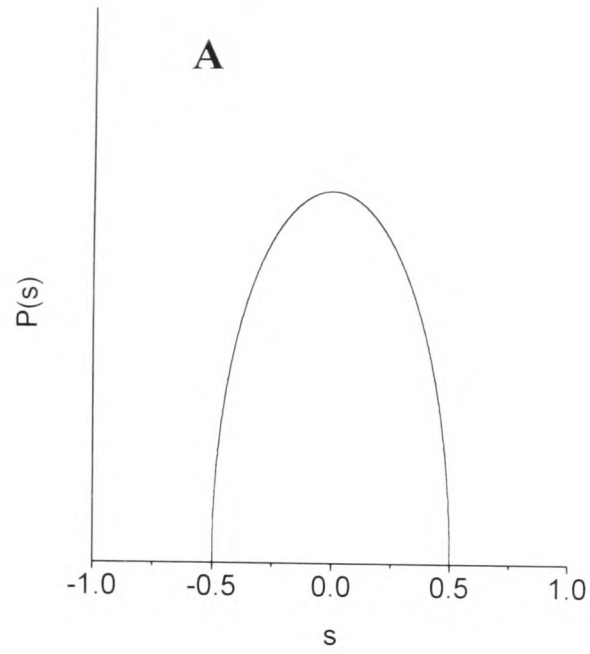

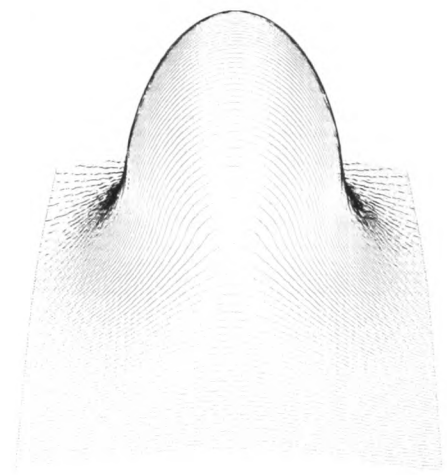

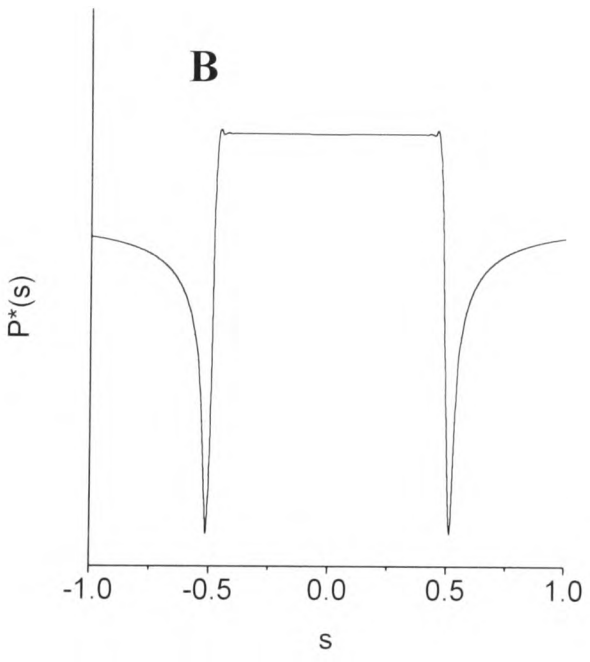

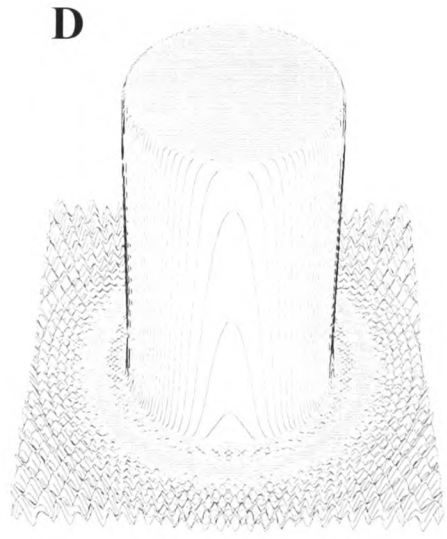

Figure 7.8: Projections and images of a circular disc. (A) shows unfiltered projection. (B) shows projection filtered by Shepp–Logan filter. (C) shows image formed by combining unfiltered projections. (D) shows image formed from filtered projections. Images formed by combining 45 projections. Filter was applied as though sample had been fitted to 40 strips, similar to much of our data. The distance along a projection is given by s (see text for details).

the bandlimit b of the filter. The inverse Fourier transform of $H(k)$ is

$$h(s) = \frac{2(2a - 2a\cos(ba/2)\cos(bs) - 4s\sin(ba/2)\sin(bs))}{\pi a(a^2 - 4s^2)} \tag{7.9}$$

For the special case in which s is sampled at ma where m is an integer, the filter takes on the simpler form

$$h(ma) = \frac{4}{\pi a^2(1 - 4m^2)} \tag{7.10}$$

Figure 7.9 shows the frequency response and the effect on an impulse in real space of the Ram–Lak and Shepp–Logan filters. The effect of the Shepp–Logan filter on the projection of the circular disc discussed above is shown in figure 7.8.

When examining experimental data the projections used were the spin distributions determined by iterative deconvolution as explained in §7.3.3. As these consisted of strips of discrete values, there were very sharp changes, which when filtered gave rise to high frequency oscillations. It was therefore necessary to smooth the projections before filtering, as a means of further low-pass filtering the data. This was done by convolution with a narrow Gaussian function. All of the convolutions were done numerically in real space.

The actual image reconstruction was performed by the program described in appendix A.3. This program started with the spin distribution for each orientation, and performed the smoothing, filtering, and combination to generate a two-dimensional array describing the image. The limitations on array size are discussed in the next section. Figure 7.15 in §7.6 shows the importance of filtering to obtain even reasonable resolution and to record the shape of the sample.

7.3.6 Sampling requirements

The image of five pieces of DPPH shown in figure 7.7 was generated without deconvolving the lineshape to generate a spin distribution, and without filtering to ensure sharp edges. Because of the presence of five discrete DPPH crystals the overall pattern is still very clear to see. However, what is equally clear on examining the surface plot (figure 7.7(B)) is the presence of a large number of artifacts in the image, showing

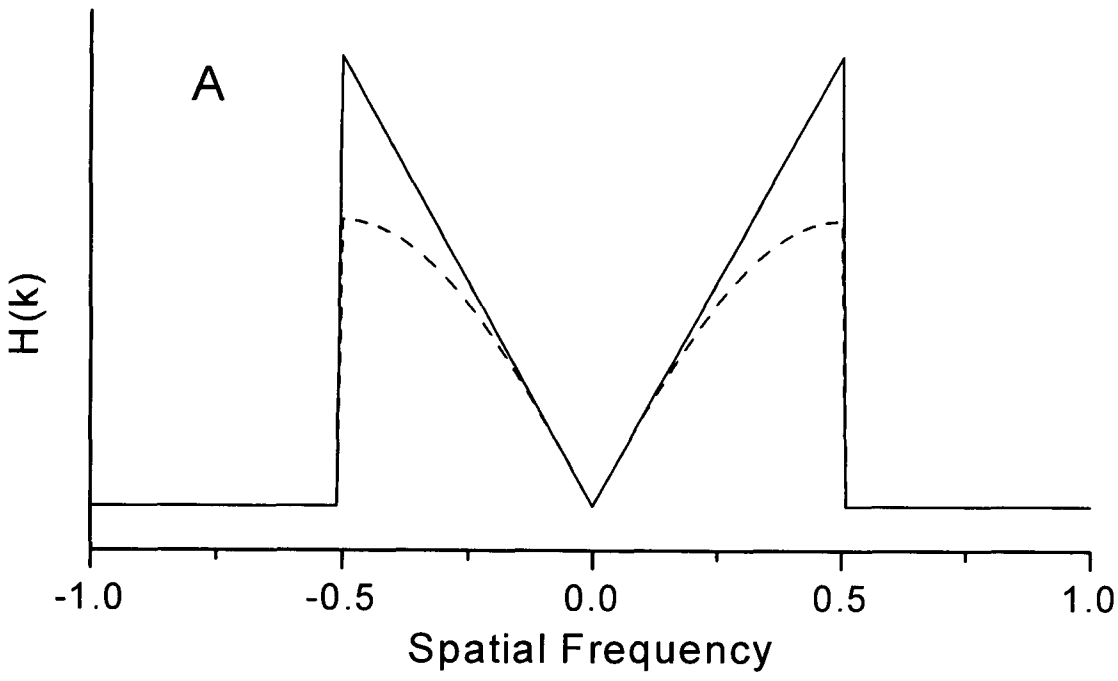

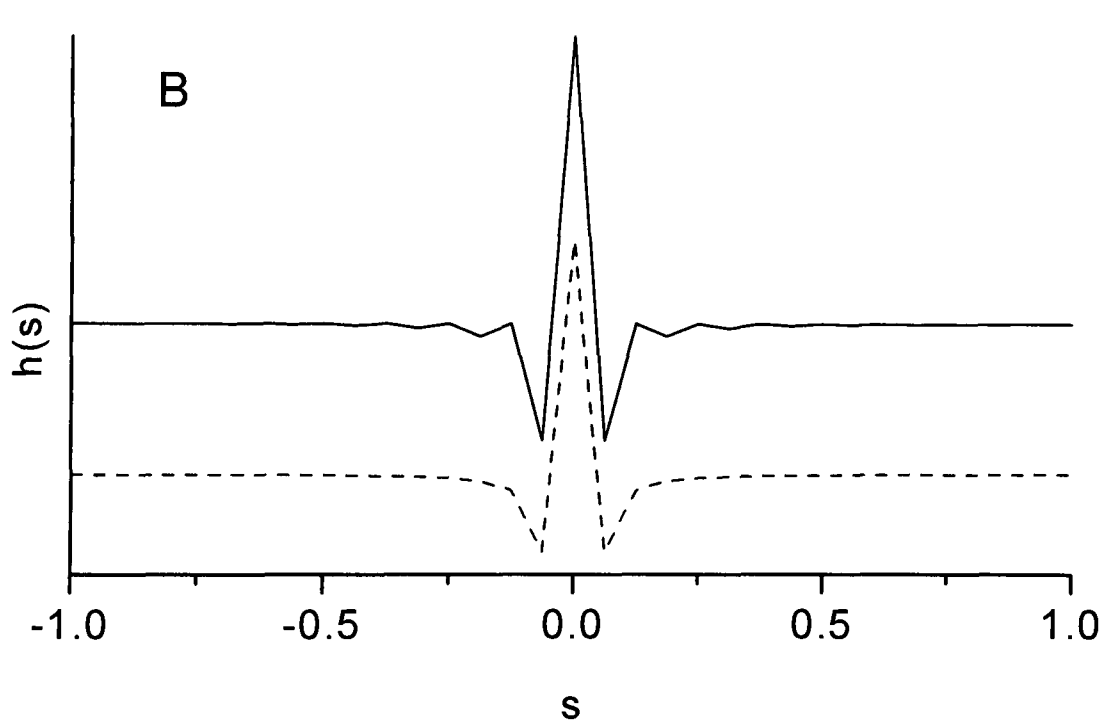

Figure 7.9: A comparison of the frequency response (A) and 33-point impulse response (B) of the Ram–Lak (solid line) and Shepp–Logan (dashed line) filters.

up as "ripples" between the clear pieces of DPPH. Although they are fairly small, this sample should have a very flat base "plane" as there is nothing at all between the pieces of DPPH. These ripples arise because the image is generated from a 128×128 pixel array, and the sampling rate is not high enough to support that.

In general, the limits on the number of pixels that can be used are determined by:

1. The angular sampling rate. In order to use an array of $N \times N$ pixels, it is necessary to use $\pi N/4$ projections [17, 226, 204]. Use of more pixels than is consistent with the number of projections recorded is merely "picture–drawing".

2. The radial sampling rate. If an $m \times m$ image is displayed on a $N \times N$ display, artifacts can be created from the high frequency ringing that accompanies the filtering in regions where the spin distribution is changing quickly. In the case of the DPPH cross in figure 7.7 this is not a problem because no deconvolution or filtering has taken place so the radial sampling rate is very high, but when we have spin distributions of 40 or fewer strips this becomes a factor. This is explained in more detail by Woods [223].

7.4 Nitrogen distribution through CVD films

7.4.1 The role of nitrogen in CVD growth

The role of nitrogen in the chemistry of CVD diamond growth is far from being well understood. It is known that the addition of nitrogen to the source gases can have a dramatic effect on the growth habit [178, 227], growth rate [228] and quality [178, 227, 228, 229] of diamond films produced by chemical vapour deposition. Jin and Moustakas [178] prepared nitrogen doped films by microwave plasma assisted CVD from gas mixtures containing $CH_4 + H_2 + N_2$. The nitrogen to carbon ratio in the gas phase (N/C) was varied from 0.01 to 0.4, but in all cases the nitrogen concentration in the diamond films was found to be below the detection limit of X-

ray photoemission spectroscopy ($9 \times 10^{20}\,cm^{-3}$). They also found that the growth habit changed from {111} to {100} and the growth rate increased by a factor of 1.6 with increasing nitrogen in the gas phase ($CH_4/H_2 = 0.5/99.5$ vol %, ratio N/C in gas phase 0.01–0.4, pressure 45 Torr, substrate temperature 850 °C, microwave power 950 Watts). Samlenski *et al.* [179] studied the incorporation of nitrogen in CVD grown homoepitaxially on {100} and {111} orientated diamond substrates. They found that nitrogen incorporation into {100} growth sectors was a factor of 3–4 higher than in the {111} growth sectors, and that the incorporation probability of nitrogen was about 7×10^{-4} and 2×10^{-4}, respectively ($CH_4/H_2 = 0.5/99.5$ vol %, ratio N/C in gas phase 0.02 or 0.007, pressure 50 mBar, substrate temperature 850°C, microwave power not given). Müller-Sebert *et al.* [228] found that the growth rate could be increased by a factor of 5 (compared to nitrogen free growth), to 12 μm per hour by the addition of nitrogen to the source gases ($CH_4/H_2 = 3/97$ vol %, ratio N/C in gas 0.003, pressure 220 mBar, substrate temperature 830°C, microwave power 4.2 kW). They also found that the addition of nitrogen affected the rate at which growth occurred in different parts of the film: with low nitrogen the centre of the film grew faster, whereas with 50 ppm N_2 in the source gas the edges grew faster.

The low nitrogen incorporation ratios suggest that it is not nitrogen incorporation that affects growth rates but the role it plays in surface processes. Müller-Sebert *et al.* speculated that nitrogen could increase the generation of growth steps on {100} faces. It is now well known that low nitrogen concentrations in the gas phase can cause considerable change in the growth rate, crystallinity, morphology and texture of deposited diamond films. However, other parameters such as microwave power and methane concentrations have dramatic effects and the role of nitrogen is far from being understood. Where this work can help is in determining to a very high resolution the distribution of nitrogen incorporation in a film. EPR has an unrivalled sensitivity to N_S^0, and it is a technique that can probe inside the bulk of a sample when optical methods cannot (e.g. in unpolished samples).

Sample	Concentration N_S^0 (No. cm^{-3})	Concentration of defects centred on g=2.0028 (No. cm^{-3})
4	3.3×10^{17}	1.4×10^{17}
7	1.3×10^{17}	$\sim 1 \times 10^{16}$
9	0.4×10^{17}	0.2×10^{16}
8	0.9×10^{17}	$\sim 1 \times 10^{16}$
35	0.4×10^{16}	2.5×10^{16}

Table 7.1: Average bulk spin concentrations determined by double integration of EPR spectra and comparison to a reference. The relative concentrations of different samples are accurate to ± 10 %, but the errors on the absolute values are ± 20 %.

7.4.2 Measurements

The distribution of nitrogen through the thickness of CVD diamond films is particularly important when considering the role of nitrogen in the growth process. Although it is known that sometimes only a fraction of the nitrogen incorporated into a film is in the form of N_S^0 (see §5.4.1 and Zhou [140, 125]), the distribution of N_S^0 can still give some idea of the rate of incorporation. This can potentially be compared with the nitrogen content of the plasma and the growth rate at various points during the growth process.

Samples used

The free standing CVD diamond samples showed the same properties as those studied in §5.4.1. The films were between 700 and 2500 μm thick. All samples showed a strong diamond Raman line at 1332 cm^{-1} with only weak non-diamond features in the Raman spectra. The bulk EPR concentrations are given in table 7.1. All the samples were unpolished. Individual crystallites were not visible by eye on the growth surface of sample 4, but large (up to $\sim$ 100μm) crystals were visible on the growth surfaces of the other samples. Samples 4, 7, 8 and 9 measured 10 × 5 mm in the plane perpendicular to the growth direction; sample 35 measured 10 × 0.5 mm perpendicular to the growth direction.

Orientation

All of these investigations were carried out at room temperature, so the ESR900 flow cryostat was not used. The samples were mounted on the sample rod described in §4.3.3 going right through the cavity, to minimise vibration. This rod had a square top aligned with the sample, so the sample could be orientated with the growth direction exactly parallel to the Zeeman field. This is of paramount importance, because a misorientation of even 0.2° can degrade the resolution.

Resolution

The linewidth of the N_S^0 signal is typically 0.025 mT so in principle, given a large enough signal, with a field gradient of $\partial B_z/\partial z = 1.3$ mT mm^{-1}, a resolution of 18 μm is possible. For narrow samples with high bulk concentrations we found that this was indeed the case. For samples with very low concentrations (e.g. sample 35), in order to obtain a reasonable signal to noise in the distribution, the gradient had to be smaller so the resolution was lower.

Sensitivity

The absolute N_S^0 sensitivity of the spectrometer, extrapolating to a signal to noise of 1:1, is about 10^{12} centres. In order to distinguish slices successfully, the number of spins in each slice needs to be above $\sim 5 \times 10^{12}$ (signal to noise of 5:1). This theoretical sensitivity was achieved in sample 35, which is discussed in §7.5.

Spin distributions

The N_S^0 distributions though the thickness of the five different samples are shown in figure 7.10. The spectra were taken at low microwave powers and field modulations, to avoid saturation and broadening of the line. At these powers the g=2.0028 defect had a very small amplitude and the distribution of N_S^0 was easy to distinguish. The fit to the experimental data in obtaining one of these spin distributions is shown in

figure 7.4. The gradient used was 0.18 mT mm^{-1} for sample 35, and 1.3 mT mm^{-1} for the other four. All of the samples studied displayed homogeneous distributions in other directions.

Infrared absorption measurements

Infrared absorption measurements were made with the samples at room temperature using a Perkin–Elmer 1710 FTIR spectrometer. Sample 4 was darker than the others and showed weak absorption in the CH region 2800–3200 cm^{-1} (see §5.4.3); the other samples showed only very weak absorption in this region. No appreciable absorption was detected in the one-phonon region.

7.4.3 Discussion

Since the samples studied here were produced by a proprietary process we do not have knowledge of the growth conditions, so it is unreasonable to speculate as to the specific origins for the changes in N_S^0 concentrations through the thickness of the films.

However, it is clear from the data presented in figures 7.10 that EPR imaging can be used to study the through-thickness N_S^0 distribution to a resolution of $\sim 20\,\mu m$ when the mean bulk concentration is only a few hundred parts per billion carbon atoms ($\sim 5 \times 10^{16}\,cm^{-3}$). The data also shows that the local through-thickness concentration of N_S^0 can vary by at least a factor of 5. It would appear that the growth of sample 4 was stopped and started a number of times during the growth process, and the peaks and troughs in the EPR image reflect that.

It is clear that precise orientation of the sample is important. A small misorientation of the sample may contribute to the change in concentration observed in the first and last 80 μm of the samples 7, 8 and 9. However, the surface roughness and a real change in concentration could also explain this feature. The slow rise in N_S^0 concentration during the initial growth of sample 4 is a real feature.

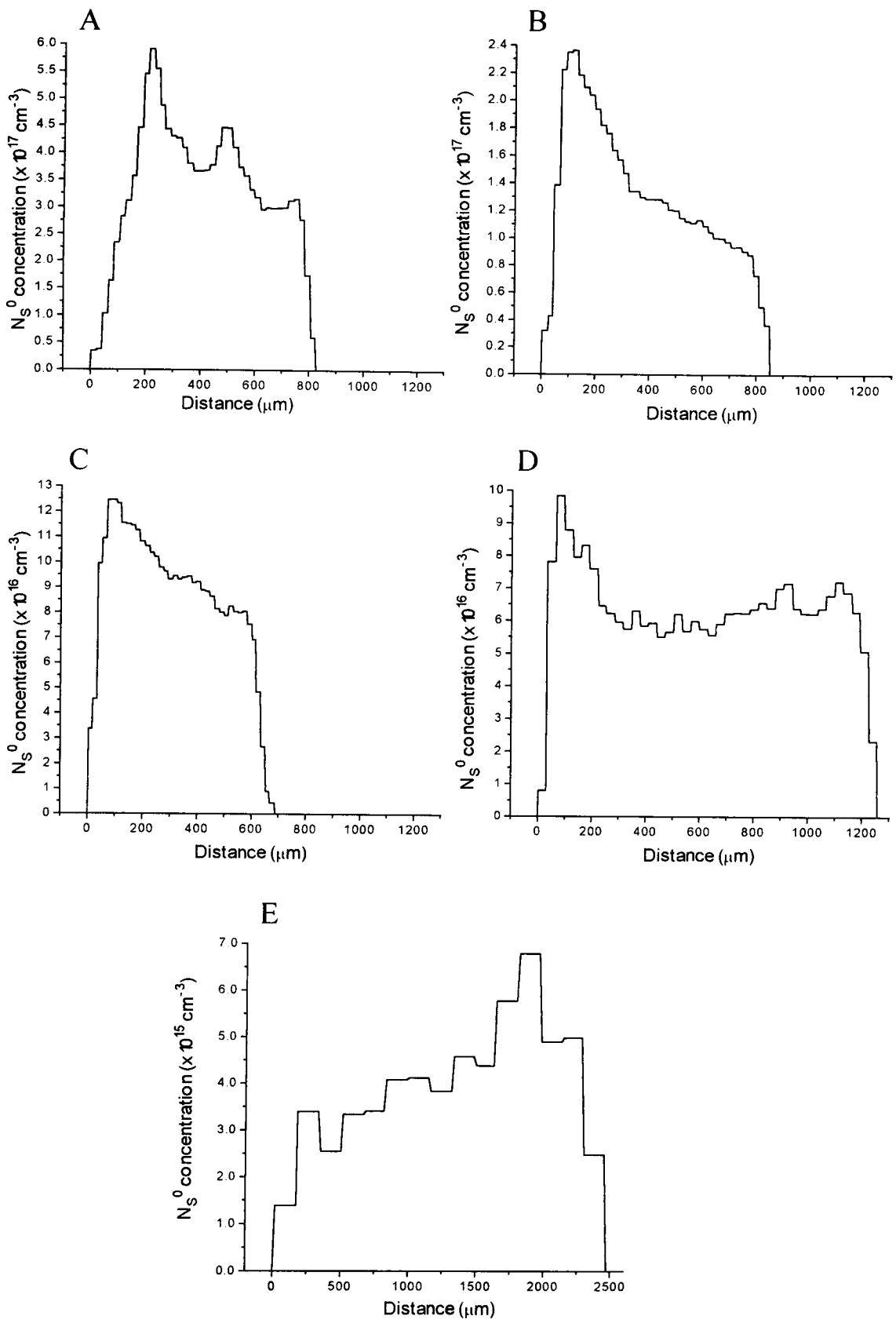

Figure 7.10: N_S^0 distribution through samples:
(A) Sample 4. Mean N_S^0 concentration $3.35 \times 10^{17}\text{cm}^{-3}$ (1.9 ppm.)
(B) Sample 7. Mean N_S^0 concentration $1.3 \times 10^{17}\text{cm}^{-3}$ (0.74 ppm.)
(C) Sample 9. Mean N_S^0 concentration $8.6 \times 10^{16}\text{cm}^{-3}$ (0.49 ppm.)
(D) Sample 8. Mean N_S^0 concentration $6.3 \times 10^{16}\text{cm}^{-3}$ (0.36 ppm.)
(E) Sample 35. Mean N_S^0 concentration $4 \times 10^{15}\text{cm}^{-3}$ (0.023 ppm.)
Nucleation surface at $z = 0$.

A considerable amount of experimental evidence indicates that nitrogen can have a dramatic effect on CVD diamond growth. It is known that N_S^0 incorporation can change during growth. EPR imaging could well become an important tool for studying the effect of nitrogen on CVD diamond growth. It will undoubtedly be useful in correlating changes in the nitrogen content of the plasma with N_S^0 uptake in the sample. It could provide a method of studying possible nitrogen out-gassing in a reactor leading to high initial nitrogen contamination and an exponential fall off as growth proceeds. The different uptake of nitrogen in {111} and {100} growth surfaces could allow EPR imaging to be used to study changes in growth morphology.

7.5 Distribution of N_S^0 and defects at g=2.0028 through films

7.5.1 Measurements

Sample 35, discussed in the previous section, was the thickest of the samples studied. It also had the lowest concentration of N_S^0 and a g=2.0028 defect concentration six times higher than that of N_S^0. It was also very small in the directions perpendicular to the growth direction. This had the following consequences:

- At high microwave powers, high magnetic field modulation and low temperature (4K) it was possible to saturate the N_S^0 signal so that it was not visible under the g=2.0028 defect. It was therefore possible to determine the distribution of the g=2.0028 defect *in the same sample* as the N_S^0.

- The overall distribution of the g=2.0028 defect was clear despite the low resolution caused by the large linewidth of this defect, because the sample was 2500 μm thick.

- Because of the very low concentration and small sample size the resolution of the N_S^0 distribution was comparable to that of the g=2.0028 defect, allowing a

direct comparison between the two.

In fact, even at low microwave powers the g=2.0028 defect line was still visible under the N_S^0 line, but after the g=2.0028 defect distribution had been determined, it was possible to generate the theoretical lineshape of the g=2.0028 defect at low power and low field gradient, and subtract it out to leave only the nitrogen lineshape. The distributions of g=2.0028 defect and N_S^0 are shown in figure 7.11, and the fits to experimental data in figure 7.12. A photograph of the side of the film is shown in figure 7.13. This clearly shows the columnar growth structure of the film. It is also clear that at the end of the growth there is an increase in the amount of lower quality material—there is more "dark substance" than at the beginning.

7.5.2 Discussion

The first point that is abundantly clear from studying figure 7.11 is that the two distributions are very different. This adds yet more evidence to back up the hypotheses of the previous two chapters that the N_S^0 and the g=2.0028 defect are in different parts of the sample.

Secondly, sample 35 is a very thick sample. The absolute bulk concentrations of both defects are very low—particularly the g=2.0028 defect, and this correlates with it being a very high quality sample. The fact that the g=2.0028 defect is largely concentrated within 200 μm of the nucleation face and 500 μm of the growth face suggest that the 1800 μm in the middle are of very high quality indeed—with a spin concentration as low as 1.5×10^{16} cm^{-3}. So if the outer faces were polished away there could be a very thick optical quality piece of CVD diamond.

The presence of the g=2.0028 defect in the first 200 μm is probably unavoidable—the crystallites are small, with a correspondingly large ratio of surface area to volume; and there is no preferential orientation, so the quantity of non-diamond material is large. However, the increase in the concentration of g=2.0028 defect at the other end raises an important question: is this increase connected with the termination of the

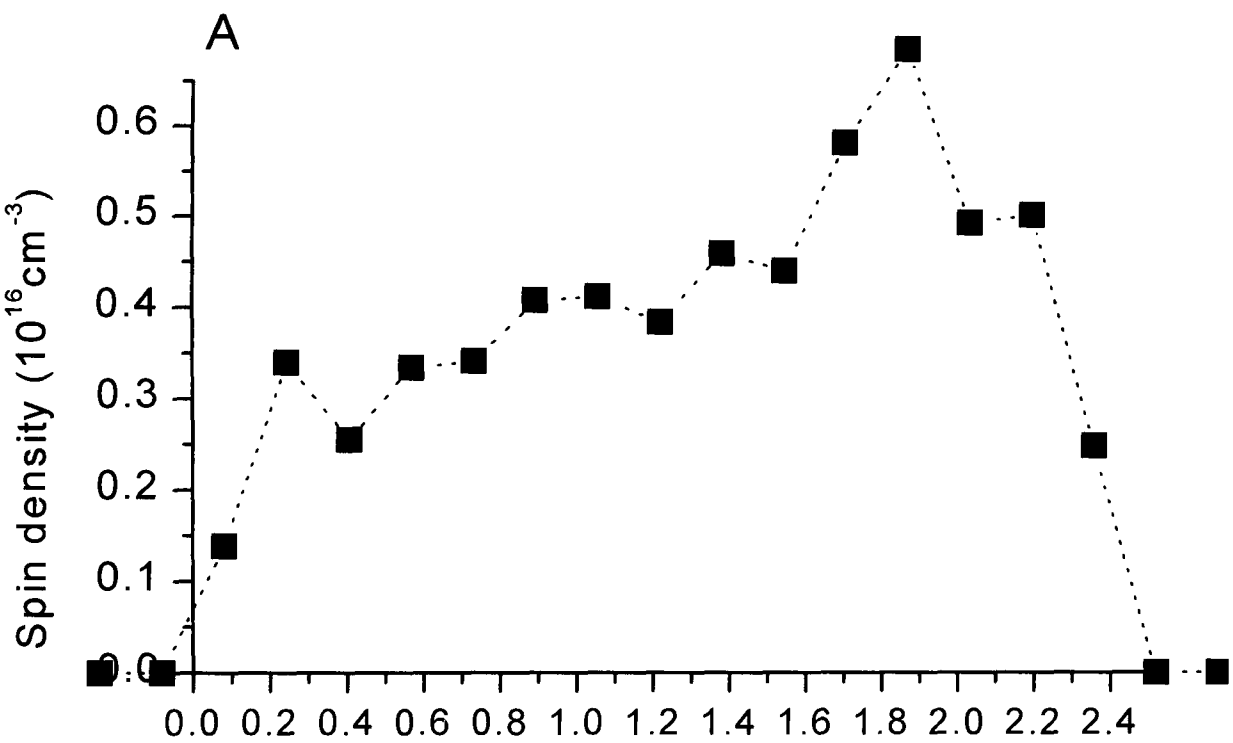

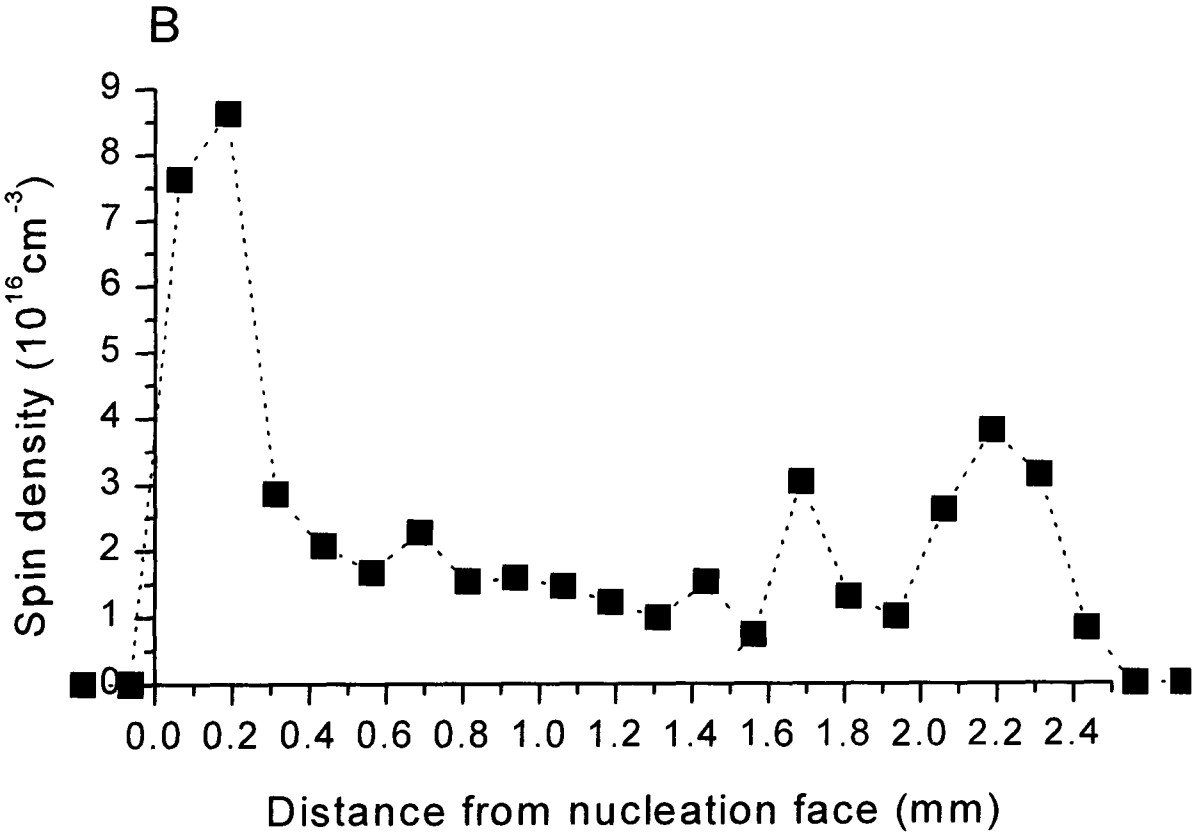

Figure 7.11: Comparison of spin distribution of (A) N_S^0 and (B) g=2.0028 defect through thickness of sample 35. Note concentration of g=2.0028 defect at edges of sample. The "spike" at 1.7mm is a real effect. Distribution (A) determined at room temperature, distribution (B) at 5 K.

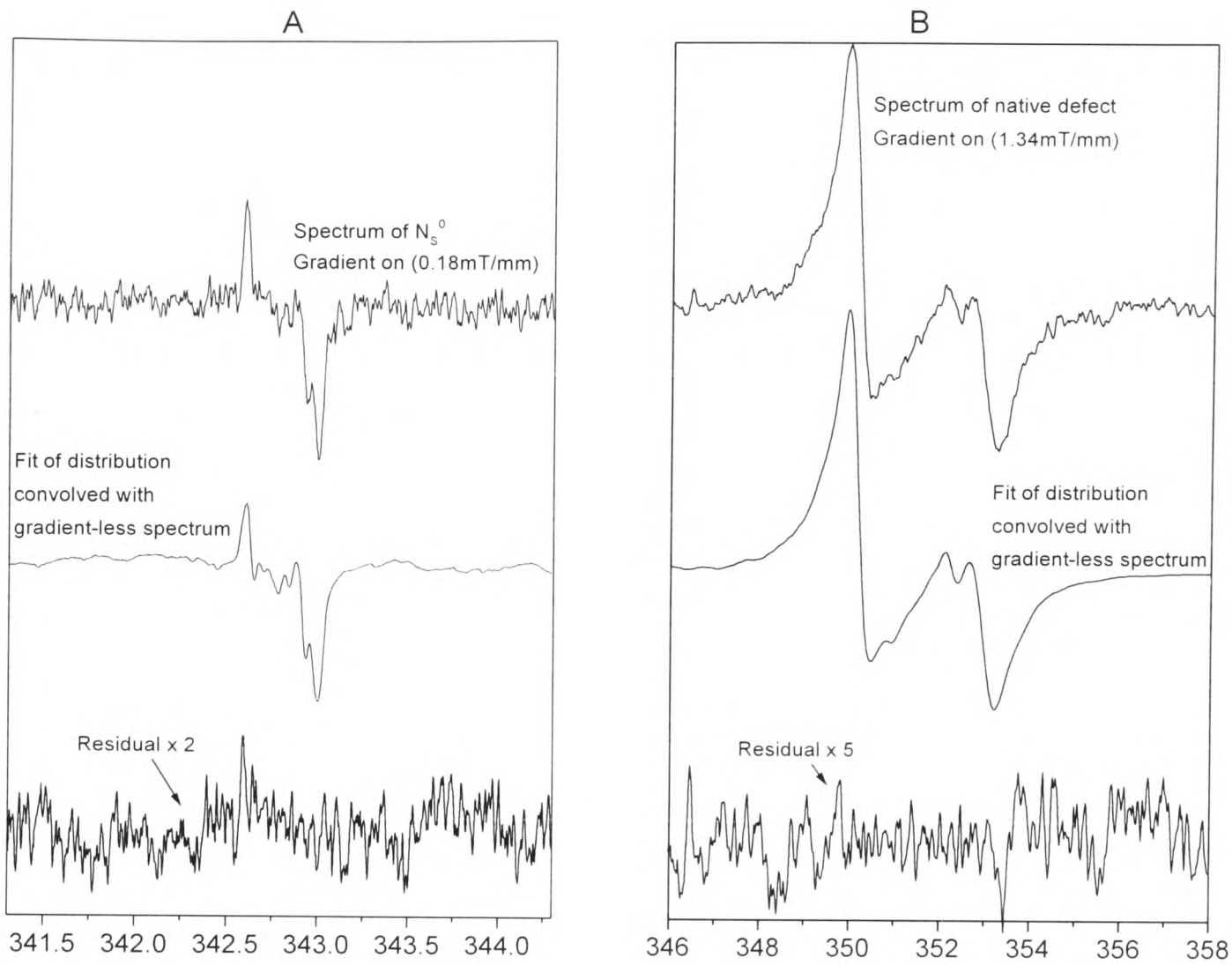

Figure 7.12: Fit to experimental data of spin distributions of (A) N_S^0 and (B) g=2.0028 defect in sample 35.

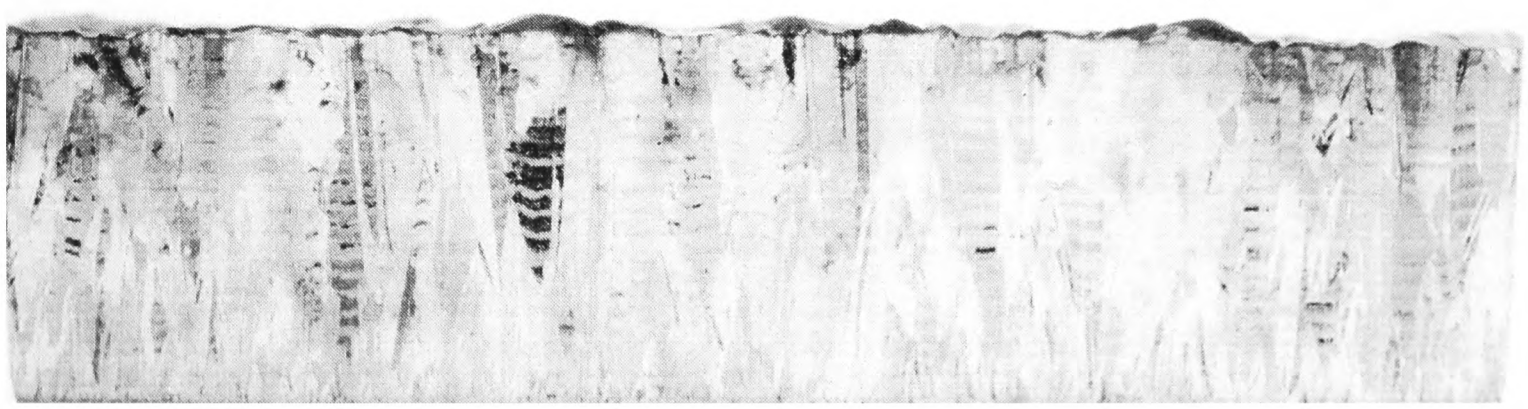

Figure 7.13: Photograph of columnar growth structure of sample 35. Nucleation face is at the bottom of the picture. Sample 2.5 mm thick.

process, or has the process started getting worse again after 2 mm? Without knowing anything about the growth conditions it is not a question that can be answered here, but it is crucial to the production of high quality samples. Another possibility is that the grain sizes are big enough at this stage that spaces start to appear between them, with a corresponding increase in the quantity of non-diamond material in the sample. If this is the case EPRI could be a useful technique for investigating the morphology of films: in a polished sample the change in grain size through the sample could not be monitored optically. With higher gradient this technique could be used in much narrower films as a good measure of the optical quality through the films. The cause of the "spike" at 1.7 mm in figure 7.11(B) is unclear.

Another interesting point is the distribution of the nitrogen. As mentioned earlier this is a very high quality sample, and the gradual increase in the uptake of nitrogen through the sample may be a measure simply of the gradual increase of preferential orientation of the crystallites during the growth, or it may be due to the increase of the quantity of nitrogen in the plasma. This gradual increase was not observed in any of the other four samples imaged.

7.6 2-D imaging of N_S^0 in single crystal synthetic Ib diamonds

The CVD images in the previous section have given useful information about defect distribution. For this system to be useful in the long term we need to be able to determine spin distributions inside samples in two dimensions as well, at as high resolution as possible.

7.6.1 Samples

As a means of testing what resolution we could obtain in two dimensions, two single crystal synthetic Ib diamond plates $\sim 500\,\mu$m thick were used. These samples had

two main advantages:

1. High concentration of N_S^0.
2. Well defined growth sectors with large differences in the concentration of N_S^0 between them.

These two advantages cause one problem. The regions with different concentrations of N_S^0 will give rise to signals with different linewidths if the concentrations are high enough, because the dipole–dipole broadening will be bigger in the regions with higher concentrations. If this becomes significant it means the deconvolutions cannot be performed, because it would be necessary to deconvolve a broad lineshape out of the signal from regions of high concentration, and a narrow lineshape from the regions with low concentrations. This is clearly impossible. In the end it was found not to be significant, but it something to be borne in mind. In samples with lower concentrations all through it would be even less significant.

A detailed discussion of the growth sector dependence of the incorporation of N_S^0 will not be given here. Burns *et al.* [230] conducted an exhaustive study into the growth sector dependence of optical centres, particularly nitrogen and boron, in large synthetic diamonds. Their results show that the N_S^0 concentration is highest in {111} sectors, somewhat less in {001} sectors and less still for {113} sectors. They found hardly any N_S^0 at all in {110} sectors even in their sample with a high nitrogen concentration.

7.6.2 Measurements

Measurements were made at room temperature. The samples were rotated and spectra recorded every 4°. A potential problem, not discussed before, in examining the distribution of a defect where the EPR signal has hyperfine structure, as in this case, is that the broadening of the central line in the field gradient could overlap with the broadening of the satellite lines. [203, 223, 204]. There are two solutions to this. The more straightforward solution is to use a field gradient which keeps the central line

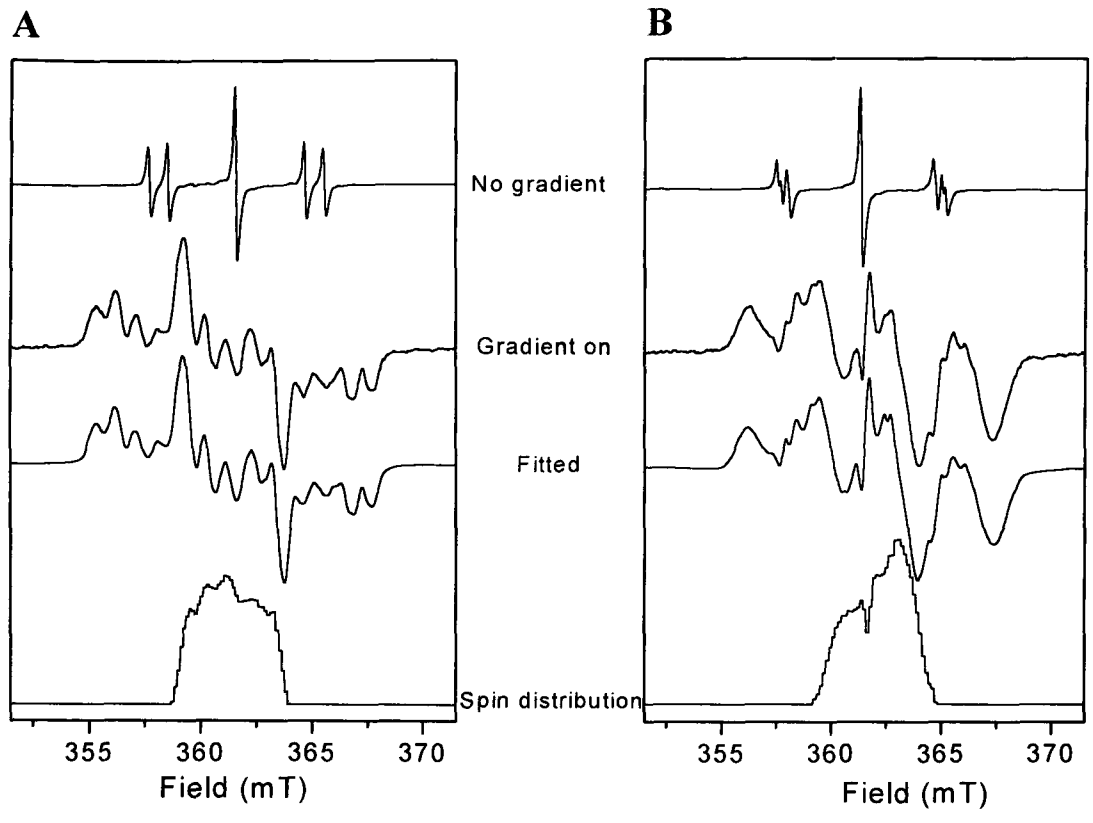

Figure 7.14: Deconvolution of N_S^0 including hyperfine structure in two different directions in sample S1-1B. (A) 4° from start. (B) 156° from start.

inside the satellites, but this drastically limits the available resolution. The alternative is to take spectra at each orientation both with and without the gradient, and deconvolve all of the lines together to generate the spin distribution. This second approach was used, and an example of a deconvolution of all the lines including the hyperfine structure is given in figure 7.14.

The spin distributions were all generated using 40 strips, giving a resolution of 100 μm. The linewidth of the central line was 0.1 mT for both samples, so the predicted resolution is of this order. The gradient used was again 1.3 mT mm^{-1}. The images were generated using the smoothing, filtering and recombination techniques discussed in §7.3.4 and §7.3.5 above. Figure 7.15 shows the image of sample NLO generated with and without filtering to demonstrate the difference in resolution that using a filter makes, and compares the EPR image to a picture recording the optical absorption of the sample. The areas of high optical absorption correspond to high concentrations of N_S^0. Figure 7.16 compares the EPR image to the optical absorption distribution in sample S1-1B.

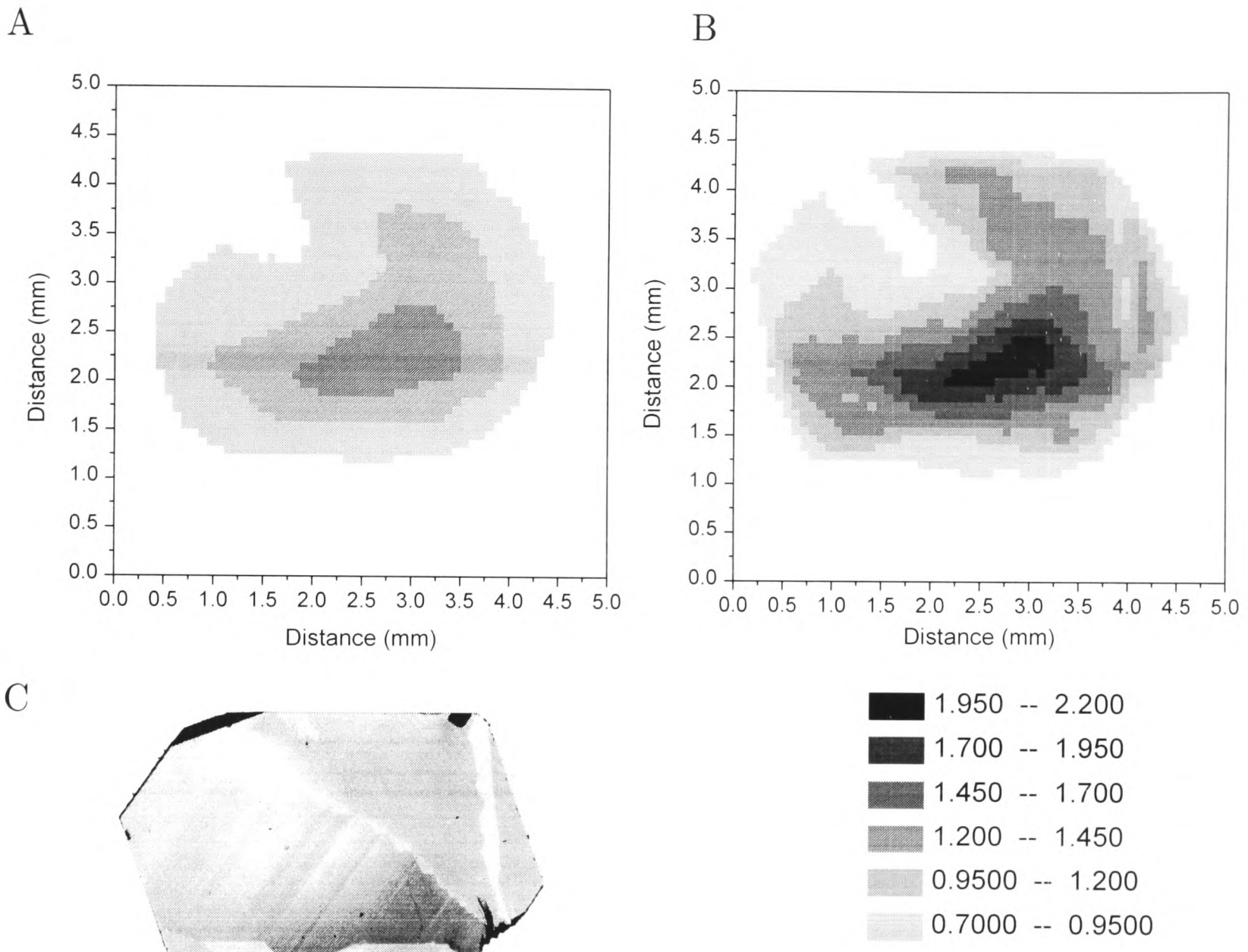

Figure 7.15: Images of sample NLO. (A) EPR image without filtering in reconstruction. (B) EPR image including filtering. (C) Picture of N_S^0 distribution determined from optical absorption. Dark areas correspond to high N_S^0 concentration. EPR projections obtained at room temperature, 3 mW microwave power, 0.1 mT field modulation. 45 projections used, image displayed on 50×50 pixel grid.

A

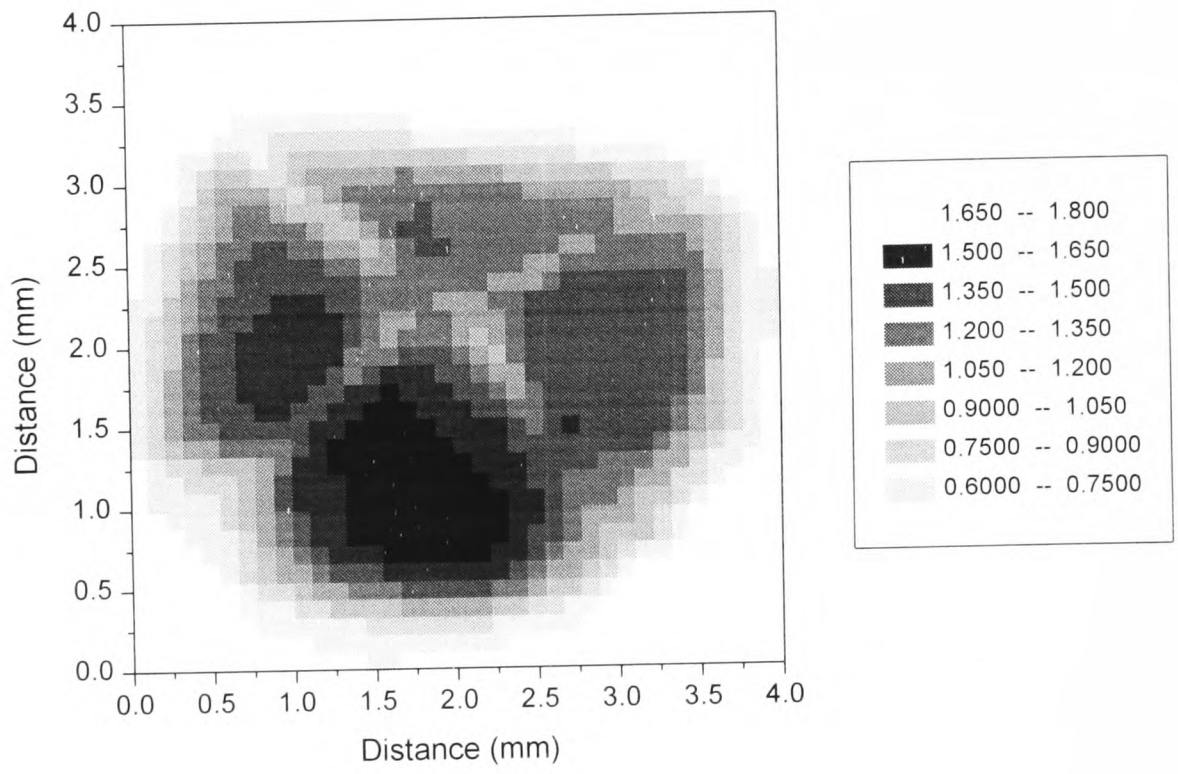

B

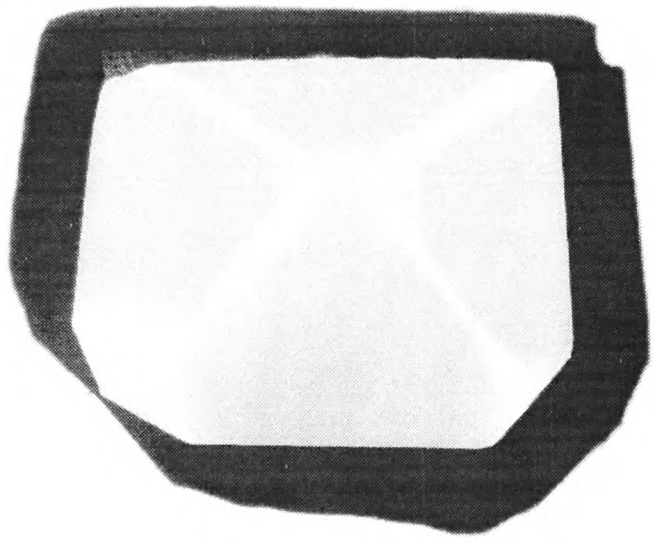

Figure 7.16: Images of sample S1-1B. (A) EPR image of N_S^0 distribution. (B) Photograph of light transmitted through sample. Dark regions correspond to high N_S^0 concentration. Dark ring round the edge due to sloping edges of sample.

7.6.3 Discussion

The images show the resolution of which this process is capable. The strip on the right hand side of NLO is 160 μm across, but is clearly identified by the EPR image. Similarly, the growth sectors in sample S1-1B that run from the centre to the corners are 100 μm across, and are also clearly visible in the EPR image. The EPR images match with the visible pictures extremely well. The challenge arises when there is no visible picture to work from. Then, the differences between artifacts produced by oversampling and overoptimistic determination of the possible resolution, and real effects corresponding to the spin distribution in the sample, are of importance. However, we have shown that the resolution quoted of 100 μm is realistic with this gradient, and further that this resolution is not greatly reduced when translated into a 2D image, and that no false components have been generated by the reconstruction. This suggests that for defects in diamond where there is no convenient optical method for examining the distribution, EPR may still be capable of doing so. Much of the defect distribution can depend on growth processes, but there is potential for examining natural diamonds where the growth conditions are not known, or intrinsic radiation damage defects [16, 231] in good quality diamonds. Although in practice most samples will not have the convenient sharp changes between regions that these two display, they do show that it is a feasible technique.

7.7 2-D imaging of g=2.0028 defect distribution

The main problem with attempts to image the g=2.0028 defect distribution in CVD films is the resolution limitation due to the width of the line. Apart from sample 35 discussed in §7.5, all of the samples were 1300 μm thick or less. So through-thickness distributions would not give much meaningful information. However, in the plane of the film the dimensions are large enough that the maximum resolution of $\sim 200\,\mu$m is useful. Using the experience gained from the measurements in the previous section it was possible to attempt to gain a 2-D image in the plane of a CVD film.

7.7.1 Measurements

The samples that we examine are typically $10 \times 5 \times 0.5$ mm, but are not grown with those dimensions. The diamond is grown in larger plates and cut to the required size. To get an idea of the homogeneity of the diamond across the growth surface it is of course possible to examine samples from different places in the same growth run. However, in regions where the growth conditions may be changing rapidly with respect to position, there can be changes across the dimensions of a single sample. A possible reason for this is outlined in §7.4.1: depending on the nitrogen concentration in the source gas and the shape and size of the plasma ball, the sample could be grown at different rates in different regions [228].

One such sample was 36, which is shown in figure 7.18. This was cut to a length of 5.4 mm in order to fit it in the ESR900 flow cryostat. The bulk concentration of defects with g=2.0028 was 10^{17} spins cm^{-3}. It was particularly unusual in that there was a marked change in optical quality across the sample, with black flecks clearly visible on the left hand side. There was evidence of N_S^0 centres in the sample, but at too low a concentration to isolate from the g=2.0028 defect and obtain a distribution.

Spectra were recorded every 10° at 5 K, under conditions where the line was not saturated and not broadened. Although for really high resolution there should be more projections we were only seeking the general behaviour through the sample, rather than closely identifying the exact position of the defect at this stage. The theoretical resolution for a peak to peak linewidth of 0.3 mT is 230 μm. The data was fitted to 20 strips for each projection, which corresponds to a resolution of 270 μm in the longest dimension, and the fits were found to be very good indeed. In such a case there is no point in trying to produce spin distributions with higher resolution—we would be simply introducing more parameters into the fitting algorithm.

With only 20 points in each projection, the biggest array that we can use when generating the image is therefore 20×20 pixels over the region of the sample, for which our 18 projections are sufficient. A typical projection and fit to experimental data is shown in figure 7.17, and the image obtained is shown in figure 7.18. A distribution

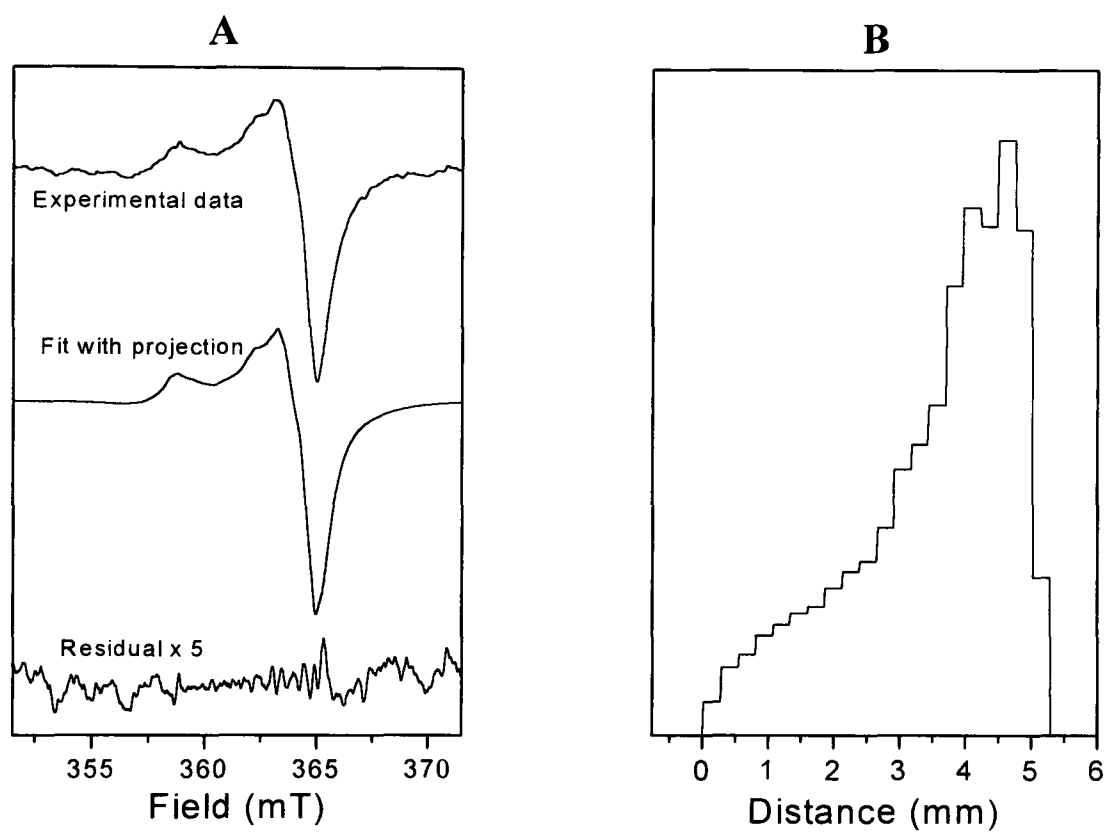

Figure 7.17: Fit to experimental data (A) and spin distribution (B) for the projection with $\theta = 100°$ in sample 36. Spectra recorded at 5 K, 1.7 mW microwave power. Field gradient 1.3 mT mm^{-1}. $g = 2.0028$ defects imaged.

A

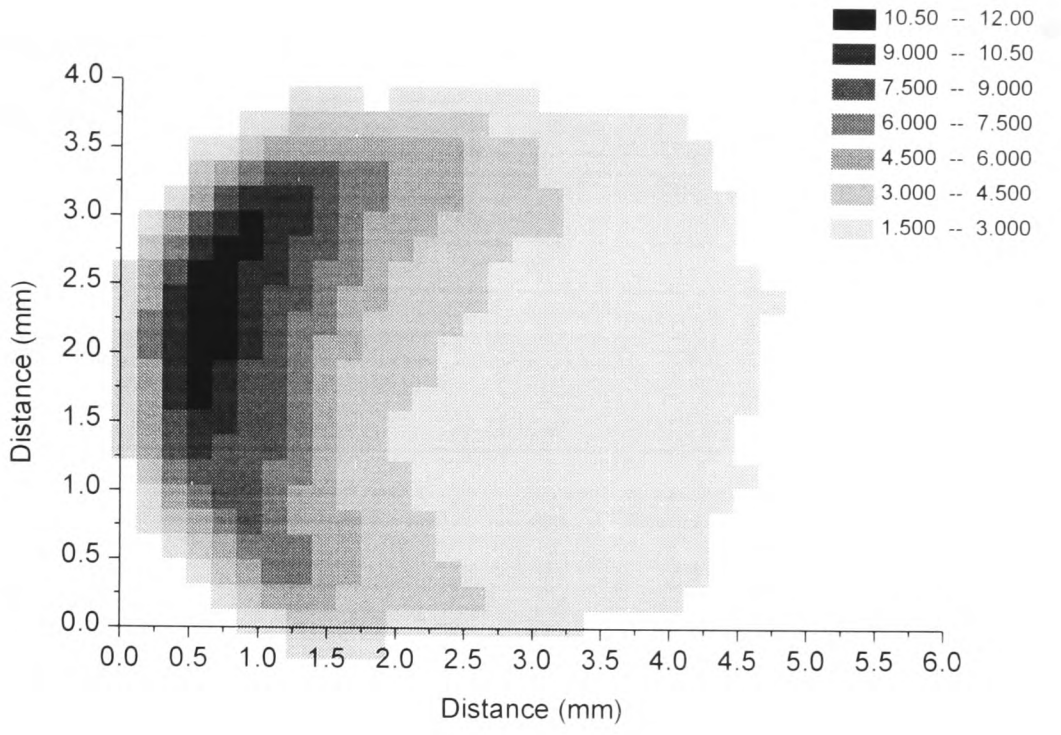

B

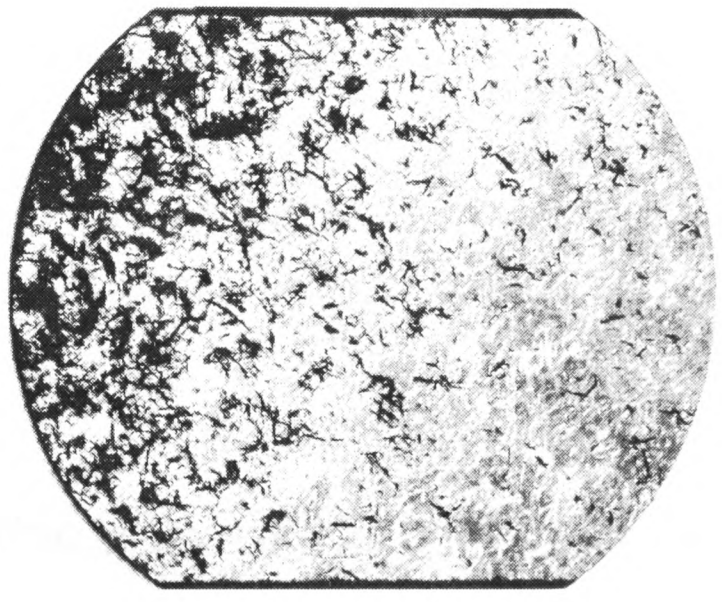

Figure 7.18: EPR image of spin distribution of g=2.0028 defect (A) and photograph (B) of sample 36. Photograph taken with sample lit from behind. The black specks are non-diamond material between the crystallites. Projections used as shown in figure 7.17. 18 projections, image shown on 25 × 25 pixel grid. Experimental conditions given in figure 7.17.

was also obtained at high microwave power, when the line from the H1 centre was saturated, and there was just a narrower central line. The spin distributions at each orientation essentially looked the same, but there was more spectrometer noise, and hence more uncertainty in the fitting. The image produced was the same as for the unsaturated defect, but noisier.

7.7.2 Discussion

It has been postulated throughout this thesis that the g=2.0028 defect in a polycrystalline film is not in the diamond crystallites, but in the non-diamond material between them. §7.5 showed unequivocally that the g=2.0028 defect and nitrogen distributions in a sample were different. What is clear now is that the distributions of intergranular material as seen in the optical photograph and the distributions of the g=2.0028 defect are very similar. Without going to very high gradients it would be difficult to match the individual black "flecks" to regions of high H1 concentration, but the general trend is still clear.

What is also true is that at high powers, when the H1 is saturated, whatever is left is also concentrated in the dark regions. This still leaves open the question of whether it is related to the H1 defect in some way, whether it occurs in the same regions, or whether it is simply a different defect that also occurs in the non-diamond regions of the sample.

7.8 Distribution of $[N–N]^+$ centre

This section marks a departure from the previous four, as imaging in a direction perpendicular to the Zeeman field was attempted.

7.8.1 Background

The W24 EPR signal was first reported by van Wyk and Loubser in 1983 [232], and was shown to be an unpaired electron in an orbital on two equivalent neighbouring substitutional nitrogen atoms. The W24 centre is only observed under illumination by light of wavelength shorter than 415 nm. They proposed that this centre was the ionized A-centre, or $[N–N]^+$. Tucker [16, 21] confirmed this in 1994 using ^{14}N ENDOR experiments. The distribution of this defect through samples was thought to be inhomogeneous, again confirmed by Tucker [16, 21], who cut his sample into two different sized pieces and compared the size of EPR signal. EPR imaging could provide a way to determine this distribution.

7.8.2 Experiment

Light was introduced into a natural Cape Yellow diamond using the quartz rod and xenon lamp described in §4.3.6. Initially, a prism was used so that the light was entering the sample in the z-direction, and so that the field gradient was in the same direction as the light. However, this precluded the use of the cryostat, and the EPR signal was found to be too small to be of practical use at room temperature. Therefore it was necessary to find another method for which the field gradient and light direction were parallel.

7.8.3 $\partial B_z/\partial x$ gradient coils

If the sample is mounted in the optimum configuration for illumination, it is on the end of a quartz rod, with the light entering it from above. In this configuration, for the sample used, this also allows the use of the ESR900 flow cryostat.

However, in order to determine the distribution of $[N–N]^+$ in the direction of illumination, the field gradient must be in the x-direction rather than the z-direction. So "figure of eight coils" were constructed in the form of two pairs of Helmholtz coils offset from each other in the x-direction, to generate a field gradient $\partial B_z/\partial x$ (see

figure 7.19). These were made purely for this experiment and were cooled by blowing air over them. The coils were also offset in the z-direction in order to get them as close to the resonator as possible, and to get the centres of the coils as close together as possible in the x-direction. The field gradient generated was $\sim$ 0.2mT mm^{-1} in the x-direction; this is discussed in more detail in the next section.

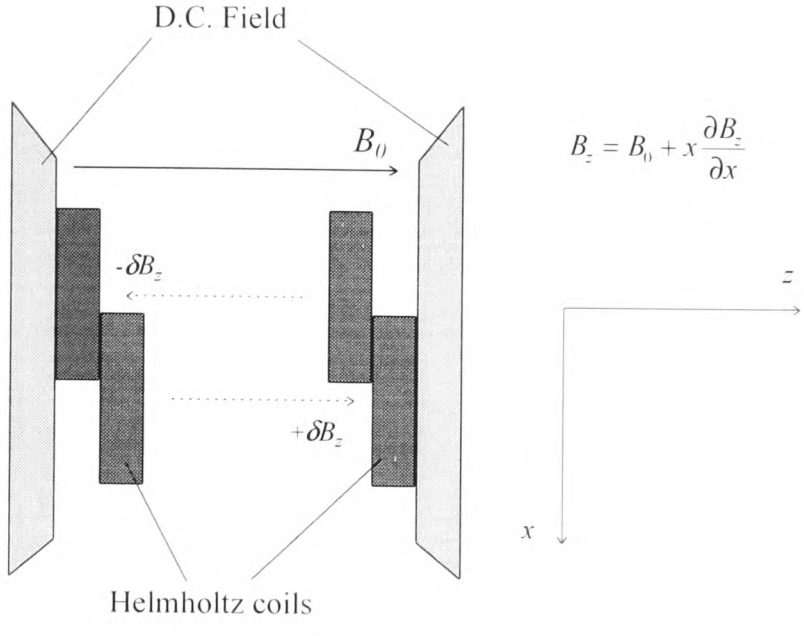

Figure 7.19: Configuration of coils to generate gradient $\partial B_z/\partial x$.

7.8.4 Measurements

The spectrum of this sample under illumination at 5 K at two microwave powers is shown in figure 7.20. It was aligned as close to the (100) direction as possible using the N_S^0 lines as guidance. The P2 lines in the centre, although saturated, were used to determine the field gradient. The sample contained the W21 defect as well, although at 5 K it was hardly visible [21]. The two W24 lines at low field were used for the imaging, as there was a large gap between them and any other lines.

Deconvolution was performed using both lines, and a spin distribution obtained. This is shown in figure 7.21. What is immediately obvious from this distribution is that the start and end of the sample are not clearly defined: there is a very pronounced slope.

There are two possible explanations for this, at least at the front end where the

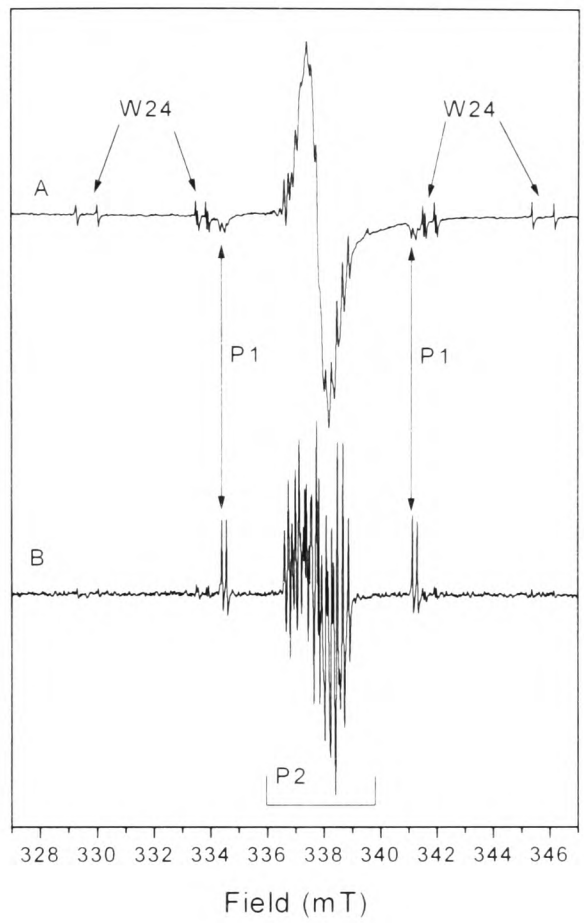

Figure 7.20: Spectra of defects in sample used to image $[N–N]^+$. (B) is recorded at a microwave power 30 dB lower than (A). Low field W24 lines in (A) used for imaging. Spectra recorded at 5 K. W24 is $[N–N]^+$, P1 is N_S^0.

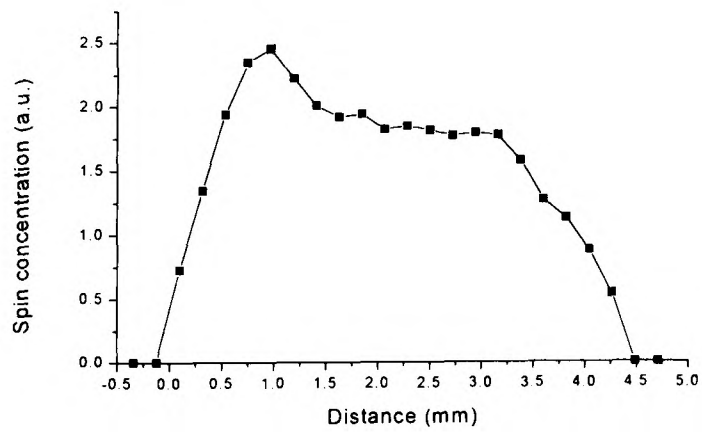

Figure 7.21: Spin distribution of $[N–N]^+$ through sample

light enters the sample:

1. The amount of energy dissipated in the first few hundred microns of the sample heats that small region to such a temperature that the EPR sensitivity is greatly reduced. At 5 K the thermal conductivity and heat capacity of diamond are low, so this is a physically reasonable situation.

2. The field gradient is not purely in the x-direction—there is a component along the z-direction as well.

The fact that there is a slope at both ends points to the second explanation, so the field was measured at various points between the coils using a proton NMR probe, and it was found that the field gradient was at an angle of more than 15° to the x-direction. This made the spin distribution much harder to analyse, but a first guess in such a case would be that the intensity falls off exponentially in the direction of the light.

In this case we need to check to see if our distribution agrees with this hypothesis. Let the spin distribution through the sample of width w and length l be a function of z and x, f(z, x) and assume the field gradient is at an angle θ to the x direction. If all the y–z planes have the same spin concentration we need only consider the x–z plane, and strips through it. The distribution in the x-direction is given by

$$P(x) = \int_0^w f(z, x)\,\mathrm{d}z \tag{7.11}$$

For a simple exponential,

$$f(z, x) = A\mathrm{e}^{-bx} + k \tag{7.12}$$

But the gradient is in the X-direction, as shown in figure 7.22, at an angle θ to x, and the distribution in this direction is given by

$$S(X) = \int_{Z_1}^{Z_2} g(Z, X)\,\mathrm{d}Z \tag{7.13}$$

The function $g(Z, X)$ is given by

$$g(Z, X) = A\mathrm{e}^{-b(Z\sin\theta + X\cos\theta)} + k \tag{7.14}$$

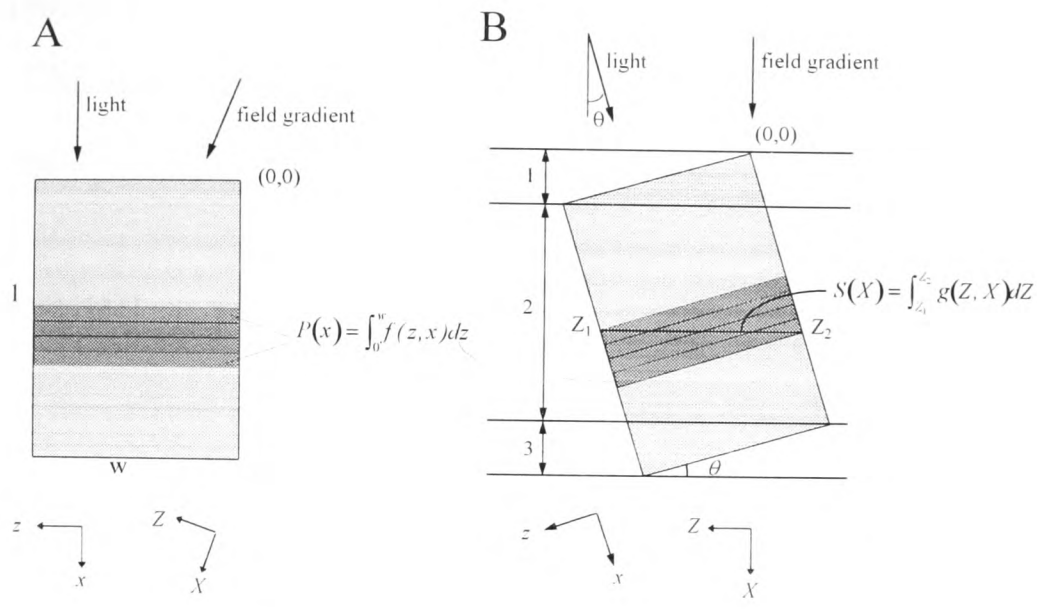

Figure 7.22: Coordinates for illumination and gradient in different directions. (A) shows the orientation of the sample, with the field in the z-direction, and the gradient $\partial B_z/\partial X$. Strips show spin distribution, which is only a function of x. (B) shows the three regions over which analytical integration is possible in the Z-direction, and the way the strips are combined with the gradient in the X-direction.

So

$$S(X) = \int_{Z_1}^{Z_2} k\,\mathrm{d}Z + A\mathrm{e}^{-bX\cos\theta}\int_{Z_1}^{Z_2}\mathrm{e}^{bZ\sin\theta}\,\mathrm{d}Z \tag{7.15}$$

These integrals can be split into three regions and solved analytically in each region (see figure 7.22 above).

For region (1), $0 < X < w\sin\theta$

$$S(X) = kX\sec\theta\csc\theta + \frac{A}{b\sin\theta}(1-\mathrm{e}^{-bX\sec\theta}) \tag{7.16}$$

For region (2), $w\sin\theta < X < l\cos\theta$

$$S(X) = kw\sec\theta + \frac{A}{b\sin\theta}(\mathrm{e}^{bw\tan\theta}-1)\mathrm{e}^{-bX\sec\theta} \tag{7.17}$$

For region (3), $l\cos\theta < X < w\sin\theta + l\cos\theta$

$$S(X) = k(w\sec\theta + l\csc\theta - X\sec\theta\csc\theta) + \frac{A}{b\sin\theta}(\mathrm{e}^{bw\tan\theta - bX\sec\theta}-\mathrm{e}^{-bl}) \tag{7.18}$$

If the distribution of the $[\mathrm{N}\text{–}\mathrm{N}]^+$ is modelled like this a reasonable fit to the spin distribution is obtained. It is also possible to generate the spin distribution like this

from scratch, convolve it with the W24 lineshape and compare directly with the experimental data. The spin distribution determined in this way from the experimental data is shown in figure 7.23.

7.8.5 Discussion

The measurements described above are consistent with a distribution of $[N–N]^+$ in the form of a single exponential fall-off through the sample. This is physically reasonable, and the parameters obtained (given in figure 7.23) are also reasonable.

However, because of the basic nature of the experiment, it is not possible to say that this is unambiguously the case. What we have shown is that there is a fall-off through the sample, and that it is realistic to attempt to measure this distribution in more detail using better coils. There are many questions to be answered here: how does the spatial behaviour of W24 vary with the wavelength of the light? How does it vary with the absorption of the light by other defects (e.g. P1, W21)? How does it vary with temperature?

In short, this could become another tool in correlating optical and EPR data, and is potentially very useful in probing the nature of defects which are so far not understood.

7.9 Imaging—where to go from here

The experiments described in this chapter have largely been of an exploratory nature, to determine what is and is not likely to be possible using this technique. None of the published experiments using EPR imaging have attempted to determine the distributions of defects within single samples to anything like the 20 μm resolution that we have achieved. The limitations we have come up against can be summarised by three points:

1. The sensitivity of the resonator has been the limiting factor in all experiments where the dimensions of the sample are large or the concentrations of the defects

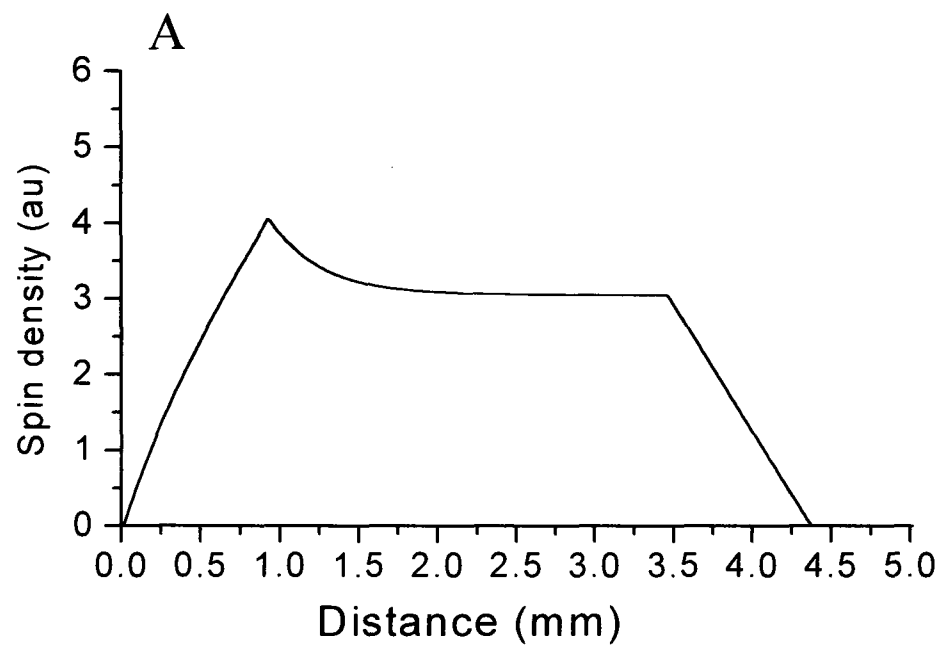

Figure 7.23: $[N–N]^+$ distribution in sample. (A) shows fit to experimental data, i.e. spin distribution in direction of field gradient. (B) shows spin distribution in direction of light with parameters determined in (A): $S(x) = Ae^{-bx} + k$.
$A = 0.9, \quad b = 3\,\mathrm{mm}^{-1}, \quad k = 0.9.$
Tucker [21] predicted $b = 0.7\,\mathrm{mm}^{-1}$, $k = 0$.

being examined have been small. This limits the size of gradient that we can use and thus the resolution.

2. The highest gradient we obtained using water cooled coils was 1.3 mT mm^{-1}. For higher resolution of defects having broad EPR lines, a higher gradient is required, without compromising homogeneity.

3. The gradient has only been in the z-direction, and for many experiments homogeneous $\partial B_z/\partial x$ gradients are needed.

These are limitations of the particular experimental setup that we used, and can, to a certain extent, be overcome.

Resonator sensitivity

The loop–gap resonators that we used gave a more homogeneous microwave field than the equivalent TE_{102} cavities and and a comparable sensitivity. However, if the central loop was much smaller the sensitivity would be increased by up to an order of magnitude. For room temperature experiments this would not be a problem, but to do any experiments at lower temperatures a liquid nitrogen bath would have to be built. Another possibility is to do the experiments at Q-band (35 GHz). The higher frequency results in a further increase in sensitivity, although the maximum sample size is then greatly reduced.

Maximum gradient

We used water-cooled coils designed and wound in the Clarendon. They were designed around the resonator we used, and in particular the gap between them could be greatly reduced with a smaller resonator. Cooling the coils by passing liquid nitrogen rather than water through them was tried, and it was found that the gradient could be increased by a factor of two for a short period of time, although this was rather dangerous! If the coils were designed to be cooled with liquid nitrogen it is realistic that gradients of 4–5 mT mm^{-1} could be achieved.

Gradient direction

Coils with a gradient of the Zeeman field in the x-direction were described in §7.8.3. However, these coils were very rudimentary, having been wound with no expertise in a hurry to do a specific job. They also had a problem with inhomogeneity, in that the field gradient was not, as originally thought, purely in the x-direction, but at an angle of $\sim 15°$ to it. However, again it was shown to be possible, and it is realistic to imagine nitrogen cooled coils generating a $\partial B_z/\partial x$ gradient of 1 mT mm^{-1}, either as part of a setup including $\partial B_z/\partial z$ coils or as a separate unit. These are particularly important for examining the distribution of defects excited by illumination, and also give the possibility of examining the three-dimensional distribution of defects in samples. Figure of eight coils and saddle coils are standard in many NMR imaging experiments, and some low frequency EPR experiments [203, 204, 205].

7.10 Conclusions

Although this chapter has mainly been about the experimental techniques of imaging, and its possible applications, there are still some definite conclusions to be drawn:

- The distribution of N_S^0 through the thickness of polycrystalline films can be determined to a resolution of 20 μm, enabling its role in the growth processes of such films to be studied further.

- The distribution of N_S^0 and defects with g=2.0028 through the thickness of a film are different, showing that they occur in different regions.

- The g=2.0028 defect is found in the "black" part of a CVD film, where there is a high proportion of non-diamond material, adding more evidence to the hypothesis that it is either decorating grain boundaries or actually in the intergranular material.

- The two-dimensional distribution of defects in a diamond can be determined to a resolution of at least 100 μm: with higher gradients this resolution will be improved.

While much further work is needed, the groundwork has now been done, and many of the problems associated with the experimental setup and analysis of the data have been solved.

Appendix A

Data collection, convolution and fitting software

A.1 Data Collection

The changes made to the data collection software are outlined in §4.5.1. Essentially, the program alternately increments the magnetic field by one step (defined as Sweep width / 4096) and collects a data point. The program *ESRnew5* below determines what action to take : if a key is pressed some aspect of the setup is changed, otherwise it runs the data collection loop. All programs are in Borland Pascal.

```
program esrnew5;
{Version 1.1   28th November 1996}

uses
       Dos, Crt, Graph, DullBits, Printer, ESRPro5;

begin
   HerculesInitialise;
   Welcomescreen(version,'collects your EPR Spectra','28 November 1996');
   UserPath;
   IEEEinitialise(7);
        readyflag := false; runflag :=false; WaitTune :=true;
        MenuLine;
   ResetRunParamDefaults1;
   while keypressed do firstkey := ReadKey;

   repeat
      StatusLine(RunFlag);
      Keyhandle(FirstKey);                                    {Control of spectrometer}
                case FirstKey of
         'G','g' : Go;
         'S','s' : begin        {Make this the last scan}
```

```
                  waitanykey('Are you sure this is to be the last scan?',escapeflag,centre);
                  if not(escapeflag) then ScanLimit := ScanNumber;
               end;
      'L','l' : begin                                                {Make this the last angle}
                  waitanykey('Are you sure this is to be the last angle?',escapeflag,centre);
                  if not(escapeflag) then AngleScanLimit := AnglescanNo;
               end;
      'W','w' : begin                                                {Pause to retune spectrometer}
                  waitanykey('Wait after next goniometer turn?',escapeflag,centre);
                  if not (escapeflag) then WaitTune := false;
               end;
      'M','m' : ManGonimove;                                         {Rotate sample}
      'F','f' : Manfieldset;                                         {Set magnetic field}
      'P','p' : pause;
      'R','r' : ResetRunParameters;
      'D','d' : DataSave;
      'Q','q' : finish;
      #224{up}: ResetY(ymax*2);                                      {Rescale screen}
      #225{dn}: ResetY(ymax/2);
    end;
    if RunFlag then DataCollect;                                     {Collect data point}
  until false;
end.
```

The main portion of the program is contained in the unit *ESRpro5*. This contains all the procedures called from the program above and controls the interface between the computer and the different parts of the spectrometer.

```
unit ESRpro5;

interface

uses
        Dos, Crt, graph, dullBits, Printer ;

type
       ud=(up,down);

var
   direction                                                : ud;
   path                                                     : string;
   hour, min, sec, sec100                                   : word;
   FirstKey                                                 : char;
   YearStr,MonthStr,DayStr                                  : string;
   timestr, oldtimestr                                      : string[8];
   AutoFilename                                             : string;
   Datapointerstr                                           : string;
   CentreFieldoutStr                                        : string;
   CentreFieldStr,SweepFieldStr,directionstr,PSDSensOutStr  : string;
   StartFieldStr,EndFieldStr,ModFreqStr,SweepFieldOutStr    : string;
   SampleNumberStr,ScanLimitStr, FieldStepStr,ModLevelOutStr : String;
   FieldStr,ModLevelStr,PSDSensStr,TimeConstStr,ReadFieldStr : String;
   TimeConstOutStr,ModFreqOutStr,scanNumberstr,microfreqstr : string;
   AngVarStr,AngleScanLimitStr,AngleStr                     : string;
   RunFlag, ReadyFlag, Datasavedflag, WaitTune              : boolean;
   channel, lsb, hsb                                        : byte;
   ReadField,Field, CentreField,ModFreq,PSDSens,ModLevelNew : real;
   Sweepfieldout,StartField, EndField, FieldStep,PSDSig     : real;
   MaximumPSDSig, MinimumPSDSig,Ymax, Yzero, ModLevel       : real;
   Angle,AngVar,BeginAngle                                  : real;
   SampleNumber,DataPointer,DataPointerMax,ModLevelOut      : integer;
   SweepField, ScanNumber, ScanLimit,TimeConst              : integer;
```

```
   AngleScanNo,AngleScanLimit                                    : integer;
   CentreFieldout                                                : longint;
   Microfreq                                                     : array[1..1000] of single;

const
   ConfigFileName = 'config.txt';
   MenuPort : ViewPortType = (x1:0; y1:301; x2:719; y2:347; clip:clipon);
   Centre : boolean = true;
   GainLevels : array[1..2] of integer = (200,2000);
   tone : integer = 400;        {400Hz ref for sounds!!!}
   version : string = 'EPR v1.1';
   MaxNumPoints : integer = 4096;
      {This number should match the dimension of type Datalist below}

type
   DataList = array[1..4096,1..3] of single;
var
   ESRData : DataList;

procedure StatusLine(NotTimeOnly : boolean);
procedure MenuLine;
procedure ResetRunParamDefaults1;
procedure ResetRunParameters;
procedure ResetY(ym : real);
procedure DataCollect;
procedure datasave;
procedure datasave2;
procedure finish;
procedure go;
procedure pause;
procedure userpath;
procedure saveparamdefaults;
procedure ManFieldSet;
Procedure ManGoniMove;
function  readieee : string;
function  readhpfreq : real;

implementation

{*************************************************************************}

procedure SetRunFlag(flag : boolean);                          {Determines whether or not}
                                                                data is being collected. }
begin
   if (flag = true) and (ReadyFlag = false) then exit;
   RunFlag := Flag;
   ViewBox(650,304,716,318);
   ClearViewPort;
   if RunFlag = true then begin
      OutTextXY(4,12,'RUNNING');                               {Outputs information to screen}
      Datasavedflag:=false;
   end else
      OutTextXY(4,12,'STOPPED');
   ResetGraphArea;
end;

{*************************************************************************}

procedure SetReadyFlag(flag : boolean);                        {Checks to see whether ready}
                                                               {to start collecting data   }
begin
   ReadyFlag := Flag;
   ViewBox(570,304,645,318);
   ClearViewPort;
   if ReadyFlag = true then
```

```
      OutTextXY(8,12,'READY')
   else
   begin
      OutTextXY(2,12,'NOT READY');
      setrunflag(false);
   end;
   ResetGraphArea;
end;

{*****************************************************************************}

procedure saveparamdefaults;                                    {Saves having to retype every}
var configfile : text;                                          {time you load the program   }
begin
 assign(configfile,path+configfilename);
 rewrite(configfile);
 writeln (configfile,Centrefieldstr);                           {Field at centre of sweep}
 writeln (configfile,SweepFieldstr);                            {Sweep width}
 writeln (configfile,Directionstr);                             {Sweep direction}
 writeln (configfile,SampleNumberstr);                          {Number of averages per point}
 writeln (configfile,ScanlimitStr);                             {Number of scans}
 writeln (configfile,ModLevelstr);                              {Field modulation}
 writeln (configfile,PSDSensstr);                               {PSD sensitivity}
 writeln (configfile,TimeConststr);                             {PSD time constant}
 writeln (configfile,ModFreqstr);                               {Field modulation frequancy}
 writeln (configfile,AngleScanLimitStr);                        {Number of orientations}
 writeln (configfile,AngVarStr);                                {Angle between orientations}
 writeln (configfile,AngleStr);                                 {Angle on goniometer}
 Close (configfile);
end;

{*****************************************************************************}

procedure finish;                                               {Leaves program, checking if}
                                                                {you have unsaved data      }
begin
   If datasavedflag=false then begin
     waitanykey('Do you want to save data first?, <ESC> if no',Escapeflag,false);
     If escapeflag=false then datasave;
   end;
   WaitAnyKey('Press any key to go to DOS or <esc> to continue',EscapeFlag, false);
   if not(escapeflag) then
   begin
      saveparamdefaults;
      CheckIEEEPresence;
      rewrite(ieeedata);                                        {Close down I/O to GPIB interface}
      close(ieeedata);
      rewrite(ieeectrl);
      close(ieeectrl);
      textmode(7);
      halt;
   end
   else
      setrunflag(false);
end;

{*****************************************************************************}

procedure StatusLine;                                           {plots time, field, mw freq and}
                                                                {datapointer in menuline box   }
var
   Xmark : integer;
   Ystr, OutStr1, OutStr2, ScanNumberStr : string;
   Hourstr, minstr, secstr : string[2];

const
```

```
   x1 : word = 100;
   y1 : word = 304;

begin
   if NotTimeOnly then                                          {this only occurs when RunFlag=true}
   begin                                                        {i.e. data is being collected      }
      ViewBox(x1,y1,x1+465,y1+14);
      ClearViewPort;

      str((DataPointer):4,DataPointerStr);
      str(PSDSig:5:0,Ystr);
      str(scannumber:2,ScanNumberStr);
      str(microfreq[scannumber]:7:3,microfreqstr);
      OutStr1 := concat({TimeStr}microfreqstr,'MHz',' Scan=',ScanNumberStr,'   ',datapointerstr,' points');
      OutStr2 := concat(' Field=',FieldStr,'G ','y=',Ystr);             {Outputs the values to screen}
      OutTextXY(2,12,outstr1+outstr2);

      SetViewPort(1,320,719,330,ClipOn);
      SetLineStyle(SolidLn,0,ThickWidth);
      Xmark := round(abs(Field-StartField)/(SweepField)*718 );
      Line( Xmark,0,Xmark,10 );
      SetLineStyle(SolidLn,0,NormWidth);
   end
   else
      if oldtimestr <> timestr then
      begin
         SetViewPort(101,305,170,317,ClipOn);
         ClearViewPort;
         OutTextXY(2,12,TimeStr);
         oldtimestr := timestr;
      end;
   ResetGraphArea;
end;

{*************************************************************************}
procedure MenuLine;                                             {Writes available options to screen}
{this takes approx 0.1 sec}

const
   Str1 : string = '[G]o [P]ause [R]eset [L]ast [F]ield Goni[M]ove [';
   Str2 : string = ']scale [S]top [W]ait Save_[D]ata [Q]uit';

begin
   ViewBox2(MenuPort);
   clearviewport;
   OutTextXY(5,15,Version);
   OutTextXY(5,40,str1+chr(24)+chr(25)+str2);
   SetReadyFlag(ReadyFlag);
   SetRunFlag(RunFlag);
   ResetGraphArea;
end;

{*************************************************************************}


procedure GetStatus;                                            {This is a procedure that gets  }
                                                                {the IEEE bus status into status}
   var
      loose  : string[12];
      status : string[2];
      InByte : char;

   begin
      Reset(ieeectrl);
      Read(ieeectrl,loose,status);
```

```
      IF status <> '00' then InByte := Chr(13); {terminate on EOI or Badst}
   end;


{*************************************************************************}

function readieee:string;                                    {Gets in the information from     }
                                                             {IEEE eg from freq counter and PSD}
var
  count:WORD;
  instr:string;
  Binstr:char;

begin
  Reset(ieeedata); instr:=''; count:=0;
  Repeat
    read(ieeedata,Binstr);                                   {Rather complex series of commands in an }
    If (Binstr<>Chr(10)) and (Binstr<>Chr(13)) then          {effort to avoid errors in importing data}
    instr := instr + Binstr; {add new byte in}
    count :=count +1;  {bump the count}
    IF count = 255 THEN Binstr :=Chr(13);  {Terminate On Buffer Full}
    {GetStatus;  { Terminate on EOI, Timeout or No Device Present}
  UNTIL Binstr = Chr(13);
  readieee:=instr;
end;

{*************************************************************************}

Function ReadHPFreq;                                         {Reads microwave frequency from   }
                                                             {Hewlett-Packard frequency counter}
var
  readinga,readingb : string;
  ir,code           : integer;
  readingc          : real;
Begin
  rewrite(IEEEctrl);
  writeln(ieeectrl,1);
  rewrite(ieeedata);
  writeln(ieeedata,'SR6');
  writeln(ieeedata,'T0');
  writeln(ieeedata,'ST1');
  readinga := readieee;
  readingb := '';
  ir:=0;
  repeat                                                     {Renders jumbled number into a useful form}
    inc(ir);
    if (readinga[ir]=' ') or (readinga[ir]='F') then readinga[ir]:='0';
    readingb := readingb + readinga[ir];
  until readinga[ir]='E';
  readingb := copy(readingb,1,length(readingb)-1);
  val (readingb,readingc,code);
  ReadHpFreq := readingc;
  rewrite(ieeedata);
  writeln(ieeedata,'T0');
  rewrite(ieeectrl);
  writeln(ieeectrl,'LOCAL 1');
End;

{*************************************************************************}

procedure ResetRunParamDefaults2;                            {Sets up parameters at beginning.}

var ii : integer;

begin
   DataPointer := 1;
```

```
   DataPointerMax := 1;
   ScanNumber := 1;
   Anglescanno := 1;
   OldTimeStr := '';
   SetRunFlag(False);
   Ymax := 1000;
   Yzero := 0;
   MaximumPSDSig :=-15000;
   MinimumPSDSig := 15000;
   For ii := 1 to 1000 do microfreq[ii] := 0;
end;


procedure ResetRunParamDefaults1;                    {Gets parameters from configuration}
                                                     {file when program is loaded in.   }
var configfile : text;                               {If no configuration file then use }
begin                                                {the defaults below.               }
   DataSavedFlag:=True;
   SetReadyFlag(False);
   FieldStr := '......';
 {$I-}
 Assign(configfile, path+configFileName);
 Reset(configFile);
 Close(configFile);
 {$I+}
 if IOResult=0 then begin
   Reset (configfile);
   Readln (configfile,Centrefieldstr);
   Readln (configfile,SweepFieldstr);
   Readln (configfile,Directionstr);
   Readln (configfile,SampleNumberstr);
   Readln (configfile,ScanlimitStr);
   Readln (configfile,ModLevelstr);
   Readln (configfile,PSDSensstr);
   Readln (configfile,TimeConststr);
   Readln (configfile,ModFreqStr);
   Readln (configfile,AngleScanLimitStr);
   Readln (configfile,AngVarStr);
   Readln (configfile,AngleStr);
   Close (configfile);
  end else begin  {I.e. no configfile found}
   CentreFieldStr := '3400';
   SweepFieldStr := '200';
   DirectionStr :='up';
   SampleNumberStr := '1';
   ScanLimit := 10;
   ScanLimitStr := '10';
   ModLevelStr := '0.75';
   PSDSensStr := '1';
   TimeConstStr := '300';
   ModfreqStr := '115';
   AngVarStr := '5';
   AngleScanLimitStr := '1';
   AngleStr := '0';
 end;
   ResetRunParamDefaults2;
end;

{*****************************************************************************}

procedure ResetRunParameters;                        {This is called when R is pressed,     }
                                                     {and sets up every parameter imaginable}
var
   code : integer;

const
```

```
   Rport : ViewPortType = (x1:170; y1:50; x2:420; y2:200; clip:clipon);
   xoff1 : byte = 5;
   xoff2 : byte = 140;
   xoff3 : byte = 220;
   CFy : byte = 30;
   FSy : byte = 40;
   SDy : byte = 50;
   NAy : byte = 60;
   NSy : byte = 70;                                          {Positions of lines within box}
   MLy : byte = 80;                                          {on screen in which parameters}
   PSy : byte = 90;                                          {are displayed                 }
   TCy : byte = 100;
   MFy : byte = 110;
   ANy : byte = 120;
   AVy : byte = 130;
   PAy : byte = 140;

procedure txt(str1,str2,str3 : string; y:byte);
   begin
      OutTextXY(xoff1,y,str1);
      OutTextXY(xoff2,y,str2);                               {Making the ouput of lines easier}
      OutTextXY(xoff3,y,str3);
   end;

procedure edtreal(var str : string; var num : real ; pos:byte);
   begin
      repeat
         Str := EditString(xoff2+rport.x1,pos-10+rport.y1,xoff2+rport.x1+70,pos+3+rport.y1,Str,6,10);
         val(Str,num,code);
      until code = 0;                                        {Overwrites existing number, ending}
   end;                                                      {up with a number and a string     }

procedure edtint(var str : string; var num : integer ; pos:byte);
   begin
      repeat
         Str := EditString(xoff2+rport.x1,pos-10+rport.y1,xoff2+rport.x1+70,pos+3+rport.y1,Str,6,10);
         val(Str,num,code);
      until code = 0;
   end;

begin
   If datasavedflag=false then begin
     waitanykey('Do you want to save data first?, <ESC> if no',Escapeflag,false);
     If escapeflag=false then datasave;
   end;
   with rport do
   begin
      pop_up(rport,295,330);                                 {Make box and write  }
      txt('SETTING RUN PARAMETERS...','','',10);             {parameters to screen}
      txt('Centre Field',CentreFieldStr,'G',CFy);
      txt('Field Sweep',SweepFieldStr,'G',FSy);
      txt('Sweep Direction',directionstr,'',SDy);
      txt('No. of averages',SampleNumberStr,'',NAy);
      txt('Number of Scans',ScanLimitStr,'',NSy);
      txt('Modulation level',ModLevelStr,'V',MLy);
      txt('PSD Sensitivity',PSDSensStr,'mV',PSy);
      txt('Time Constant',TimeConstStr,'ms',TCy);
      txt('Mod freq',ModFreqStr,'kHz',MFy);
      txt('Number of angles',AngleScanLimitStr,'',ANy);
      txt('Angle step',AngVarStr,'deg',AVy);
      txt('Present angle',AngleStr,'deg',PAy);

                                                             {Change parameters, keeping them}
      repeat                                                 {within allowed constraints     }
         repeat
           edtreal(CentreFieldStr,CentreField,CFy);          {Field for controller}
```

```
   until (CentreField>0) and (CentreField<12000);
   repeat
     edtint(SweepFieldStr,SweepField,FSy);
   until ((SweepFieldStr[2]='0') or (SweepField<10))                {Sweep width}
     and ((SweepField<=10000) and (Sweepfield>0));
until ((CentreField+SweepField/2)<=12000) and ((CentreField-SweepField/2)>=0);
repeat
   directionstr := EditString(xoff2+rport.x1,SDy-10+rport.y1,xoff2+rport.x1+70,SDy+3+rport.y1,directionstr,6,1
until (((directionstr='UP') or (directionstr='DOWN'))
   or ((directionstr='U') or (directionstr='D')))                   {Sweep direction}
   or (((directionstr='up') or (directionstr='down'))
   or ((directionstr='u') or (directionstr='d')));
repeat
   edtint(SampleNumberStr,SampleNumber,NAy);                        {No. of averages}
until (SampleNumber > 0) and (sampleNumber <= 100);
repeat
   edtint(ScanLimitStr,ScanLimit,NSy);
until (ScanLimit > 0) and (ScanLimit < 1000);                       {No. of scans}
repeat
   Modlevel := 0;
   edtreal(ModLevelStr,ModLevel,MLy);                               {Field modulation}
until (ModLevel>=0.001) and (ModLevel<=2);
repeat
   edtreal (PSDSensStr,PSDSens,PSy);
until ((((PSDSensStr='0.0001') or (PSDSensStr='0.0003')) or ((PSDSensStr='0.001') or (PSDSensStr='0.003')))
    or (((PSDSensStr='0.01') or (PSDSensStr='0.03')) or ((PSDSensStr='0.1') or (PSDSensStr='0.3'))))
   or ((((PSDSensStr='1')    or (PSDSensStr='3'))    or ((PSDSensStr='10')   or (PSDSensStr='30')))
    or (((PSDSensStr='100')  or (PSDSensStr='300'))  or ((PSDSensStr='1000') or (PSDSensStr='3000'))));
repeat                                                              {PSD sesnsitivity}
   edtint (TimeConstStr,TimeConst,TCy);
until ((((TimeConst=1e0) or (TimeConst=3e0)) or ((TimeConst=1e1) or (TimeConst=3e1)))
   or  (((TimeConst=1e2) or (TimeConst=3e2)) or ((TimeConst=1e3) or (TimeConst=3e3))))
   or   ((TimeConst=1e4) or (TimeConst=3e4));                       {Time constant}
repeat
   edtreal (ModFreqStr,ModFreq,MFy);                                {Modulation frequency}
   until (ModFreq>=100) and (ModFreq<=120);
   repeat
      edtint (AngleScanLimitStr,AngleScanLimit,ANy);                {No. of orientations}
   until (AngleScanLimit>=1) and (AngleScanLimit<=720);
   repeat
      edtreal (AngVarStr,AngVar,AVy);                               {Angle between orientations}
   until (AngVar>=0.03) and (AngVar<=360/AngleScanLimit);
   repeat
      edtreal (Anglestr,Angle,PAy);                                 {Present angle on goniometer}
   until (Angle>=0) and (Angle<360);
end;
                                                                    {The following sorts the parameters}
CentreFieldout := Trunc(CentreField*10);                            {into forms acceptable to the IEEE }
CentreFieldoutStr := '';
Str(CentreFieldout:0,CentreFieldoutStr);
If  CentreFieldout<10 then CentreFieldoutStr := '00000'+CentrefieldoutStr;
If (CentreFieldout>=10) and (Centrefieldout<100) then CentreFieldoutStr := '0000'+CentrefieldoutStr;
If (CentreFieldout>=100) and (CentreFieldout<1000) then CentreFieldoutStr := '000'+CentrefieldoutStr;
If (CentreFieldout>=1000) and (CentreFieldout<10000) then CentreFieldoutStr := '00'+CentrefieldoutStr;
If (CentreFieldout>=10000) and (Centrefieldout<100000) then CentreFieldoutStr := '0'+CentrefieldoutStr;
SweepFieldOutStr := '';
If SweepField<10 then SweepFieldOutStr := SweepFieldStr[1]+'E'+'-1';
If (SweepField>=10) and (SweepField<100) then SweepFieldOutStr := SweepFieldStr[1]+'E'+'0';
If (SweepField>=100) and (SweepField<1000) then SweepFieldOutStr := SweepFieldStr[1]+'E'+'1';
If (SweepField>=1000) and (SweepField<10000) then SweepFieldOutStr := SweepFieldStr[1]+'E'+'2';
If SweepField=100000 then SweepFieldOutStr := SweepFieldStr[1]+'E'+'3';
Case upcase(directionstr[1]) of
  'U' : begin
        direction:=up;
        StartField := CentreField-SweepField/2;
        EndField := CentreField+SweepField*(2047/4096);
```

```
        Str(startField,startFieldStr);
        Str(endField,endFieldStr);
        FieldStep := SweepField/4096;
       end;
  'D' : begin
        direction:=down;
        StartField := CentreField+SweepField*(2047/4096);
        EndField := CentreField-SweepField/2;
        Str(startField,startFieldStr);
        Str(endField,endFieldStr);
        FieldStep := -SweepField/4096;
       end;
end;
Str(FieldStep,FieldStepStr);
Field := startField;
ModLevelNew := ModLevel*1000;
Modlevelout := Round(ModlevelNew);
Modleveloutstr := '';
Str(Modlevelout,Modleveloutstr);
If ModLevelOut<10 then ModlevelOutStr:='000'+ModLevelOutStr;
If (ModlevelOut>=10) and (ModLevelOut<100) then ModLevelOutStr:='00'+ModLevelOutStr;
If (ModlevelOut>=100) and (ModLevelOut<1000) then ModLevelOutStr:='0'+ModLevelOutStr;
If PSDSensStr = '0.0001' then PSDSensoutStr := '0';
If PSDSensStr = '0.0003' then PSDSensoutStr := '1';
If PSDSensStr = '0.001' then PSDSensoutStr := '2';
If PSDSensStr = '0.003' then PSDSensoutStr := '3';
If PSDSensStr = '0.01' then PSDSensoutStr := '4';
If PSDSensStr = '0.03' then PSDSensoutStr := '5';
If PSDSensStr = '0.1' then PSDSensoutStr := '6';
If PSDSensStr = '0.3' then PSDSensoutStr := '7';
If PSDSensStr = '1' then PSDSensoutStr := '8';
If PSDSensStr = '3' then PSDSensoutStr := '9';
If PSDSensStr = '10' then PSDSensoutStr := '10';
If PSDSensStr = '30' then PSDSensoutStr := '11';
If PSDSensStr = '100' then PSDSensoutStr := '12';
If PSDSensStr = '300' then PSDSensoutStr := '13';
If PSDSensStr = '1000' then PSDSensoutStr := '14';
If PSDSensStr = '3000' then PSDSensoutStr := '15';
Case timeConst of
  1 : TimeConstOutStr := '0';
  3 : TimeConstOutStr := '1';
  10 : TimeConstOutStr := '2';
  30 : TimeConstOutStr := '3';
  100 : TimeConstOutStr := '4';
  300 : TimeConstOutStr := '5';
  1000 : TimeConstOutStr := '6';
  3000 : TimeConstOutStr := '7';
  10000 : TimeConstOutStr := '8';
  30000 : TimeConstOutStr := '9';
end;
Str(ModFreq*10:0,ModFreqoutStr);
Beginangle := angle;

rewrite(ieeectrl);                                          {Output parameters to field controller}
writeln(ieeectrl,7);
rewrite(ieeedata);
writeln(ieeedata,'WCF',CentreFieldoutStr);
writeln(ieeedata,'WSW',SweepFieldOutStr);
If direction=up then writeln(ieeedata,'WSPD') else writeln(ieeedata,'WSPU');
writeln(ieeedata,'WSM4');
rewrite(ieeectrl);
writeln(ieeectrl,12);                                       {Parameters to PSD}
writeln(ieeectrl,'CLEAR12');
rewrite(ieeedata);
delay(500);
writeln(ieeedata,'OA',ModLevelOutStr);
```

```
   delay(500);
   writeln(ieeectrl,'CLEAR12');
   delay(500);
   writeln(ieeedata,'SEN',PSDSensOutStr);
   delay(500);
   writeln(ieeectrl,'CLEAR12');
   delay(500);
   writeln(ieeedata,'XTC',TimeConstOutStr);
   delay(500);
   writeln(ieeectrl,'CLEAR12');
   delay(500);
   writeln(ieeedata,'FF1150,4'{,ModFreqOutStr,',4'});
   delay(500);
   writeln(ieeectrl,'CLEAR12');
   delay(500);
   writeln(ieeedata,'OF11500,5'{,ModFreqOutStr,'0,5'});
   delay(500);
   writeln(ieeectrl,'CLEAR12');
   delay(500);
   writeln(ieeedata,'OUTFF1');
   SetReadyFlag(True);
   ResetRunParamDefaults2;
   pop_off;
   Menuline;
end;

{*************************************************************************}
Procedure GoniMove(AngleMove:real; wait:integer);
                                                          {Move goniometer. More complicated than }
Var startangle,stopangle : real;                          {strictly necessary in order to allow   }
                                                          {the exact angle moved to be known and  }
begin                                                     {recorded. 0.03 arises because 12000    }
  Startangle := angle;                                    {steps in 360 deg. Angle and Anglestr   }
  Stopangle := angle;                                     {are global variables that are known all}
  If Anglemove > 0 then begin                             {the time.                              }
    Repeat
      Port[$378] := 255;                                  {Write pulses to LPT1}
      Delay(wait);
      Port[$378] := 0;
      Delay(wait);
      Stopangle := Stopangle + 0.03;
    Until Stopangle-Startangle >= AngleMove;
    Angle := Stopangle;
  end;
  If Anglemove < 0 then begin
    Repeat
      Port[$378] := 255;
      Delay(wait);
      Port[$378] := 0;
      Delay(wait);
      Stopangle := Stopangle - 0.03;
    Until Stopangle-Startangle <= AngleMove;
    Angle := Stopangle;
  end;
  If angle>=360 then angle:= angle-360;
  If angle<0 then angle := angle+360;
  Str(angle:6:2,anglestr);
end;

{*********************************************************}

Procedure ManFieldSet;                                    {Allows field to be set manually}
const
   Rport : ViewPortType = (x1:170; y1:50; x2:420; y2:200; clip:clipon);
   xoff1 : byte = 5;
   xoff2 : byte = 140;
```

```
   xoff3 : byte = 220;

var
   ManFieldStr,ManFieldOutStr : string;
   ManField    : real;
   ManFieldOut : longint;
   code        : integer;

procedure edtreal(var str : string; var num : real ; pos:byte);
   begin
      repeat
         Str := EditString(xoff2+rport.x1,pos-10+rport.y1,xoff2+rport.x1+70,pos+3+rport.y1,Str,6,10);
         val(Str,num,code);
      until code = 0;
   end;

procedure txt(str1,str2,str3 : string; y:byte);
   begin
      OutTextXY(xoff1,y,str1);
      OutTextXY(xoff2,y,str2);
      OutTextXY(xoff3,y,str3);
   end;

begin
  ManFieldStr := CentrefieldStr;
  ManField := Centrefield;
  rewrite(ieeectrl);
  writeln(ieeectrl,7);
  rewrite(ieeedata);
  writeln(ieeedata,'WSPC');                                    {Send field controller}
                                                               {to middle of range   }
  With rport do begin
   pop_up (rport,295,330);
   txt('MANUAL FIELD SETTING','','',10);
   txt('Enter field you want to go to','','',30);
   txt('Field',ManFieldStr,'G',50);
   txt('Enter 0 to exit','','',70);

   repeat                                                      {Render field into form}
     repeat                                                    {acceptable to IEEE    }
      edtreal(ManFieldStr,ManField,50);
     until (ManField>=0) and (ManField<12000);
     If Manfield>0 then begin
       ManFieldout := Trunc(ManField*10);
       ManFieldoutStr := '';
       Str(ManFieldout:0,ManFieldoutStr);
       If  ManFieldout<10 then ManFieldoutStr := '00000'+ManfieldoutStr;
       If (ManFieldout>=10) and (Manfieldout<100) then ManFieldoutStr := '0000'+ManfieldoutStr;
       If (ManFieldout>=100) and (ManFieldout<1000) then ManFieldoutStr := '000'+ManfieldoutStr;
       If (ManFieldout>=1000) and (ManFieldout<10000) then ManFieldoutStr := '00'+ManfieldoutStr;
       If (ManFieldout>=10000) and (Manfieldout<100000) then ManFieldoutStr := '0'+ManfieldoutStr;
       writeln(ieeedata,'WCF',ManFieldoutStr);
     end;
   until Manfield=0;
  end;
  pop_off;
  Menuline;
  SetReadyFlag(False);
end;

{*****************************************************************************}
Procedure ManGoniMove;                                         {Rotate sample}

const
   Rport : ViewPortType = (x1:170; y1:50; x2:420; y2:200; clip:clipon);
   xoff1 : byte = 5;
```

```
   xoff2 : byte = 140;
   xoff3 : byte = 220;

var
  Angmove    : real;
  AngmoveStr : string;
  code,wait  : integer;
  resetangle,waitstr  : string;

procedure txt(str1,str2,str3 : string; y:byte);
   begin
      OutTextXY(xoff1,y,str1);
      OutTextXY(xoff2,y,str2);
      OutTextXY(xoff3,y,str3);
   end;

procedure edtreal(var str : string; var num : real ; pos:byte);
   begin
      repeat
         Str := EditString(xoff2+rport.x1,pos-10+rport.y1,xoff2+rport.x1+70,pos+3+rport.y1,Str,6,10);
         val(Str,num,code);
      until code = 0;
   end;

procedure edtint(var str : string; var num : integer ; pos:byte);
   begin
      repeat
         Str := EditString(xoff2+rport.x1,pos-10+rport.y1,xoff2+rport.x1+70,pos+3+rport.y1,Str,6,10);
         val(Str,num,code);
      until code = 0;
   end;

begin
  Resetangle := 'N';
  AngMoveStr := AngVarStr;
  WaitStr := '5';
  With rport do begin
   pop_up (rport,295,330);
   txt('MANUAL GONIOMETER MOVE','','',10);
   txt('Enter angle to turn','','',30);
   txt('Angle',AngMoveStr,'deg',40);
   txt('Enter 0 to exit,','','',60);
   txt('Delay',WaitStr,'mS',80);
   txt('Reset angle to 0?',Resetangle,'',100);
   txt('Present angle',AngleStr,'deg',120);

   repeat
     repeat
       edtreal(AngMoveStr,AngMove,40);
     until (AngMove>-360) and (AngMove<360);
     repeat
       edtint(WaitStr,Wait,80);
     until (Wait>=4) and (Wait<=5000);
     Gonimove(AngMove,Wait);                                    {Call goniometer move procedure}
     txt('Present angle',AngleStr,'deg',120);
   until AngMove=0;
   repeat
     Resetangle := EditString(xoff2+rport.x1,100-10+rport.y1,xoff2+rport.x1+70,100+3+rport.y1,resetangle,6,10);
   until (upcase(resetangle[1])='Y') or (upcase(resetangle[1])='N');
   if upcase(resetangle[1]) = 'Y' then begin angle := 0; anglestr:='0'; end;
  end;
  pop_off;
  Menuline;
  SetReadyFlag(ReadyFlag);
  SetRunFlag(false);
end;
```

```
{*************************************************************************}

procedure ResetY(Ym : real);                                    {Screen reset. Although this takes}
                                                                {finite time, nothing else is     }
var                                                             {happening in the meantime        }
   PlotP, xpos, ypos : integer;
   ymaxstr : string;

begin
   ymax := ym;
   yzero := (maximumPSDSig+minimumPSDSig)/2;

   resetgrapharea;
   clearviewport;
   if Datapointermax > 1 then
   begin
      {redraw points}
      for PlotP := 1 to DataPointermax do
      begin
         xpos :=round(abs((ESRData[PlotP,1]-StartField)/(SweepField)*720));
         {xpos :=round(abs(PlotP*720/4096));}
         ypos :=round((ESRData[PlotP,2]-Yzero)/Ymax*150)+150;
         if (ypos > 0) and (ypos < 300) then
            PutPixel(xpos,(300-ypos),1);
      end;
   end;

   str((ymax-yzero):5:1,ymaxstr);
   outtextxy(10,10,ymaxstr);
   str(-(yzero+ymax):5:1,ymaxstr);
   outtextxy(10,290,ymaxstr);
end;

{*************************************************************************}

procedure DataCollect;                                          {Read in data point}

var
   xpos, ypos, ii     : integer;
   readin,tempangvar : real;
   code               : integer;

procedure backup(num : string);                                 {Save backup file}

var
   datafile : text;
   x : longint;
   waitcount : integer;

begin
   setupdate(yearstr,monthstr,daystr);
   assign(datafile,path+'backup'+num+'.dat');
   rewrite(datafile);
   writeln(datafile,'Original Filename : ',anglestr,'deg');
   writeln(datafile,'Number of Points  : ',DataPointerMax);
   Writeln(datafile,'Frequency         : ',microfreqstr,' MHz');
   writeln(datafile,'Number of Scans   : ',ScanNumber);
   for x := 1 to DataPointerMax do
      writeln(datafile,ESRData[x,1]:11:5,'   ',ESRData[x,2]*PSDSens:6:2);
   close(datafile);
end;


begin
```

```
if (datapointer>=MaxNumPoints+1) then                                {ie. if it's time for next scan}
begin
   rewrite(ieeectrl);
   writeln(ieeectrl,7);
   rewrite(ieeedata);
   If direction=up then writeln(ieeedata,'WSPD') else writeln(ieeedata,'WSPU');
                                                                     {return field to initial value}
   if ScanNumber >= ScanLimit then                                   {Correct no. of scans reached}
   begin
      If anglescanno >= anglescanlimit then begin                    {Final angle reached}
        setrunflag(false);                                           {Stop collecting}
        setreadyflag(false);
        sound(100);
        Microfreq[scannumber+1] := ReadHpFreq;
        waitanykey('Finished....press any key to continue',EscapeFlag,centre);
        nosound;
      end
      else
      begin
        setrunflag(false);                                           {End of one scan but}
        setreadyflag(false);                                         {more angles to go  }
        datasave2;
        TempAngVar := beginangle+anglescanno*AngVar-angle;           {Ensures angular errors}
        Gonimove(TempAngVar,5);                                      {do not add up         }
        If Waittune = false then begin
          sound(100);
          waitanykey('Retune spectrometer then press any key',EscapeFlag,centre);
          Waittune := true;
          nosound;
        end;
        inc(anglescanno);
        Scannumber :=0;
        Resetgrapharea;
        ClearViewPort;
      end;
   end
   else
   begin
      Str(scannumber,scannumberstr);                                 {Only backup on perfect squares}
      If sqrt(scannumber)=round(sqrt(scannumber)) then begin
        If scannumber<10 then Backup(scannumberstr[1])
          else Backup(scannumberstr[1]+scannumberstr[2]);
      end;
      inc(scannumber);
      delay(15000);                                                  {let the poor thing catch up!}
      Microfreq[scannumber] := ReadHpFreq;
      datapointermax := datapointer - 1;
      datapointer := 1;

      SetViewPort(5,320,716,330,ClipOn);                             {clear the timer bar}
      clearviewport;
      resetgrapharea;
   end;
   Field := startField;
   str(Field:6:2,FieldStr);
   exit;
end;


rewrite(ieeectrl);                                                   {Actual data collection.}
writeln(ieeectrl,12);                                                {This loop run for each }
PSDSig:=0;                                                           {data point.            }
for ii:= 1 to samplenumber do begin
  val(Readieee,Readin,code);                                         {Average for each point}
  PSDSig:=PSDSig+Readin;
end;
```

```
PSDSig := PSDSig/samplenumber;
if ScanNumber > 1 then
begin
   xpos :=round(abs((Field-StartField)/abs(SweepField)*720));        {erase old point}
   ypos :=round((ESRData[DataPointer,2]-Yzero)/Ymax*150)+150;

   if (xpos >= 0) and (xpos <= 720) and (ypos <= 320) and (ypos >= 0) then
      PutPixel(xpos,(300-ypos),0);

   ESRData[DataPointer,1] := Field;                                  {Scan averaging}
   ESRData[DataPointer,2] := (ESRData[DataPointer,2]*(ScanNumber-1) + PSDSig) / (ScanNumber);
end
else
begin
   ESRData[DataPointer,1] := Field;
   ESRData[DataPointer,2] := PSDSig;
   DataPointerMax := DataPointer;
   if PSDSig > MaximumPSDSig then MaximumPSDSig := PSDSig;
   if PSDSig < minimumPSDSig then minimumPSDSig := PSDSig;
end;

if abs(ESRData[DataPointer,2]-Yzero) > Ymax then ResetY(abs(ESRData[DataPointer,2]-yzero)*1.1);
xpos := round(abs((Field-StartField)/(SweepField)*720));
ypos :=round((ESRData[DataPointer,2]-Yzero)/Ymax*150)+150;

if (xpos < 0) or (xpos > 720) or (ypos > 300) or (ypos < 0) then
                    writeln('error - point off scale on plotting')
else
   PutPixel(xpos,(300-ypos),1);

                                                                  {do the incrementing HERE so}
      inc(DataPointer);                                           {that system has a few ms to}
      Field := StartField + FieldStep * (datapointer - 1);        {stabilise before reading   }
                                                                  {Field CALCULATED   }
str(Field:6:2,FieldStr);                                          {rather than read in}
if Field <> StartField then
   begin
      rewrite(ieeectrl);
      writeln(ieeectrl,7);
      rewrite(ieeedata);
      if direction=up then writeln(ieeedata,'WS+') else writeln(ieeedata,'WS-');
   end;                                                           {Increase field controller by}
end;                                                              {one point                   }

{*****************************************************************************}

procedure datasave;                                               {Save data}

var
   NumPointsToSave, oldday, oldmonth                    : string;
   filename, filenumstr, microstart,microstop, anglestr : string;
   datafile, namefile : text;
   outcount,filenumber : integer;

begin
   ViewBox2(MenuPort);
   ClearViewPort;
   setupdate(yearstr,monthstr,daystr);
   assign(namefile,path+'lastname.txt');
   reset(namefile);
   readln(namefile,oldday);
   readln(namefile,oldmonth);

   if (oldday <> daystr) or (oldmonth <> monthstr) then
      FileNumber := 1
   else
   begin
```

```
   readln(namefile,FileNumber);
   inc(FileNumber);
end;
str(microfreq[1]:7:3,microstart);
str(microfreq[scannumber+1]:7:3,microstop);
str(angle:7:3,anglestr);

AutoFilename := path+daystr+monthstr;
str(filenumber, filenumstr);
filename := Autofilename + '#' + FileNumStr + '.DAT';
str((datapointermax), NumPointsToSave);
OutTextXY(5,15,'You have '+NumPointsToSave+' points to save.  What filename do you want?');
filename := editstring(500,295,700,320,filename,20,20);
ViewBox2(MenuPort);
EscapeFlag := true;
waitanykey('Press <RETURN> to save '+filename+' or <ESC> to quit',EscapeFlag,centre);
if (EscapeFlag = false) then
begin
   assign(datafile,filename);
   rewrite(datafile);
   writeln(datafile,'Original Filename : ',anglestr,' deg');
   writeln(datafile,'Number of Points  : ',DataPointerMax);
   writeln(datafile,'Frequency         : ',microstart,' MHz   ',microstop,' MHz');
   writeln(datafile,'Number of Scans   : ',ScanNumber);

   for outcount :=1 to DataPointerMax do
      writeln(datafile,ESRData[OutCount,1]:11:5,'   ',ESRData[OutCount,2]*PSDSens:6:2);

   close(datafile);
   Rewrite(namefile);
   writeln(namefile,daystr);
   writeln(namefile,monthstr);
   writeln(namefile,FileNumber);
   close(namefile);
   Datasavedflag:=true;
   end;
   Menuline;
   SetReadyFlag(ReadyFlag);
   SetRunFlag(false);
end;

{*************************************************************************}
procedure datasave2;                                          {Automatic save for sets of     }
                                                              {scans at different orientations}
var
   NumPointsToSave, oldday, oldmonth                    : string;
   filename, filenumstr, microstart,microstop ,anglestr : string;
   datafile, namefile : text;
   outcount,filenumber : integer;

begin
   ViewBox2(MenuPort);
   ClearViewPort;
   setupdate(yearstr,monthstr,daystr);
   assign(namefile,path+'lastname.txt');
   reset(namefile);
   readln(namefile,oldday);
   readln(namefile,oldmonth);

   if (oldday <> daystr) or (oldmonth <> monthstr) then
      FileNumber := 1
   else
   begin
      readln(namefile,FileNumber);
      inc(FileNumber);
   end;
```

```
   str(microfreq[1]:7:3,microstart);
   str(microfreq[scannumber+1]:7:3,microstop);
   str(angle:7:3,anglestr);

   AutoFilename := path+daystr+monthstr;
   str(filenumber, filenumstr);
   filename := Autofilename + '#' + FileNumStr + '.DAT';
   str((datapointermax), NumPointsToSave);
   ViewBox2(MenuPort);
      assign(datafile,filename);
      rewrite(datafile);
      writeln(datafile,'Original Filename : ',AngleStr,' deg');
      writeln(datafile,'Number of Points  : ',DataPointerMax);
      writeln(datafile,'Frequency         : ',microstart,' MHz   ',microstop,' MHz');
      writeln(datafile,'Number of Scans   : ',ScanNumber);

      for outcount :=1 to DataPointerMax do
         writeln(datafile,ESRData[OutCount,1]:11:5,'   ',ESRData[OutCount,2]*PSDSens:6:2);

      close(datafile);
      Rewrite(namefile);
      writeln(namefile,daystr);
      writeln(namefile,monthstr);
      writeln(namefile,FileNumber);
      close(namefile);
      Datasavedflag:=true;
   Menuline;
   SetReadyFlag(true);
   SetRunFlag(true);
end;

{*************************************************************************}

procedure go;                                                {Start collecting data}

begin
        if ScanNumber = 1 then Microfreq[1] := ReadHPFreq;
        if (ScanNumber <= ScanLimit)
           and (anglescanno <= anglescanlimit) then
   begin
      SetRunFlag(True);
      sound(tone);
      delay(50);
      nosound;
   end;
end;

{*************************************************************************}

procedure pause;                                             {No action until key pressed}

begin
   if runflag then
   begin
      SetRunFlag(False);
      sound(tone div 2);
      delay(60);
      nosound;
   end;
end;

{*************************************************************************}

procedure UserPath;                                          {Set up where to save data}

const
```

```
   user : array[1..4] of string[20]=
                         ('d:\dftp\data\',
                          'd:\djt\data\',
                          'd:\damian\data\',
                          'd:\mark\data\');

begin
   ViewBox(260,100,460,200);
   Outtextxy(10,15,'  WHAT IS YOUR NAME?');
         outtextxy(10,35,'    1  Daniel T-P');
         outtextxy(10,45,'    2  Daniel Twitchen');
   outtextxy(10,55,'    3  Damian');
   outtextxy(10,65,'    4  Mark');
   outtextxy(10,80,'  TYPE A NUMBER');
   repeat
      keyhandle(firstkey);
   until (firstkey = '1') or (firstkey = '2') or (firstkey = '3') or (firstkey = '4');
   path := user[ord(firstkey)-48];
   resetgrapharea;
   clearviewport;
end;

{*****************************************************************************}

end.
```

A.2 Least squares fitting

Experimental data was fitted using a standard Levenburg–Marquadt algorithm [169]. The fitting software was written by McNamee [233] and developed by Tucker [21]. It was developed for this work to make it more flexible, but the bulk of the software was already in existence. Routines were added to the program *Lorentsi* to enable fitting to up to five Lorentzian or Gaussian lines in the first derivative. It was also possible to constrain two or three of the lines to have the same width and intensity but variable positions.

Below are given a couple of routines illustrating typical situations. The functions *Loren* and *Gauss* call 1st derivative Lorentzian and Gaussian lineshape equations.

The first routine takes the parameters for two Gaussian lines, with widths and intensities held at the same value, and two independent Lorentzian lines.

```
procedure LinkGauLorLorObj.GetModelDetails;
begin
  model  := 'Fitting Lorentzian and two linked Gaussians';
  npar   := 12;
  an[1]  := 'Base line m    ';                                    {Parameters}
  an[2]  := 'Base line c    ';

  an[3]  := 'Gauss intens1&2';
```

```
  an[4]  := 'HW @ H height  ';

  an[5]  := 'Position 1     ';
  an[6]  := 'Position 2     ';

  an[7]  := 'Lore intens.   ';
  an[8]  := 'HW @ H height 3';
  an[9]  := 'Position 3     ';

  an[10]  := 'Lore intens. 4 ';
  an[11]  := 'HW @ H height 4';
  an[12]  := 'Position 4     ';
end;

{--------------------------}

procedure LinkGauLorLorObj.GetFitDataSet;

{ This routine obtains the fitted data set using the current parameters. }

var
  x0,y0    : integer;                  { To hold cursor pos for monitor  }
  i        : integer;

  amp2     : single;


  for i:=imin to imax do
  begin
    With data^ do fit^.y[i]  := a[1]*x[i]+a[2]                          {Determines fit from parameters}
                              + Gauss(a[3],a[4],a[5],x[i])
                              + Gauss(a[3],a[4],a[6],x[i])
                              + Loren(a[7],a[8],a[9],x[i])
                              + Loren(a[10],a[11],a[12],x[i]);
  end;

  fit^.x := data^.x;
  fit^.n := data^.n;
end;
```

The routines fit into an object-orientated program and are easily interchangable. It was also possible to simulate line positions and intensities using EPR.FOR for a theoretical system, e.g. a biradical electron pair, and fit to Lorentzian widths and other independent Lorentzians. At L-band such a routine is as follows:

```
procedure L2_BandLorLorObj.GetModelDetails;
begin
  model  := 'Fitting Biradicals at low frequency';
  npar   := 11;
  an[1]  := 'Base line m    ';
  an[2]  := 'Base line c    ';

  an[3]  := 'Intens factor  ';
  an[4]  := 'HW @ H height  ';
  an[5]  := 'Centre Position';

  an[6]  := 'Lore intens. 2 ';
  an[7]  := 'HW @ H height 2';
  an[8]  := 'Position 2     ';
```

```
  an[9]  := 'Lore intens. 3 ';
  an[10]  := 'HW @ H height 3';
  an[11]  := 'Position 3     ';
end;

{---------------------------}
procedure L2_BandLorLorObj.GetFitDataSet;

{ This routine obtains the fitted data set using the current parameters. }

var
  x0,y0    : integer;
  i        : integer;

  amp      : array[1..4] of real;
  pos      : array[1..4] of real;

  amp2     : single;

begin

  amp[1] := a[3]*0.003790;                                  {Relative intensities of lines}
  amp[2] := a[3]*0.494599;                                  {Determined by EPR.FOR        }
  amp[3] := a[3]*0.494436;
  amp[4] := a[3]*0.003786;

  pos[1] := a[5]-4.56;                                      {Relative positions of lines}
  pos[2] := a[5]-0.04;                                      {Determined by EPR.FOR      }
  pos[3] := a[5]+0.03;
  pos[4] := a[5]+4.56;


  for i:=imin to imax do
  begin
    With data^ do fit^.y[i]  := a[1]*x[i]+a[2]
                              + Loren(amp[1],a[4],pos[1],x[i])
                              + Loren(amp[2],a[4],pos[2],x[i])
                              + Loren(amp[3],a[4],pos[3],x[i])
                              + Loren(amp[4],a[4],pos[4],x[i])
                              + Loren(a[6],a[7],a[8],x[i])
                              + Loren(a[9],a[10],a[11],x[i])
  end;

  fit^.x := data^.x;
  fit^.n := data^.n;
end;
```

A.2.1 Fitting to convolutions

When analysing imaging data it is necessary to deconvolve the lineshape of the spectrum taken without a field gradient (see §7.3.3). Rather than deconvolve using Fourier transforms, it was found to be more reliable to convolve test spin distributions with experimental (gradient-off) spectra and compare with experimental (gradient-on) spectra. This was achieved by using the same Levenburg–Marquadt routines as before, with a few modifications:

- Rather than a single experimental spectrum being compared to a theoretical fit, an experimental spectrum is compared to a *second* experimental spectrum convolved with a test distribution. So the program had to import an extra array to store the gradient-off spectrum.

- The convolutions were performed in the same routines as the "getfitdataset" routines above. They were performed numerically in real space.

- All the arrays were fixed at length 1024 points to make life easier.

- The test distribution consisted of up to 40 "strips", each of the same width. Outside these strips the distribution function was set to zero.

The base program for performing the convolutions is shown here. It is essentially the same program as for fitting to Lorentzians and Gaussians, except that there is no choice of what is being fitted to.

```
program Convolvefit;

uses CRT, FronEnd1, ComProcs, Objects, Menu;

var chosen : OptionType;

type

  PFitObj = ^FitObj;                                          {Sets up the fitting object}
  FitObj = object(FrontEndObj)
    procedure   GetModelDetails ; virtual;
    procedure   GetFitDataSet   ; virtual;
    constructor Init;
    destructor  ShutDown;
  end;

procedure TMenu;                                              {Opening screen}
var
 menu1 : optionType;
 XYPos : coord;
 range : word;

begin
 TextBackground(0);
 TextColor(4);
 range := 10;
 ClrScr;
 Randomize;
 GotoXY(1,1); InsLine;
 XYPos[x] := 10;
 XYPos[y] := 2;
 NewMenu(menu1,XYPos,15,1,5,14,FALSE,FALSE,'Menu one');
 UseMenu(menu1);
 AddMenuOption('Experimental fn convoluted with strips');
```

```
 AddMenuOption('Quit');
 Chosen:=menu1
end;
{---------------------------}
constructor FitObj.Init;                                    {Allocates memory}
begin
  FrontEndObj.Init;
end;

{---------------------------}
procedure FitObj.GetModelDetails;                           {Sets up parameters}
                                                            {i.e. strips       }
var
  i    : integer;
  istr : string[2];
begin
  model  := 'Step + polynomial convoluted with experimental data';
  npar   := 43;

  an[1]  := 'Start of step ';
  an[2]  := 'End of step   ';
  an[3]  := 'No. of strips ';
  For i:= 4 to 43 do begin
    str(i-3,istr);
    an[i]  := 'Strip no. '+istr+'  ';
  end;

end;

{---------------------------}
procedure FitObj.GetFitDataSet;

{ This routine obtains the fitted data set using the current parameters. }

var
  i,j,k      : integer;
  total      : real;
  i1,i2      : integer;
  numstrips  : integer;
  stripwidth : single;                  {This is in field}

begin                                                       {Generate spin distribution}
  numstrips := trunc(a[3]);
  For i:=-511 to 1536 do L[i]:=0;
  With data^ do begin
    i1:=round((a[1]-x[1])/(x[1024]-x[1])*1023+1);
    stripwidth:=(a[2]-a[1])/numstrips;
    i:=i1;
    j:=1;
    Repeat
      k:=0;
      Repeat
        L[i]:=a[j+3];
        i:=i+1;
      Until x[i] >= a[1]+j*stripwidth;
      j:=j+1;
    Until (x[i]>=a[2]);
  end;

{***********      Convolve          ***************}
{       Have not worried about wrap around problems}

        for i:= 1 to 1024 do begin
            total:= 0;
                for j:= 1 to 1024 do
                begin
```

```
                    total:= total+line^.y[1025-j]*L[i+j-513];
                  end;
              With data^ do fit^.y[i]  := total ;
          end;

  fit^.x := data^.x;
  fit^.n := data^.n;
end;

{---------------------------}
destructor FitObj.ShutDown;
begin
  FrontEndObj.ShutDown;
end;


{---------------------------}
{       MAIN PROGRAM        }
{---------------------------}


var
  FitPointer : PFitObj;
  Quit : Boolean;

BEGIN
  TMenu;
  Repeat
    Case Runmenu(Chosen) of
      0 : FitPointer:=New(PFitObj,Init);
      1,253 : Quit:=True;
    end;

    If (FitPointer<>nil) and Quit=false then with FitPointer^ do begin
      Mainmenu;                                          {Go into fitting routines}
      Dispose(FitPointer,Shutdown);
    end;
  Until Quit;
  Clrscr;
END.
```

A.3 Projection recombination

In §7.3.4 the theory behind the generation of 2-dimensional EPR images was explained. One program was used both to filter individual projections (see §7.3.5) and to combine the projections. The two formulations used are described in equation 7.10 describing the filter:

$$P^*(ma) = \frac{4}{\pi a^2(1-4m^2)}$$

where $s = ma$,

and equation 7.7 summing the projections:

$$f(\vec{x}_2) = \frac{1}{N_1} \sum_{i=1}^{N_1} P^*(s, \theta_i) W$$

where $s = x_1 \cos(\theta_i) + x_2 \sin(\theta_i)$, and $W = 1$.

The program used was called *Circle.* Due to memory constraints up to 180 projections could be used, and the projections could consist of up to 1024 data points. The image could be generated on a grid of maximum size 128×128 pixels. The filter parameters depended on how many strips had been used to determine the distribution, although it was possible to run without filtering. The program is given below:

```
program circle2;

uses crt,dos;

type signalset = array[-1024..1023] of single;                    {Set up arrays}
     yvalue    = array[-64..63] of single;
     spectptr  = ^signalset;
     yvalueptr = ^yvalue;
var
  numpointsin,numpointsout,halfpointsout: integer;
  halfpointsin                          : integer;
  configfilename,fileout,fractionstr    : string;
  samplewidthstr,numpointsoutstr,phistr : string;
  gausswidthstr                         : string;
  configfile                            : text;
  filename                              : array[1..180] of string;
  i,j,k,numspectra,code,numstrips       : integer;
  angle,integral                        : array[1..180] of single;
  spectrum                              : array[1..180] of spectptr;    {2D array containing projections}
  gridvalue                             : array[-64..63] of yvalueptr;  {2D array for grid}
  factor,spectwidth,samplewidth         : real;
  fraction,phi,gausswidth               : real;
  Filterflag,Smoothflag                : boolean;


procedure filenamechoose;                                         {Files containing projections}
                                                                  {are listed in a single      }
begin                                                             {configuration file. The     }
  for i:= 1 to 180 do filename[i]:= '';                           {integrated intensity of each}
  Writeln('Where are the files you want to use?');                {projection is given with the}
  Readln(configfilename);                                         {filename of that projection.}
  Assign(configfile,configfilename);                              {At the top of the           }
  Reset(configfile);                                              {configuration file are the  }
  Readln(configfile,numspectra);                                  {parameters for filtering.   }
  Readln(configfile,numpointsin);
  Halfpointsin := trunc(numpointsin/2);
  Readln(configfile,spectwidth);
  Readln(configfile,numstrips);
  For i:= 1 to numspectra do begin
    Readln(configfile,filename[i]);
    Readln(configfile,angle[i]);
    Readln(configfile,integral[i]);
```

```
    Angle[i] := angle[i]+phi;                    {Angle of each projection is}
  end;                                           {given here                  }
  Close(configfile);
  Writeln('Filenames chosen successfully');
  Writeln(numspectra,' files to bring in');
end;

{*************************}

procedure Readspectra;                           {Imports projectiona}

var datafilein : text;
begin
  for i:= 1 to numspectra do begin
    New (spectrum[i]);
    for j:= -1024 to 1023 do begin
      spectrum[i]^[j] := 0;
    end;
  end;
  for i:= 1 to numspectra do begin
    Assign (datafilein,filename[i]);
    Reset (datafilein);
    for j:=-halfpointsin to halfpointsin-1 do begin
      Readln(datafilein,spectrum[i]^[j]);
      spectrum[i]^[j]:=spectrum[i]^[j]*40/integral[i];
    end;
    close(datafilein);
    Write(i,'..');
  end;
Writeln;Writeln('Files imported');
end;

{*************************}
Procedure smoothspectra;                         {Smooths projections by      }
                                                 {convolution with a Gaussian.}
var                                              {This is necessary to prevent }
  total,bk,ck: real;                             {the "steps" in the distribution }
  j          : integer;                          {being exaggerated by the filter.}
  tempspect  : signalset;

begin
{***********      Convolute         ***************}
{       Have not worried about wrap around problems}
  Writeln('Smoothing spectra . . .');
  For j:= -1024 to 1023 do tempspect[j]:=0;
  for i:= 1 to numspectra do begin
    for j:= -halfpointsin to halfpointsin-1 do begin
      total:= 0;
      for k:= -halfpointsin to halfpointsin-1 do begin
        bk := -ln(2)*(k-j)*(k-j)/(gausswidth*gausswidth);
        If bk >= -1e4 then ck := sqrt(ln(2)/pi)*exp(bk)/gausswidth else ck := 0;
        total:= total + spectrum[i]^[k]*ck;
      end;
      Tempspect[j] := total;
    end;
    For j := -halfpointsin to halfpointsin-1 do spectrum[i]^[j] := tempspect[j];
    Write(i,'..');
  end;
  Writeln('Done');

end;
{*************************}

Procedure filterspectra;                         {Convolves projections with }
                                                 {Shepp-Logan filter function}
var
```

```
  total      : real;
  bk,j       : integer;
  tempspect  : signalset;

begin

{***********      Convolute         ***************}
{       Have not worried about wrap around problems}
  Writeln('Filtering spectra . . .');
  factor := samplewidth*numpointsin/(spectwidth*numstrips);
  For j:= -1024 to 1023 do tempspect[j]:=0;
  for i:= 1 to numspectra do begin
    for j:= -halfpointsin to halfpointsin-1 do begin
      total:= 0;
      for k:= -halfpointsin to halfpointsin-1 do begin
        bk := round((k-j)/factor);
        total:= total+spectrum[i]^[k]*4/(pi*(1-4*sqr(bk)));
      end;
      Tempspect[j] := total;
    end;
    For j := -halfpointsin to halfpointsin-1 do spectrum[i]^[j] := tempspect[j];
    Write(i,'..');
  end;
  Writeln('Done');

end;
{*************************}
function signalvalue(xin,yin:integer; signal:signalset; ang:single) : real;
                                                                  {Determines contribution of}
var                                                               {one projection at any     }
 x1    : real;                                                    {given point on the grid.  }
 x2,x3 : integer;
 y1,y2 : real;

begin
  ang:= -ang*pi/180;
  x1 := xin*cos(ang)*numpointsin*fraction/numpointsout+yin*sin(ang)*numpointsin*fraction/numpointsout;
  x2 := trunc(x1+300)-300;
  x3 := x2+1;
  y1 := signal[x2];
  y2 := signal[x3];
  signalvalue := y1*(x3-x1)+y2*(x1-x2);
end;

{*************************}

Procedure calculatedata;                                          {Determines all points on the}
                                                                  {grid from equation above    }
var
 x,y : integer;

begin
  Writeln('Calculating data');
  For x:= -halfpointsout to halfpointsout-1 do begin
    New (gridvalue[x]);
    For y:= -halfpointsout to halfpointsout-1 do begin
      gridvalue[x]^[y] := 0;
      For i:= 1 to numspectra do begin
        gridvalue[x]^[y] :=  gridvalue[x]^[y]+signalvalue(x,y,Spectrum[i]^,angle[i]);
      end;
      gridvalue[x]^[y] := gridvalue[x]^[y]/numspectra;
    end;
  Write(x,'..');
  end;
Writeln;
end;
```

```
{**************************}

Procedure exportdata;

var
 datafileout : text;
 x,y         : integer;

begin
  Writeln ('Output filename?');
  Readln (fileout);
  Assign (datafileout,fileout);
  Rewrite (datafileout);
  For y:= -halfpointsout to halfpointsout-1 do begin {At some stage this needs swapping over}
    For x:= -halfpointsout to halfpointsout-1 do begin
      Writeln(datafileout,x,#9,y,#9,gridvalue[x]^[y]:12:8);
    end;
  end;
  Close(datafileout);
end;

{**************************}

Procedure freememory;

begin
  for i:=1 to numspectra do begin
    dispose(spectrum[i]);
    spectrum[i]:= nil;
  end;
  for i:=-halfpointsout to halfpointsout-1 do begin
    dispose(gridvalue[i]);
    gridvalue[i]:= nil;
  end;
end;

{**************************}
{***** MAIN PROGRAM *********}
{**************************}

begin
Writeln('Size of output grid?');                          {Choices about resolution}
Repeat                                                    {made here               }
  Readln(numpointsoutstr);
  Val(numpointsoutstr,numpointsout,code);
until (code=0) and ((numpointsout<=128) and (numpointsout>1));
Halfpointsout :=trunc(numpointsout/2);

Writeln('Filter? (Y/N)');                                 {To filter or not to filter}
Repeat until (Upcase(readkey)='Y') or (upcase(readkey)='N');
If Upcase(readkey)='Y' then begin
  Filterflag := true;
  Writeln('Width of sample for filtering?');
  Repeat
    Readln(samplewidthstr);
    Val(samplewidthstr,samplewidth,code);
  until (code=0) and ((samplewidth<=400) and (samplewidth>1));
end else Filterflag := false;

Writeln('Smooth? (Y/N)');
Repeat until (Upcase(readkey)='Y') or (upcase(readkey)='N');
If Upcase(readkey)='Y' then begin
  Smoothflag := true;
  Writeln('Width of gaussian for smoothing');
  Repeat
```

```
    Readln(gausswidthstr);
    Val(gausswidthstr,gausswidth,code);
  until (code=0) and ((gausswidth<=400) and (gausswidth>0.1));
End else Smoothflag := false;

Writeln('Fraction of total spectra to use?');                    {If projections have large}
Repeat                                                           {regions with no signal at}
  Readln(fractionstr);                                           {the edges these can be   }
  Val(fractionstr,fraction,code);                                {discarded.               }
until (code=0) and ((fraction<=1) and (fraction>0));

Writeln('Angle to rotate?');                                     {Enables final image to be}
Repeat                                                           {rotated.                 }
  Readln(phistr);
  Val(phistr,phi,code);
until (code=0) and ((phi<360) and (phi>-360));

Filenamechoose;
Readspectra;
If Smoothflag then Smoothspectra;
If Filterflag then Filterspectra;
Calculatedata;
exportdata;
Freememory;
end.
```

Appendix B

Samples and concentrations

Sample no.	Weight (mg)	Raman width (cm^{-1})	Spin conc. (No. cm^{-3})		Anneal	Image
			N_S^0	g=2.0028		
1	65.5	2.5	$< 2 \times 10^{15}$	0.6×10^{17}	Yes	
2	30.0	2.4	1.2×10^{17}	1.4×10^{17}		
3	121	2.5	2.3×10^{17}	0.9×10^{17}	Yes	N_S^0
4	114	2.8	3.3×10^{17}	1.4×10^{17}		N_S^0
5	61.5	2.2	$< 2 \times 10^{15}$	1.4×10^{17}	Yes	
6	30.6		1.5×10^{17}	0.95×10^{17}		
7	51.4		1.3×10^{17}	$\sim 1 \times 10^{16}$		N_S^0
8	78.8		0.7×10^{17}	$\sim 1 \times 10^{16}$		N_S^0
9	82.9		0.86×10^{17}	0.2×10^{17}		N_S^0
10	37.1	1.8	0.9×10^{17}	0.9×10^{17}	Yes	
11	25.0	2.2	$< 2 \times 10^{15}$	3.5×10^{17}		
12	33.7	2.6	0.28×10^{17}	$\sim 1 \times 10^{16}$		
13	50.0	3.0	$< 2 \times 10^{15}$	3.7×10^{17}		
14	44.3	3.4	0.17×10^{17}	7.6×10^{17}		
15	30.1	2.3	$< 2 \times 10^{15}$	1.8×10^{17}		

Sample no.	Weight (mg)	Raman width (cm^{-1})	Spin conc. (No. cm^{-3})		Anneal	Image
			N_S^0	g=2.0028		
16	93.0		$< 2 \times 10^{15}$	0.2×10^{17}		
17	53.8		$< 2 \times 10^{15}$	0.3×10^{17}		
18	61.0		$< 2 \times 10^{15}$	0.4×10^{17}		
19	35.3	4.5	$< 2 \times 10^{15}$	19×10^{17}		
20	38.2	3.9	$< 2 \times 10^{15}$	14×10^{17}	Yes	
21	63.8	1.9	$< 2 \times 10^{15}$	0.9×10^{17}		
22	44.3	3.1	$< 2 \times 10^{15}$	1.9×10^{17}		
23	37.9	2.9	0.9×10^{17}	7.2×10^{17}		
24	48.4		$< 2 \times 10^{15}$	0.4×10^{17}		
25	34.1	3.2	$< 2 \times 10^{15}$	3.8×10^{17}	Yes	
26	69.3	2.5	$< 2 \times 10^{15}$	0.8×10^{17}		
27	60.4	2.4	$< 2 \times 10^{15}$	0.7×10^{17}		
28	40.8	1.9	0.3×10^{17}	0.9×10^{17}	Yes	
29	36.1	3.0	1.5×10^{17}	11×10^{17}	Yes	
30	27.6	1.8	0.6×10^{17}	0.9×10^{17}	Yes	
31	11.4	2.3	$< 2 \times 10^{15}$	1.4×10^{17}		
32	94.8	2.4	0.3×10^{17}	2.4×10^{17}		
33	48.6	1.6	5×10^{15}	1×10^{16}	Yes	
34	45.3		$\leq 1 \times 10^{15}$	1×10^{17}		2D H1
35	72.7		4×10^{15}	0.25×10^{17}		N_S^0 & H1

Bibliography

[1] R. H. Wentorf Jr. and H. P. Bovenkerk. *Astrophysics Journal*, 34:995, 1961.

[2] D. M. Bibby. In P. A. Thrower, editor, *Chemistry and Physics of Carbon*, page 1, New York, 1977. Marcel Dekker.

[3] F. P. Bundy, H. T. Hall, H. M. Strong, and R. H. Wentorf. *Nature*, 176:51, 1955.

[4] E. Wilks and J. Wilks. *Properties and Applications of Diamond.* Butterworth-Heineman, 1994.

[5] W. Eversole. *U.S. Patents 3030187, 3030188*, 1962.

[6] B. V. Spitsyn, L. L. Bouliov, and B. V. Derjaguin. *J. Cryst. Growth*, 52:219, 1981.

[7] S. Matsumoto, Y. Sato, M. Kamo, and N. Setaka. *Jpn. J. Appl. Phys.*, 21:L183, 1982.

[8] M. Kamo, Y. Sato, S. Matsumoto, and N. Setaka. *J. Cryst. Growth*, 62:642, 1983.

[9] Anon. *Industrial Diamond Review*, 39:69, 1979.

[10] M. Seal. *Industrial Diamond Review*, 45:58, 1985.

[11] A. Mainwood, L. Allers, A. T. Collins, J. F. Hassard, A. R. Mahon, H. L. Parsons, T. Sumner, J. L. Collins, G. A. Scarsbrook, R. S. Sussmann, and A. J. Whitehead. *J. Phys. D: Appl. Phys.*, 28:1279, 1995.

[12] L. Allers, A. S. Howard, J. F. Hassard, and A. Mainwood. *Diam. Relat. Mater*, 6:353, 1997.

[13] A. T. Collins. n-type conduction and electron mobility in diamond. In G. Davies, editor, *Properties and Growth of Diamond*, chapter 9.6. INSPEC, 1994.

[14] G. Meaden, P. G. Partridge, E. Nicholson, J. Nicholson, A. Wisbey, and M. N. R. Ashfold. *Diam. Relat. Mater*, 6:898, 1997.

[15] A. Cox, M. E. Newton, and J. M. Baker. *J.Phys.C.*, 6:551, 1994.

[16] O. D. Tucker, M. E. Newton, and J. M. Baker. *Phys.Rev.B*, 49:15586, 1994.

[17] W. Zommerfelds and M. J. R. Hoch. *J. Magn. Reson.*, 67:177, 1986.

[18] A. T. Collins and P. M. Spear. *J. Phys. C*, 19:6845, 1986.

[19] M. E. Newton. D.Phil thesis, 1989. University of Oxford.

[20] A. Cox. D.Phil thesis, 1993. University of Oxford.

[21] O. D. Tucker. D.Phil thesis, 1995. University of Oxford.

[22] D. J. Twitchen. D.Phil thesis, 1997. University of Oxford.

[23] J. E. Field, editor. *The Properties of Diamond.* Academic Press, London, 1979.

[24] J. E. Field, editor. *The Properties of Natural and Synthetic Diamond.* Academic Press, London, 1992.

[25] G. Davies, editor. *Properties and Growth of Diamond.* INSPEC: Instituion of Electrical Engineers, London, 1994.

[26] J. C. Angus, H. A. Will, and W. S. Stanko. *J. Appl. Phys.*, 39:2915, 1968.

[27] B. V. Derjaguin, D. V. Fedoseev, and V. M. Lukyanovich. *J. Cryst. Growth*, 2:380, 1968.

[28] Y. Hirose and Y. Terasawa. *Jpn. J. Appl. Phys.*, 25 (6):L519, 1986.

[29] R. Brunsteiner, R. Haubner, and B. Lux. *Diam. Relat. Mater.*, 2:1263, 1993.

[30] R. Haubner and B. Lux. Techniques of hot-filament assisited deposition of diamond. In G. Davies, editor, *Properties and Growth of Diamond*, chapter 11.2. INSPEC, 1994.

[31] R. Gat and J. C. Angus. Principles of hot-filament assisited deposition of diamond. In G. Davies, editor, *Properties and Growth of Diamond*, chapter 11.1. INSPEC, 1994.

[32] Y. Hirose and N. Kondo. In *Japan Applied Physics 1988 spring meeting*, page 434, Tokyo, 1988. Japanese Physical Society.

[33] Y. Hirose, S. Ananuma, N. Okada, and K. Komaki. In J. P. Dismukes, editor, *Diamond and Diamond-like films*, page 80, Pennington, N.J., 1989. Electrochemical Society.

[34] Y. Hirose. *Carbon*, 28:776, 1990.

[35] L. M. Hanssen, K. A. Snail, W. A. Carrington, and J. E. Butler. *Thin Solid Films*, 196:271, 1991.

[36] W. A. Carrington, L. M. Hanssen, K. A. Snail, D. B. Oakes, and J. E. Butler. *Metall. Trans.*, A20:1282, 1989.

[37] J. E. Butler, F. G. Celii, D. B. Oakes, L. M. Hanssen, W. A. Carrington, and K. A. Snail. *High Temp. Sci.*, 27:183, 1990.

[38] D. B. Oakes and J. E. Butler. *J. Appl. Phys.*, 69:2602, 1991.

[39] C. M. Marks, H. R. Burris, J. L. Grun, and K. A. Snail. *J. Appl. Phys.*, 73:755, 1993.

[40] P. W. Morrison Jr, J. E. Cosgrove, J. R. Markham, and P. R. Solomon. *Carbon*, 28:767, 1990.

[41] Y. Matsui, A. Yuuki, M. Sahara, and Y. Hirose. *Jpn. J. Appl. Phys.*, 28:1718, 1989.

[42] R. S. Yalamanchi and K. S. Harshavardhan. *J. Appl. Phys.*, 68:5941, 1990.

[43] P. W. Morrison Jr. and J. T. Głass. Flame characteristics for combustion grown diamond. In G. Davies, editor, *Properties and Growth of Diamond*, chapter 11.6–11.8. INSPEC, 1994.

[44] H. R. Thorsheim, F. G. Celii, J. E. Butler, L. S. Plano, and J. M. Pinneo. In R. F. Messier, J. T.Glass, J. E.Butler, and R. Roy, editors, *New Diamond Science and Technology*, page 207, Pittsburgh, P.A., 1991. Materials Research Society.

[45] K. Suzuki, A. Sawabi, H. Yasuda, and T. Inuzuka. *Appl. Phys. Lett.*, 50:728, 1987.

[46] K. Suzuki, A. Sawabi, H. Yasuda, and T. Inuzuka. *Jpn. J. Appl. Phys.*, 29:153, 1990.

[47] B. Singh, O. R. Mesker, A. W. Levine, and Y. Arie. *Appl. Phys. Lett.*, 52:1658, 1988.

[48] K. Kurihara, K. Sasaki, M. Kawaranda, and N. Koshino. *Appl. Phys. Lett.*, 52:437, 1988.

[49] G. Lu and L. K. Bigelow. In P. K. Bachmann and A. Matthews, editors, *Diamond, Diamond-Like and Related Films*, page 207, Lausanne, 1992. Elsevier Sequoia.

[50] S. Matsumoto. In G. H. Johnson, A. R. Badzian, and M. W. Geis, editors, *Diamond and Diamond-Like Materials Synthesis*, page 119, Pittsburgh, P.A., 1988. Mater. Res. Soc. Symp. extended abstracts, EA-15.

[51] P. K. Bachmann. Plasma cvd synthesis of diamond. In G. Davies. editor, *Properties and Growth of Diamond*, chapter 11.4. INSPEC, 1994.

[52] S. Matsumoto. *J. Mater. Sci. Lett.*, 4:600, 1985.

[53] D. E. Meyer, R. O. Dillon, and J. A. Woolham. *J. Vac. Sci. Technol.*, 7:2325, 1989.

[54] P. Wood, T. Wydeven, and O. Tsuji. In S. Saito, O. Fukanaga, and M. Yoshikawa, editors, *Science and Technology of New Diamond*, page 167, Tokyo, 1990. KTK.

[55] R. A. Rudder et al. In R. F. Messier, J. T. Glass, J. E. Butler, and R. Roy, editors, *New Diamond Science and Technology*, page 425, Pittsburgh, P.A., 1991. Materials Research Society.

[56] S. Matsumoto, M. Hino, and T. Kobayashi. *Appl. Phys. Lett.*, 51:737, 1987.

[57] T. G. Owano, D. G. Goodwin, C. H. Kruger, and M. A. Cappelli. In R. F. Messier, J. T. Glass, J. E. Butler, and R. Roy, editors, *New Diamond Science and Technology*, page 497, Pittsburgh, P.A., 1991. Materials Research Society.

[58] M. Kohzaki, K. Higuchi, S. Noda, and K. Uchida. In P. K. Bachmann, A. T. Collins, and M. Seal, editors, *Diamond 1992*, Lausanne, 1993. Elsevier Sequoia.

[59] S. Miyake, W. Chen, A. Hoshino, and Y. Arata. *Trans. JWRI*, 17:323, 1988.

[60] A. R. Badzian, B. Simonton, T. Badzian, R. Messier, K. E. Spear, and R. Roy. *Proc. SPIE-Int. Soc. Opt. Eng.*, 683:127, 1986.

[61] P. K. Bachmann, W. Drawl, D. Knight, R. Weimer, and R. F. Messier. In A. R. Badzian, M. W. Geis, and G. H. Johnson, editors, *Diamond and Diamond-Like Materials*, page 99, Pittsburgh, P.A., 1988. Mater. Res. Soc. extended abstracts, EA-15.

[62] K. Kobashi, K. Nishimura, Y. Kawate, and T. Horiuchi. *Phys. Rev. B*, 38:4067, 1988.

[63] Y. Mitsuda, T. Yoshida, and K. Akashi. *Rev. Sci. Instrum*, 60:249, 1989.

[64] M. Aklufi and D. Brock. In J. P. Dismukes, editor, *Proc. 1st Int. Symp. on Diamond and Diamond-like films*, page 114, Pennington, N.J., 1989. Electrochemical Society.

[65] X. Jiang and C. Klages. In P. K. Bachmann, A. T. Collins, and M. Seal, editors, *Diamond 1992*, Lausanne, 1993. Elsevier Sequoia.

[66] P. K. Bachmann, D. Leers, and H. Lydtin. *Diamond and Related Materials*, 1:1, 1991.

[67] F. G. Celii and J. E. Butler. *Annu. Rev. Phys. Chem.*, 42:643, 1991.

[68] M. Frenklach and H. Wang. *Phys. Rev. B*, 43:1520, 1991.

[69] W. A. Yarbrough and R. Messier. *Science*, 247:688, 1990.

[70] Z. J. Chen, G. P. Wirtz, and S. D. Brown. *J. Am. Ceram. Soc.*, 75:688, 1992.

[71] J. C. Angus and C. C. Hayman. *Science*, 241:913, 1988.

[72] S. J. Harris. *Appl. Phys. Lett.*, 56:2298, 1990.

[73] S. Skokov, B. Weiner, and M. Frenklach. *J. Phys. Chem.*, 98:7073, 1994.

[74] S. Skokov, B. Weiner, and M. Frenklach. *J. Phys. Chem.*, 99:5616, 1995.

[75] M. I. Heggie, C. D. Latham, R. Jones, and P. R. Briddon. In *Proc. 4th Int. Symp. on Diamond Materials, 187th meeting of the Electrochemical Society*, Pennington, N.J., 1995. Electrochemical Society.

[76] Y. Matsui and H. Yabe. *Diam. Relat. Mater.*, 2:7, 1993.

[77] J. E. Butler and R. L. Woodin. *Phil. Trans. R. Soc. Lond A*, 342:15, 1993.

[78] M. I. Heggie, G. Jungnickel, and C. D. Latham. *Diam. Relat. Mater.*, 5:236, 1996.

[79] Y. Bar-Yam and T. D. Moustakas. *Nature*, 342:786, 1989.

[80] R. Sussmann. *Ind. Diamond Rev.*, 53:63, 1993.

[81] B. Dischler, C. Wild, W. Müller-Sebert, and P. Koidl. *Physica B*, 185:217, 1993.

[82] K. M. McNamara, B. E. Williams, K. K. Gleason, and B. E. Scruggs. *J.Appl.Phys.*, 76:2466, 1994.

[83] D. F. Talbot-Ponsonby, M. E. Newton, J. M. Baker, G. A. Scarsbrook, R. S. Sussmann, J. R. Brandon, C. N. Dodge, and S. Pfenninger, 1996. Submitted Phys. Rev. B.

[84] D. F. Talbot-Ponsonby, M. E. Newton, J. M. Baker, G. A. Scarsbrook, R. S. Sussmann, J. R. Brandon, and C. N. Dodge, 1996. Submitted Phys. Rev. B.

[85] V. S. Vavilov, A. A. Gippius, A. M. Zaitsev, B. V. Derjaguin, B. V. Spitsyn, and A. E. Aleksenko. *Sov. Phys. Semicond.*, 14:1078, 1980.

[86] L. H. Robins, L. P. Cook, E. N. Farabaugh, and A. Feldman. *Phys. Rev. B*, 39:13367, 1989.

[87] Y. Yokota, H. Kawarada, and A. Hiraki. In J. T. Glass, R. F. Messier, and N. Fujimori, editors, *Diamond, Boron Nitride, Silicon Carbide and Related Wide Band Gap Semiconductors*, Pittsburgh, P.A., 1990. Mater. Res. Soc. Symp. Proc. 162.

[88] A. T. Collins, M. Kamo, and Y. Sato. *J. Mater. Res.*, 5:2507, 1990.

[89] A. T. Collins, L. Allers, C. J. H. Wort, and G. A. Scarsbrook. *Diam. Rel. Mater.*, 3:932, 1994.

[90] H. Sternschulte, K. Thonke, J. Gerster, W. Limmer, R. Sauer, J. Spitzer, and P. C. Münzinger. *Diam. Rel. Mater.*, 4:1189, 1995.

[91] C. D. Clark, H. Kanda, I. Kiflawi, and G. Sittas. *Phys. Rev. B*, 51:16681, 1995.

[92] J. Ruan, W. J. Choyke, and K. Kobashi. *Appl. Phys. Lett.*, 62:1379, 1993.

[93] J. A. Freitas Jr., J. E. Butler, and U. Strom. *J. Mater. Res.*, 5:2502, 1990.

[94] D. S. Knight and W. B. White. *Proc. SPIE*, 1055:144, 1989.

[95] E. S. Etz, E. N. Farabaugh, A. Feldman, and L. H. Robins. *Proc. SPIE*, 969:86, 1988.

[96] L. H. Robins, E. N. Farabaugh, and A. Feldman. *Proc. SPIE*, 1325:130, 1990.

[97] A. T. Collins and S. C. Lawson. *J.Phys.: Condens. Matter*, 1:6929, 1989.

[98] G. Davies and M. F. Hamer. *Proc.R.Soc.(Lond.) A.*, 348:285, 1976.

[99] L. Bergman, M. T. McClure, J. T. Glass, and R. J. Nemanich. *J. Appl. Phys.*, 76:3020, 1994.

[100] A. T. Collins, M. Kamo, and Y. Sato. *J. Phys. D: Appl. Phys.*, 22:1402, 1989.

[101] P. Joeris, I. Schmidt, and C. Benndorf. *Diam. Relat. Mater.*, 5:603, 1996.

[102] D. Behr, J. Wagner, C. Wild, and P. Koidl. *Appl. Phys. Lett.*, 63:3005, 1993.

[103] J. Ruan, W. J. Choyke, and W. D. Partlow. *J. Appl. Phys.*, 69:6632, 1991.

[104] A. T. Collins, M. Kamo, and Y. Sato. *J. Phys. Condens. Matter*, 1:4029, 1989.

[105] Y. L. Khong, A. T. Collins, and L. Allers. *Diam. Rel. Mater.*, 3:1023, 1994.

[106] A. T. Collins. *Ceramics International*, 22:321, 1996.

[107] J. A. von Windheim, V. Venkatessen, D. M. Malta, and K. Das. *Diam. Relat. Mater.*, 2:841, 1993.

[108] B. R. Stoner, C. Kao, and D. M. Malta. *Appl. Phys. Lett.*, 62:2347, 1993.

[109] N. Fujimori, H. Nakahata, and T. Imai. *Jpn. J. Appl. Phys.*, 29:824, 1990.

[110] G. Sh. Gildenblat, S. A. Grot, and A. Badzian. *Proc. IEEE.*, 79:647, 1991.

[111] H. Karawada. In M. Kamo, H. Kanda, Y. Matsui, and T. Sekine, editors, *Advanced Materials '94, Proc. NIRIM Int. Symp.*, page 163, Tokyo, 1994. International Communications Specialists Inc.

[112] K. Okumura, J. Mort, and M. Maxhonkin. *Appl. Phys. Lett.*, 57:1907, 1990.

[113] V. S. Veerasamy, G. A. J. Amaratunga, C. A. Davies, A. E. Timbs, W. I. Milne, and D. R. Mckenzie. *J. Phys. Condens. Matter*, 5:L169, 1993.

[114] S. N. Schauer, J. R. Flemish, R. Wittstruck, M. I. Landstrass, and M. A. Plano. *Appl. Phys. Lett.*, 64:2094, 1994.

[115] R. Berman, P. R. W. Hudson, and M. Martinez. *J.Phys.C.*, 8:L430, 1975.

[116] T. R. Anthony, W. F. Banholzer, J. F. Fleisher, L. Wei, P. K. Kuo, R. L. Thomas, and R. W. Pryor. *Phys. Rev. B.*, 42:1104, 1990.

[117] R. Berman. *Phys. Rev. B*, 45:5726, 1992.

[118] D. T. Morelli, C. P. Beetz, and T. A. Perry. *J. Appl. Phys.*, 64:3063, 1988.

[119] D. T. Morelli, C. Uher, and C. J. Robinson. *Appl. Phys. Lett.*, 62:1085, 1993.

[120] K. M. McNamara-Rutledge, B. E. Scruggs, and K. K. Gleason. *J. Appl. Phys.*, 77:1459, 1995.

[121] J. E. Graebner, S. Jin, G. W. Kammlott, B. Bacon, L. Seibles, and W. Banholzer. *J. Appl. phys.*, 71:5353, 1992.

[122] J. E. Graebner, T. M. Hartnett, and R. P. Miller. *Appl. Phys. Lett.*, 64:2549, 1994.

[123] I. Watanabe and K. Sugata. *Japanese J.Appl.Phys.*, 27:1808, 1988.

[124] M. Hoinkis, E. R. Weber, M. I. Landstrass, M. A. Plano, S. Han, and D. R. Kania. *Appl.Phys.Lett.*, 59:1870, 1991.

[125] X. Zhou, G. D. Watkins, K. M. Mcnamara-Rutledge, R. P. Messmer, and Sanjay Chawler. *Phys. Rev. B*, 54:7881, 1996.

[126] E. Rohrer, C. F. O. Graeff, R. Janssen, C. E. Nebel, M. Stutzmann, H. Güttler, and R. Zachai. *Phys. Rev. B*, 54:7874, 1996.

[127] C. F. O. Graeff, E. Rohrer, C. E. Nebel, M. Stutzmann, H. Güttler, and R. Zachai. *Appl. Phys. Lett.*, 69:3215, 1996.

[128] P. B. Lukins and J. Khachan. *Appl. Phys. Lett.*, 65:3320, 1994.

[129] C. F. O. Graeff, C. E. Nebel, M. Stutzmann, A. Flöter, and R. Zachai. *J. Appl. Phys.*, 81:234, 1996.

[130] W. Zhang, F. Zhang, Q. Wu, and G. Chen. *Materials Letters*, 15:292, 1992.

[131] M. Fanciulli and T. D. Moustakas. *Diam. Relat. Mater.*, 1:773, 1992.

[132] M. Fanciulli and T. D. Moustakas. *Phys. Rev. B.*, 48:14982, 1993.

[133] H. Jia, J. Shinar, D. P. Lang, and M. Pruski. *Phys. Rev. B.*, 45:17595, 1993.

[134] M. E. Zvanut, W. E. Carlos, J. A. Freitas Jr., K. D. Jamison, and R. P. Hellmer. *Appl. Phys. Lett.*, 65:2287, 1994.

[135] K. Fabisiak, J. K. Patyk, and F. Rozploch. *Acta Physica Polonica A*, 87:145, 1994.

[136] Y. von Kaenel, J. Staegler, E. Blank, O. Chauvet, Ch. Hellwig, and K. Plamann. *Phys. Stat. Sol. A*, 154:219, 1996.

[137] I. Watanabe, K. Haruta, and Y. Shimamura. *Jpn. J. Appl. Phys.*, 33:2035, 1994.

[138] M. Fanciulli and T. D. Moustakas. *Materials Science Forum*, 143-147:35, 1994.

[139] S. L. Holder, L. G. Rowan, and J. J. Krebs. *Appl.Phys.Lett.*, 64:1091, 1994.

[140] X. Zhou, G. D. Watkins, and K. M. McNamara-Rutledge. *Materials Science Forum*, 196-201:825, 1996.

[141] D. J. Keeble and B. Ramakrishnan. *Appl. Phys. Lett.*, 69:3836, 1996.

[142] B. Ramakrishnan, D. J. Keeble, H. Rodrigo, and A. Kulkarni. *Mat. Res. Soc. Symp. Proc.*, 423:501, 1996.

[143] Y. Show, M. Iwase, and T. Izumi. *Thin Solid Films*, 274:50, 1996.

[144] Y. Show, Y. Nakamura, T. Izumi, M. Deguchi, M. Kitabatake, T. Hirao, Y. Mori, A. Hatta, T. Ito, and A. Hiraki. *Thin Solid Films*, 281-282:275, 1996.

[145] D. F. Talbot-Ponsonby, M. E. Newton, J. M. Baker, G. A. Scarsbrook, R. S. Sussmann, and C. J. H. Wort. *J.Phys.: Condens. Matter*, 8:837, 1996.

[146] M. Hoinkis, E. D. Tober, R. L. White, and M. S. Crowder. *Appl. Phys. Lett.*, 61:2653, 1992.

[147] E. Colineau, A. Deneuville, J. Mambou, and E. Gheeraert. *Appl. Phys. Lett.*, 68:2123, 1996.

[148] J. A. Weil, J. R. Bolton, and J. E. Wertz. *Electron Paramagnetic Resonance: Elementary Theory and Practical Applicatons.* Wiley-Interscience, New York, 1994.

[149] P. W. Atkins. *Molecular Quantum Mechanics.* OUP, Oxford, 1983.

[150] J. R. Morton and K. F. Preston. *J. Magn. Reson.*, 30:577, 1978.

[151] C. P. Slichter. *Priciples of Magnetic Resonance.* Springer-Verlag, New York, 1963.

[152] C. Kittel and E. Abrahams. *Phys. Rev.*, 90:238, 1953.

[153] J. H. van Vleck. *Phys. Rev.*, 74:1168, 1948.

[154] R. C. Barklie and J. Guven. *J. Phys. C: Solid State Phys.*, 14:3621, 1982.

[155] G. Feher. *Phys. Rev.*, 105:1122, 1957.

[156] A. Abragam and B. Bleaney. *Electron Paramagnetic Resonance of Transition Ions.* Dover Publications Inc., New York, 1986.

[157] J. S. Hyde, G. H. Rist, and L. E. Eriksson. *J.Phys.Chem.*, 72:4269, 1968.

[158] L. Kevan and L. D. Kispert. *Electron Spin Double Resonance Spectroscopy.* Wiley-Interscience, New York, 1976.

[159] H. Seidel. *Z. Phys.*, 165:239, 1961.

[160] A. Abragam. *Phys. Rev.*, 98:1729, 1955.

[161] V. L. Hochmann, V. Ya. Zevin, and B. D. Shanina. *Sov. Phys. Solid State*, 10:269, 1968.

[162] P. A. Narayana, R. N. Schwartz, M. Bowman, D. Becker, and L. Kevan. *J. Chem. Phys.*, 67:1990, 1977.

[163] C. P. Poole. *Electron Spin Resonance: A comprehensive treatise on experimental techniques.* John Wiley, New York, 1983.

[164] J. S. Hyde and W. Froncisz. Loop gap resonators. In A J Hoff, editor, *Adv. EPR in Biology and Biochemistry.* Elsevier, Amsterdam, 1988.

[165] R. L. Wood, W. Froncisz, and J. S. Hyde. *J. Magn. Reson.*, 58:243, 1984.

[166] J. S. Hyde, W. Froncisz, and T. Oles. *J. Magn. Reson.*, 82:223, 1989.

[167] A. J. O'Connell. D.Phil thesis, 1992. University of Oxford.

[168] M. J. Mombourquette, J. A. Weil, and D. G. McGavin. Program eprnmr.for. Written at the Department of Chemistry, University of Saskatchewan, Saskatoon, Saskatchewan, Canada, S7N 0W0. Any correspondance should be addressed to Prof.J.A.Weil.

[169] W. H. Press, B. P. Flannery, S. A. Tenkolsky, and W. T. Vetterling. *Numerical Recipies in Pascal.* Cambridge University Press, Cambridge, 1989.

[170] G. S. Woods, J. A. van Wyk, and A. T. Collins. *Phil.Mag.B*, 62:589, 1990.

[171] W. V. Smith, P. P. Sorokin, I. L. Gelles, and G. J. Lasher. *Phys. Rev.*, 115:1546, 1959.

[172] P. R. Briddon and R. Jones. *Physica B*, 185:179, 1993.

[173] S .A. Kajihara, A. Antonelli, and J. Bernholc. *Phys. Rev. Lett.*, 66:2010, 1991.

[174] J. Mort, M. A. Machonkin, and K. Okumura. *Appl.Phys.Lett.*, 59:3148, 1991.

[175] K. Meykens, M. Nesládek, C. Quaeyhaegens, L. M. Stals, M. Vaněček, J. Rosa, G. Janssen, and J. J. Schermer. *Diam. Relat. Mater.*, 5:958, 1996.

[176] H. Spicka, M. Griesser, H. Hutter, M. Grasserbauer, S. Bohr, R. Haubner, and B. Lux. *Diam. Relat. Mater.*, 5:383, 1996.

[177] A. Bergmaier, G. Dollinger, T. Faestermann, C. M. Frey, M. Ferguson, H. Guttler, G. Schulz, and H. Willerscheid. *Diam. Relat. Mater.*, 5:995, 1996.

[178] S. Jin and T. D. Moustakas. *Appl.Phys.Lett.*, 65:403, 1994.

[179] R. Samlenski, C. Haug, R. Brenn, C. Wild, R. Locher, and P. Koidl. *Appl. Phys. Lett.*, 67:2798, 1995.

[180] G. S. Woods and A. T. Collins. *J. Phys. Chem. Solids*, 44:471, 1983.

[181] I. Kiflawi, D. Fisher, H. Kanda, and G. Sittas. The creation of the 3107cm^{-1} hydrogen absorption peak in synthetic single crystal diamond. In J. E. Field, editor, *Diamond Conference, Cambridge 1996*, page 28, United Kingdom, 1996. De Beers Industrial Diamond Division.

[182] N. M. Johnson, D. K. Biegelsen, and M. D. Moyer. *Appl.Phys.Lett.*, 40:882, 1982.

[183] N. H. Nickel, N. M. Johnson, and C. G. Van de Walle. *Phys. Rev. Lett.*, 72:3393, 1994.

[184] M. Mermoux, F. Roy, B. Marcus, L. Abello, and G. Lucazeau. *Diamond and Related Materials*, 1:519, 1992.

[185] National Biomedical ESR Centre, Medical College of Wisconsin, MACC Fund Research Center Building, 8701 Watertown Plank Road, Milwaukee, WI 53226 USA. WWW: http://www.biophysics.mcw.edu/BRI-EPR.

[186] W. Froncisz and J. S. Hyde. *J. Magn. Reson.*, 47:515, 1982.

[187] S. Zhang, S. C. Ke, M. E. Zvanut, H. T. Tohver, and Y. K. Vohra. *Phys. Rev. B*, 49:15392, 1994.

[188] G. D. Watkins and J. W. Corbett. *Phys. Rev.*, 134:A1359, 1964.

[189] J. H. Freed, D. S. Leniart, and J. S. Hyde. *J. Chem. Phys.*, 47:2762, 1967.

[190] J. M. Baker and M. E. Newton. *Applied Magnetic Resonance*, 7:209, 1994.

[191] K. M. McNamara, D. H. Levy, K. K. Gleason, and C. J. Robinson. *Appl.Phys.Lett.*, 60:580, 1992.

[192] L. A. Shul'man and G. A. Podzyarei. *Teor. Eksp. Khim.*, 1:830, 1965.

[193] L. J. Bellamy. *The Infrared Spectra of Complex Molecules.* Chapman and Hall, New York, 1980.

[194] G. Socrates. *Infrared Characteristic Group Frequencies.* Wiley, New York, 1980.

[195] R. P. Chin, J. Y. Huang, Y. R. Shen, T. J. Chuan, H. Seki, and M. Buck. *Phys. Rev. B*, 45:1522, 1992.

[196] S. Mitra and K. K. Gleason. *Diamond and Related Materials*, 2:126, 1993.

[197] G. Davies and T. Evans. *Proc.R.Soc. London Ser. A.*, 277:413, 1972.

[198] R. M. Chrenko, R. E. Tuft, and H. M. Strong. *Nature (London)*, 270:141, 1977.

[199] A. T. Collins. *J.Phys.C.*, 13:2641, 1980.

[200] T. Evans and Z. Qi. *Proc.R.Soc. London Ser. A.*, 381:159, 1982.

[201] T. Evans. The agregation of nitrogen. In J.E. Field, editor, *The Properties of Natural and Synthetic Diamond*, chapter 6. Academic, London, 1992.

[202] A. T. Collins. In *Inst. Phys. Conf. Ser. No. 59*, page 247, London, 1981. Institute of Physics.

[203] S. A. Fairhurst, D. G. Gillies, and L. H. Sutcliffe. *Spectroscopy World*, 2:14, 1990.

[204] S. S. Eaton and G. R. Eaton. Electron spin resonance imaging. In M. K. Bowman and L. Kevan, editors, *Modern pulsed and continuous wave electron spin resonance*, chapter 9. 1990.

[205] G. R. Eaton, S. S. Eaton, and K. Ohno, editors. *EPR Imaging and In Vivo EPR*. CRC, Boca Raton, FL., 1991.

[206] M. J. R. Hoch and A. R. Day. *Solid State Comm.*, 30:211, 1979.

[207] M. J. R. Hoch. In *Diamond Conference, Reading*, page 128. Unpublished, 1988.

[208] S. S. Eaton and G. R. Eaton. *J. Magn. Reson.*, 59:474, 1984.

[209] E. V. Galtseva, O. Ye Yakimchenko, and S. Ya Lebedev. *Chem. Phys. Lett.*, 99:301, 1983.

[210] D. A. Cleary, Y.-K. Shin, D. J. Shneider, and J. H. Freed. *J. Magn. Reson.*, 79:474, 1988.

[211] H. J. Halpern, D. P. Spencer, J. van Polen, M.K . Bowman, A. C. Nelson, E. M. Dowey, and B. A. Teicher. *Rev. Sci. Instrum.*, 60:1040, 1989.

[212] K. Ohno. *J. Magn. Reson.*, 64:109, 1985.

[213] K. Ohno. *Jap. J. Appl. Phys.*, 23:L224, 1984.

[214] T. Herrling, N. Klimes, W. Karthe, U. Ewert, and B. J. Ebert. *J. Magn. Reson.*, 49:203, 1982.

[215] G. G. Maresch, A. Grupp, M. Mehring, J. U. von Shutz, and H. C. Wolf. *J. Physique*, 46:461, 1985.

[216] D. J. Sloop, H.-L. Yu, and T.-S. Chen. *Chem. Phys. Lett.*, 99:301, 1986.

[217] D. J. Lurie, D. M. Bussell, L. H. Bell, and J. R. Mallard. *J. Magn Reson.*, 76:366, 1988.

[218] M. M. Maltempo. *J. Magn Reson.*, 69:156, 1986.

[219] R. Turner. Gradient coil systems. In D. M. Grant and R. K. Harris, editors, *Encyclopedia of Nuclear Magnetic Resonance*, page 2223. John Wiley, Chichester, 1996.

[220] W. Karthe and E. Wehrsdorfer. *J. Magn. Reson.*, 33:107, 1979.

[221] M. J. R. Hoch. *Solid State Comm.*, 14:5659, 1981.

[222] W. E. Blass and G. W. Halsey, editors. *Deconvolution of Absorption Spectra*. Academic Press, New York, 1981.

[223] R. K. Woods, W. B. Hyslop, R. B. Marr, and P. C. Lauterbur. Image reconstruction. In G. R. Eaton, S. S. Eaton, and K. Ohno, editors, *EPR Imaging and In Vivo EPR*, chapter 10. CRC, 1991.

[224] G. N. Ramachandran and A.V. Lakshiminarayan. *Proc. Natl. Acad. Sci. U.S.A.*, 68:2236, 1971.

[225] L. A. Shepp and B. F. Logan. *I.E.E.E. Trans. Nucl. Sci.*, NS-21:21, 1974.

[226] H. H. Barrett and W. Swindell. *Proc. I.E.E.E.*, 65:89, 1977.

[227] G. Z. Cao, J. J. Schermer, W. J. P. van Enckevort, W. A. L. M. Elst, and L. J. Gilling. *J.Appl.Phys.*, 79:1357, 1996.

[228] W. Müller-Sebert, E. Wörner, F. Fuchs, C. Wild, and P. Koidl. *Appl.Phys.Lett.*, 68:759, 1996.

[229] P. K. Bachmann and D. U. Weichert. *Diamond and Related Materials*, 1:422, 1992.

[230] R. C. Burns, V. Cvekovic, C. N. Dodge, D. J. F. Evans, M.-L. T. Rooney, P. M. Spear, and C. M. Welbourn. *J. Cryst. Growth*, 104:257, 1990.

[231] D. J. Twitchen, M. E. Newton, J. M. Baker, O. D. Tucker, T. R. Anthony, and W. F. Banholzer. *Phys. Rev. B.*, 54:6988, 1996.

[232] J. A. van Wyk and J. H. N. Loubser. *J.Phys.C.*, 16:1501, 1983.

[233] M. McNamee. D.Phil thesis, 1992. University of Oxford.